RELAXATION IN GLASSY SYSTEMS

LIGHT-SCATTERING STUDY OF IN AND OUT OF EQUILIBRIUM DYNAMICS

TECHNISCHE
UNIVERSITÄT
DARMSTADT

Vom Fachbereich Physik
der Technischen Universität Darmstadt

zur Erlangung des Grades
eines Doktors der Naturwissenschaften (Dr. rer. nat.)

genehmigte Dissertation von
TILL LUKAS BÖHMER

1. Gutachten: Apl. Prof. Dr. Thomas Blochowicz
2. Gutachten: Prof. Dr. Michael Vogel
3. Gutachten: Prof. Dr. Jeppe C. Dyre

Darmstadt 2024

Relaxation in Glassy Systems - Light-scattering study of in and out of equilibrium dynamics

Genehmigte Dissertation von Till Lukas Böhmer

ERSTGUTACHTER: Apl. Prof. Dr. Thomas Blochowicz
ZWEIT- UND DRITTGUTACHTER: Prof. Dr. Michael Vogel und Prof. Dr. Jeppe C. Dyre

TAG DER EINREICHUNG: 13. Mai 2024
TAG DER PRÜFUNG: 19. Juni 2024

Darmstadt, Technische Universität Darmstadt
Jahr der Veröffentlichung der Dissertation auf TUprints: 2024

Bitte zitieren Sie dieses Dokument als:
URN: urn:nbn:de:tuda-tuprints-279025
URI: https://tuprints.ulb.tu-darmstadt.de/id/eprint/27902

Dieses Dokument wird bereitgestellt von tuprints,
E-Publishing-Service der TU Darmstadt
http://tuprints.ulb.tu-darmstadt.de
tuprints@ulb.tu-darmstadt.de

ABSTRACT

Supercooled liquids and glasses are universally characterized by the non-Arrhenius temperature-dependence of relaxation times, the non-exponential shape of the α-process and the non-linear response to temperature changes. Despite decades of research, a comprehensive theory of the glass-transition phenomenon is still pending. The present work attempts to contribute to the understanding of two of the three aspects by employing dynamic light scattering experiments.

In the frequency domain, the non-exponential shape of the α-process manifests as an asymmetrically broadened relaxation peak with $\nu^{-\beta}$ high-frequency behavior. For molecular supercooled liquids, the common belief based on results from dielectric spectroscopy has been that values of β depend on the molecular structure and are distributed between 0.3 and 1. On the contrary, it is shown for various supercooled liquids that the relaxation shape of the α-process probed by dynamic light scattering shows a generic $\nu^{-1/2}$ high-frequency behavior. The discrepancy with regard to results from dielectric spectroscopy is resolved by showing that dipolar cross-correlation contributions influence the relaxation shape considerably and lead to larger values of β. Building on this, a quantitative relation between β and the degree of static dipolar cross-correlations quantified in terms of the Kirkwood correlation factor g_K is established. It resolves the previously identified empirical correlation between β and the dielectric relaxation strength. The developed concepts are applied to disentangle the relaxation spectra of hydrogen-bonding supercooled liquids, which are complex to interpret due to containing different contributions associated with structure-formation. Cross-correlation effects also contribute considerably to relaxation spectra of asymmetric binary mixtures. In this regard it is shown that solute-induced solvent-solvent cross-correlations are the origin of apparent slow solvent relaxation, which are commonly observed in binary mixtures.

The non-linear response to temperature changes is universal for physical aging, i.e. the slow and gradual evolution of material properties. One formalism for describing physical aging is the concept of material time, which can be thought of as time measured on a clock whose rate changes as the glass ages. Material time, however, has never been determined experimentally. Here, multispeckle dynamic light scattering is used to probe time-resolved intensity autocorrelation functions of an aging molecular glass. It is demonstrated that the material time can be extracted from these data. Going further, it is shown that time-irreversible thermal fluctuations during aging become reversible when replacing time with material time. Also other aging materials are shown to obey material-time reversibility, i.e. a physically aging colloidal glass, a chemically aging polymerizing epoxy and a physically aging computer-simulated glass. Thus, the present work confirms aging of various different systems being controlled by a material time. Finally, the evolution of the material-time clock rate is explored after small temperature changes and quenches deep into the glassy state. The former can be described in terms of a simple logistic differential equation, while a sub-linear aging behavior is observed for the latter, thus challenging current theories of physical aging.

KURZZUSAMMENFASSUNG

Die nicht-arrheniusartige Temperaturabhängigkeit der Relaxationszeit, die nicht-exponentielle Form des α-Prozesses sowie die nicht-lineare Antwort auf Temperaturänderungen sind universelle Eigenschaften unterkühlter Flüssigkeiten und Gläser. Trotz jahrzehntelanger Forschung existiert bis heute keine allumfassende Theorie des Glasübergangs. Die vorliegende Arbeit trägt mittels dynamischer Lichtstreuexperimenten (DLS) an unterkühlten Flüssigkeiten und Gläsern zum Verständnis von zwei der drei diskutierten Aspekte bei.

In der Frequenzdarstellung zeigt sich die nicht-exponentielle Form des α-Prozesses als asymmetrisch verbreiterter Relaxationspeak mit $\nu^{-\beta}$-Hochfrequenzverhalten. Ausgehend von Ergebnissen der dielektrischer Spektroskopie (DS) wurde bisher angenommen, dass β abhängig von der molekularen Struktur ist und Werte zwischen 0.3 und 1 annimmt. Stattdessen zeigen nun DLS-Ergebnisse ein generisches $\nu^{-1/2}$-Hochfrequenzverhalten für unterschiedliche unterkühlte Flüssigkeiten. Der Widerspruch zu DS-Ergebnissen erklärt sich durch dipolare Kreuzkorrelationsbeiträge, die das Hochfrequenzverhalten erheblich beeinflussen und zu größeren Werten von β führen. Ausgehend davon wird eine quantitative Beziehung zwischen β und dem Kirkwood-Korrelationsfaktor hergestellt. Letzterer quantifiziert die Stärke statischer dipolarer Kreuzkorrelationen. Der ermittelte Zusammenhang liefern eine physikalische Erklärung für die empirisch beobachtete Korrelation zwischen β und der dielektrischen Relaxationsstärke. Die im Rahmen der Arbeit entwickelten Konzepte werden zudem angewandt um Relaxationsspektren verschiedener wasserstoffbrückenbildender Systeme zu entschlüsseln, deren Interpretation aufgrund von Überlagerung unterschiedlicher Beiträge erschwert ist. Auch zum Relaxationsverhalten asymmetrischer binärer Mischungen tragen Kreuzkorrelationseffekte erheblich bei. Ferner sind Orientierungskreuzkorrelationen zwischen Lösungsmittelmolekülen die Ursache für das Auftreten augenscheinlich langsamer Lösungsmitteldynamik, die häufig in binären Mischungen beobachtet wurde.

Die nichtlineare Antwort auf Temperaturänderungen ist universell für physikalische Alterungsprozesse in Gläsern. Ein Formalismus zur Beschreibung physikalischer Alterung ist das Konzept der Materialzeit, die als Zeitmaß betrachtet werden kann, dessen Rate sich mit dem Altern des Glases verändert. Die Materialzeit konnte jedoch bisher nicht experimentell bestimmt werden. Um dieses Ziel zu erreichen wird in der vorliegenden Arbeit multispeckle-DLS eingesetzt, wodurch die Intensitätsautokorrelationsfunktionen eines alternden molekularen Glases mit Zeitauflösung bestimmt werden können. Mithilfe eines iterativen Verfahrens lässt sich daraus die Materialzeit extrahieren. Zusätzlich zeigt sich, dass die zeitlich unumkehrbaren thermische Fluktuationen während des Alterns zeitumkehrbar werden, wenn sie statt als Funktion der Zeit, als Funktion der Materialzeit betrachtet werden. Auch verschiedene andere alternde Materialien verhalten sich materialzeitumkehrbar, wie für ein physikalisch alterndes Kolloidglas, ein chemisch alterndes Epoxidpolymer und ein physikalisch alterndes simuliertes Glas gezeigt wird. Abschließend wird untersucht wie sich die Rate der Materialzeit im Falle kleiner Temperaturänderungen und nach dem Abkühlen weit unterhalb die Glasübergangstemperatur entwickelt. Ersteres Szenario wird durch eine einfache logistische Differentialgleichung beschrieben, während in letzterem ein sublineares Verhalten bezüglich der Wartezeit beobachtet wird.

CONTENTS

1

INTRODUCTION

Once a liquid is cooled below its melting point while avoiding crystallization it is referred to as being *supercooled* [1]. Supercooling a liquid leads to a dramatic slowdown of its structural relaxation: While the characteristic relaxation times above the melting point are of the order of picoseconds, they ranges from nanoseconds to seconds for supercooled liquids, depending on the exact temperature. As a material's viscosity is usually coupled to structural relaxation, supercooled liquids are highly viscous and flow slowly. Upon further cooling, structural relaxation becomes so slow that its characteristic time scale exceeds typical periods of observation, such that the material effectively behaves like a solid. It is then referred to as a *glass*. Clearly, this definition of glassiness depends on what timescale of observation is considered. To give a more precise definition, supercooled liquids are in metastable *thermal equilibrium*, while glasses are *out of equilibrium* systems. Remarkably, unlike in crystal formation, no significant changes of the microscopic structure are observed during the transition from liquid to glass, thus glasses are considered as disordered solids.

In fact, a broad variety of materials appearing in everyday life are glasses, which however can be very different in terms of their molecular structure: Most materials referred to as a "glass" in current language are obtained from inorganic melts [2, 3], e.g. SiO_2; plastics are polymer glasses made from long chain-like molecules composed of repeating subunits [4, 5]; but glasses are also made from metal alloys [6], or from non-polymeric organic liquids [7]. Finally, some systems are not composed of molecules, but share many similarities with molecular glasses and, thus, attract attention as model systems. These are spin glasses [8, 9], i.e. disordered compositions of interacting spins, and colloidal glasses [10, 11], i.e. densely packed colloid particles dissolved in a liquid solvent, for which the colloid volume-fraction instead of temperature is the control parameter that drives the glass transition.

Although all these materials can have quite different properties reflecting their specific microscopic composition, they all share some fundamental similarities due to them being glassy. Despite their relevance and frequent use in everyday life, a comprehensive theory of the glass transition phenomenon able to explain the physical origin of the extreme slow-down of microscopic dynamics and other universal features of supercooled liquids and glasses is lacking.

The universal characteristics of supercooled liquids and glasses can be expressed in terms of *the three non's* [12]. These are the *non-Arrhenius* temperature dependence of relaxation times, the *non-exponential* relaxation shape of the structural-relaxation process and the *non-linearity* of the response to temperature changes. While the three non's are interconnected, each of them can be discussed independently from the others, as will be done in the following paragraphs.

Non-Arrhenius temperature dependence of relaxation times

The average structural relaxation time τ of a liquid above its melting point approximately evolves as an exponential function of temperature [13]

$$\tau(T) \propto \exp\left(\frac{E}{k_B T}\right) \tag{1.1}$$

i.e. an Arrhenius law with a constant activation energy E. By contrast, the temperature dependence of structural relaxation times in the supercooled regime is super-Arrhenius, meaning the activation energy increases as a function of decreasing temperature. It is commonly modeled in terms of the empirical Vogel-Fulcher-Tammann (VFT) equation [14–16]

$$\tau(T) \propto \exp\left(\frac{E}{k_B(T-T_0)}\right), \tag{1.2}$$

which assumes a divergence of the relaxation time at some temperature T_0 below the glass-transition temperature T_g . There, however, exists no clear experimental evidence, but rather reasonable doubt regarding the existence of this divergence [17, 18].

The physical origin of the super-Arrhenius temperature-evolution of relaxation times is commonly believed to be associated with cooperative dynamics [19, 20]. While particles can move independently from their vicinity in the liquid phase, particle-density is larger in the supercooled-liquid state, which requires associations of particles to move cooperatively, thus leading to a larger activation energy compared to the liquid state. The increase of the activation energy with decreasing temperature is thought to reflect a gradually increasing cooperativity length-scale. But also other explanation exist that do not explicitly assume cooperativity as the origin of the super-Arrhenius behavior [21–24].

In fact, the degree of non-Arrhenius behavior varies among different materials, as best seen by plotting $\tau(T/T_g)$ of various supercooled liquids. The degree of non-Arrhenius behavior is quantified by the concept of fragility

$$m = \left.\frac{\mathrm{d}\log\tau}{\mathrm{d}\left(T/T_g\right)}\right|_{T_g} \tag{1.3}$$

proposed by Angell et al. [7], which uses the logarithmic slope of $\tau(T/T_g)$ at T_g as a measure for non-Arrhenius behavior. Supercooled liquids with large m are called *fragile*, while those with rather small m are referred to as *strong*.

Non-exponential relaxation shape

Relaxation functions of systems associated with a single structural relaxation time decay exponentially [13]. Accordingly, the respective relaxation spectra are Lorentzian-shaped, thus they appear in a double-logarithmic plot as a symmetric peak that evolves towards higher res. lower frequencies as ω^1, res. ω^{-1}. By contrast, relaxation functions reflecting structural relaxation in supercooled liquids are *non-exponential* and the respective relaxation spectra are asymmetrically broadened with $\omega^{-\beta}$, $\beta < 1$ high-frequency behavior.

The most common interpretation of the asymmetrical broadening is *dynamic heterogeneity*, in the sense that different subregions of the system are associated with different relaxation times [19, 20, 25–29]. Each subregion is commonly assumed to contribute to the overall relaxation spectrum as a Lorentzian, while their superposition finally yields an asymmetrically

broadened peak. In fact, dynamic heterogeneity in supercooled liquids is not static. Comparably fast relaxing regions have been slow before, and eventually will become slow again as the system evolves [27, 28]. Recent results support the idea of dynamic facilitation, in the sense that fast relaxing localized regions facilitate relaxation in their vicinity, thus leading to a propagation of relaxation events throughout the system [30, 31].

Characterizing dynamic heterogeneity and determining its physical origin is considered important in order to advance the understanding of the glass-transition phenomenon. In this regard, extensive experimental effort has been invested into characterizing dynamic heterogeneity of various different supercooled liquids by analyzing their respective structural relaxation shapes [32–34]. Identifying general themes and patterns within the variety of experimentally observed relaxation shapes remains an ongoing task within the field. Especially identifying universal characteristics of the relaxation shape in supercooled liquid would be promising, as it might point towards universal features of dynamic heterogeneity.

Non-linear response to temperature changes

As discussed briefly above, a glass is obtained once a supercooled liquid falls out of equilibrium due to structural relaxation becoming too slow. Because the relaxation time remains finite in the glassy state, however, all glasses slowly relax towards an equilibrium state [5, 35, 36]. This process is referred to as *physical aging* and, depending on the temperature the glass is kept at, it proceeds on timescales ranging from minutes to billions of years. The physical-aging response to temperature changes is non-linear, as it critically depends, e.g., on whether temperature up- or down-jumps are considered [36, 37]. Generally, physical aging depends on the system's history since it entered the glassy state, which is often referred to as a *memory effect*.

The non-linear behavior of glasses is usually rationalized by considering that during aging the system's relaxation rate evolves as a function of time. It is believed that compensating for these effects recovers a linear-response behavior, which is the basic idea behind the *material-time* formalism postulated by Narayanaswamy [38]. While there is evidence supporting this conjecture under specific experimental conditions [39–43], the material time has never been determined experimentally and little is known about the limitations of the formalism's applicability. Exploring these open questions, however, is challenging, as it requires to probe the time-evolution of the molecular dynamics within aging glasses. This is notoriously difficult, because most experimental techniques require extensive temporal averaging and, thus, cannot provide time-resolved access to the molecular dynamics of glasses.

This work sets out to contribute to the understanding of the physics behind two of the three non's, namely the non-exponential structural relaxation shape of equilibrium supercooled liquids in Part I, and the non-linear response to temperature changes of non-equilibrium glasses in Part II. The main experimental technique applied within this work is depolarized dynamic light scattering (DDLS), where the light scattered from supercooled or glassy samples is analyzed in order to draw conclusions on the fluctuations of molecular orientations within the sample. DDLS is complemented by dielectric spectroscopy (DS), where the frequency-dependent dielectric response of samples is analyzed. The theoretical background of both experimental techniques is discussed in Chapter 2.

In Part I results regarding the relaxation shape of structural relaxation in various different supercooled liquids are reported. Chapter 3 serves as an introduction by providing a review of

the physical origin of the asymmetrically broadened structural relaxation shape, establishing its connection to dynamic heterogeneity and discussing approaches to quantify it in terms of model functions or by applying model-free approaches.

In Chapter 4 the conjecture of a *generic structural relaxation shape* in supercooled liquids is discussed. It is shown that the structural relaxation shapes of many supercooled liquids featuring a wide variety of molecular structures are strikingly similar and display a $\nu^{-1/2}$ high-frequency behavior. These results build on earlier analyses published by Florian Pabst [44]. Moreover, it is shown that structural relaxation shapes of selected supercooled liquids obey *time-temperature superposition*, meaning it is independent of temperature if analyzed closely above T_g . Finally, the question as to what is special about the $\nu^{-1/2}$ high-frequency behavior and how it might relate to recent developments in the field is pursued.

Contrary to what is observed in DDLS, the structural relaxation shape probed by means of DS does not generally conform to the generic $\nu^{-1/2}$ high-frequency behavior and, instead, a broad variety of power law exponents $0.3 < \beta < 1$ is observed for different supercooled liquids. Again building on earlier work [44] Chapter 5 argues that *dipolar cross-correlations* contribute considerably to dielectric relaxation spectra of certain types of supercooled liquids. These cross-correlations superimpose the generic $\nu^{-1/2}$ high-frequency behavior, thus leading to various other power law exponents. The conjecture is shown to conform to experimental results obtained upon suppression of cross-correlations, as well as to various recent results in the literature. Finally, a quantitative relation between the high-frequency power law exponent β and the degree of dipolar cross-correlations is established.

Hydrogen-bonding supercooled liquids display especially complex relaxation behavior, which makes it difficult to distinguish between various contributions to their relaxation spectra. Building on the concepts established in previous chapters, Chapter 6 attempts to disentangle these different contributions by combining results from DDLS and DS. In particular, the influence of molecular architecture on the dynamics of hydrogen-bonded supra-structures is explored by analyzing isomeric or homologous series of substances, i.e. phenyl propanols, octanols and polyhydric alcohols. The comparison reveals cross-correlation effects as well as different intra-molecular relaxation mechanisms that superimpose structural relaxation and sensitively depend on molecular architecture.

Chapter 7 presents an analysis of the solvent dynamics in an asymmetric binary mixture. While relaxation in binary mixtures displays various characteristics different from what is observed in pure supercooled liquids, both have in common that cross-correlations can contribute considerably to the respective relaxation spectra. It is shown by combining experimental and computer-simulation results that the apparent slow solvent relaxation, which is commonly observed in different asymmetric binary mixtures, results from solute-induced solvent-solvent cross-correlation effects.

Part II deals with non-equilibrium glasses that age and, thus, evolve as a function of time. After summarizing some fundamental characteristic of physical aging in Chapter 8, Chapter 9 introduces multispeckle dynamic light scattering (msDLS) as the experimental technique applied to analyze non-equilibrium samples. By probing various different speckles of the scattered light by means of a camera and by performing a speckle-average instead of temporal averaging, msDLS allows to monitor the time-resolved structural relaxation dynamics of aging samples. Finally, the msDLS setup optimized within this work, as well as the sample cells and the related temperature control for physical aging experiments are discussed.

In Chapter 10 the material time of physical aging is determined experimentally for the first time. Initially, the material-time concept and required theoretical tools are established, which subsequently allow to confirm the existence of a material time and to introduce a procedure

in order to extract the material time from time-autocorrelation functions probed by means of msDLS. Finally, it is confirmed that the extracted material time does linearize physical aging according to its definition within the Tool-Naranayaswamy-Moynihan formalism.

The material-time formalism is remarkable by recovering equilibrium properties for non-equilibrium glasses. Expanding on this, Chapter 11 introduces the conjecture of material-time reversibility, which is the idea that irreversible thermal fluctuations during aging become reversible by replacing time with material time. The conjecture is verified for the intensity fluctuations of light scattered from an aging molecular glass. Also three other aging materials are shown to obey material-time reversibility, i.e. a colloidal glass, a polymerizing epoxy and a computer-simulated glass with Lennard Jones-type interactions.

After having established the existence of a material-time and its general properties, Chapter 12 explores how exactly the material time evolves as a function of time. In this regard, a simple model is proposed for describing physical aging after small temperature jumps. Moreover, aging after deep quenches into the glassy state is shown to violate common theoretical predictions.

2

EXPERIMENTAL TECHNIQUES

The following chapter introduces the necessary experimental basics that are required for the subsequent discussions of the results obtained within the present work. Section 2.1 introduces some fundamental concepts related to quantifying relaxation in supercooled liquids and glasses, namely autocorrelation functions, dynamic susceptibilities and the relations between both. The subsequent sections 2.2 and 2.3 specifically discuss the two main techniques applied during the present work, dynamic light scattering (DLS) and dielectric spectroscopy (DS). Here, the main focus is on how the measured quantities relate to the molecular dynamics of supercooled molecular liquids.

2.1 QUANTIFYING MICROSCOPIC RELAXATION DYNAMICS

Two main approaches can be distinguished to access relaxation dynamics in supercooled liquids and glasses: (i) Analyzing the equilibrium fluctuations of some quantity that reflects the fluctuations of molecular positions and orientations, and (ii) applying an external perturbation that drives the system out of equilibrium and, subsequently, monitoring its relaxation towards the new equilibrium state. It will be shown below that, ultimately, both approaches are equivalent in the limits of small external perturbations.

A system's microscopic fluctuations can be accessed by probing some property $X(\Gamma)$, the value of which depends on the system's state Γ within its phase space, meaning X is a function of the positions and orientations of molecules. Translational or orientational fluctuations of the molecules as a function of time, expressed in terms of a phase-space trajectory $\Gamma(t)$, translate into fluctuations of X.

To quantify these fluctuations it is convenient to solely regard the zero-mean fluctuations $\Delta X(t) = X(t) - \langle X \rangle$ with regard to the average value

$$\langle X \rangle = \int X(\Gamma)\rho(\Gamma)\,\mathrm{d}\Gamma, \tag{2.1}$$

given by the ensemble average of X that is expressed in terms of the probability $\rho(\Gamma)$ to observe the system in the state Γ. From the fluctuations $\Delta X(t)$, the normalized time autocorrelation function is obtained as

$$C_X(t, t+\Delta) = \frac{\left\langle \Delta X(t) \cdot \Delta X(t+\Delta t) \right\rangle}{\sqrt{\left\langle \left(\Delta X(t)\right)^2 \right\rangle \left\langle \left(\Delta X(t+\Delta t)\right)^2 \right\rangle}} = \frac{\left\langle \Delta X(t) \cdot \Delta X(t+\Delta t) \right\rangle}{\left\langle \left(\Delta X(t)\right)^2 \right\rangle}, \tag{2.2}$$

Here, the second equation only holds in equilibrium, i.e. when the fluctuations are stationary. For some fixed t, $C_X(t, t+\Delta)$ decays to zero for $\Delta t \to \infty$ and the characteristic time scale of

its decay is associated with the characteristic time scale of molecular dynamics within the system.

As the ensemble average can not be determined in experiments or computer-simulations, it is often replaced by a temporal average $\langle ... \rangle_t$. According to the ergodic hypothesis, the ensemble average is identical to a time average over a sufficient long period of time for equilibrium systems, because the average time the system occupies some state Γ within phase space is proportional to $\rho(\Gamma)$. In order to replace the ensemble average by a temporal average, the autocorrelation function should solely depend on the lag-time Δt, such that

$$C_X(\Delta t) = \frac{\left\langle \Delta X(t) \cdot \Delta X(t+\Delta t) \right\rangle_t}{\left\langle \left(\Delta X(t)\right)^2 \right\rangle_t}. \tag{2.3}$$

It is emphasized that the ensemble average can not be replaced by a time average for system that behave non-stationary, e.g. for many non-equilibrium systems like physically aging glasses.

For stationary processes the spectral density of the fluctuations $\Delta X(t)$ can be obtained as the Fourier transform of the autocorrelation function according to the Wiener-Khinchin theorem [13, 45, 46], i.e.

$$\hat{S}_X(\omega) = \int_0^\infty C_X(t) \exp(-\mathrm{i}\omega t)\ \mathrm{d}t. \tag{2.4}$$

As mentioned above, besides probing the fluctuations of X, another approach is to apply an external perturbation and to probe the system's response. For instance, consider X being the system's electric polarization $\boldsymbol{P}$, one could – instead of probing the equilibrium polarization fluctuations – apply an electric field and study the system's polarization response. While sometimes step-like external perturbations are applied, many experiments instead use harmonic external fields $\boldsymbol{F}(t,\omega) = \boldsymbol{F}_0 \exp(i\omega t)$. In the limit of weak external fields, the response of the system $\boldsymbol{R}(\omega)$ is linear to the applied field and can be expressed in terms of the dynamic susceptibility $\hat{\chi}(\omega)$ as

$$\boldsymbol{R}(\omega) = \hat{\chi}(\omega)\boldsymbol{F}(\omega). \tag{2.5}$$

$\hat{\chi}(\omega)$ is a complex quantity

$$\hat{\chi}(\omega) = \chi'(\omega) - \mathrm{i}\chi''(\omega), \tag{2.6}$$

with the real part χ' and the imaginary part χ''. Here, $\chi'(\omega)$ represents the non-dissipative and $\chi''(\omega)$ the dissipative part of the response.

The dynamic susceptibility obtained within a linear response experiment is related to the spectral density of the corresponding fluctuations via the fluctuation-dissipation relation [47]

$$\hat{\chi}(\omega) = \frac{c}{k_\mathrm{B} T}\left(1 - \mathrm{i}\omega\hat{S}(\omega)\right), \tag{2.7}$$

where c depends on the experiment under consideration [48]. For the imaginary part of the dynamic susceptibility Eq. (2.7) yields

$$\chi''(\omega) = \frac{c\,\omega}{k_\mathrm{B} T}\int_0^\infty C_X(t)\cos(\omega t)\,\mathrm{d}t. \tag{2.8}$$

Eqs. (2.7) and (2.8) imply that the identical information are obtained by probing microscopic fluctuations in equilibrium and by monitoring the linear response of a system to external perturbations. In the course of the present work, these relations will allow to compare data from different experimental techniques. A detailed discussion of the two main techniques applied in this work, dynamic light scattering and dielectric spectroscopy, will follow in the subsequent chapters.

2.2 DYNAMIC LIGHT SCATTERING

In *dynamic light scattering* (DLS) experiments a sample is illuminated by polarized laser light and the scattered light under the angle θ with respect to the laser beam is probed. The electric field of the scattered light depends on the molecular arrangement within the scattering volume and proper analyses of the scattered light allows to draw conclusions regarding the fluctuations of the molecular arrangement. In the following section, an overview of the theoretical background of DLS is given based on the comprehensive book of Berne and Pecora [49]. The discussion starts by treating light scattering on a macroscopic scale and, finally, these results are extended to the molecular scale in order to establish how DLS can be used to probe the molecular dynamics in supercooled liquids and glasses. The main technique applied during the present work is depolarized dynamic light scattering (DDLS), where only the depolarized scattered light is analyzed. As it will be shown in Section 2.2.1 by means of an approximation for symmetric top molecules, the analysis of the depolarized scattered light allows to monitor the rotational dynamics of molecules. Finally, the experimental implementations of DLS are discussed, namely photon correlation spectroscopy (PCS) and Tandem-Fabry-Perot interferometry (TFPI). Both techniques access different frequency ranges and thus, when combined, can enable a broadband investigation of reorientation dynamics in supercooled liquids. In Part II of this work, multispeckle DLS (msDLS) is applied to study non-equilibrium samples. While the general basics discussed in the following section also apply for msDLS, the specifics will be considered in Chapter 9.

2.2.1 Theoretical Background

In a first step, an expression for the electric field of light scattered from a dielectric medium is derived. It is assumed to be illuminated by a plane electromagnetic wave, which is described in terms of the incident electric field at position $\boldsymbol{r}$ and at time t

$$\boldsymbol{E}_\mathrm{i}(\boldsymbol{r},t) = \boldsymbol{n}_\mathrm{i} E_0 \exp\big(i\,(\boldsymbol{k}_\mathrm{i}\cdot\boldsymbol{r} - \omega_\mathrm{i} t)\big). \tag{2.9}$$

Here, $\boldsymbol{n}_\mathrm{i}$ is the polarization, E_0 the amplitude, $\boldsymbol{k}_\mathrm{i}$ the wave vector and ω_i the angular frequency of the incoming wave indicated by the index i. On a macroscopic scale, the scattering medium is described in term of its local dielectric constant in tensorial representation

$$\boldsymbol{\varepsilon}(\boldsymbol{r},t) = \varepsilon_0 \mathbb{1} + \delta\boldsymbol{\varepsilon}(\boldsymbol{r},t), \tag{2.10}$$

where $\varepsilon_0 = \langle\varepsilon\rangle_{\boldsymbol{r},t}$ is the average dielectric constant and $\delta\boldsymbol{\varepsilon}$ is the local dielectric constant-fluctuation tensor. Based on these definitions, comprehensive electrodynamic calculations yield a description of the scattered electric field. A condensed expression can be obtained by considering the spatial Fourier transform of the dielectric constant-fluctuation tensor

$$\delta\boldsymbol{\varepsilon}(\boldsymbol{q},t) = \int_V \exp\big(i\boldsymbol{q}\cdot\boldsymbol{r}\big)\,\delta\boldsymbol{\varepsilon}(\boldsymbol{r},t)\,\mathrm{d}\boldsymbol{r}, \tag{2.11}$$

where integration is performed over the entire scattering volume V, $\boldsymbol{q} = \boldsymbol{k}_\mathrm{f} - \boldsymbol{k}_\mathrm{i}$ is the scattering vector and $\boldsymbol{k}_\mathrm{f}$ is the wave vector of the scattered light. The portion of the scattered electric field with a certain polarization $\boldsymbol{n}_\mathrm{f}$ is then given by

$$E_\mathrm{s}(\boldsymbol{R},t) = -\frac{k_\mathrm{f}^2 E_0}{4\pi R \varepsilon_0} \exp\big(i(\boldsymbol{k}_\mathrm{f}\boldsymbol{R} - \omega_\mathrm{i} t)\big) \underbrace{\boldsymbol{n}_\mathrm{f} \cdot \delta\boldsymbol{\varepsilon}(\boldsymbol{q},t) \cdot \boldsymbol{n}_\mathrm{i}}_{\delta\varepsilon_\mathrm{if}(\boldsymbol{q},t)}. \tag{2.12}$$

In this equation $\boldsymbol{R}$ is the distance relative to the scattering volume, while the index f indicates the properties of the scattered light. During the derivation of Eq. (2.12) it was assumed that light scattering is quasi-elastic, i.e. $|\boldsymbol{k}_\mathrm{i}| = |\boldsymbol{k}_\mathrm{f}|$. This in turn implies that $\boldsymbol{q}$ solely depends on the scattering angle θ. Although light scattering can be inelastic, which e.g. is utilized in Raman spectroscopy, the techniques applied during the present work do only consider the quasi-elastically scattered light, thus the assumption is justified.

With the scattered electric field being established, the time autocorrelation function of the electric-field is found to be proportional to the time autocorrelation function of dielectric constant fluctuations, i.e.

$$\left\langle E_\mathrm{s}^\star(\boldsymbol{R},0) E_\mathrm{s}(\boldsymbol{R},t)\right\rangle \propto \left\langle \delta\varepsilon_\mathrm{if}^*(\boldsymbol{q},0)\delta\varepsilon_\mathrm{if}(\boldsymbol{q},t)\right\rangle. \tag{2.13}$$

The exact result depends on the polarization of the incoming light, as well as on what polarization of the scattered light is probed, as indicated by the index if. The electric-field autocorrelation function can be accessed indirectly in photon correlation spectroscopy experiments, as will be discussed below.

Eq. (2.4) yields an expression for the corresponding spectral density

$$\hat{S}_\mathrm{if}(\boldsymbol{q},\omega) \propto \int_0^\infty \exp(-i\omega t)\left\langle \delta\varepsilon_\mathrm{if}^*(\boldsymbol{q},0)\delta\varepsilon_\mathrm{if}(\boldsymbol{q},t)\right\rangle \,\mathrm{d}t \tag{2.14}$$

Here, $\omega = \omega_\mathrm{f} - \omega_\mathrm{i}$ represents the frequency shift of the scattered light. Hence, if the local dielectric constant temporally fluctuates within the sample, scattered light with $\omega \neq 0$ is observed at the detector. Vice versa, probing the frequency shift of the scattered light compared to the incoming light allows to draw conclusions on the temporal dielectric-constant fluctuations within the sample. This is the main idea behind Tandem-Fabry-Perot interferometry.

Approach on the molecular scale

Having established how the scattered electric field and the related time autocorrelation function, respectively spectral density depend on temporal and spatial fluctuations of the dielectric constant within the sample, the following considerations relate these results to the molecular scale. Irradiating a molecule by an electromagnetic wave with polarization $\boldsymbol{n}_\mathrm{i}$ induces a molecular dipole moment that can be described in terms of the molecular polarizability tensor $\boldsymbol{\alpha}$. The light with polarization $\boldsymbol{n}_\mathrm{f}$ scattered by the molecule is given by

$$E_\mathrm{if}^\mathrm{mol}(\boldsymbol{R},t) \propto \exp\big(i\boldsymbol{q}\cdot\boldsymbol{R}(t)\big) \underbrace{\big(\boldsymbol{n}_\mathrm{f}\cdot\boldsymbol{\alpha}(t)\cdot\boldsymbol{n}_\mathrm{i}\big)}_{\alpha_\mathrm{if}(t)}. \tag{2.15}$$

The light detected in a DLS experiment is the superposition of light scattered from all N molecules within the scattering volume. Therefore, the total scattered electric field is given by

$$E_\mathrm{if}^\mathrm{mic}(\boldsymbol{R},t) = \sum_{j=1}^{N} E_\mathrm{if}^{\mathrm{mol},j}(\boldsymbol{R},t) = \sum_{j=1}^{N} \alpha_\mathrm{if}^j(t)\exp\big(\mathrm{i}\boldsymbol{q}\cdot\boldsymbol{R}_\mathrm{j}(t)\big), \tag{2.16}$$

where j denotes the j^{th} molecule. Calculating the time autocorrelation function of the scattered electric field yields

$$\left\langle E_{\text{if}}^{\text{mic},\star}(\boldsymbol{R},0)E_{\text{if}}^{\text{mic}}(\boldsymbol{R},t)\right\rangle \propto \sum_{j,k}^{N}\left\langle \alpha_{\text{if}}^{j}(0)\alpha_{\text{if}}^{k}(t)\,\exp\left[i\boldsymbol{q}\left(\boldsymbol{r}_j(t)-\boldsymbol{r}_k(0)\right)\right]\right\rangle \tag{2.17}$$

Without any further assumptions, Eq. (2.17) is difficult to interpret, as in principle, numerous mechanisms can contribute. The majority of the present work considers the depolarized light scattered from pure supercooled liquids and glasses. With this in mind, some assumptions can be discussed that considerably reduce the complexity of Eq. (2.17). First of all, the exponential term considers translational dynamics on length-scales of the order of the light's wavelength, which in pure molecular liquids are much slower than molecular rotations. Thus, the exponential term can be considered being unity to good approximation. Another typical assumption is to disregard cross-terms. Although it will be shown within the present work that this approximation is not always valid, disregarding cross-terms helps to establish a relation that illustrates how DDLS probes the rotational dynamics of molecules. This relation will be derived in the following section, by considering an approximation for the molecular polarizability tensor.

Depolarized scattering from symmetric top molecules

As an approximation, the polarizability tensor of anisotropic molecules is approximated to be cylindrical, or symmetric top, as commonly denoted in the literature. For symmetric top molecules the polarizability tensor reads as

$$\alpha_{ij} = \alpha\delta_{ij} + \underbrace{\beta\left(u_i u_j - \frac{1}{3}\delta_{ij}\right)}_{\beta_{ij}}, \tag{2.18}$$

where u_i (with $i,j \in \{1,2,3\}$) are the components of the unit vector $\boldsymbol{u}$ along the symmetry axis of the cylindrical tensor and δ_{ij} is Kronecker's delta. The constants are given by

$$\alpha = \frac{1}{3}(\alpha_{\parallel} + 2\alpha_{\perp}) \tag{2.19a}$$

$$\beta = (\alpha_{\parallel} - \alpha_{\perp}), \tag{2.19b}$$

where $\alpha_{\parallel}$ and $\alpha_{\perp}$ quantify the polarizabilities of the molecule along and perpendicular to the symmetry axis. The tensor β_{ij} in Eq. (2.18)) is called the optical anisotropy tensor.

These assumptions allow to calculate the self-part of the polarizability-tensor autocorrelation function in Eq. (2.17) for the depolarized (if=vh) polarization geometry. Extensive calculations yield

$$\left\langle E_{\text{vh}}^{\text{mic},\star}(\boldsymbol{R},0)\,E_{\text{vh}}^{\text{mic}}(\boldsymbol{R},t)\right\rangle \propto \langle N\rangle\beta^2\left\langle P_2\left(\boldsymbol{u}(0)\cdot\boldsymbol{u}(t)\right)\right\rangle = \langle N\rangle\beta^2\left\langle P_2\left(\cos\left(\Theta_{\boldsymbol{u}}(t)\right)\right)\right\rangle \tag{2.20}$$

Here, $P_2(x) = (3x^2-1)/2$ is the second-rank Legendre polynomial and $\Theta_{\boldsymbol{u}}(t)$ denotes the angle between $\boldsymbol{u}(0)$ and $\boldsymbol{u}(t)$. Eq. (2.20) represents an approximation of how the decay of the scattered-light electric-field autocorrelation function relates to the rotational dynamics of molecules in (supercooled) liquids. It is emphasized that cross-terms and the exponential term related to translational dynamics from Eq. (2.17) have been disregarded in these considerations following the arguments given above.

2.2.2 Photon correlation spectroscopy

The following section discusses the general concept of photon correlation spectroscopy (PCS) and the experimental implementation used within this work. It is referred to the "standard" PCS experiment that involves temporal averaging and is applied to study equilibrium supercooled liquids. The extension towards the multispeckle experiment for the investigation of non-equilibrium systems used in Part II of this work will be discussed in Chapter 9.

As derived above, the electric-field autocorrelation function contains information on the rotational dynamics of molecules in (supercooled) liquids. In experiments, however, it is not directly accessible, because only the intensity $I = |E|^2$ of the scattered light can be probed by detectors. Thus, the time-averaged normalized intensity autocorrelation function

$$g_2(t) = \frac{\langle I(0)\, I(t)\rangle}{\langle I\rangle^2}. \tag{2.21}$$

is determined in PCS experiments. Here and in the remainder of this section, $\langle ...\rangle$ denotes a moving-time average.

As discussed previously, the autocorrelation function of interest is the one of the scattered electric field

$$g_1(t) = \frac{\langle E^\star(0)E(t)\rangle}{\langle I\rangle}. \tag{2.22}$$

$g_2(t)$ and $g_1(t)$ can be related to each other under certain approximations. However, the exact relation depends on whether only light scattered from the sample is probed at the detector, or whether it is superimposed by additional static-field contributions, e.g. light reflected from the windows of the sample cell. The following section first discusses the two extreme cases, i.e. the homodyne case and the fully heterodyne case, and, subsequently, treats the intermediate case, which is the scenario that is typically encountered in most experiments.

Homodyne Case, Heterodyne Case and Somewhere in Between

In the homodyne case, only light scattered from molecules within the scattering volume is probed by the detectors. The signal can then be considered to represent a superposition of signals from distinct statistically independent subregions within scattering volume. This implies the total electric field probed at the detector to be Gaussian-distributed, which yields the simplest form of the Siegert relation [50]

$$g_2(t) = 1 + \Lambda |g_1(t)|^2. \tag{2.23}$$

Here Λ is the spatial coherence factor, which depends on the geometry of the experiment and in the ideal case equals unity. As will be shown in Chapter 9, Λ can be estimated by probing $g_2(t)$ of a strongly diluted solution of spherical particles and amounts to $\Lambda = 0.98$ for the PCS setup used within this work.

The heterodyne case refers to a scenario where the electric field probed at the detector represents a superposition of light scattered from the sample, $E_\mathrm{s}(t)$, and static local oscillator contributions, $E_\mathrm{LO}(t)$, i.e.

$$I(t) = |E_\mathrm{s}(t) + E_\mathrm{LO}(t)|^2. \tag{2.24}$$

Contrary to $|E_\mathrm{s}(t)|$, $|E_\mathrm{LO}(t)|$ does not fluctuate as a function of t.

In the fully heterodyne limit $|E_{\mathrm{LO}}(t)| \gg |E_{\mathrm{s}}(t)|$, which yields

$$g_2(t) = \frac{\left\langle |E_{\mathrm{s}}(t)+E_{\mathrm{LO}}(t)|^2 |E_{\mathrm{s}}(0)+E_{\mathrm{LO}}(0)|^2 \right\rangle}{\langle |E_{\mathrm{s}}(t)+E_{\mathrm{LO}}(t)|^2 \rangle^2} \approx 1 + 2\frac{I_{\mathrm{s}}}{I_{\mathrm{LO}}}|g_1(t)|. \tag{2.25}$$

Here, $I_{\mathrm{LO}} = \langle |E_{\mathrm{LO}}(t)|^2 \rangle$ and $I_{\mathrm{s}} = \langle |E_{\mathrm{s}}(t)|^2 \rangle$. In contrast to the homodyne case, for which $g_2(t)$ is a quadratic function of $g_1(t)$, the heterodyne case yields a linear relation.

In experiments, some contributions of local oscillator fields might need to be considered, however $|E_{\mathrm{LO}}(t)| \gg |E_{\mathrm{s}}(t)|$ is usually not satisfied. Such intermediate scenarios have been treated by Bremer at al. [51] and later by Pabst et al. [52], which finally yields

$$g_2(t) = 1 + \Lambda C^2 |g_1(t)|^2 + 2\Lambda C(1-C)|g_1(t)|, \tag{2.26}$$

where $C = I_{\mathrm{s}}/(I_{\mathrm{s}}+I_{\mathrm{LO}})$ denotes the relative intensity of light scattered from the sample [51]. The value of C is determined indirectly by solving Eq. (2.26) for $t \to 0$ and considering $g_1(0) = 1$, which for $A = g_2(0) - 1$ yields

$$C = 1 - \sqrt{1 - A/\Lambda}. \tag{2.27}$$

For supercooled liquids, however, it has to be considered that fast dynamics reduce the values of $g_1(t)$ at the shortest available time scale of the PCS experiment, t_0, thus

$$g_1(t_0) = 1 - A_{\mathrm{fast}} = \lambda. \tag{2.28}$$

This finally yields the expression used within the present work [52], i.e.

$$C = \frac{1 - \sqrt{1 + A/\Lambda - 2A/(\lambda\Lambda)}}{2-\lambda}. \tag{2.29}$$

λ can, in principle, be determined by performing TFPI measurements, however is estimated as $\lambda = 0.93$ for most supercooled liquids analyzed within this work. The potential errors resulting from this assumption for the average relaxation times extracted from $g_1(t)$ have been estimated to be small compared to other experimental uncertainties, like e.g. temperature [44].

Due to the limited temporal resolution of the detectors and the hardware correlator, autocorrelation functions are accessible, at best, within $10^{-8}\,\mathrm{s} < t < 10^{2}\,\mathrm{s}$. To access shorter time scales, the spectral density $\hat{S}(\omega)$ of the scattered light can be probed using a TFPI, as will be discussed in the following section.

Experimental Implementation

The PCS setup utilized to study equilibrium supercooled liquids within this work is presented in Fig. 2.1. Here, a Cobolt Samba 500 Nd:YAG laser is used as the light source, emitting frequency-doubled light with $\lambda = 532\,\mathrm{nm}$ in vertical polarization. To further suppress residual horizontal polarization contributions, the light is passed through a vertically orientated polarizer (P1). The beam is directed and focused into the optical Cryovac cold-finger cryostat containing the sample by an adjustable mirror (M) and a converging lens (L). The horizontally polarized scattered light under $\theta = 90°$ is probed by guiding the scattered light through a second polarizer (P2) from B. Halle with extinction ratio 10^{-7}. Subsequently it is filtered by a 2 nm bandpass filter (F) and finally coupled into an optical fiber (FC). The light is split into two portions of equal intensity by a fiber beam splitter (BS) and the intensity of each portion is probed by a Laser Components COUNT T100 avalanche photo diode (APD). The time-averaged intensity autocorrelation function is calculated by an ALV 7004 hardware correlator (CC) and the resulting correlation function $g_2(t)$ is recorded by the ALV software on the computer (PC).

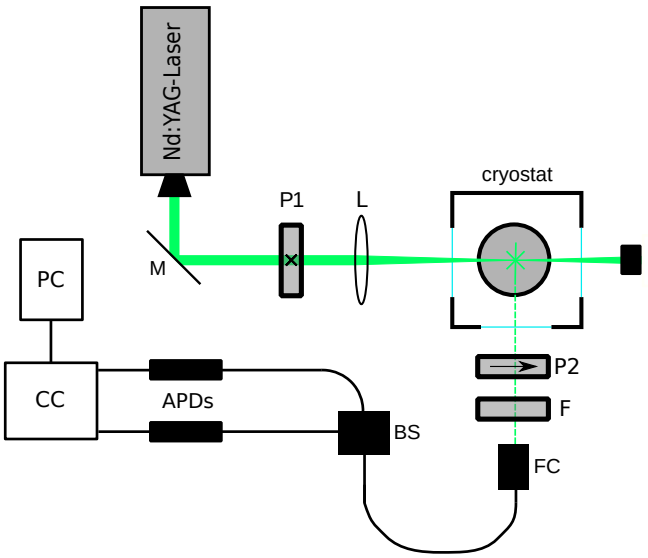

Figure 2.1: Schematic illustration of the PCS setup used within the present work. It contains the following components (see text for details): Nd:YAG laser, mirror (M), two polarizers (P1 and P2), converging lens (L), cryostat with sample cell, bandpass filter (F), fiber coupler (FC), fiber beam splitter (BS), two avalanche photo diodes (APDs), hardware correlator (CC), computer with ALV software (PC)

2.2.3 Tandem Fabry Perot Interferometry

A Tandem-Fabry-Perot interferometer (TFPI) combines two Fabry-Perot interferometers (FPI) to probe the real part of the spectral density of electric-field fluctuations, see Eq. (2.14). It allows to probe the frequency-shift of scattered light with respect to the incoming laser beam between 0.3 GHz and 3 THz, which allows to extend data obtained from PCS experiments to higher frequencies. In the following, first the transmission of a single FPI is discussed, which, subsequently, is extended to the TFPI. Finally, the experimental implementation used within this work is introduced. The following sections follow the book by Hecht [53] as well as the manual of the TFP-1 by Sandercock [54]

The Fabry Perot Interferometer

A FPI consists of two plane-parallel mirrors with spacing d, each of which being highly reflective. Light entering the interferometer is reflected between the mirrors multiple times, while during each reflection cycle only a small portion of the light passes through one of the mirrors. As a result, the transmitted light is subject to multi-beam interference, as each reflection cycle introduces a path length difference of $2d$ (for light entering the FPI perpendicular to the mirror planes).

Considering the interference effects yields a criterion for transmitted light, i.e. the wavelength λ needs to obey

$$d = \frac{1}{2} n\lambda \quad \text{with} \quad n \in \mathbb{N}. \tag{2.30}$$

The full transmission function of the FPI is given by

$$T(\lambda) = \frac{T_0}{1 + (4F^2/\pi^2)\sin^2(2\pi d/\lambda)}, \tag{2.31}$$

where T_0 is the maximum possible transmission and F is the finesse of the FPI. $T(\lambda)$ displays maxima at those wavelengths that obey Eq. (2.30). The spectral separation between two consecutive transmitted wavelengths is denoted as $\Delta\lambda$, or free spectral range (FSR). Transmission peaks are slightly broadened with full width at half maximum (FWHM) $\delta\lambda$. The finesse depends on the reflectivities of the mirrors, but is also related to $\Delta\lambda$ and $\delta\lambda$ as

$$F = \frac{\Delta\lambda}{\delta\lambda}. \tag{2.32}$$

Thus, F quantifies the quality of a FPI in terms of its functionality as a spectrometer.

In order to characterize the spectrum of light scattered from a liquid sample, the mirror spacing d is varied and the transmitted intensity $I(d)$ is probed. According to Eq. (2.30), there only exists a one-to-one relation between $I(d)$ and $I(\lambda)$ within a single FSR, while $I(\lambda)$ can not be determined unambiguously once the spectrum of the scattered light exceeds one FSR. In a TFPI, this issue is resolved by introducing a second FPI with a slightly different mirror spacing, which enhances the FSR of the spectrometer.

The Tandem Fabry Perot Interferometer

In a TFPI, two FPIs with slightly different mirror spacings d_1 and d_2 are coupled. In order for light to be transmitted by both FPIs, two transmission criteria have to be met, i.e.

$$d_1 = \frac{1}{2}n\lambda \qquad d_2 = \frac{1}{2}m\lambda \qquad \text{with } n, m \in \mathbb{N}. \tag{2.33}$$

Fig. 2.2a shows the transmission spectrum of a TFPI for the fixed ratio $d_2/d_1 = 0.95$ as the black line. Global maxima are observed at frequencies where the corresponding wavelength meets both criteria given in Eq. (2.33). For the given choice of $d_2/d_1 = 0.95$, the transmission maxima of both FPIs do coincide only in every 20^{th} order, thus the FSR of the TFPI is twenty times larger than the FSRs of the single FPIs. This allows to characterize light with a significantly larger bandwidth compared to what would be possible by using a single FPI.

Although the basic idea and the advantages of a TFPI are straight-forward, the technical implementation is difficult, as the mirror-spacing ratio d_2/d_1 needs to be fixed while d_1 and d_2 are varied. Within the present work, the high-precession TFP-1 designed by Sandercock and manufactured by Scientific Instruments [54] is used. The following section briefly discusses the TFP-1 and how it is implemented.

TFP-1 and Measurement Set-Up

A schematic illustration of the experimental setup including the TFP-1 is shown in Fig. 2.2b. A frequency-doubled Verdi Coherent Nd:YAG laser is used as the light source. In order to automatically fine-tune the mirror positions and spacings inside the TFP-1, a small portion of the laser light is coupled directly into the TFPI, which is achieved by using a beam splitter and an attenuator to prevent overexposure of the APDs. The residual light is first guided through a polarizer to ensure a vertical polarization of the light and, subsequently, focused into the sample by a small prism and a converging lens. The backscattered light is collected by a converging lens, defocused and finally guided around the prism, where only a small portion of the scattered light is lost. A second lens is used to refocus the light into the pinhole entrance of the TFP-1, while it passes a horizontally orientated polarizer to ensure that only the depolarized portion of the scattered light is probed.

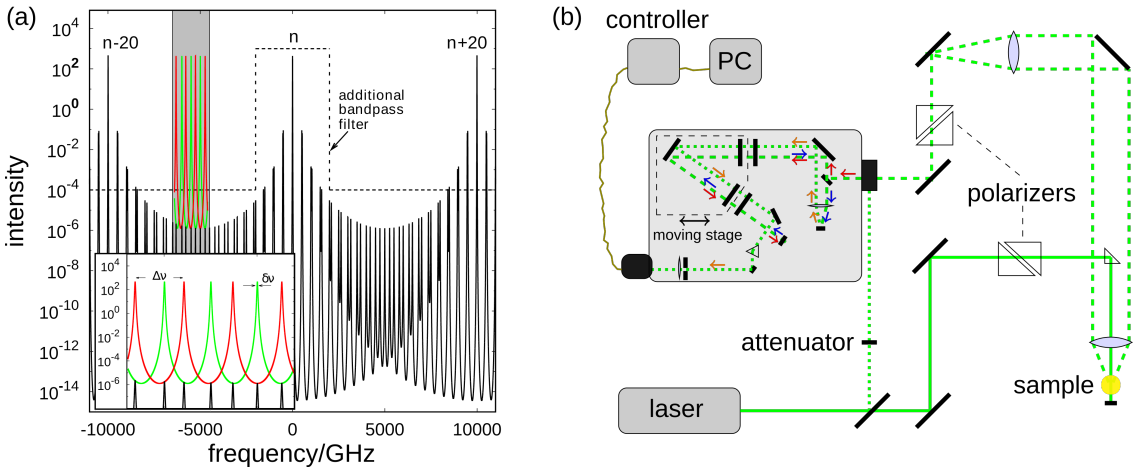

Figure 2.2: (a) Transmission spectrum of a TFPI with $d_2/d_1 = 0.95$. The transmission maxima of both FPIs do only coincide at every 20$^{\text{th}}$ order, which produces a global maximum in the TFPI transmission spectrum. Otherwise, the transmission maxima of both FPIs are not synchronized, as shown in the inset, where the colors indicate the transmission spectra of the respective single FPIs. An additional bandpass filter is used to filter out the $(n-20)^{\text{th}}$ and the $(n+20)^{\text{th}}$ order global maxima. (b) Schematic illustration of the TFPI used within this work. Details can be found in the text. Both figures are adapted from Ref. [48].

The pinhole of the TFPI is equipped with a shutter motor in order to switch between the non-scattered laser beam and the light scattered from the sample entering the TFP-1. The unscattered light is used to fine-tune the mirror positions and orientations. Within the TFP-1, the scattered light is defocused, guided into the the first FPI and, afterwards, into the second FPI. To increase the extinction ratio, the light passes every FPI three times. Finally, the transmitted light is collected and its intensity is probed by a JRS APD connected to the TFPI controller and the PC.

After appropriate adjustments according to the manual [54], one measuring run consists of numerous acquisition runs of 0.5 s each. During one acquisition run, the mirror spacing of both FPIs are varied approx. 500 nm around the coarse-adjusted mirror spacings, which typically are chosen between 3 and 30 mm. The small variations of the mirror spacings are carried out using a specially shaped translation stage, displayed by the dashed line around the mirror pairs in Fig. 2.2b. During an acquisition run it is shifted by piezo elements. The geometry of the translation stage ensures the mirror-spacing ratio to be fixed at $d_2/d_1 = 0.95$. Performing an appropriate number of acquisition runs yields an accurate representation of the spectral density $\mathrm{Re}\,\hat{S}(\omega)$. Repeating the same procedure for different course-adjusted mirror spacings allows to obtain broadband results between 0.3 GHz and 3 THz.

2.3 DIELECTRIC SPECTROSCOPY

In dielectric spectroscopy (DS), the frequency-dependent response of a sample to an external electric field is probed. The following section discusses the theoretical background and relates the dielectric response to the molecular dynamics of supercooled liquids. If not marked otherwise, the discussion grounds on the book by Kremer and Schönhals [47] and the PhD thesis of Thomas Blochowicz [55].

2.3.1 Theoretical Background

Following the considerations in Section 2.1, the linear polarization response to an external harmonic electric field $\boldsymbol{E}(t,\omega)=\boldsymbol{E}_0\exp(i\omega t)$ with angular frequency ω is given by

$$\boldsymbol{P}(t,\omega)=\varepsilon_0\big(\hat{\varepsilon}(\omega)-1\big)\boldsymbol{E}(t,\omega). \tag{2.34}$$

Here, $\hat{\varepsilon}(\omega)$ is the complex dielectric permittivity, which can be expressed in terms of its real part ε' and imaginary part ε'' as

$$\hat{\varepsilon}(\omega)=\varepsilon'(\omega)-\mathrm{i}\varepsilon''(\omega). \tag{2.35}$$

It can be shown that ε' and ε'' are related to each other via the Kramers-Kronig relations [56–58]

$$\varepsilon'(\omega_0)=\varepsilon_\infty+\frac{2}{\pi}\int_0^\infty \varepsilon''(\omega)\frac{\omega}{\omega^2-\omega_0^2}\,\mathrm{d}\omega \tag{2.36}$$

$$\varepsilon''(\omega_0)=\frac{\sigma_{\mathrm{dc}}}{\varepsilon_0\omega_0}+\frac{2}{\pi}\int_0^\infty \varepsilon'(\omega)\frac{\omega}{\omega^2-\omega_0^2}\,\mathrm{d}\omega. \tag{2.37}$$

Taking this into account it becomes clear that ε' and ε'' contain the same information, apart from the high-frequency limit of the dielectric constant

$$\varepsilon_\infty=\lim_{\omega\to\infty}\varepsilon'(\omega) \tag{2.38}$$

and the dc conductivity σ_{dc}. Relevant dc conductivity contributions are observed if the sample contains a substantial amount of ions and, in certain cases, can mask the relevant physics contained in ε''. A conductivity-free representation of ε'' can, in principle, be obtained by utilizing Eq. (2.37), however the calculation of the integral presents a challenge, since it is difficult to evaluate around the integrand's singularity at ω_0 [58]. Instead, the first-order approximation of equation (2.37) can be considered, which yields

$$\varepsilon''_{\mathrm{der}}(\omega)=-\frac{\pi}{2}\frac{\partial\varepsilon'(\omega)}{\partial\ln\omega}, \tag{2.39}$$

where $\varepsilon''_{\mathrm{der}}$ denotes the conductivity-free representation of ε'' [59]. After having established the quantities obtained in a DS experiment, their relation to the microscopic dynamics within the sample are discussed in the following section.

Fluctuation-Dissipation Approach to BDS

As discussed previously in Section 2.1, the complex dielectric permittivity obtained in a DS experiment is related to the equilibrium fluctuations of the polarization at $\boldsymbol{E}=0$ via the fluctuation-dissipation relation. The equilibrium fluctuations are expressed in terms of the normalized orientation-polarization autocorrelation function

$$C_P(t)=\frac{\langle\boldsymbol{P}_{\mathrm{or}}(t)\cdot\boldsymbol{P}_{\mathrm{or}}(0)\rangle}{\langle\boldsymbol{P}_{\mathrm{or}}(0)\cdot\boldsymbol{P}_{\mathrm{or}}(0)\rangle}. \tag{2.40}$$

Here, the orientation polarization $\boldsymbol{P}_{\mathrm{or}}$ is considered, which excludes instantaneous polarization contributions related to ε_∞.

The orientation polarization is related to the total number of N molecular dipoles $\boldsymbol{\mu}$ as

$$\boldsymbol{P}_{\mathrm{or}} = \frac{1}{V}\sum_{j=1}^{N}\boldsymbol{\mu}_j. \tag{2.41}$$

A microscopic interpretation of the orientation-polarization autocorrelation function can be established by explicitly considering n dipoles in a spherical cavity and by treating the remaining $N-n$ dipoles as a continuum [48]. This finally yields

$$C_P(t) = \frac{\left\langle \boldsymbol{\mu}_i(t)\cdot\sum_{j=1}^{n}\boldsymbol{\mu}_j(0)\right\rangle}{\left\langle \boldsymbol{\mu}_i(0)\cdot\sum_{j=1}^{n}\boldsymbol{\mu}_j(0)\right\rangle} = \frac{\left\langle \boldsymbol{\mu}_i(t)\cdot\boldsymbol{\mu}_i(0)\right\rangle + \left\langle \boldsymbol{\mu}_i(t)\cdot\sum_{i\neq j}\boldsymbol{\mu}_j(0)\right\rangle}{\left\langle \boldsymbol{\mu}_i(0)\cdot\sum_{j=1}^{n}\boldsymbol{\mu}_j(0)\right\rangle}. \tag{2.42}$$

Here, the self-correlation and cross-correlation parts are separated in the last equation. While the self-correlations indicate how the orientation of some dipole is correlated to itself at different times, cross-correlations quantify the orientational correlations between adjacent dipoles. The dynamics of dipolar cross-correlations have usually been disregarded in previous studies, which yields

$$C_P^{\mathrm{self}}(t) = \frac{1}{\mu^2}\left\langle \boldsymbol{\mu}(t)\cdot\boldsymbol{\mu}(0)\right\rangle = \left\langle P_1\big(\cos\Theta_\mu(t)\big)\right\rangle, \tag{2.43}$$

where $P_1(x) = x$ indicates the first-rank Legendre polynomial and $\Theta_\mu(t)$ denotes the angle between some dipole at times zero and t. However, as will be discussed in Chapter 5, disregarding the dynamics of dipolar cross-correlations is not a valid assumption for various different supercooled liquids.

While the dynamics of dipolar cross-correlations have been mostly disregarded, their effect on the static permittivity

$$\varepsilon_{\mathrm{s}} = \lim_{\omega\to 0}\varepsilon'(\omega) \tag{2.44}$$

is well established. It is usually quantified in terms of the Kirkwood correlation factor

$$g_{\mathrm{K}} = 1 + \frac{1}{\mu^2}\left\langle \boldsymbol{\mu}_i\cdot\sum_{i\neq j}\boldsymbol{\mu}_j\right\rangle \tag{2.45}$$

and can be obtained as an extension to the Onsager equation, i.e.

$$g_{\mathrm{K}} = \frac{9k_{\mathrm{B}}\varepsilon_0 MT}{\rho N_{\mathrm{A}}\mu^2}\frac{(\varepsilon_{\mathrm{s}}-\varepsilon_\infty)(2\varepsilon_{\mathrm{s}}+\varepsilon_\infty)}{\varepsilon_{\mathrm{s}}(\varepsilon_\infty+2)^2}. \tag{2.46}$$

Here T is temperature, M molar mass, ρ density and μ the absolute value of the gas-phase molecular dipole moment. Within the present work, the high-frequency contribution to the dielectric constant was estimated at optical frequencies in terms of the squared refractive index, i.e. $\varepsilon_\infty = n^2$. g_{K} can be interpreted as a measure for the average orientational correlation between adjacent dipoles. $g_{\mathrm{K}} > 1$ indicates preferably parallel and $g_{\mathrm{K}} < 1$ preferably anti-parallel orientation of dipoles. However, these considerations have to be taken with care, as (i) g_{K} is an average quantity, thus might yield misleading results in cases where parallel and anti-parallel orientations coexist; and (ii) g_{K} does not consider induced dipole moments, which have been shown to be of considerable importance [60]. Nevertheless, g_{K} is a powerful tool to identify dipolar cross-correlation effects in supercooled liquids, a detailed discussion of which will be given in Chapter 5.

2.3.2 Experimental setups

During the present work most DS data are acquired using the Alpha-Analyzer from Novocontrol Technologies GmbH & Co. KG, which is an impedance analyzer that accesses the frequency range from 10^{-2} Hz up to 10^{7} Hz. Here, liquid samples are filled into home-built stainless steel sample holders, which contain a plate capacitor and are sealed by O-rings. The design of the sample cells allows to fill the entire capacitor with the sample liquid, thus the obtained absolute relaxation strengths are reliable, which is important, e.g., for calculating g_K. The sample temperature was controlled via the Novocontrol Quatro cryosystem. Sample temperatures have been calibrated carefully in a previous work [44] and are comparable to the temperatures in the DDLS setup with an accuracy of at least ±0.5 K.

In some cases, the data are extended to lower frequencies by using a home-built time-domain setup up, which is described in Refs. [55, 61]. It records the dielectric permittivity as a function of t during charging after an electric field step is applied at time zero and during discharging after the field is switched off. By this, frequencies between 10^{-6} Hz and 10^{0} Hz can be accessed to extend the data obtained in the frequency-domain setup.

2.4 COMBINATION AND COMPARISON OF METHODS

As it has been discussed in the previous sections, DDLS and DS both probe molecular reorientation dynamics. The following section discusses aspects that have to be considered when the results from these techniques are compared to each other. The focus here is on the self-correlations, as there exists no consensus on how cross-correlation contributions to the respective techniques should be treated. Within the present work cross-correlation effects have been characterized in some systems, which will be discussed in the respective chapters.

The self-parts of the DDLS and DS autocorrelation functions relate to the reorientation dynamics of molecules as

$$C_{\mathrm{DS}}(t) \propto \left\langle P_1\big(\cos\Theta_\mu(t)\big)\right\rangle \tag{2.47}$$

$$C^{\mathrm{vh}}_{\mathrm{DDLS}}(t) \propto \left\langle P_2\big(\cos\Theta_{\boldsymbol{u}}(t)\big)\right\rangle \tag{2.48}$$

Two main differences can be identified. First, the autocorrelations are associated with Legendre polynomials of different ranks, namely $\ell = 1$ for DS and $\ell = 2$ for DDLS. This can lead to certain differences, which, however, depend on the exact motional mechanism, thus are difficult to estimate for systems with complex dynamics like supercooled liquids. Therefore, only the two limiting cases are discussed, i.e. rotational diffusion and large-angle jump rotations. In the latter case, the characteristic relaxation time constants would be independent of ℓ, i.e. $\tau_1 = \tau_2$. For rotational diffusion, however, $\tau_1 = 3\tau_2$ is obtained, reflecting the fact that a smaller angle Θ is required for the $\ell = 2$ Legendre polynomial to decay to zero than for the $\ell = 1$ case. Another discrepancy would be expected for relaxation processes that are restricted to small angles, e.g. high-frequency relaxation contributions in supercooled liquids. Here, the small-angle reorientation is weighted stronger by the $\ell = 2$ Legendre polynomial, thus a larger relaxation strength would be observed for such processes in the $\ell = 2$ case compared to $\ell = 1$.

A further difference concerns the different molecular axes that are considered by the two techniques, i.e. the dipole-moment vector in DS and the symmetry axis of the anisotropic part of the polarizability tensor in DDLS. Different dynamics can be observed for these two axes in case of anisotropic reorientation mechanisms or if intra-molecular degrees of freedom play a role. These aspects have to be considered individually for each system and are discussed in subsequent chapters upon comparison of DDLS and DS data.

Part I

RELAXATION SPECTRA OF SUPERCOOLED LIQUIDS

3

THE STRUCTURAL RELAXATION SHAPE

3.1 PHYSICAL ORIGIN OF RELAXATION STRETCHING

The physical origin of the asymmetrically broadened structural relaxation peak has been, and still is, matter of intense debate for decades. While herein a summary of selected experimental and computational results is given, it is emphasized that these matters have been discussed in more detail in several excellent reviews, e.g. by Böhmer [25, 62], Ediger [27], Richert [28], Richert et al. [29] and Sillescu [26]. Moreover, it is noted that the discussion refers to the relaxation shape of the structural relaxation or α-process, while additional high-frequency relaxation contributions are not considered explicitly.

Regarding the origin of relaxation stretching in supercooled liquids, two "extreme" scenarios have been discussed: the heterogeneous and the homogeneous one (cf. Refs. [25, 26, 28] and references therein). In the heterogeneous scenario it is assumed that relaxation times of particles are distributed according to some distribution $g(\tau)$, while each particle relaxes exponentially and contributes to the susceptibility spectrum as a Lorentzian, reflecting it to be associated with one single relaxation time. The asymmetrically broadened relaxation peak is then obtained as an ensemble average over all particles and reads

$$\chi''(\omega) = \int_0^\infty g(\tau) \frac{\omega\tau}{1+(\omega\tau)^2} \, \mathrm{d}\tau. \tag{3.1}$$

Therefore, in this scenario relaxation stretching is assumed to originate from *dynamic heterogeneity*.
On the other side, in the homogeneous scenario the relaxation of each particle is assumed to be intrinsically stretched, while particle relaxation times are not distributed. Of course, in addition, numerous in-between scenarios can be considered that combine a certain degree of intrinsic stretching and some distribution of relaxation times.

Unfortunately, many commonly used experimental techniques are not suited to distinguish between these different scenarios, as they probe the average over all particles in the sample using two-time correlators, or the respective linear response equivalents. However, over the years several experimental approaches have been developed that have been able to confirm the existence of dynamic heterogeneity on the particle level. The general idea of early experiments was to selectively probe only a certain dynamic sub-ensemble of particles, e.g. by applying a low-pass filter and probing only the slower-than-average portion of particles. This can be done either by using four-dimensional nuclear magnetic resonance (NMR) experiments, where certain stimulated echo sequences allow for such filtering [25, 62–65]; or by deep photo-bleaching, where fast-relaxing probe molecules dispersed in a supercooled liquid are selectively destroyed and, subsequently, the relaxation of the remaining probes is observed [27,

66, 67]. Both experimental approaches found significantly slower relaxation for the obtained sub-ensemble than for the entire system. This observation could only be rationalized in terms of dynamic heterogeneity on the particle level. Similar conclusions could be drawn from dielectric hole burning [68] and solvation dynamics experiments [69]. Moreover, it was found that after waiting sufficiently long, the slow subset displayed the average behavior, thus indicating that rate exchange limits the lifetime of dynamic heterogeneity [25, 27, 67]. More recently, insightful contributions to the ongoing debate came from fluorescence microscopy experiments [70]. While these experiments have to rely on indirectly probing supercooled dynamics using probe molecules, they offer the unprecedented opportunity to study rotational dynamics of single molecules. Collecting relaxation data of many probe molecules revealed a continuous distribution of relaxation times, thus confirming the established picture of dynamic heterogeneity [70].

While these experimental findings seem to rule out the purely homogeneous scenario, they are well in line with all in-between scenarios, where some degree of intrinsic broadening instead of pure exponential relaxation exists on the particle level. In this regard, experimental findings are more ambiguous: On the one hand, solvation dynamics [71], dielectric hole burning [68, 72, 73] as well as NMR [25] can estimate indirectly the degree of intrinsic broadening and seem to be most compatible with the purely heterogeneous scenario. Noteworthy, this does not necessarily hold for polymers [28, 74] and binary mixtures [73], where the results suggest some degree of intrinsic broadening, possibly related to chain-connectivity effects in the prior and local concentration fluctuations in the latter case. On the other hand, single-molecule studies explicitly observe stretched exponential relaxation of probe molecules. However, these results are difficult to interpret, as substantial temporal averaging is required to obtain adequate data quality [70]. Thus, the observed intrinsic broadened relaxation could be a manifestation of rate exchange, in the sense that initially fast relaxing probes become slow during the window of observation and vice versa. This conjecture is supported by the observation that the degree of intrinsic broadening is reduced when shorter windows of observation are analyzed.

More insight is provided with recent advances in computer simulations, which allow to study relaxation of single particles or small clusters *with temporal resolution* using isoconfigurational averaging, i.e. averaging over parallel simulation runs starting with identical particle positions but varying particle velocities [75, 76]. It was found that the relaxation of fast particles tend to display some intrinsic broadening, while slow particles relax close to exponential. These results indicate that intrinsic relaxation broadening results from dynamic heterogeneity itself, in the sense that the onset of rate exchange makes single particles experience slightly different heterogeneous environments already during a single relaxation cycle, which results in slightly stretched relaxation.[76]

Another ongoing debate concerns the spatial nature of dynamic heterogeneity. More specifically the question is as to whether particle mobility is clustered into slow and fast regions associated with some characteristic length scale. While this is suggested for supercooled molecular liquids by some specific experiments [77–79], a large part of the experimental evidence comes from microscopic imaging experiments on colloidal glasses [80–83], which could be assumed to resemble molecular glasses in terms of dynamic heterogeneity. Noteworthy, recent advances in computer-simulations have opened the pathway to obtain in-depth information on spatial dynamic heterogeneity in deeply supercooled liquids. This was possible upon introduction of swap Monte-Carlo algorithms [84] that allow to equilibrate supercooled liquids down to the glass-transition temperature by performing unphysical particle swaps. With this advance, the fundamental issue of computer simulations, being unable to reach the

deeply supercooled temperature range where typical experiments are performed, is resolved, allowing to extend the existing evidence from high temperatures [85] to low temperatures. First pioneering studies following such approaches confirmed the picture of pronounced spatial dynamic heterogeneity, suggesting a coexistence of slow and fast regions and the importance of dynamic facilitation [30, 86].

3.2 QUANTIFYING THE RELAXATION SHAPE

In order to compare relaxation shapes of different supercooled liquids, or to study their temperature dependence, the relaxation shape of the α-process has to be quantified using a set of well-defined parameters. The most commonly analyzed parameter is the high-frequency power-law exponent β. Occasionally, also the logarithmic half-width $w_{1/2}$ is considered. Both are illustrated in Fig. 3.1a for an exemplary spectrum of the silicone oil DC704. While it may seem that both parameters are easily determined, in most other supercooled liquids additional contributions from so-called β-processes that appear at high frequencies as distinct shoulders or excess wings usually mask the structural relaxation shape on the high-frequency side. For this reason, β can usually not be determined by simply fitting a power law to the high-frequency side of the peak, but instead, more involved approaches are required. Most common are fitting procedures that are used to model the entire relaxation spectrum, including additional high-frequency contributions like β-processes. Under certain assumptions, this allows to isolate the relaxation shapes of the different processes. Unfortunately, the choice of these model functions is quite arbitrary and different models usually yield quite different results. Moreover, appropriate models require at least six (usually more) free parameters, thus the decision which of these parameters are treated as free variables and which are kept constant introduces additional bias.

In the following section, first, typical model functions are defined, second, the mentioned difficulties when applying these model functions are discussed in more detail and, finally, the fit model used in the remainder of this work is introduced. In the second section a model-free approach for determining β is introduced that can serve as an alternative to fitting procedures, due to being well-defined and bias-free.

3.2.1 Frequently used model functions

As discussed in Section 3.1, the relaxation shape in supercooled liquids is commonly interpreted in terms of a distribution of relaxation times, each of which contributes as a Lorentzian to the relaxation spectrum. The two most commonly used model functions for the α-process, however, are not explicitly defined in terms of a distribution of relaxation times, but as analytical function of frequency or time. First, the Cole-Davidson (CD) function

$$\chi''_{\mathrm{CD}}(\omega) = \mathrm{Im}\left[\frac{\Delta\chi}{(1+i\omega\tau_{\mathrm{CD}})^{\beta_{\mathrm{CD}}}}\right] = \Delta\chi\left(1+(\omega\tau_{\mathrm{CD}})^2\right)^{-\beta_{\mathrm{CD}}/2}\sin\left(\beta_{\mathrm{CD}}\arctan(\omega\tau_{\mathrm{CD}})\right) \tag{3.2}$$

is defined as a function of frequency and produces an asymmetrically broadened peak with low-frequency power law ω^1, high-frequency power law $\omega^{-\beta_{\mathrm{CD}}}$ and average relaxation time $\langle\tau\rangle = \tau_{\mathrm{CD}}\beta_{\mathrm{CD}}$.

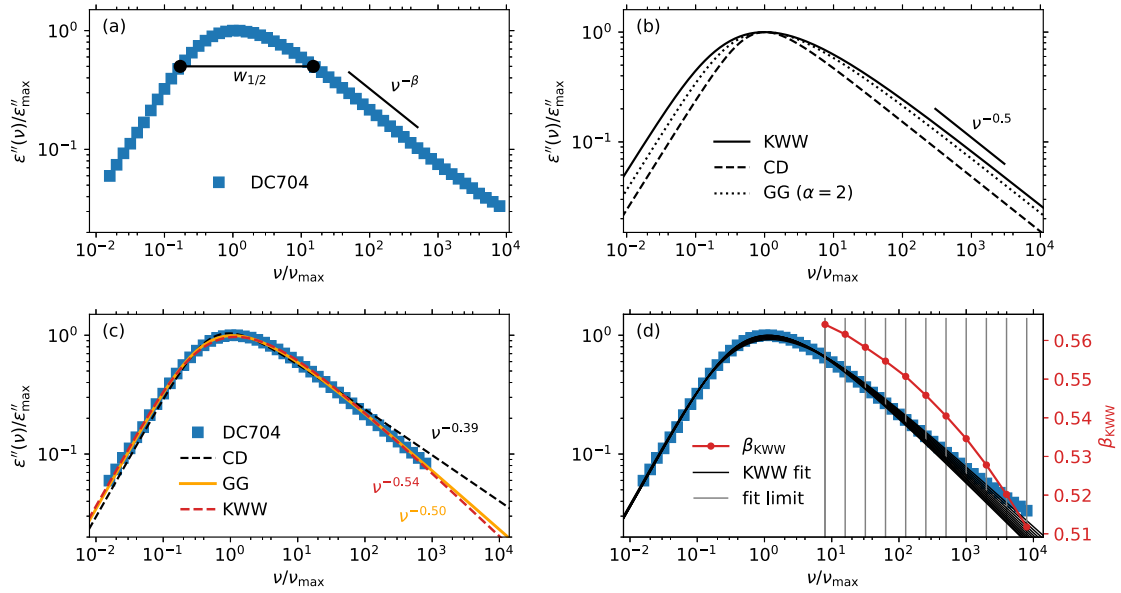

Figure 3.1: Quantifying the relaxation shape. (a) Demonstration of frequently used measures to quantify the relaxation shape (demonstrated for DC740-data), namely the high-frequency power-law exponent β and the half-width $w_{1/2}$. (b) Overview of the intrinsic shapes of commonly used model functions with $\beta = 0.5$. Despite having the same high- and low-frequency power-law exponents, the widths of the peaks are quite different. (c) DC704-data are fitted using different model functions, which all yield different values for the high-frequency power-law exponent. (d) Illustration how β_{KWW} (right axis) varies depending on the chosen high-frequency fit limit (vertical gray lines). Fits (black lines) are performed with logarithmic residuals.

Second, the Kohlrausch-Williams-Watts (KWW) stretched exponential function is defined as a function of time. However, it can be obtained as a function of frequency via Laplace transformation, which yields

$$\chi''_{KWW}(\omega) = \Delta\chi\,\omega \int_0^\infty \exp\left[-\left(\frac{t}{\tau_{KWW}}\right)^{\beta_{KWW}}\right] \cos\omega t\,\mathrm{d}t. \tag{3.3}$$

It features a low-frequency power law ω^1, a high-frequency power law $\omega^{-\beta_{KWW}}$ and average relaxation time $\langle\tau\rangle = \tau_{KWW}\beta_{KWW}^{-1}\Gamma(\beta_{KWW}^{-1})$, where Γ denotes the gamma function.

Both functions with $\beta_{CD} = \beta_{KWW} = 0.5$ and normalized to their respective peak maximum frequencies and amplitudes are compared in Fig. 3.1b. Although high- and low-frequency power-law exponents are identical, the KWW relaxation shape is significantly broader than the CD relaxation shape. As a consequence, fitting data using the CD and the KWW function usually yields quite different results for β. This is demonstrated in Fig. 3.1c, where $\beta_{CD} = 0.39$ and $\beta_{KWW} = 0.54$ are obtained from fits to the DC704 data. The main reason for this large discrepancy is that both, the width and the high-frequency power-law exponent of the peaks, are controlled by the single shape-parameter β_{CD} res. β_{KWW}. As a consequence, the value of β_{CD} res. β_{KWW} that minimizes the regression of the fit represents a compromise between an accurate description of the peak and of the high-frequency power law. This also implies that the result of a fit can depend on the frequency fit range that is analyzed, or on whether logarithmic or linear residuals are considered. The prior effect is analyzed in Fig. 3.1d, where a KWW function is fitted to data ranging from $10^{-2} < \nu/\nu_{max} < \nu_{up}$ for different choices of

the upper fit limit ν_{up}, each of which indicated by a gray vertical lines. Different values β_{KWW} are obtained (red points and right axis). The dependence on the fit range poses a problem, because for many supercooled liquids an upper fit limit is naturally given by the on-set of a β-process or excess wing.

Altogether, the discussed problems and biases introduced by the commonly applied model functions make it difficult to perform systematic analyses of structural relaxation shapes or to compare the results obtained for various supercooled liquids. In the following sections, two solutions to some of these issues are discussed; first, a fit model with two independent shape parameters to control width and high-frequency power-law exponent of the peak. And second, a model-free approach for determining high-frequency power-law exponents.

3.2.2 Fit model based on the generalized gamma distribution

In the remainder of this work, a fit model based on a generalized gamma (GG) distribution of relaxation times is applied, which was originally proposed by Blochowicz et al. [55, 87]. The distribution of relaxation times for the α-process is given by

$$G_{\mathrm{GG}}(\ln\tau) = N_{\mathrm{GG}}(\alpha,\beta)\,\exp\!\left(-\frac{\beta}{\alpha}\left(\frac{\tau}{\tau_{\mathrm{GG}}}\right)^{\alpha}\right)\left(\frac{\tau}{\tau_{\mathrm{GG}}}\right)^{\beta}, \tag{3.4}$$

with normalizing factor

$$N_{\mathrm{GG}}(\alpha,\beta) = \left(\frac{\beta}{\alpha}\right)^{\beta/\alpha}\frac{\alpha}{\Gamma(\beta/\alpha)}. \tag{3.5}$$

The resulting relaxation function in the time-domain is obtained as

$$\Phi(t) = \int_{-\infty}^{\infty} G_{\mathrm{GG}}(\ln\tau)\,\exp\!\left(-\frac{t}{\tau}\right)\mathrm{d}\ln\tau, \tag{3.6}$$

which is the time-domain equivalent of Eq. (3.1). The relaxation spectrum is obtained analogous to the procedure in Eq. (3.3), yielding an asymmetric peak with low-frequency power law ω^1, high-frequency power law $\omega^{-\beta}$ and average relaxation time

$$\langle\tau\rangle = \tau_{\mathrm{GG}}\left(\frac{\alpha}{\beta}\right)^{1/\alpha}\frac{\Gamma\left(\frac{\beta+1}{\alpha}\right)}{\Gamma\left(\frac{\beta}{\alpha}\right)}. \tag{3.7}$$

In contrast to the previously discussed model functions, however, the width can be adjusted by varying $0<\alpha<\infty$. In fact, $\alpha=1$ reproduces the KWW function, wheres $\alpha\to\infty$ converges to a relaxation shape similar to the CD function. As will be discussed in a later chapter of this work, the α-process of many supercooled liquids is best described by $\alpha=2$ and $\beta=0.5$. The respective relaxation shape is compared to the KWW and CD functions in Fig. 3.1b and is used to fit the relaxation spectrum of DC704 in Fig. 3.1c. It should be noted that an extended version of Eq. (3.4) has been reported that includes an additional excess wing (cf. Eq. 7 of Ref. [87]), which, however, is not used within the present work unless indicated otherwise. All fits using the GG distribution of relaxation times are performed logarithmically, in the sense that the logarithm of the fit model is fitted to the logarithm of the relaxation spectrum in order to avoid strongly different weighting of the residuals between peak maximum and the regions of the high- res. low-frequency power laws.

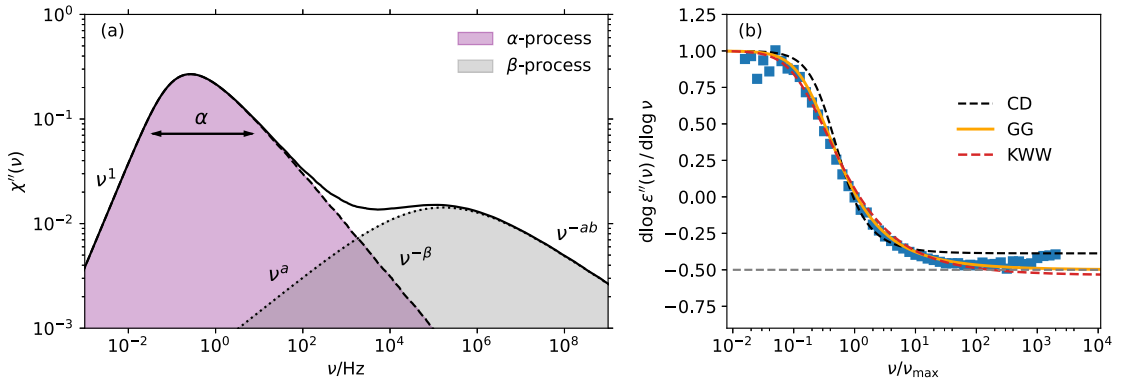

Figure 3.2: (a) Fit model for relaxation spectra used in this work. In the frequency domain it is obtained via convolution of an α-process , based of the GG distribution of relaxation times Eq. (3.4), and a β-process , based of the the distribution defined in Eq. (3.8). High-frequency power-law exponent and width of the α-process can be controlled via the parameters β, res. α, while width and asymmetry of the β-process are controlled via a and b. (b) Model-free approach for determining the high-frequency power-law exponent by determining the minimum of the logarithmic derivative $(\mathrm{d}\log\varepsilon'')/(\mathrm{d}\log\nu)$. The symbols represent DC704 data and the derivative of the fits from Fig. 3.1c are included as lines.

As mentioned above, an additional β-process contributes to the relaxation spectra of most supercooled liquids at larger frequencies than the α-process peak-maximum frequency. While β-processes are not the focus of this work, they need to be included in the fit model to allow a full description of relaxation spectra. Finally, this allows to separate the β-process contribution from the α-process. In order to describe β-processes, another distribution of relaxation times

$$G_\beta(\ln\tau) = N_\beta(a,b)\left(b\left(\frac{\tau}{\tau_\beta}\right)^a + \left(\frac{\tau}{\tau_\beta}\right)^{-ab}\right)^{-1} \tag{3.8}$$

with normalizing factor

$$N_\beta(a,b) = \frac{a(b+1)}{\pi}\, b^{b/(b+1)} \sin\left(\frac{\pi b}{b+1}\right) \tag{3.9}$$

is employed. The corresponding process features a peak with low-frequency power law ω^a and high-frequency power law ω^{-ab}. Thus, a controls the width and b the asymmetry of the peak. It is noted that assuming a temperature-independent distribution of activation energies implies $a \propto T^{-1}$ [87]. This relation is considered in subsequent analyses that involve an extensive description of the β-process.

Finally, the coupling between α- and β-process remains to be discussed. Here, the William-Watts approach [88] is applied, which assumes that all molecules contribute to the β-process at short times and, finally relax via the α-process at longer times, while both processes are statistically independent. This implies a multiplicative form of the combined relaxation function,

$$\Phi(t) = \big(f + (1-f)\,\Phi_\beta(t)\big)\,\Phi_\alpha(t), \tag{3.10}$$

where $\Phi_\alpha(t)$ and $\Phi_\beta(t)$ are the individual relaxation functions of α- res. β-process. An illustration of an exemplary combined relaxation spectrum is shown in Fig. 3.2. In frequency representation, the William-Watts approach corresponds to the convolution of both individual relaxation peaks. It should be noted that the difference between the convolution and an additive treatment of relaxation peaks is minor, as soon as the β-process contributes at much

shorter timescales than the α-process, i.e. at low temperatures. Thus, none of the conclusions drawn from the analyses within this work depend on the validity of the assumptions of the William-Watts approach.

3.2.3 Model-free approach

A model-free approach for determining the high-frequency power-law exponent was introduced by Nielsen et al. [33]. Here, β is defined as the logarithmic slope at the frequency of steepest descent on the high-frequency side of the relaxation spectrum, i.e.

$$\beta_{\mathrm{d}} = -\min\left(\frac{\mathrm{d}\log\varepsilon''}{\mathrm{d}\log\nu}\right). \tag{3.11}$$

The procedure is illustrated in Fig. 3.2b, where the logarithmic derivative of DC704-data is shown as a function of frequency. The value at the minimum equals $\beta_{\mathrm{d}} \sim 0.5$, in concordance to the high-frequency power-law exponent determined via a fit using the GG distribution of relaxation times. In contrast to fitting procedures, the disadvantage of the model-free approach is that it is impossible to separate contributions of β-process, which are observed in Fig. 3.2b at $\nu/\nu_{\max} > 5 \cdot 10^2$ as an increase of the derivative compared to its minimum value. Therefore, the best results are obtained at temperatures close to T_{g} , where the dynamic separation between the α- and β-process is large. As the dynamic separation of α- and β-process is strongly temperature dependent around T_{g} , the validity of results from Eq. (3.11) can be verified by making sure that the variation of β_{d} as a function of temperature is small. The great advantage of the model-free approach, however, is that it is well-defined and can easily be reproduced, independent of any assumptions of model functions. Therefore, it is preferred for comparing the structural relaxation shapes of various different supercooled liquids, e.g. in Section 5.4.

4

THE GENERIC RELAXATION SHAPE

The following chapter discusses the conjecture of a generic relaxation shape of the α-process. For the sake of brevity, the latter is referred to as *relaxation shape* below without explicitly indicating that it is referred to the α-process.

As discussed extensively in Section 3.1, various experimental results indicate the asymmetrically broadened relaxation shape in supercooled liquids to reflect dynamic heterogeneity. Understanding the physics behind dynamic heterogeneity is presumed to be of major importance for solving the glass-transition problem. Thus, it has been an important experimental effort to elucidate what exactly controls the relaxation shape. In this regard, mainly dielectric-loss data have been analyzed, as these are easily obtained and usually provide the best resolution and highest signal-to-noise ratio, especially at frequencies above the peak-maximum frequency where β is determined. It was found that the relaxation shape in general, and the values of β specifically, vary significantly among various different supercooled liquids [32–34]. This observation is illustrated in Fig. 4.1a, where $\varepsilon''(\nu)$ of various different supercooled liquid is plotted. Each spectrum is normalized with regard to its respective peak-maximum amplitude and frequency. Values of β obtained for these data range from 1 to ~0.35, as indicated by the dashed gray lines.

It was attempted to relate the various values of β to several other characteristics of supercooled liquids and glasses. Böhmer et al. reported that larger values of β are associated with smaller values of the fragility index m [32]. The analysis also included polymers and network glasses, while the evidence for supercooled molecular liquids alone is rather weak and thus, has been discussed critically [89, 90]. In the coupling model proposed by Ngai et al. (see Ref. [91] and references therein), β is predicted to be related to the dynamic separation of the α- and the Johari-Goldstein β-process . Here, the latter was argued to be associated with the primitive relaxation of the system. Moreover, as β oftentimes is considered as a measure for the degree of dynamic heterogeneity, its relation to the lengthscale of dynamic heterogeneity has been studied using NMR techniques by Qui et al. [92]. Although the "expected" correlation of smaller values of β being associated with larger dynamic heterogeneity lengthscale was observed, the study considered only four substances with quite different molecular structures and even included a polymer, thus no definite conclusions can be drawn. Paluch et al. [34] reported a correlation between β and the dielectric relaxation strength $\Delta\varepsilon$ for a broad variety of molecular supercooled liquids. Here, larger β are associated with larger $\Delta\varepsilon$, meaning the relaxation spectra of highly polar liquids tend to be less stretched than those of less polar ones. Initially, this observation was rationalized by arguing that strong dipole-dipole interactions increase the harmonicity of the inter-molecular potentials. This is thought to affect the distribution of relaxation times and, thus, the relaxation stretching [34]. As will be argued in Section 5.4, the results obtained during this work do not support the conjecture posed by Paluch et al. and, instead, a mechanism involving dipolar cross-correlations is more likely to

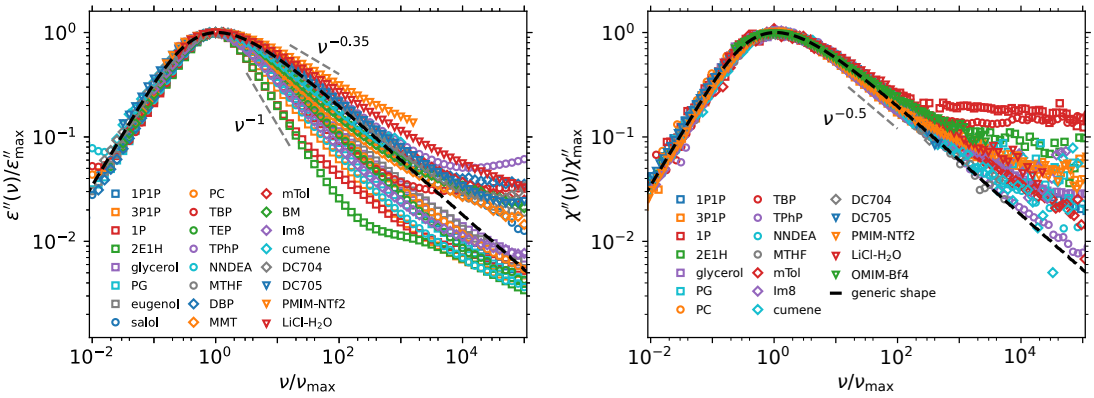

Figure 4.1: Comparing the relaxation shapes of different supercooled liquids. (a) Dielectric loss $\varepsilon''(\nu)$ and (b) DDLS $\chi''(\nu)$ spectra normalized with regard to peak-maximum frequency and amplitude. The shape of $\varepsilon''(\nu)$ varies strongly among the different systems, with high-frequency power-law exponents ranging from 0.35 to 1.0. On the other hand, all $\chi''(\nu)$-data approximately collapse onto a single master curve, which is well-described by the relaxation shape based on the GG distribution of relaxation times with parameters $\alpha = 2.0$ and $\beta = 0.5$ (dashed black line, cf. Eq. (3.4)). Abbreviations: 1-phenyl-1-propanol (1P1P), 3-phenyl-1-propanol (3P1P), 1-propanol (1P), 2-ethyl-1-hexanol (2E1H), propylene glycol (PG), propylene carbonate (PC), tributyl phosphate (TBP), triethyl phosphate (TEP), triphenyl phosphite (TPhP), N,N-diethylacetamide (NNDEA), 2-methyltetrahydrofuran (MTHF), dibuthyl phthalate (DBP), methyl-m-toluate (MMT), m-toluidine (mTol), butyl methacrylate (BM), 1-octylimidazole (Im8), 17% LiCl-water solution(LiCl-H_2O).

be the origin of the observed correlation between β and $\Delta\varepsilon$. Another comprehensive approach was reported by Nielsen et al., who analyzed the dielectric relaxation shape, and its temperature dependence, for a large number of supercooled liquids. They determined the distribution of β-values among these substances and found that its median is $\beta \approx 0.5$ [33]. Remarkably, substances with larger or smaller values of β tend to converge to $\beta = 0.5$ approaching low temperatures close to or below T_g, as hypothesized earlier by Olsen et al [93].

Contrary to most of these observations from dielectric spectroscopy, in recent years growing evidence supports the conjecture of a *generic α-process relaxation shape* with $\beta \sim 0.5$ in supercooled molecular liquids. These observations have been enabled by advances in other experimental techniques, e.g. dynamic light scattering, reaching experimental resolutions comparable to the previously superior dielectric experiments. The initial report of the generic relaxation shape was published in Ref. [94] and in the PhD-thesis of Florian Pabst [44]. These studies were continued during the present work, thus the results reported below reproduce some earlier results from Refs. [44, 94] and extend them in several regards. First, the remarkable similarity of relaxation shapes observed for DDLS spectra of different supercooled liquids is presented. Second, the degree to which these relaxation spectra obey time-temperature-superposition is discussed. Finally, as an outlook, the question as to what is special about the generic high-frequency power law of $\nu^{-1/2}$ is addressed briefly. While the present chapter focuses mainly on results from DDLS, the discrepancies with regard to dielectric-loss data are resolved in Chapter 5. Here it is argued that contributions from dipolar cross-correlations strongly affect the dielectric relaxation shape. The discussion of relaxation shapes of hydrogen bonding liquids is continued in Chapter 6, with the focus lying on how the molecular architecture affects their respective hydrogen bonding characteristics and, in turn, the corresponding relaxation shapes. Finally, these results allow to explain under which experimental conditions the generic relaxation shape can be observed in Section 6.3.

4.1 COMPARING RELAXATION SHAPES OF SUPERCOOLED LIQUIDS

Fig. 4.1b shows DDLS relaxation spectra of 19 different substances, each normalized to the respective peak-maximum frequency and amplitude. Besides few exceptions, the plot covers the same substances included in the equivalent plot of dielectric data in Fig. 4.1a. In stark contrast to the latter, however, all DDLS spectra approximately collapse onto a single master curve. Deviations due to β-processes occur only at $\nu/\nu_{\max} > 10^2$, the amplitudes and shapes of which are individual for each substance. The master curve is well-described by the model-function based on the GG distribution of relaxation times, Eq. (3.4), with parameters $\alpha = 2.0$ and $\beta = 0.5$. Thus, it features a $\nu^{-1/2}$ high-frequency behavior and a width in-between the one of the CD and a KWW function with $\beta_{\mathrm{CD}} = \beta_{\mathrm{KWW}} = 0.5$.

Notably, Fig. 4.1 includes data of monohydroxy alcohols, polyhydric alcohols, high-polar and low-polar van-der-Waals liquids, as well as ionic systems like a water-salt mixture and ionic liquids. Thus, it covers the full spectrum of organic low-molecular-weight glass formers. Recently, the same exponent of $\beta \approx 0.5$ was observed for the inorganic supercooled liquids GeO_2 [95] and $(Na_2O)_x(GeO_2)_{100-x}$ [96] at temperatures close to T_g by using polarized dynamic light-scattering. This observation suggests that the observed generic behavior might even apply for a broader variety of substances. It is striking that, despite the chemical variety, these systems share a common generic relaxation shape in the supercooled regime, suggesting that this shape represents a deep-rooted characteristic feature of deeply supercooled liquids.

4.2 TIME-TEMPERATURE SUPERPOSITION

For each substance, Fig. 4.1b considers the relaxation spectrum obtained at one single temperature. This procedure of comparing relaxation shapes can only be valid if the $\chi''(\nu)$-data obey *time-temperature superposition* (TTS), meaning the temperature-dependence of the normalized relaxation spectrum obeys $\chi''(\omega, T) = \phi(\omega\tau(T))$. Here, $\tau(T)$ is the average relaxation time of the α-process , while $\phi(x)$ represents the temperature-reduced relaxation spectrum [93]. It has to be noted that TTS inevitably fails as soon as β-processes contribute, because the average relaxation times of the α- and the β-process have different temperature dependences, thus the β-process does not obey a scaling relation based on the α-process relaxation time. Consequently, TTS is only considered regarding the relaxation shape of the α-process. While $\varepsilon''(\nu)$-data of some supercooled liquids were reported to obey TTS within experimental resolution [93], deviations are commonly observed [33, 93]. Interestingly, deviations from TTS are especially apparent for supercooled liquids with values of β extracted from $\varepsilon''(\nu)$ that strongly deviate from 0.5 [33, 93]. It is thus interesting to verify to what degree $\chi''(\nu)$-data of such substances obey TTS. This is done in Fig. 4.2, where TTS is qualitatively tested for four selected supercooled liquids, i.e. glycerol, propylene glycol (PG), 3-phenyl-1-propanol (3P1P) and 3-methyl-3-heptanol (3M3H), by plotting normalized relaxation spectra obtained at several temperatures as functions of $\tau_{\max}\omega = \tau_{\max} 2\pi\nu$. These four substances were chosen, due to data over a broad temperature range with comparably high experimental resolution being available. In all four cases, TTS is obeyed to good approximation in the temperature range, where $10^{-1} < \nu_{\max}(T)/\mathrm{Hz} < 10^5$ (see data as a function of ν in the inset). For 3P1P and 3M3H, a distinct β-process contributes at high frequencies that starts to merge with the α-process at the highest temperatures. The onset of this merging inevitably leads to deviations from TTS.

For glycerol, a high-temperature spectrum obtained at 350 K (above the melting temperature $T_m = 290\,\mathrm{K}$) is included as the gray line. Its relaxation shape visibly deviates from the

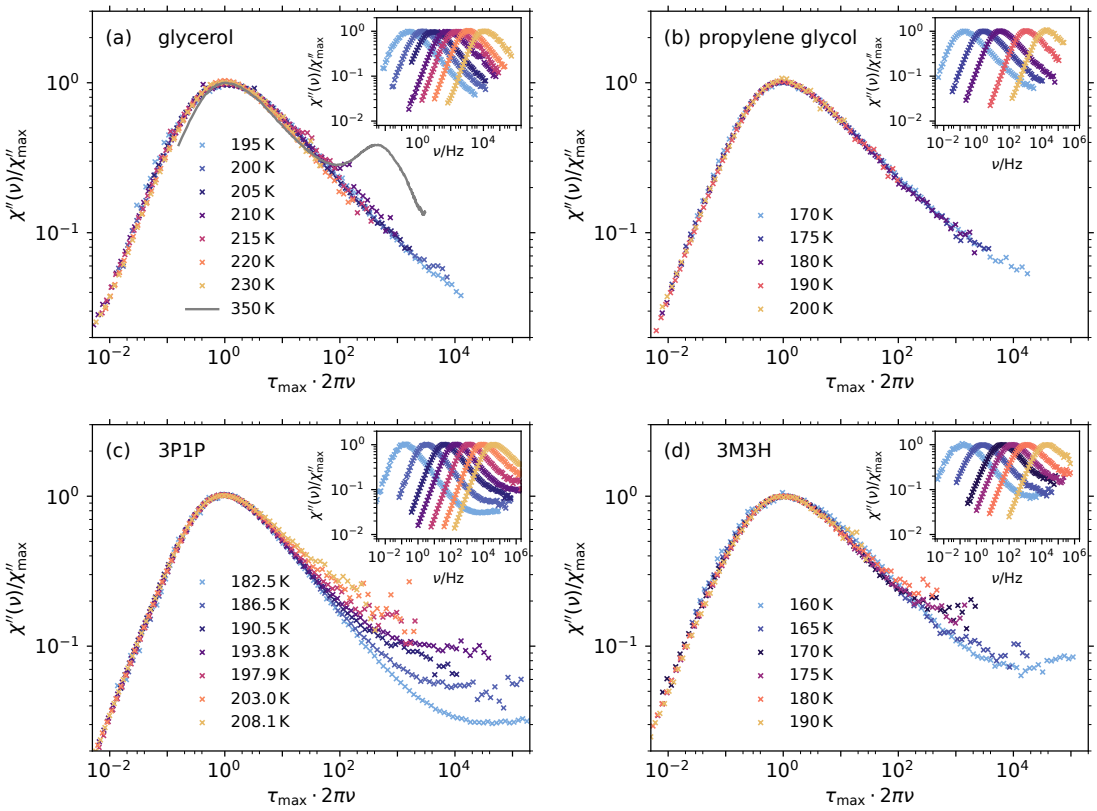

Figure 4.2: Testing TTS for $\chi''(\nu)$-data of (a) glycerol, (b) propylene glycol (c) 3-phenyl-1-propanol and (d) 3-methyl-3-heptanol. For this purpose, normalized relaxation spectra obtained at different temperatures are plotted as a function of $\tau_{max}\omega = \tau_{max} 2\pi\nu$. The insets show the same data as a function of ν. For glycerol, the high-temperature relaxation spectrum obtained at 350 K using a TFPI is included as the gray line.

ones at temperatures close to T_g. Notably, the high-frequency power law remains close to $\nu^{-0.5}$, in contrast to the notion that liquids above the melting point display a Lorentzian-shaped relaxation spectrum. While the relaxation spectrum of glycerol at high temperatures is less broadened than at low temperatures, also the opposite behavior is observed in other substances. An example of this is shown in Section 6.2 for sorbitol.

In summary, $\chi''(\nu)$-data seem to obey TTS in the deeply supercooled regime ($\nu_{max}(T) < 10^5$ Hz) within the experimental resolution. Exceptions are given by contributions from β-processes. At higher temperatures, the relaxation shape usually deviates from the low-temperature shape, however is almost never Lorentzian. A systematic study of the transition from low- to high-temperature relaxation shapes should be the focus of future investigations.

4.3 WHAT IS SPECIAL ABOUT $\nu^{-1/2}$?

The observation of a generic $\nu^{-1/2}$ high-frequency power law in a broad variety of deeply supercooled liquids is striking and suggests a deep-rooted connection to the glass-transition phenomenon. An obvious question is: What is special about $\nu^{-1/2}$? And what is the underlying physical origin of this exact power law behavior? Interestingly, numerous theoretical studies

following different approaches have predicted the $\nu^{-1/2}$ high-frequency behavior (see Ref. [97] and references therein for a brief review).

Recently, Dyre provided a review of the *solid-that-flows* perspective on deeply supercooled liquids, which involved a qualitative discussion of the structural relaxation shape [31]. It was argued that structural relaxation proceeds via various localized flow events that start in highly mobile regions with low local energy barriers and finally induce dynamic facilitation by reducing large local energy barriers in less mobile regions. The time scale at which dynamic facilitation mobilizes even the least mobile regions marks the long-time cutoff of the distribution of relaxation times and, thus, determines the frequency below which the ν^1 low-frequency behavior is observed. At larger frequencies, solidity leads to the asymmetric loss peak with a $\nu^{-\beta}$ high-frequency behavior. In previous considerations [98], $\beta = 1/2$ was predicted by translating the *solid-that-flows* conjecture into an expression for density fluctuations, which was solved in the Gaussian approximation.

Dynamic facilitation in supercooled liquids has also been studied in recent computer-simulation approaches [30, 86]. In harmony with the above mention notions it was found that relaxation begins in localized highly-mobile regions that facilitate relaxation events in their vicinity. Interestingly, close connections have been identified between dynamic facilitation and the high-frequency power-law exponent of the respective relaxation spectra: The high-frequency power-law exponent extracted from the relaxation spectra was found to also describe the short-time evolution of the number of highly-mobile clusters, as well as the waiting time distribution for the emergence of new clusters.

Considering these findings, it is tempting to contemplate whether the generic high-frequency power law might reflect generic features of dynamic facilitation. Computer simulations are a promising tool to elucidate this conjecture. However drawing more quantitative conclusions for molecular liquids will require the study of more realistic simulation models, e.g. with reduced polydispersity [99] or including rotational degrees of freedom [100, 101].

5

THE IMPACT OF DIPOLAR CROSS-CORRELATIONS

The observation of a generic relaxation shape of various supercooled molecular liquids in DDLS raises the question as to how these findings can be reconciled with the apparently non-generic shape of corresponding dielectric loss spectra. In the following sections it is argued that this apparent inconsistency can be resolved by considering that dipolar cross-correlations contribute considerably to the dielectric-loss spectra of certain supercooled liquids and mask the generic high-frequency power law. This idea is based on joint analyses of $\varepsilon''(\nu)$ and $\chi''(\nu)$-spectra obtained at the same temperature, as discussed in Section 5.1. In Section 5.2, the assumption that suppressing dipolar cross-correlations should resolve the discrepancy between $\varepsilon''(\nu)$ and $\chi''(\nu)$-spectra is verified. Additional evidence is provided by other experimental and computational studies in the literature, which are briefly reviewed in Section 5.3. Finally, a quantitative relationship between the strength of dipolar cross-correlations and the relaxation shape is established in Section 5.4. It allows to verify theories of dielectric relaxation in polar liquids. Parts of the results discussed in Sections 5.1 and 5.2 were published previously in Refs. [94, 102] and in the PhD-thesis of Florian Pabst [44]. To provide context for subsequent sections, the main arguments and ideas are reproduced, as well as complemented by additional data obtained during the present work.

5.1 COMBINED ANALYSIS OF BDS AND DDLS SPECTRA

Fig. 5.1 presents a comparison of $\varepsilon''(\nu)$- and $\chi''(\nu)$-data of a selection of different supercooled liquids, both obtained at the same temperature, respectively. Here, substances are considered for which a visible difference with regard to the high-frequency power-law exponent between the $\varepsilon''(\nu)$ and $\chi''(\nu)$-data is observed in Fig. 4.1. Three different sub-classes of supercooled liquids are covered: Monohydroxy alcohols (left panels), polyhydric alcohols (middle panels) and polar non-hydrogen bonding liquids (right panels). While the upper panels are reproduced from Refs. [44, 94, 102], the lower panels show data obtained during the present work, which were published in Refs. [103–105].

Immediately, two general conclusions can be drawn from Fig. 5.1: First, for all six substances the peak-maximum frequency extracted from $\varepsilon''(\nu)$ is markedly smaller than the one from $\chi''(\nu)$, i.e. the peak-relaxation time obtained from the dielectric loss is larger than the one probed by DDLS. Second, $\varepsilon''(\nu)$ is well-described by the weighted sum of the $\chi''(\nu)$-spectrum and an additional slow and narrow relaxation contribution depicted by the gray shaded area. The latter is either Debye-shaped, or in some cases slightly broadened, as described by the Laplace-transform of the KWW stretched exponential function with $0.8 < \beta_{\mathrm{KWW}} < 1$. The quantitative description for the case of a Debye-shaped contributions reads as

$$\varepsilon''(\nu) = \Delta\varepsilon_{\mathrm{self}} \cdot \chi''(\nu) + \Delta\varepsilon_{\mathrm{cross}} \cdot \frac{\omega\tau_{\mathrm{cross}}}{1+(\omega\tau_{\mathrm{cross}})^2}. \tag{5.1}$$

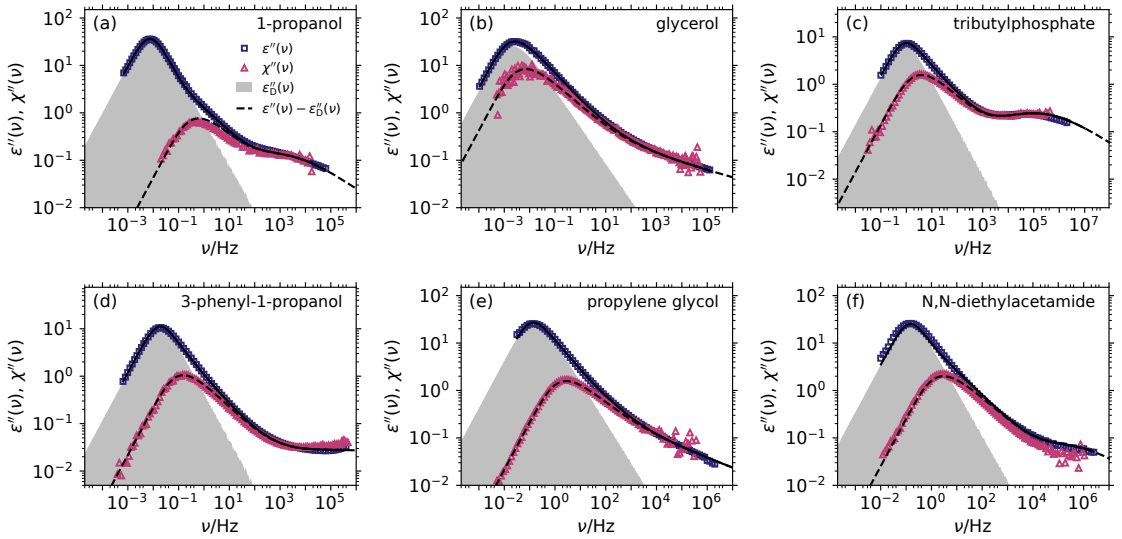

Figure 5.1: Comparison of $\varepsilon''(\nu)$- and $\chi''(\nu)$-data of a selection of different supercooled liquids, both obtained at the same temperature. Upper panels (a)-(c) are reproduced from Refs. [44, 94], while the lower panels (d)-(f) were obtained during the present work. The substances in the left hand panels (a) and (d) are monohydroxy alcohols, in the middle panels (b) and (e) are polyhydric alcohols and in the right hand panels (c) and (f) are polar vdW liquids. The solid black lines represent fits to $\varepsilon''(\nu)$ by Eq. (5.1), the gray shaded areas illustrate the slow cross-correlation contributions $\varepsilon''_{\text{cross}}(\nu)$ and the dashed black lines represent the self-correlation contribution $\varepsilon''(\nu)-\varepsilon''_{\text{cross}}(\nu)$. The normalized DDLS spectra $\chi''(\nu)$ were multiplied by $\Delta\varepsilon_{\text{self}}$ according to Eq. (5.1). For all substances, besides the polyhydric alcohols, the cross-correlation contribution is described by a Lorentzian, while the Laplace transform of the KWW function with $\beta_{\text{KWW}} = 0.78$ and $\beta_{\text{KWW}} = 0.86$ is used for glycerol and propylene glycol, respectively.

Here, $\Delta\varepsilon_{\text{self}}$ and $\Delta\varepsilon_{\text{D}}$ are the respective relaxation strengths of both contributions and τ_{D} is the relaxation time of the Debye-contribution. The validity of Eq. (5.1) is illustrated in Fig. 5.1, where the slow and narrow relaxation contribution is subtracted from $\varepsilon''(\nu)$, which yields the black dashed line that almost perfectly coincides with $\chi''(\nu)$.

To unveil the physical origin of the additional slow contribution, monohydroxy alcohols are discussed first. For these substances the existence of two distinct relaxation contributions to $\varepsilon''(\nu)$ is well established and understood: Via hydrogen-bonding, most monohydroxy alcohols form chain-like supra-structures. Within these supra-structures, orientations of adjacent molecular dipoles are correlated. In the static limit $\nu \to 0$, these dipolar cross-correlations can be quantified in terms of the Kirkwood correlation factor g_{K} (cf. Eq. (2.45)), which for most monohydroxy alcohols yields values significantly above unity. Due to the fact that the supra-structures persist to much longer times than the average relaxation time of self-correlations, an additional relaxation contribution to $\varepsilon''(\nu)$ is observed that reflects the slow relaxation of dipolar cross-correlations. Its relaxation time reflects the reorientation of the supra-structures and can be up to a factor of thousand slower than the decay of self-correlations. The slow contribution is usually referred to as *Debye process*, due to its unique relaxation shape, which had been predicted by the Debye model of dielectrics (see Section 6.1 for a detailed discussion). Considering the data of 1-propanol in Fig. 5.1a, DDLS apparently is insensitive to these dipolar cross-correlations and does only probe the self-correlations, i.e. the rotation of single alcohol molecules. This empirical conclusion is discussed and tested in more detail below, but for now it is concluded that $\chi''(\nu)$ does reflect the self-correlation dynamics.

For a qualitative explanation on why the slow dipolar cross-correlation contribution is Debye-shaped one can follow the line of argument by Anderson et al. [106]: In the limit of the cross-correlation relaxation being significantly slower than that of the self-correlations, the former is also slower than rate exchange. As a consequence, the slow relaxation of cross-correlations reflects an average over various different heterogeneous environments. Thus it is associated with one single average relaxation time and Debye-shaped. For cross-correlations being only moderately slower than self-correlations, the averaging of dynamic heterogeneity might be incomplete, leaving the cross-correlation contribution slightly broadened on the high-frequency side.

While the discussed ideas seem to be broadly accepted for monohydroxy alcohols, the middle and right-side panels of Fig. 5.1 reveal equivalent observations also for polyhydric alcohols and some polar van-der-Waals (vdW) liquids. These results suggest that a slow dipolar cross-correlation contribution, i.e. a Debye process, is a much more general feature, which is not specific for monohydroxy alcohols. Actually, this might not be entirely unexpected: The intermolecular interaction mechanisms in polyhydric alcohols (hydrogen bonding) and polar vdW liquids (dipole-dipole interactions) are *anisotropic*, thus could lead to some sort of structure formation. At least for polyhdric alcohols, the formation of a hydrogen-bonded network structure is well-established. Moreover, similar to monohydroxy alcohols, these substances exhibit significant *static* dipolar cross-correlations, as indicated by $g_K > 1$ (see detailed discussion in Section 5.4).

In fact, a recent theory of dielectric relaxation by Déjardin et al. suggests that $g_K > 1$ alone is a sufficient condition to observe a slow cross-correlation contribution to the dielectric loss [109]. The theory determines the static dielectric permittivity of an isotropic polar fluid from the Langevin equations describing the dynamics of particles [60]. From the values of the molecular dipole moment, the refractive index and the mass density, the theory correctly predicts the static permittivity and the Kirkwood correlation factor as functions of temperature for real molecular liquids, e.g. primary alcohols and various other vdW liquids. It introduces only a single temperature-independent free parameter that quantifies inter-particle interactions. Although the theory does not consider any complex intermolecular interactions like hydrogen-bonding, it predicts that $g_K > 1$ can be observed for polar liquids simply due to electrostatic interactions of permanent dipoles as well as induction and dispersion forces.[110] At the same time, the theory considers the dynamic susceptibility, where for $g_K > 1$ an additional slow cross-correlation process is observed, similar to what is is found for experimental data in Fig. 5.1 [109].

The results presented in Fig. 5.1 suggest that, in certain supercooled liquids, dipolar cross-correlations considerably contribute to $\varepsilon''(\nu)$. They significantly affect the respective relaxation shape and lead to the discrepancies observed between the $\varepsilon''(\nu)$- and $\chi''(\nu)$-relaxation shapes. Conversely, this idea implies that, once there are no relevant contributions from dipolar cross-correlations, the same relaxation shape should be observed for $\varepsilon''(\nu)$ and $\chi''(\nu)$-data. This conjecture is verified in Fig. 5.2a, where a detailed comparison of $\varepsilon''(\nu)$ (colored symbols) and $\chi''(\nu)$-spectra (black symbols) obtained at different temperatures of the low-polar and non-hydrogen bonding silicone oil DC704 is shown. The analysis is reproduced from Refs. [44, 94]. Evidently, data from both techniques perfectly coincide and the relaxation shape corresponds to the generic relaxation shape observed in Fig. 4.1b. Fig. 5.2b presents an overview of $\varepsilon''(\nu)$-data obtained for various supercooled liquids with very low polarities, including different branched alkanes, aromatic compounds and silicone oils. Some of these data were obtained from the literature (see caption for details) [107, 108]. In contrast to the broad variety of relaxation shapes observed in Fig. 4.1a, $\varepsilon''(\nu)$-data of these low-polarity supercooled liquids

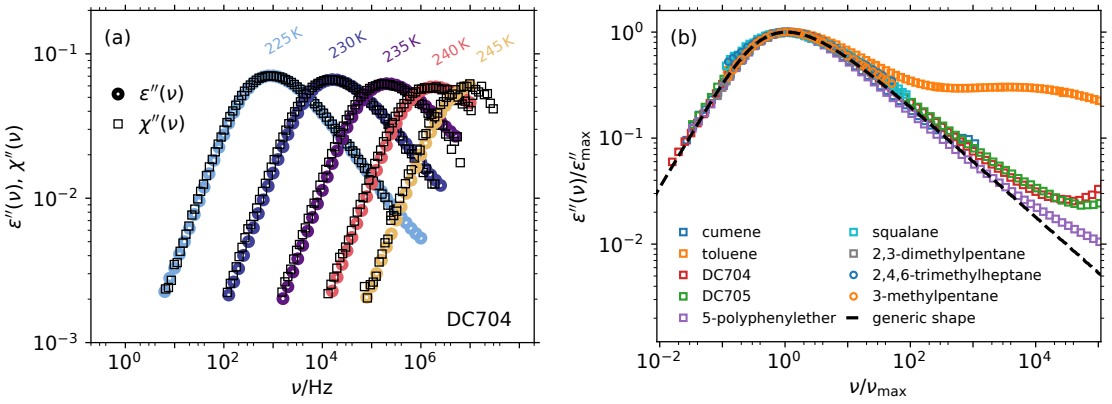

Figure 5.2: Relaxation spectra of low-polarity supercooled liquids, for which, most likely, no dipolar cross-correlations contribute to $\varepsilon''(\nu)$. Panel (a) shows a comparison of $\varepsilon''(\nu)$ and $\chi''(\nu)$-data of the silicone oil DC704. Relaxation spectra from both techniques superimpose almost perfectly. Data are reproduced from Refs. [44, 94] In panel (b), $\varepsilon''(\nu)$-relaxation shapes of various other low-polarity supercooled liquids are compared by plotting the data normalized with regard to the respective peak-maximum frequencies and amplitudes. Very similar relaxation shapes are observed that agree well to the generic relaxation shape identified from DDLS data in Fig. 4.1b(dashed black line). Data of the branched alkanes, 2,3-dimethylpentane, 2,4,6-trimethylheptane and 3-methylpentane, were obtained from Ref. [107], toluene-data from Ref. [108] were kindly provided by Prof. Ernst Rössler. All other data were obtained either by Florian Pabst [44] or during this work.

share very similar relaxation shapes, which are shown to coincide well to the generic relaxation shape. This observation indicates that, indeed, the generic relaxation shape is observed also in DS once dipolar cross-correlations are absent.

5.2 SUPPRESSION OF CROSS-CORRELATIONS

Following the conjectures discussed above, the generic relaxation shape should be recovered in DS once cross-correlations are suppressed by some suitable experimental procedure. Fig. 5.3 presents three examples of such procedures for two different supercooled liquids.

Panel (a) reproduces data from Ref. [44, 102] for the non-hydrogen bonding supercooled liquid tributyl phosphate (TBP), which features a distinct slow cross-correlation contribution, see Fig. 5.1b. Most likely, these cross-correlations result from dipole-dipole interactions between TBP molecules, as suggested by the theory of Déjardin et al. [60, 110]. In an attempt to suppress these cross-correlations, Pabst et al. studied mixtures of TBP with the non-polar solvent n-pentane. This procedure is expected to increase the average distance between TBP molecules, thus weakening dipole-dipole interactions. For a direct comparison, the relaxation spectra in Fig. 5.3 are normalized to their respective peak-maximum frequencies and amplitudes. For pure TBP, a significantly more narrow relaxation shape is observed for $\varepsilon''(\nu)$ (green symbols) compared to $\chi''(\nu)$ (blue symbols). After sufficient dilution by n-pentane, however, the $\varepsilon''(\nu)$-relaxation shape of TBP broadens and coincides with the $\chi''(\nu)$-relaxation shape. Moreover, it was confirmed that the broadening saturates at high n-pentane concentrations, thus, it could be excluded that the broadening reflects enhanced dynamic heterogeneity in the binary mixture compared to the pure TBP. These results indicate that dilution by a non-polar solvent suppresses dipolar cross-correlations in TBP.

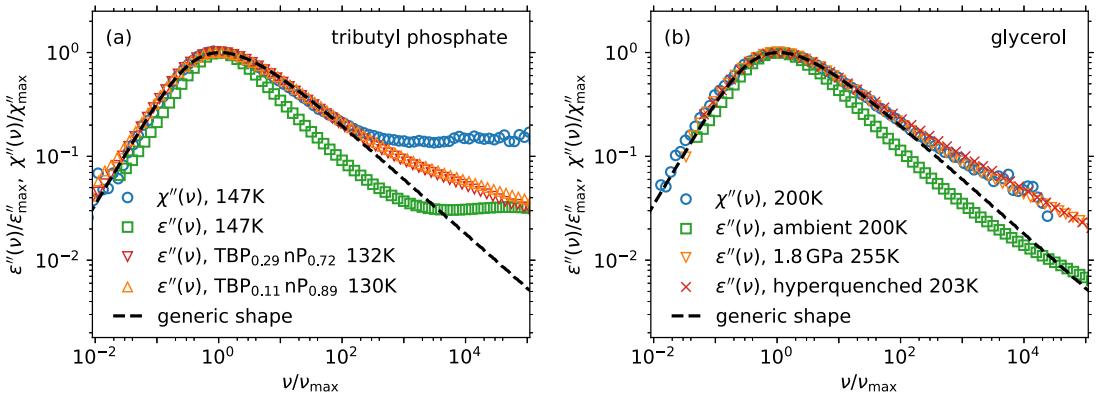

Figure 5.3: Verifying whether suppressing dipolar cross-correlations recovers the generic relaxation shape for $\varepsilon''(\nu)$-data. Panel (a) is reproduced from Refs. [44, 102] and shows $\varepsilon''(\nu)$- (green symbols) and $\chi''(\nu)$-data (blue symbols) of pure TBP, as well $\varepsilon''(\nu)$-data from two mixtures with n-pentane with different concentrations indicated in the legend (red and orange symbols). Dilution suppresses dipolar cross-correlations and recovers the generic relaxation shape. Similar data are shown in panel (b) for glycerol, where hydrogen bonding is suppressed either by applying 1.8 GPa hydrostatic pressure (orange symbols) [111], or by hyperquenching from room temperature with 80,000 K/s (red symbols) [112]. Both procedures recover the generic relaxation shape.

Panel (b) shows similar results for glycerol, but based on different procedures to suppress cross-correlations, which in glycerol most likely result from hydrogen-bond interactions. One possibility to suppress hydrogen-bonding is to apply large hydrostatic pressures [113, 114]. A second possibility is to hyperquench glycerol from room-temperature directly into the deeply supercooled state. This procedure essentially freezes the high-temperature structure of the liquid, due to giving the system insufficient time for structural equilibration. Since hydrogen bonding is less pronounced at high temperatures, the state of glycerol obtained after hyperquenching is expected to feature a less pronounced hydrogen-bonded network. In Fig. 5.3, the $\varepsilon''(\nu)$-relaxation shape of pressurized glycerol at 1.8 GPa from Hensel-Bielowka et al. [111], as well as hyper-quenched glycerol cooled with 80,000 K/s from Gainaru et al. [112] are compared to data of pure glycerol. Again, $\varepsilon''(\nu)$ of pure glycerol is more narrow than $\chi''(\nu)$, however both procedures of suppressing hydrogen bonding lead to an almost perfect collapse of $\varepsilon''(\nu)$ and $\chi''(\nu)$. The results summarized in Fig. 5.3 support the conjecture that dipolar cross-correlations are the reason for the narrow $\varepsilon''(\nu)$-relaxation shape observed for glycerol and TBP.

5.3 EVIDENCE FROM OTHER EXPERIMENTAL AND COMPUTATIONAL TECHNIQUES

Evidence for the significant impact of dipolar cross-correlations on the dielectric relaxation shape is not only provided by DDLS experiments, but also by several other techniques. The following section gives a brief review of the corresponding literature.

Important contributions to answering the question as to whether dipolar cross-correlations alter the dielectric relaxation shape are provided by ^{2}H-NMR. The reason for this it that ^{2}H-NMR directly probes an orientational self-correlation function and, thus, the interpretation of the corresponding results does not rely on any assumptions, like the empirical observation

that DDLS is mostly insensitive to orientational cross-correlations in pure supercooled liquids. Analysis of NMR data for a wide variety of different supercooled liquids, mostly obtained from field-cycling experiments, for the most part support the findings from DDLS, i.e. the NMR and DDLS relaxation shapes agree well in many cases, while they differ from the dielectric relaxation shape [115–117]. Still, a broader variety of high-frequency power-law exponents is observed in NMR compared to DDLS. It is difficult to judge, however, whether some of these discrepancies might result from the fitting procedures applied to NMR data. This is supported by the fact that quite different results were obtained for different fit models [115].

Cross-correlation contributions were also identified in comprehensive analyses of shear rheological data. For MAs, the shear modulus is dominated by the α-process, which is observed at similar frequencies as in DDLS. However, an additional low-frequency contribution is commonly identified that resembles chain-connectivity effects in polymers [118, 119]. A similar contribution was also identified by Arrese-Igor et al. for glycerol in the complex viscosity representation. It was found to coincide with the peak-maximum frequency of the dielectric loss spectrum [120], thus supporting the latter's assignment as a cross-correlation contribution. Similar conclusions regarding the coexistence of self-correlational and collective modes in shear rheological spectra of glycerol were drawn by Gabriel et al. for the shear compliance [121]. While it might not be surprising that hydrogen-bonded structures contribute considerably in shear rheology, due to the fact that hydrogen bonds have to be broken in order to make these systems flow [122], it is not clear whether the same behavior is to be expected for dipole-dipole interactions induced cross-correlations. For TBP, Moch et al. identified a single contribution to the real part of the shear compliance, the average relaxation time of which roughly coincides with the one of the dielectric loss. This, among other observation, let these authors conclude that the collective relaxation mode instead of the self-correlations are associated with the glass transition [123]. Arresse-Igor et al. came to a different conclusion, as they clearly identified a self- as well as cross-correlation contribution to the imaginary part of the viscosity and the derivative of the real part of the shear compliance [124]. The latter can be thought of as an approximation of the imaginary part of the shear compliance. These findings support the DDLS results discussed above and clearly show that self-correlational and collective modes contribute differently to the different shear rheological representations.

Similar observations were recently reported by Paluch et al., who proposed an approach for identifying dipolar cross-correlations via the dielectric modulus $\hat{M}(\omega)$ [125], i.e. the dielectric response upon applying a constant charge instead of an electric field. Because $\hat{M}(\omega) = \hat{\varepsilon}(\omega)^{-1}$, relaxation processes contribute to the dielectric modulus with different weighting factors compared to the dielectric permittivity. Processes with a rather large $\Delta\varepsilon$, e.g. dipolar cross-correlations, contribute to $\hat{M}(\omega)$ with a rather small ΔM. As a consequence, the dielectric modulus in many cases is dominated by dipolar self-correlations, as shown by Paluch et al. through comparison to DDLS data [125].

Slow dipolar cross-correlations were also identified in some computer-simulation studies. While such analyses are inherently limited to higher temperatures beyond the deeply supercooled regime, they can serve as valuable tools to unambiguously disentangle dipolar self- and cross-correlations, because both can be directly calculated from the simulation trajectories.

Koperwas et al. studied the dipolar dynamics of two model-systems – one composed of highly and one of weakly polar rhombus-like molecules. For both systems the macroscopic polarization autocorrelation function $C_{\boldsymbol{P}}(t)$ was decomposed into self- and cross-correlations. While for the weakly polar system, $C_{\boldsymbol{P}}(t)$ was shown to almost exclusively contain self-correlations, it is dominated by cross-correlations for the highly polar system. The observed cross-correlations are Debye-shaped and relax at significantly longer times than the

self-correlations, thus supporting the experimental observation of a slow and narrow dipolar cross-correlation contribution. Due to the choice of the particular model system, the observed dipolar cross-correlations can be unambiguously identified to originate from dipole-dipole interactions instead of other interaction mechanisms like hydrogen bonding.

A similar approach was taken by Hénot et al. for the "real" liquid glycerol [126]. They identified significant cross-correlation contributions that decay slower and with a steeper high-frequency power law than the self-correlations. The analysis of preferred local dipolar associations revealed a pattern that approximately reflects the dipole-dipole interaction potential with some additional contributions due to other effects, e.g. hydrogen-bonding or sterical constraints. Moreover, Hénot et al. showed that considering the $\ell = 2$ Legendre polynomial instead of $\ell = 1$ drastically reduces the cross-correlation contribution, such that the corresponding $\ell = 2$ relaxation spectrum is almost entirely dominated by self-correlations [126]. The reason for this seem to be the different angular sensitivities of the respective Legendre polynomials, i.e. orientations of molecules are anti-correlated at an angle of 90° for $\ell = 2$, but at 180° $\ell = 1$. These result can be considered as a first rationalization of the empirical observation that cross-correlations do not contribute to the DDLS relaxation spectrum. An open question remains whether the results for glycerol can be generalized to other liquids with pronounced dipolar cross-correlations.

Finally, several studies dealing with the dynamics of liquid water have to be mentioned. Similar to what is found for many other strongly polar liquids, the dielectric response of water was found to be dominated by dipolar cross-correlations [127–129]. Notably, one of these studies [128] used ab initio techniques and, thus, did not rely on using classical force-fields to model hydrogen bonding. These observations of slow cross-correlation contributions to the dielectric loss of water allow to rationalize the previously observed discrepancy between dielectric and Raman spectra [130, 131]. Equivalent to what is observed for deeply supercooled liquids, Raman spectroscopy, which is a high-frequency DDLS technique, is found to be mostly insensitive to the dipolar cross-correlations in water.

5.4 QUANTITATIVE RELATIONS BETWEEN CROSS-CORRELATIONS AND RELAXATION STRETCHING

All observations discussed in the previous sections clearly suggest that the narrow relaxation shapes of the dielectric loss observed for various supercooled liquids are related to dipolar cross-correlation contributions. So far, this relation is qualitative in the sense that no quantitative connection between the strength of dipolar cross-correlations in a supercooled liquid and its dielectric relaxation shape has been formulated. This section aims to establish such a quantitative relation.

5.4.1 Correlation between g_K and β

The underlying hypothesis of the following analyses is that the strength of dipolar cross-correlations is correlated to the high-frequency power-law exponent β of the dielectric loss. This conjecture is based on two assumptions: (i) In the absence of any dipolar cross-correlations, $\beta \approx 0.5$ is found for the dielectric loss spectrum. It grounds on the observations for substances with low-polarity and for DDLS data of various supercooled liquids above. In cases where cross-correlations contribute, $\beta \approx 0.5$ is assumed to also hold for the self-part $\varepsilon''_{\text{self}}$ of the dielectric loss. (ii) Dipolar cross-correlations $\varepsilon''_{\text{cross}}$ contribute as a slow Debye-shaped

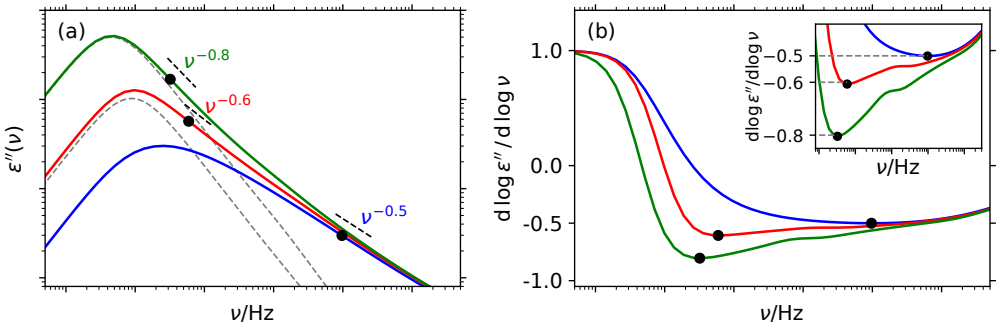

Figure 5.4: Illustration how a slow Debye-shaped cross-correlation process (dashed lines) that superimposes the self-part of the dielectric loss (blue line) affects the overall shape of the dielectric loss. The blue curve is based on a GG distribution of relaxation times with parameters $\alpha = 2$ and $\beta = 0.5$ (cf. Eq. (3.4)) [87, 94]. Superposition by an additional cross-correlations contribution leads to a larger values of β that increase as functions of $\tau_{\text{cross}}/\tau_{\text{self}}$ and $\Delta\varepsilon_{\text{cross}}/\Delta\varepsilon_{\text{self}}$, as shown here for two examples (green and red lines). (b) The exponent of the high frequency power law can be determined in a model-free approach by calculating the minimum value of the the logarithmic derivative, cf. Eq. (3.11). The inset represents a magnified plot of the region around the minimum.

peak. The dynamic separation with regard to the self-correlations, $\tau_{\text{cross}}/\tau_{\text{self}}$, increases with increasing quotient of the respective relaxation strengths, $\Delta\varepsilon_{\text{cross}}/\Delta\varepsilon_{\text{self}}$.

Such scenarios and the respective effects on β are explored exemplarily in Fig. 5.4a. Here, the blue line shows the dielectric loss spectrum found for a supercooled liquid without any cross-correlations, thus it is modeled with $\beta = 0.5$. The red and the green spectrum each are obtained by superimposing the blue curve by a Debye function (dashed gray line) according to different values of $\tau_{\text{cross}}/\tau_{\text{self}}$ and $\Delta\varepsilon_{\text{cross}}/\Delta\varepsilon_{\text{self}}$. The resulting high-frequency power-laws are steeper with exponents $\beta = 0.6$ and 0.8, respectively. Thus, it is concluded that β critically depends on the specific properties of dipolar cross-correlations in each liquid and can result in a variety of different values for β.

To quantify the strength of dipolar cross-correlations, in the following analyses the Kirkwood correlation factor g_{K} (cf. Eq. (2.45)) is considered. It is important to note that g_{K} quantifies the *average* strength of *static* dipolar cross-correlations. Thus, $g_{\text{K}} = 1$ does not necessarily imply the absence of any dipolar cross-correlations, but could as well reflect an ensemble average over coexisting parallel and anti-parallel dipolar alignments. Most likely, the dynamic signature of dipolar cross-correlations is associated with a more local degree of cross-correlations instead of with the ensemble average. For instance, in a scenario where chain-like and ring-like supra-structures coexist in a monohydroxy alcohol, one still would expect to observe a slow contribution to the dielectric loss that reflects the reorientation of the chain-like structures although g_{K} could be unity. Indeed, this has been observed experimentally for the monohydroxy alcohol 5-methyl-3-heptanol, as shown in Refs. [132–135] and discussed in Section 6.1.2. As a consequence, substances where it has to be expected that g_{K} does not reflect the local geometry of dipolar associations, e.g. some octanol isomers, are not considered in the following. Moreover, it is stressed that determining g_{K} requires knowledge of the molecular dipole moment μ, which needs to reflect the conformational states of the molecules in the liquid phase and can be determined via dilution experiments [136, 137]. Typically, no such data are available in the literature for more exotic molecules, like most pharmaceuticals considered in a previous meta-analysis of the dielectric relaxation shape [34]. One of the reasons is that these molecules are quite flexible and consist of several functional groups that

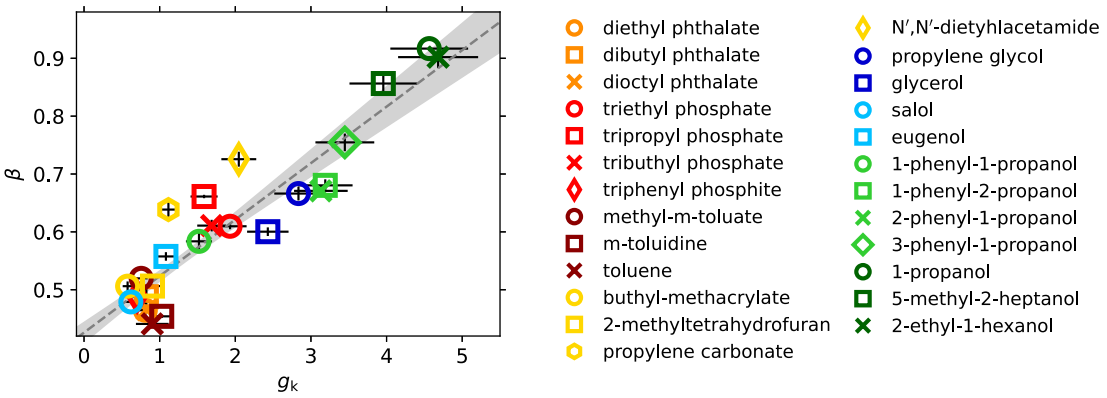

Figure 5.5: β as a function of g_K for various supercooled liquids. Substances from different subcategories are plotted in the same color (orange: phthalates, red: phosphates, dark red: aromatic vdW, yellow: non-aromatic vdW, blue: polyhydric alcohols, light blue: phenols, light green: aromatic monohydroxy alcohols, dark green: non-aromatic monohydroxy alcohols).
For each substance one temperature-averaged point over various temperatures that obey $10^{-1}\,\mathrm{Hz} < \nu_{\mathrm{peak}}(T) < 10^{5}\,\mathrm{Hz}$ is included. Error bars reflect the standard deviation of the temperature dependence of β and g_K, as well as the uncertainty of the parameters used for calculation g_K ($\Delta\mu/\mu = 0.05$, $\Delta n = 0.01$, $\Delta\rho/\rho = 0.05$ and $\Delta\varepsilon_s/\varepsilon_s = 0.01$). All parameters used for the calculation of g_K can be found in Appendix A.
The dashed gray line represents the result of a linear regression analysis that yields $\beta = (9.76\pm0.61)\cdot10^{-2}\cdot g_K + (0.42\pm0.01)$ and a Pearson correlation coefficient of $\rho_{g_K,\beta} = 0.91\pm0.02$. The gray shaded area indicates the 2σ-confidence interval.

carry a substantial dipole moment. In this case, the total molecular dipole moment strongly depends on the conformational state of the molecule, making it impossible to assign one single value of μ in order to calculate g_K, let alone to determine μ in a dilution experiment (cf. Section 6.2 for the example of sorbitol). Thus, the present analysis focuses on smaller molecules, for which μ is readily available, which is the reason why a smaller number of substances is considered compared to previous work [34].

β is determined using the model-free approach from Nielsen et al. [33] based on determining the minimum of the logarithmic derivative of the dielectric loss, cf. Eq. (3.11) and Fig. 5.4b. This procedure is favored over fitting procedures, as it is well-defined and, thus, well-suited to compare the relaxation shape of various supercooled liquids without introducing bias from the choice of applied model functions.

Fig. 5.5 displays β as a function of g_K for 25 different deeply supercooled liquids. It confirms the hypothesized correlation between both quantities. For clarity each point represents the temperature-averaged value of both quantities. This temperature-averaging procedure is valid as $\beta(T)$ and $g_K(T)$ do not vary strongly as functions of temperature, at least in the deeply supercooled regime. This is illustrated in both panels of Fig. 5.6, where β and g_K are plotted as functions of reduced temperature T/T_g. As far as crystallization could be avoided, for each liquid temperatures were considered for which the peak-maximum frequency of the dielectric loss is $10^{-1}\,\mathrm{Hz} < \nu_{\mathrm{peak}}(T) < 10^{5}\,\mathrm{Hz}$. The error bars reflect the estimated uncertainty due to the uncertainty of parameters for determining g_K (see figure caption and Appendix A for details), as well as the variation of g_K and β as functions of temperature.

From Fig. 5.5 it is immediately clear that higher values of β are associated with larger g_K. Both quantities are strongly correlated with a Pearson correlation coefficient of $\rho_{g_K,\beta} = 0.91 \pm 0.02$ as determined via a linear regression that yields $\beta = (9.76 \pm 0.61)\cdot 10^{-2}\cdot g_K + (0.42 \pm 0.01)$ (gray

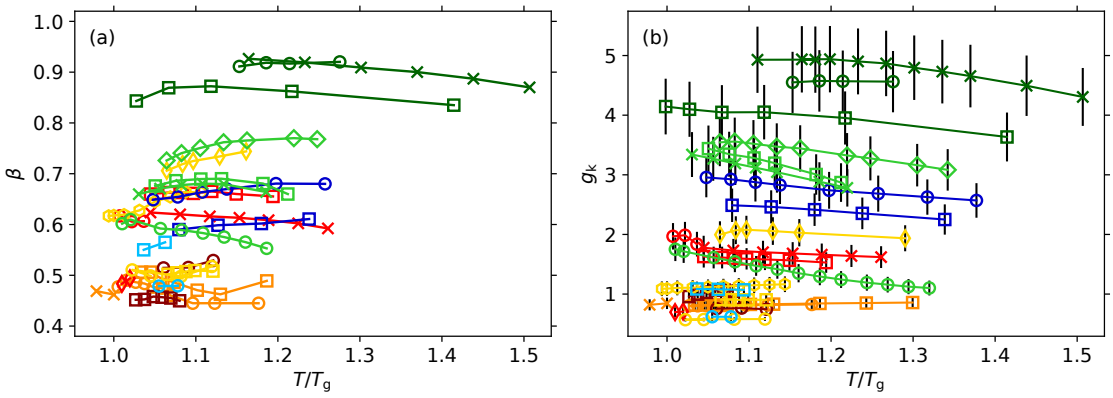

Figure 5.6: β and g_K as a function of reduced temperature T/T_g. Both quantities vary weakly with temperature, thus temperature-averaged values can be considered. The symbols are the same as in Fig. 5.5. Error bars for g_K reflect the following uncertainties of parameters: $\Delta\mu/\mu = 0.05$, $\Delta n = 0.01$, $\Delta\rho/\rho = 0.05$ and $\Delta\varepsilon_s/\varepsilon_s = 0.01$.

dashed line). Here, the uncertainties of $\rho_{g_K,\beta}$ and the 2σ-confidence intervals of the linear regression (gray shaded area) were determined by Monte-Carlo sampling the uncertainty distributions of each point in Fig. 5.5.

Around $g_K \approx 1$ and $\beta \approx 0.5$, a clustering of data points from different substances is observed. This confirms the premise that the generic power-law exponent $\beta = 0.5$ is observed as soon as dipolar cross-correlations are absent ($g_K \approx 1$). The opposite extreme is represented by 1-propanol, 2-ethyl-1-hexanol and 5-methyl-2-hexanol, i.e. three monohydroxy alcohols for $g_K \sim 4-5$ is found in agreement with their strong tendency to form supra-structures via hydrogen bonding. In between both extremes, at $1 < g_K < 4$, a broad variety of different substances is found. These have very different chemical structures and can be sorted into different sub-categories, namely non-hydrogen bonding liquids with and without aromatic groups, hydroxy aromatics, polyhydric alcohols, as well as monohydroxy alcohols with and without aromatic groups. The same colors are used in Fig. 5.5 for substances that are similar with regard to their assignment to one of these categories.

Obviously, the physical origin for dipolar cross-correlations must be fairly different among these substances. For instance, hydrogen bonding, dipole-dipole interactions, π-π-interactions and possibly also steric effects might be relevant. Remarkably, the relation between g_K and β appears to be similar for all the different sub-classes of substances. This finding suggests that the dynamic signature of dipolar cross-correlation resulting from different microscopical origin have a similar effect on the dielectric loss.

Notably, the observed correlation between g_K and β also rationalizes the physical origin of the correlation between the dielectric relaxation strength $\Delta\varepsilon$ and β reported by Paluch et al., which hereafter is referred to as *Paluch correlation*. Initially this correlation was explained by the authors by arguing that strong dipole-dipole interactions increase the harmonicity of the inter-molecular potentials, which is thought to affect the distribution of relaxation times and leads to less stretched relaxation shapes in highly polar substances [34]. This conjecture, however, does contradict the more recent observations discussed above, as such effects on the distribution of relaxation times should also be observed in DDLS or NMR experiments. Evidently, this is not the case. Instead, the Paluch correlation can be understood as an indirect consequence of the correlation between g_K and β: Large values of g_K are associated with larger values of β. At the same time, according to the Kirkwood-Fröhlich equation, large g_K are associated with larger $\Delta\varepsilon$ compared to what would be observed for a system with the same

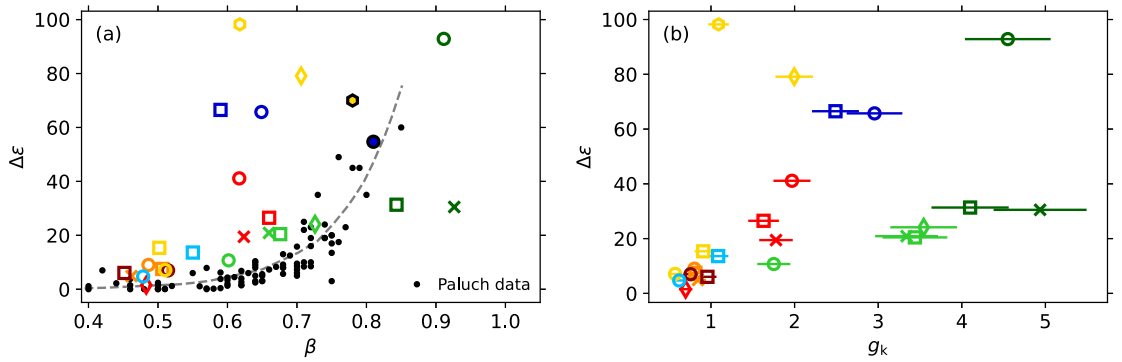

Figure 5.7: Analysis of how the β-g_K correlation is related to the β-$\Delta\varepsilon$ Paluch correlation [34]. (a) Comparison of $\Delta\varepsilon$ as a function of β obtained during this work (colored open symbols) to the Paluch correlation (black symbols and gray dashed line). The assignment of the colored symbols is the same as in Fig. 5.5. For comparison, propylene carbonate and propylene glycol data from Paluch et al. are highlighted using colored symbols with black border that correspond to the respective data from this work regarding color and shape of the symbol. The discrepancy reflects the different ways of determining β (model-free in this study, KWW by Paluch et al.). (b) $\Delta\varepsilon$ as a function of g_K. A correlation between both parameters is observed that suggests that the Paluch correlation indirectly follows from the β-g_K correlation.

dipole density but $g_K = 1$. Thus, the probability that a liquid with large $\Delta\varepsilon$ also has $g_K > 1$, and therefore $\beta > 0.5$, is enhanced compared to liquids with small $\Delta\varepsilon$.

These considerations are treated quantitatively in Fig. 5.7. Panel (a) attempts to reproduce the Paluch correlation by plotting $\Delta\varepsilon$ at one temperature close to T_g as a function of β for all supercooled liquids considered in this work as the open colored symbols. The assignment of colors and symbols is equivalent to the one in Fig. 5.5. The black symbols represent the data reproduced from the original publication by Paluch et al. [34]. While the open colored symbols from this work roughly follow the trend of the Paluch correlation, the spread of the data points is significantly larger. There are two main reasons for this: First, the work by Paluch et al. did not consider monohydroxy alcohols (dark green symbols), which have large values of β at comparatively low $\Delta\varepsilon$. Second, in the Paluch correlation β_{KWW} is used instead of the model-free approach for determining β_d. As discussed in Section 3.2.1, the KWW function has only a single shape parameter, β_{KWW}, that controls the high-frequency power law and the width of the peak. As a consequence, for narrow relaxation shapes the fit overestimates β_{KWW} in order to fit the data around the peak maximum. For some substances this causes quite large discrepancies between β_{KWW} and β_d, which in some cases lead to large deviations of the data obtained during this work from the general trend of the Paluch correlation. This is visualized in Fig. 5.7 for two substances that have been considered in both works, propylene glycol (open dark blue circle) and propylene carbonate (open yellow hexagon), by plotting the corresponding data from Paluch et al. as filled symbols in the same color, but with a black border. The discrepancies are significant: For propylene glycol, $\beta_d = 0.65$ while $\beta_{KWW} = 0.81$, and for propylene carbonate, $\beta_d = 0.62$ while $\beta_{KWW} = 0.78$.

In Panel (b) of Fig. 5.7 the relation between g_K and $\Delta\varepsilon$ is explored. As suspected above, both quantities are correlated, which confirms the conjecture that the Paluch correlations is an indirect consequence of the causal relation between g_K and β.

5.4.2 Relations between self- and cross-correlations

The previous analyses set out to explore the effect of dipolar cross-correlations on the relaxation shape of the dielectric loss. This was achieved by hypothesizing certain simple relations for dipolar self- and cross-correlations and by confirming the therefrom anticipated correlation between g_K and β. However, further and more direct insight can be gained by disentangling self- and cross-correlation contributions to the dielectric loss via comparison to DDLS data. It has to be noted though that, as DDLS experiments are considerably more time consuming than dielectric experiments, the number of substances that could be analyzed in this way is smaller than in the previous section. Below, various relations between dipolar self- and cross-correlations are analyzed for nine different supercooled liquids, i.e. the six substances considered in Fig. 5.1, as well as three additional monohydroxy alcohols 1-phenyl-1-propanol (1P1P), 2-phenyl-1-propanol (2P1P) and 5-methyl-2-heptanol (5M2H).

Testing the Kivelson-Madden relation

As a first step, the famous "micro-macro" relation from the theory of Kivelson and Madden (KM) [138, 139] is tested. Building on the earlier work of Keyes [140], KM attempted to obtain a theoretical framework that connects the collective dielectric response of a liquid, which is the quantity measured in a typical dielectric experiment, to the microscopic relaxation of single dipoles. Under certain assumption their theory yields the simple relation

$$\tau_M = g_K \, \tau_{self}, \tag{5.2}$$

for the average relaxation times of the collective response, τ_M, and of single dipoles, τ_{self}. Although the validity of the approach by KM was later challenged by Bordewijk [141], the KM relation is still discussed in the context of dipolar cross-correlations to date [142]. Moreover, several experimental and computer-simulation studies obtained results that support the validity of Eq. (5.2) in the liquid regime above the melting point [143–146].

Following the joint interpretation of dielectric and DDLS spectra in Section 5.1, τ_M is obtained as the peak-maximum relaxation time of $\varepsilon''(\nu)$, while the peak-maximum relaxation time of $\chi''(\nu)$ is assumed to represent τ_{self}. In Fig. 5.8a, τ_M/τ_{self} is plotted as a function of g_K obtained at various temperatures for the nine supercooled liquids. Almost all points deviate significantly from the dashed line that indicates the KM prediction Eq. (5.2). Instead, the dynamic separation between collective and single-dipole relaxation is larger for almost all studied supercooled liquids. It is thus concluded that, in contrast to high-temperature liquids, the assumptions leading to Eq. (5.2) are not justified for deeply supercooled liquids. It is noted that similar issues have been identified by Matyushov et al. [142], which these authors have resolved by introducing an additional substance-specific factor to Eq. (5.2) that compensates the discrepancies observed in Fig. 5.8a. In the context of the KM theory, this parameter can be interpreted as the dynamical correlation factor J_K, which quantifies cross-correlations of dipolar angular velocities and usually is close to unity for liquids at high temperature, which however might not necessarily be the case for supercooled liquids. These adjustment allow Matyushov et al. to predict the $\varepsilon''(\nu)$-relaxation spectrum from $\chi''(\nu)$. It has to be noted, however, that in order to make the results from Fig. 5.8a agree with KM, quite different values of J_K would be required for substances with very similar chemical structures, e.g. for the phenyl-propanol isomers $J_K \sim 1-6$ depending on the position of the hydroxy group. Further investigations are required in these regards and especially the recent advances

in computer-simulations [126, 147] are promising tools to study the relation of τ_M and τ_{self} when approaching the supercooled regime.

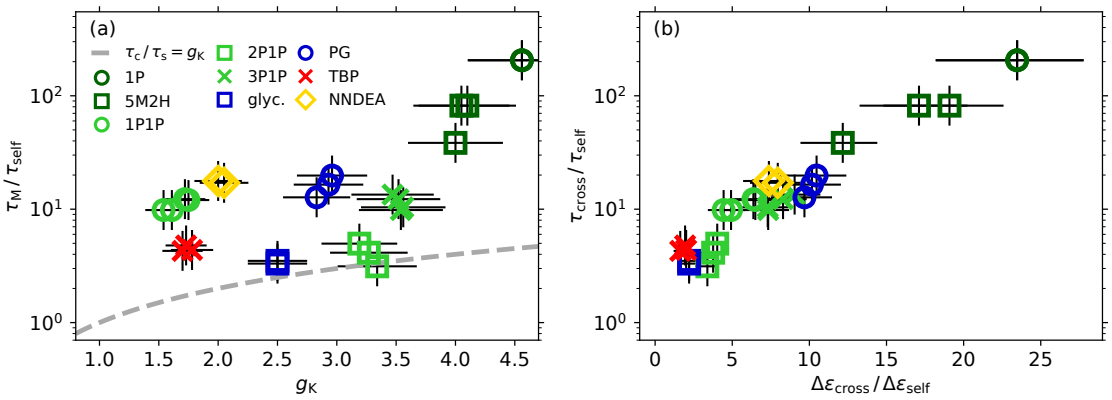

Figure 5.8: (a) Testing the KM relation Eq. (5.2) by plotting the ratio of collective and self-correlation times τ_M/τ_{self} as a function of g_K. τ_{self} is obtained via comparison of $\varepsilon''(\nu)$ and $\chi''(\nu)$-data. The data visibly deviate from the KM prediction indicated by the gray dashed line. (b) τ_{cross}/τ_{self} as a function of $\Delta\varepsilon_{cross}/\Delta\varepsilon_{self}$ for the same substances as in panel (a). All data collapse onto a single master curve suggesting a common relation for self- and cross-correlations.

Testing the assumptions leading to the prediction of the β-g_K correlation

In Section 5.4.1 the prediction of the correlation between g_K and β was rationalized based on two hypotheses: The first one was the assumption that $\beta \approx 0.5$ holds for the self-correlations of the dielectric loss $\varepsilon''_{self}(\nu)$. It is confirmed by the observed clustering of data-points around $(g_K, \beta) = (1, 0.5)$ in Fig. 5.5 and the fact that $\varepsilon''(\nu)$-data of supercooled liquids with $g_K > 1$ could be described as a superposition of $\chi''(\nu)$ with $\beta = 0.5$ and a slow cross-correlation contribution in Fig. 5.1. The second assumption was that with increasing strength of dipolar cross-correlations, $\Delta\varepsilon_{cross}/\Delta\varepsilon_{self}$, the dynamic separation of these cross-correlations with regard to the self-correlations, τ_{cross}/τ_{self}, increases. This notion is verified in Fig. 5.8b, where τ_{cross}/τ_{self} is plotted as a function of $\Delta\varepsilon_{cross}/\Delta\varepsilon_{self}$ for the nine supercooled liquids at various temperatures. Indeed, the hypothesized relation between both quantities is observed. Moreover, the data for the different substances all collapse onto a single curve, a trend which was previously reported for monohydroxy alcohols and rationalized in terms of the transient chain model [148, 149], as both, τ_{cross}/τ_{self} and $\Delta\varepsilon_{cross}/\Delta\varepsilon_{self}$, are expected to increase with increasing length of hydrogen bonded supra-structures. The interesting conclusion from Fig. 5.8b is that also polyhydric alcohols and polar vdW liquids display the same relation. This suggests the relation between τ_{cross}/τ_{self} and $\Delta\varepsilon_{cross}/\Delta\varepsilon_{self}$ to be of much more fundamental nature and to represent a common characteristic shared by dipolar cross-correlations of diverse origin. In its essence, the finding from Fig. 5.8b is similar to the identification of a spectral envelope for dielectric loss spectra reported by Gainaru [150]. The results obtained in this work suggest that the physical origin of the identified envelope likely is related to the somewhat universal way how cross-correlations contribute to the dielectric loss.

Considering that both τ_{cross}/τ_{self} and $\Delta\varepsilon_{cross}/\Delta\varepsilon_{self}$, as well as as β and g_K are correlated, one could expect that τ_{cross}/τ_{self} and $\Delta\varepsilon_{cross}/\Delta\varepsilon_{self}$ are suitable predictors for β. This conjecture is tested in panels (a) and (b) of Fig. 5.9, respectively. In both cases, a clear correlation is

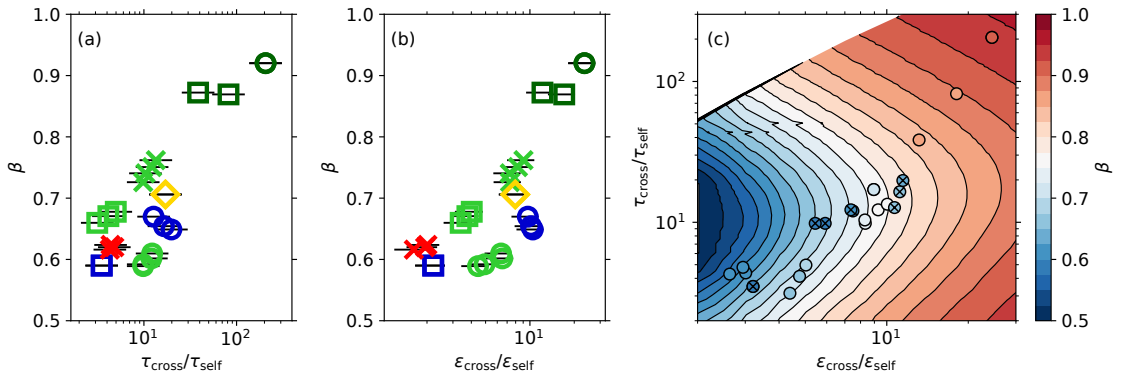

Figure 5.9: β as a function of (a) $\tau_{\mathrm{cross}}/\tau_{\mathrm{self}}$ and (b) $\Delta\varepsilon_{\mathrm{cross}}/\Delta\varepsilon_{\mathrm{self}}$ for various supercooled liquids. $\tau_{\mathrm{cross}}/\tau_{\mathrm{self}}$ and $\Delta\varepsilon_{\mathrm{cross}}/\Delta\varepsilon_{\mathrm{self}}$ have been determined using the fitting procedure explained in Eq. (5.1) and illustrated in Fig. 5.1. The assignment of the colored symbols is the same as in Fig. 5.8. (c) The heatmap illustrates the expected value of β as a function of $\tau_{\mathrm{cross}}/\tau_{\mathrm{self}}$ and $\Delta\varepsilon_{\mathrm{cross}}/\Delta\varepsilon_{\mathrm{self}}$. Iso-$\beta$ curves are indicated by the solid lines. The data were obtained by modeling the dielectric loss as the superposition of a Lorentzian shaped cross-correlation contribution and self-correlations described by the GG distribution of relaxation times with $\beta = 0.5$ and $\alpha = 2$ (generic relaxation shape). β was determined for the modeled relaxation spectra by using the model-free approach (Eq. (3.11)). Symbols represent data for real supercooled liquids from panels (a) and (b), with the fill color of the symbols indicating the respective values of β using the same color code as for the heat map. Crossed symbols indicate substances for which the cross-correlation contribution was modeled by a KWW-function with $\beta < 1$ instead of a Lorentzian.

observed, however the spread of the data is quite large and for some fixed value of $\tau_{\mathrm{cross}}/\tau_{\mathrm{self}}$ or $\Delta\varepsilon_{\mathrm{cross}}/\Delta\varepsilon_{\mathrm{self}}$, various different values of β are observed for the different substances.

To further interpret this observation, panel (c) of Fig. 5.9 shows how the dielectric relaxation shape is expected to vary as a function of $\tau_{\mathrm{cross}}/\tau_{\mathrm{self}}$ and $\Delta\varepsilon_{\mathrm{cross}}/\Delta\varepsilon_{\mathrm{self}}$. These data were obtained by modeling artificial dielectric relaxation spectra as the superposition of a self-correlation contribution with $\beta = 0.5$ and a slow Debye-shaped cross-correlation contribution and for different choices of $\tau_{\mathrm{cross}}/\tau_{\mathrm{self}}$ and $\Delta\varepsilon_{\mathrm{cross}}/\Delta\varepsilon_{\mathrm{self}}$. Subsequently, the respective high-frequency power-law exponents β were determined via the model-free approach and plotted as a heatmap including iso-β curves as black lines. Opposing the simple idea discussed previously with regard to Fig. 5.4, β does not simply increase with increasing $\tau_{\mathrm{cross}}/\tau_{\mathrm{self}}$ and $\Delta\varepsilon_{\mathrm{cross}}/\Delta\varepsilon_{\mathrm{self}}$ and, instead, the relation is more complex.

To relate the modeled relaxation-shape diagram to real supercooled liquids, the data from panels (a) and (b) are included as the circles. Their fill colors correspond to the respective experimentally observed values of β following the same color code as the heat map. It is found that the characteristic $\tau_{\mathrm{cross}}/\tau_{\mathrm{self}}$-$\Delta\varepsilon_{\mathrm{cross}}/\Delta\varepsilon_{\mathrm{self}}$ curve of real supercooled liquids does not pass perpendicular to iso-β curves, but instead runs almost parallel to these curves for $0.5 < \beta < 0.8$. As a consequence, already a rather small spread of the data points can imply that points with similar $\tau_{\mathrm{cross}}/\tau_{\mathrm{self}}$ and $\Delta\varepsilon_{\mathrm{cross}}/\Delta\varepsilon_{\mathrm{self}}$ are located in quite different β-regions, in harmony of what was found in panels (a) and (b).

Further insight can be gained by inspecting the fill color of the symbols in more detail. In most cases, the fill color is similar to the color of the respective surrounding β-region. However, this is clearly not the case for the symbols marked by the black crosses. These represent the substances for which the cross-correlation contribution to the experimental relaxation spectra could not been modeled as a Debye function (propylene glycol, glycerol

and 1-phenyl-1-propanol), but instead by a KWW function with $\beta < 1$ (see caption of Fig. 5.1). Obviously, these substances do no conform to the model the heatmap is based on. These substances are also found to be the outliers in panels (a) and (b) (light green circles, blue circles and blue squares).

To summarize, the present chapter compiled evidence supporting the notion that deviations from $\beta = 0.5$ found for the dielectric loss result from dipolar cross-correlation contributions. The final sections provided a quantitative relation between the dielectric relaxation shape and the strength of static cross-correlations, which was shown to rationalize the previously observed Paluch correlation. In addition, it provided evidence that the assumptions leading to the KM relations are not justified for supercooled liquids.

6

RELAXATION IN HYDROGEN-BONDING SYSTEMS

The following sections aim to address the question how different effects of hydrogen bonding (H-bonding) are manifested in the relaxation spectra of H-bonding supercooled liquids. The analyses rely on a detailed comparison of dielectric loss, $\varepsilon''(\nu)$, and DDLS spectra, $\chi''(\nu)$, building on the concepts established in previous chapters. Despite the influence that hydrogen bonding exerts on the molecular dynamics of these substances, in almost all cases the α-process probed by means of DDLS corresponds to the generic relaxation shape. On the other hand, dielectric-loss spectra are much more individual and depend on the specific H-bonding properties of these substances, mainly because it is dominated by signatures of dipolar cross-correlation reflecting supra-structures formed via H-bonding. Some of the data discussed in the following chapter have already been discussed in the contexts of the previous chapters 4 and 5, while this chapter focuses more specifically on their H-bonding properties.

In particular, the presented analyses attempt to clarify how the geometry and the dynamic signatures of H-bonded supra-structures depend on the molecular architecture. In this regard, the general strategy is to compare results among different isomeric or homologous series of monohydroxy and polyhydric alcohols. In Section 6.1.1, an isomeric series of phenyl propanols is considered, attempting to clarify to what degree the steric hindrance of a phenyl ring suppresses the formation of H-bonded structures. Section 6.1.2 analyses the transition from chain-like to ring-like supra-structures being favored depending on molecular architecture and temperature along an isomeric series of octanols. Here, it is found that $\varepsilon''(\nu)$ contains two distinct contributions reflecting H-bonding, namely a slow contribution due to the relaxation of supra-structures, and a signature of the attachment and detachment process of hydroxy groups to/from these structures. Finally, a homologous series of polyhydric alcohols is studied in Section 6.2, among which the relaxation shape and the relevant relaxation mechanisms sensitively vary with chain-length.

6.1 MONOHYDROXY ALCOHOLS

The study of monohydroxy alcohols (MAs) dates back to the early work of Peter Debye in the 1910s and 1920s [151], who analyzed their dielectric properties in order to confirm his model of polarization that predicted Lorentzian dielectric-loss spectra [152]. As obvious from previous chapters, it was later shown that a Lorentzian-shaped relaxation spectrum is in fact unusual and appears to be a quite unique feature of some MAs. Since the early works MAs have been intensely studied and over the years various ideas and models have been developed to describe their characteristic behavior. An overview on the rich history of the research on MAs is presented in the excellent review by R. Böhmer et al. [148], while only the key results that are relevant to this work are briefly summarized in the following introduction.

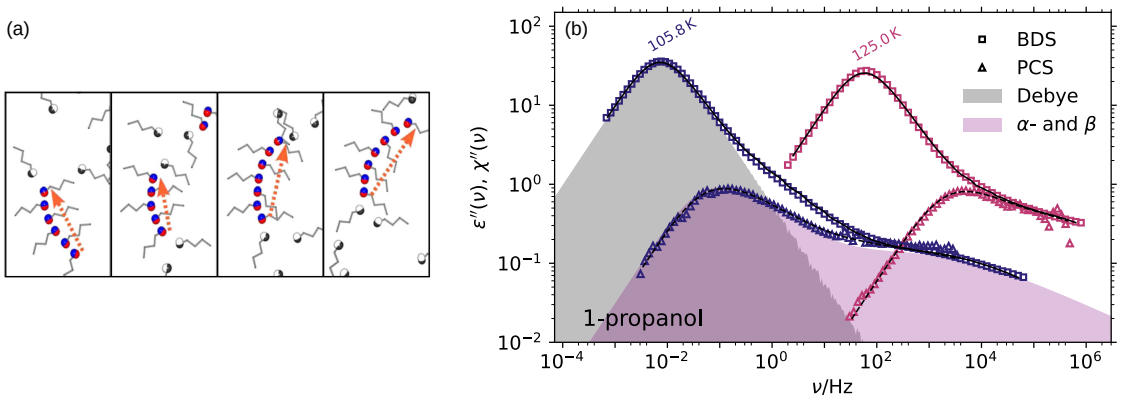

Figure 6.1: Molecular dynamics in MAs. (a) Illustration of the transient chain model adapted from Ref. [149]. MA molecules form chain-like structures with large end-to-end dipole moments. The structures rotate transiently via detachments and attachments of molecules from/to the chain. (b) $\varepsilon''(\nu)$ (squares) and $\chi''(\nu)$ (triangles) data of 1-propanol at selected temperatures. A joint analysis involves a fit to $\chi''(\nu)$ to identify the relaxation shapes of α- and β-process (dashed line, purple area), and, subsequently, a fit to $\varepsilon''(\nu)$ by Eq. (6.2) (solid line) assuming α- and β-process to be superimposed by the Debye process (grey area).

Already a few years after the work of Debye it became clear that molecular supra-structures have to be considered in order to explain the characteristic features of MAs, e.g. the low-q pre-peak in X-ray scattering [153] or their anomalously large dielectric constants [154]. Soon-after, the latter was explained in terms of orientational cross-correlations of dipoles [155] and quantified by the Kirkwood correlation factor g_K [156, 157], which to this day is still routinely used as a tool to estimate the degree of structure-formation in MAs. While early works assumed supra-structures to resemble "polymer-like" chains, it later became obvious that the geometry of structures depends strongly on the molecular architecture. Their geometry can range from chain-like to ring-like (and many in-between cases) and may even vary strongly as a function of temperature [132, 133, 158–161].

Regarding dynamics, several experimental discrepancies [148] suggested that the Lorentzian peak cannot represent the reorientation of single molecular dipoles and it was concluded that it instead reflects the relaxation of supra-structures. Improved resolution of dielectric experiments allowed the observation of a high-frequency shoulder to the Lorentzian peak [162], which later was found to correspond to calorimetric glass-transition modes and, thus, was concluded to represent the α-process [163, 164]. This finally lead to the semi-quantitative model that is applied to interpret the dielectric loss of MAs to this date. It considers α- and β-process contributions, both of which are universally observed in supercooled liquids, superimposed by the *Debye process* that reflects the dynamics of supra-structures [148], i.e.

$$\varepsilon''(\nu) = \Delta\varepsilon_D \cdot \frac{\omega\tau_D}{1+(\omega\tau_D)^2} + \Delta\varepsilon_{\alpha\beta} \cdot \varepsilon''_{\alpha\beta}(\nu). \tag{6.1}$$

Here, $\Delta\varepsilon_D$ and $\Delta\varepsilon_{\alpha\beta}$ represent the respective dielectric relaxation strengths of the contributions and the Debye process is modeled by the Debye function, associated with a single relaxation time τ_D.

While it had been well-established that the Debye process reflects the relaxation of supra-structures, details about the dynamic nature of its relaxation were only revealed much later by Gainaru et al. [149]. These authors used ^{1}H and ^{2}H NMR techniques to probe the supercooled dynamics of OD and CD isotope-labeled 1-butanol. The carbon backbones were found to

rotate on the same time scale as the dielectric α-process, while the characteristic relaxation time of hydroxy groups τ_{OH} was found to be in-between the ones of the Debye- and the α-process, i.e. $\tau_\alpha < \tau_{\mathrm{OH}} < \tau_{\mathrm{D}}$. These findings indicate that supra-structures relax transiently, with molecules frequently attaching and detaching from the structure. This mechanism is illustrated in Fig. 6.1a adapted from the original publication of the *transient chain model* by Gainaru et al. [149].

The Debye process had been assumed to solely be a dielectric phenomenon, however it was later observed also in shear rheological data, where it resembles typical chain-mode features of polymers [118]. Following the analogy to normal modes in type-A polymers [165], a relation between the relative dielectric relaxation strengths of the contributions in Eq. (6.1), $\Delta\varepsilon_{\mathrm{D}}/\Delta\varepsilon_\alpha$, and the average length of supra-structures, N, was derived. It relies on the assumption that the dielectric α-process reflects the reorientation of dipole-moment components perpendicular to chain-structures, while the components parallel to chain-structures contribute to the Debye process. This approach yields $N = 7-8$ for n-butanol at supercooled temperatures. [149]

More recently, dielectric and rheological experiments have been performed simultaneously to study how supra-structures are affected by shear [122]. The observed deviations from the dielectric spectrum obtained at equilibrium conditions could be rationalized in terms of a living polymer model [166, 167] that quantifies some qualitative ideas of the transient chain model and provides certain theoretical predictions to verify in future work.

Applying Eq. (6.1) to fit dielectric-loss data of MAs is not straight forward, as $\varepsilon''_{\alpha\beta}(\nu)$ is usually masked by the strong Debye process. Thus, some model-functions are usually assumed to describe $\varepsilon''_{\alpha\beta}(\nu)$. In this regard, DDLS experiments are useful, as they allow to determine the self-correlation contributions to the dielectric loss, as discussed previously in Chapter 5. Thus, performing complementary DDLS experiments allows to reduce Eq. (6.1) to

$$\varepsilon''(\nu) = \Delta\varepsilon_{\mathrm{D}} \cdot \frac{\omega\tau_{\mathrm{D}}}{1+(\omega\tau_{\mathrm{D}})^2} + \Delta\varepsilon_{\alpha\beta} \cdot \chi''(\nu), \tag{6.2}$$

where $\chi''(\nu)$ represents the (normalized) DDLS spectrum (cf. Eq. (5.1). Fig. 6.1b illustrates this procedure for 1-propanol [168]; $\chi''(\nu)$ (triangles) and $\varepsilon''(\nu)$ (squares) are jointly analyzed at two supercooled temperatures, which allows to identify the Debye- (grey area) and the α- and β-process (purple area) contributions to $\varepsilon''(\nu)$. The same or similar procedures have been applied to analyze relaxation spectra of various different MAs [48, 103, 168–170], some of which are discussed in the following sections. It is noted that in some cases the Laplace transform of the KWW function with $\beta < 1$ is used instead of the Debye function in order to quantify some degree of high-frequency broadening of the Debye process.

6.1.1 Phenyl propanol isomers

Phenyl alcohols are popular model systems to study how molecular architecture influences the molecular dynamics and structure-formation in hydrogen bonding systems. In particular, the combination of a hydroxy and a phenyl moiety is of interest, as both functional groups are common constituents of molecules with biological and pharmaceutical relevancy. The complex interplay of hydroxy and phenyl group introduces several additional molecular interaction mechanisms, namely π-π interactions between two or more phenyl groups, π-OH H-bonds and suppression of OH-OH H-bonds due to the sterical hindrance introduced by the phenyl group.

Especially the latter effect has been discussed in previous studies by Johari et al. [161, 171] and Kalinovskaya et al. [172] to interpret dielectric relaxation of different phenyl propanol isomers. It was found that in these substances the characteristic Debye peak is largely suppressed,

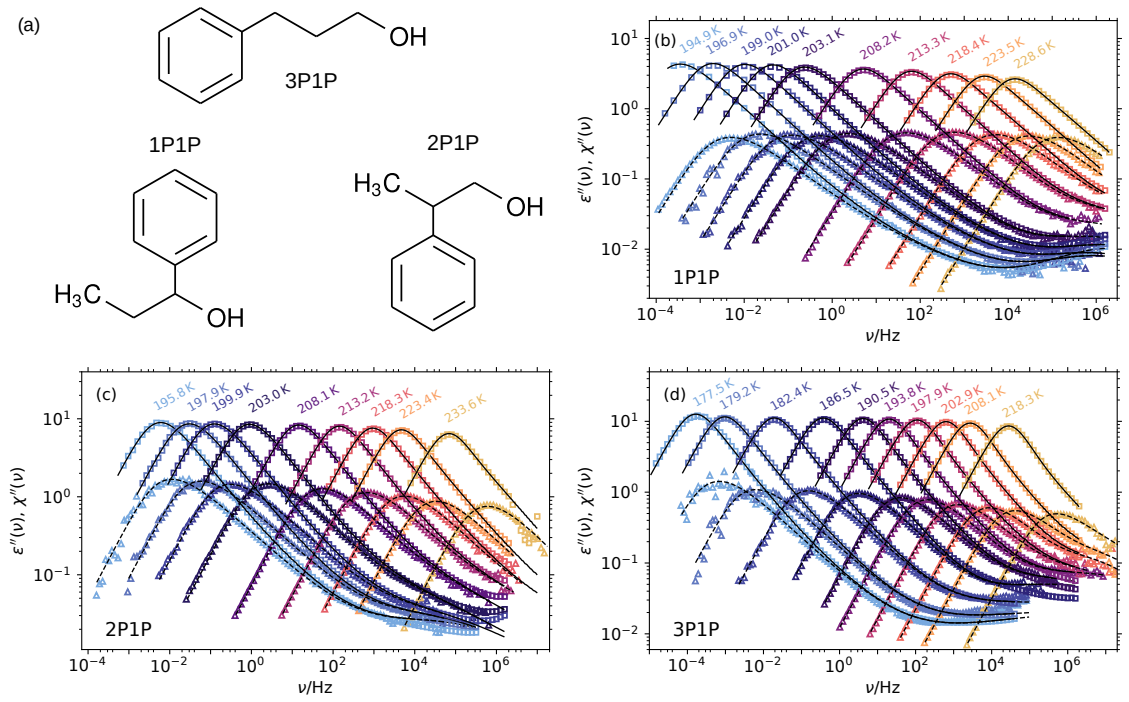

Figure 6.2: Relaxation spectra of phenyl propanol isomers. (a) Structure formulas of the investigated isomers. The hydroxy group is fixed at a terminal position, while the position of the phenyl ring is varied. (b)-(d) Combined analysis of $\varepsilon''(\nu)$ (squares) and $\chi''(\nu)$ (triangles) according to Eq. (6.2) (dashed and solid lines). For 1P1P, the Fourier transform of a KWW with $0.8 < \beta < 1$ was used to model the Debye process.

leading to dielectric loss spectra with a single asymmetrically broadened main relaxation peak that rather resembles the behavior found in non-hydrogen bonding supercooled liquids. This effect was found to be particularly strong if the phenyl group is positioned in the direct vicinity of the hydroxy group. For instance, neither any Debye process contribution, nor any static cross-correlations ($g_K \approx 1$) could be identified by the authors for 1-phenyl-1-propanol. Consequently, they concluded that the steric hindrance introduced by a phenyl group suppresses the formation of H-bonds, especially if it is located close to the hydroxy group.

Contrasting observations are presented and discussed in the following section, which were published in Ref. [103]. Here, DDLS experiments are utilized to accurately disentangle self- and cross-correlation contributions to the dielectric-loss spectra of phenyl propanols. Finally, the comparison allows to reevaluate the effect of phenyl rings on dynamics and geometry of hydrogen bonded supra-structures.

The studied phenyl propanol isomers are shown in Fig. 6.2a. While the hydroxy group is fixed at a terminal position, its distance from the phenyl ring is varied by shifting the latter along the chain; the distance is reduced from 3-phenyl-1-propanol (3P1P), over 2-phenyl-1-propanol (2P1P) to 1-phenyl-1-propanol (1P1P). Respective combined analyses of BDS and DDLS data are shown in Fig. 6.2b-d, including fits to DDLS data (dashed lines) by a model based on the GG distribution of relaxation times and fits to BDS data (solid lines) by the sum of the fit to PCS data and a KWW with $\beta \lesssim 1$ representing the Debye process, cf. Eq. (6.1). The overall picture is quite similar for all three isomers: Over the entire temperature range the comparison of the two techniques reveals pronounced Debye process contributions to the dielectric loss, which are unresolved in DDLS. Peak relaxation-time constants of Debye and α-process, τ_D and τ_α, as functions of inverse temperature are shown in Fig. 6.3a, while panel (b)

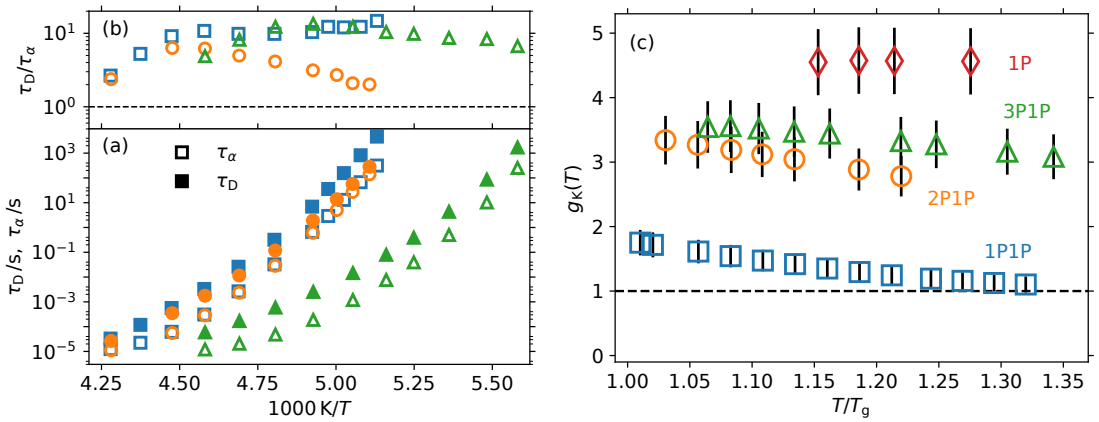

Figure 6.3: Cross-correlations in phenyl propanol isomers. (a) Relaxation time constants of Debye- (full symbols) and α-process (open symbols), τ_D and τ_α, as well as (b) dynamic separation, τ_D/τ_α, as functions of inverse temperature. The color assignments are shown in panel (c). (c) Static cross-correlations quantified by g_K as a function of normalized temperature T/T_g . Data for 1-propanol (1P) from Ref. [168] are included for reference. g_K decreases with decreasing distance between hydroxy group and phenyl ring and with increasing temperature.

displays the corresponding dynamic separation τ_D/τ_α. Evidently, the dynamic separation is comparably small ($\tau_D/\tau_\alpha < 20$) for phenyl propanols compared to many simple MAs like, e.g., 1-propanol ($\tau_D/\tau_\alpha \sim 100$, cf. Fig. 6.1a). As a consequence, the coexistence of both processes is hardly noticed by analyzing only dielectric-loss spectra, which explains the contradicting conclusions from previous studies [161, 171, 172].

Although a Debye process is observed independent of the phenyl-ring position, the latter does in fact strongly affect the degree of static dipolar cross-correlations, as evident from Fig. 6.3c. Here, g_K is shown as a function of the normalized temperature T/T_g for the three phenyl propanol isomers and their non-aromatic pendant 1-propanol. The figure confirms earlier results [161, 171, 172] by showing that introducing a phenyl ring generally reduces the degree of dipolar cross-correlations. The effect is more pronounced the closer the phenyl ring is located with regard to the hydroxy group. For 1P1P, g_K is almost unity, which is surprising considering that a pronounced Debye process contribution to the dielectric loss is identified in Fig. 6.2. This apparent discrepancy can be resolved by considering that $g_K \sim 1$ does not necessarily indicate the absence of cross-correlations, as it evaluates the average degree of dipolar associations. Instead, the coexistence of supra-structures featuring parallel (chain-like) and anti-parallel (ring-like) dipolar associations can equally lead to $g_K \sim 1$, as was observed, e.g., for certain octanol isomers [132, 133, 158]. Despite that, one expects to observe dynamic signatures of cross-correlations, reflecting the relaxation of chain-like supra-structures which manifests as a slow Debye process contribution to the dielectric loss. As this is consistent with the observations for 1P1P it is likely that the steric hindrance introduced by the close proximity of the phenyl ring to the hydroxy group favors the formation of ring-like supra-structures. This finally results in a coexistence of structures with predominantly parallel and predominantly anti-parallel dipolar associations.

Since the publication of the presented results, the isomeric series of phenyl propanol isomers has attracted further attention, leading to several insightful publications, which will be discussed briefly. The identification of self- and cross-correlation contributions to the dielectric loss presented in Fig. 6.2 has been confirmed by several other studies using shear rheology

measurements [119], logarithmic derivative analyses of dielectric data [173] and dielectric modulus data [125]. In particular for 1P1P, Gabriel at al. utilized high-electric field measurements to verify the conjecture that chain-like and ring-like structures coexist [174]. The basic idea of their approach is that, in case of aforementioned coexistence, applying high electric fields shifts the thermodynamic equilibrium towards chain-like structures being favored. This should lead to an increase of the Debye-process amplitude while the self-correlation part of the dielectric loss remains unaffected. Indeed, this effect was observed for 1P1P [174], similar as previously reported for 5-methyl-3-heptanol [134], which is the prototypical example for a MA featuring coexisting hydrogen bonded structures [132, 133, 158]. Signatures of structure-formation via OH-OH and OH-π interactions were also observed in x-ray diffraction and infrared-spectroscopy experiments [175, 176]. Recent computer-simulations support these results and provide insight on the size and geometry of supra-structures. Compared to simple monohydroxy alcohols like 1-propanol, the supra-structures in phenyl propanols are smaller and their geometry is more heterogeneous due to the additional interactions introduced by the phenyl ring. [177].

6.1.2 Octanol isomers

Octanol isomers are probably the most famous examples of how minimal changes of molecular architecture can dramatically alter the structure-formation properties of MAs. For this reason, the isomeric series n-methyl-3-heptanol has been a popular model system to study the influence of molecular architecture on the structural and dynamical properties of MAs for several decades [117, 132–135, 158–160, 178, 179]. The general observation is that by shifting the methyl group closer to the hydroxy group, the overall dielectric relaxation strength $\Delta\varepsilon$ strongly decreases [132, 133, 158]. The latter goes along with a reduction of the Debye process' relaxation strength [134]. Qualitatively, these findings are explained by assuming the prevalence of ring-like supra-structures in alcohols with large steric hindrance in proximity of the hydroxy group.

This section discusses DDLS data obtained for several octanol isomers and previously published in Ref. [170]. The presented results provide new perspectives on the dynamics of H-bonded supra-structures with different geometries. Most measurements were performed during the master thesis of Timo Richter supervised by the present author. Structure formulas of the studied octanol isomers are shown in Fig. 6.4a, including 2-ethyl-1-hexanol (2E1H), 5-methyl-3-heptanol (5M3H), 4-methyl-3-heptanol (4M3H) and 3-methyl-3-heptanol (3M3H). 2E1H was studied instead of 6M3H and 7M3H (1-octanol), as the former was not available for purchase and the latter is difficult to supercool. These three MAs, however, behave similarly in the sense that they all show the strong tendency to form chain-like supra-structures. This is confirmed for 2E1H in Fig. 6.4b, where g_K of all studied octanol isomers is plotted as a function of temperature. For 2E1H, g_K is found to be considerably larger than unity. By contrast, $g_K < 1$ is observed for 3M3H and 4M3H at all studied temperatures, indicating the prevalence of predominately ring-like supra-structures being formed. An intermediate role is taken by 5M3H, featuring a transition from $g_K < 1$ to $g_K > 1$ as a function of temperature, which can be interpreted as a transition from ring-like to chain-like supra-structures being favored. As a consequence, ring and chain-like structures coexist over a certain temperature range [134, 180].

For each of the four isomers, $\varepsilon''(\nu)$ and $\chi''(\nu)$ obtained at a selected temperature are compared in Fig. 6.5. Evidently, the shape of $\varepsilon''(\nu)$ varies strongly between the different isomers, reflecting the different geometries of supra-structures being formed predominantly. For chain-

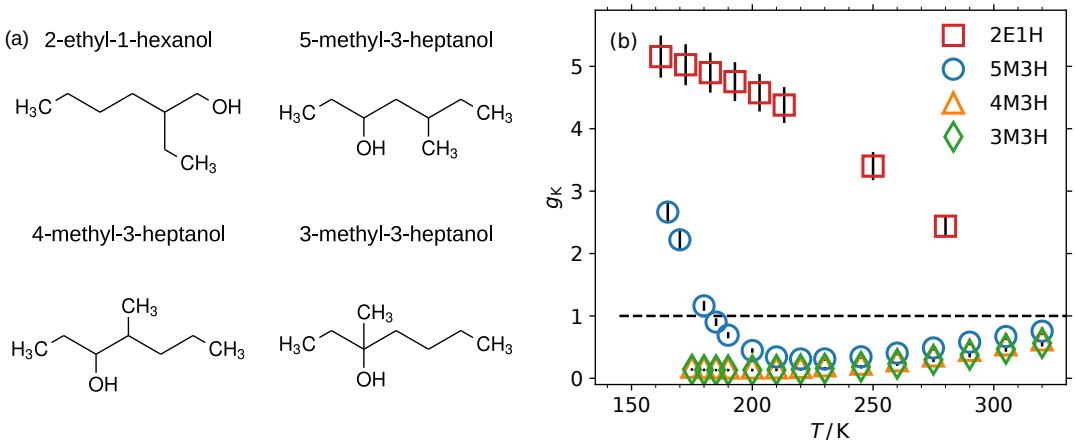

Figure 6.4: (a) Structure formulas of the studied octanol isomers. (b) g_K as a function of temperature. Chain-like supra-structures are predominant in 2E1H at all temperatures, while ring-like structures are built in 4M3H and 3M3H. 5M3H represents an in-between case, as a transition from $g_K < 1$ to $g_K > 1$ is observed as a function of temperature.

forming MAs (2E1H and also 5M3H at the displayed temperature), $\varepsilon''(\nu)$ is dominated by a narrow Debye process. In addition, a distinct shoulder is observed on the high-frequency side of the Debye process, which usually is interpreted as the α-process [181]. Ring-forming MAs (4M3H and 3M3H) display a broad multimodal peak, which has been interpreted as a superposition of a Debye-like and the α-process, and both having comparable relaxation strength [181, 182]. By contrast, the $\chi''(\nu)$-relaxation shape is very similar for all four isomers and corresponds to the generic relaxation shape discussed in Chapter 4. Thus, it does not reflect any signatures of structure-formation.

For a qualitative comparison the respective peak-maximum frequencies of $\chi''(\nu)$ are indicated in Fig. 6.5 by the black lines. For the chain-forming MAs, the peak-maximum frequency of $\chi''(\nu)$ coincides with the high-frequency shoulder in $\varepsilon''(\nu)$, suggesting the respective α-processes in both techniques to coincide. For ring-forming MAs, the main peak in $\chi''(\nu)$ is observed at approximately a factor ten larger frequencies than the broad plateau observed in $\varepsilon''(\nu)$. The β-processes probed by the two techniques are compared in the insets of Fig. 6.5. In all cases, the peak-maximum frequencies, and approximately also the shape, coincide between the techniques. For 4M3H, a high-frequency excess wing instead of a β-process is observed in both techniques, therefore no low temperature data of 4M3H are included in Fig. 6.5.

Fig. 6.6 displays the results of a quantitative analysis based on Eq. (6.1), which is included as the solid black lines. It is assumed that $\varepsilon''(\nu)$ can be described by the superposition of a self-correlation contribution, represented by $\chi''(\nu)$, and a slow Debye process fitted to the low-frequency part of $\varepsilon''(\nu)$. Details about the fitting procedure are described in the caption of Fig. 6.6. Evidently, this approach is largely insufficient to describe $\varepsilon''(\nu)$ over the entire frequency range. For all isomers the model fails to describe the data in the intermediate frequency range, suggesting the existence of an additional relaxation contribution not taken into account in Eq. (6.1). The additional contribution, which hereafter is referred to as *intermediate process*, is visualized by the black symbols obtained by subtracting the description based on Eq. (6.1) from $\varepsilon''(\nu)$. It has to be noted that qualitatively equivalent results are obtained when considering the DDLS α-process to be slower by a potential factor of three, which could result from the different Legendre polynomials probed by the two techniques (see Section 2.4). For

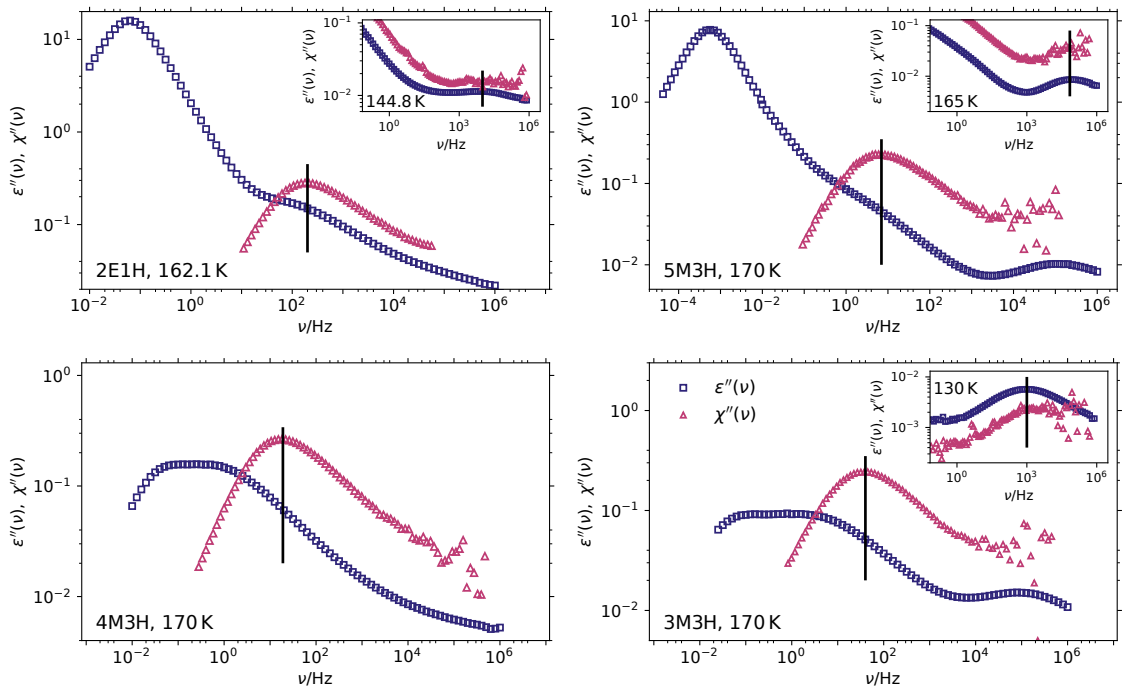

Figure 6.5: $\varepsilon''(\nu)$ (blue) and $\chi''(\nu)$ (pink) for all four octanol isomers compared at selected temperatures indicated at the bottom left of each panel. It is noted that $\chi''(\nu)$ is normalized, thus the amplitude of $\chi''(\nu)$ in this figure does not reflect any physics. The black solid lines indicate the peak maximum frequency of $\chi''(\nu)$. In the inset, the β-processes are compared between both techniques at a low temperature.

2E1H and 5M3H, a similar intermediate relaxation contribution to $\varepsilon''(\nu)$ was identified previously by Arrese-Igor et al. [183, 184] via comparison to shear mechanical data and suppression of H-bonding upon addition of salt.

Origin of the intermediate relaxation

Regarding the physical origin of the intermediate relaxation, a natural assumption could be to attribute it to the dielectric signature of hydroxy-group reorientation, as the latter was also found to proceed on time scales in between Debye- and α-process in NMR experiments [149, 185]. Starting with 2E1H, the validity of this conjecture is investigated in Fig. 6.7a, where relaxation-time constants of the different processes are plotted as a function of inverse temperature. Relaxation-time constants of Debye- and α-process, τ_{D} and τ_α, as well as of the intermediate relaxation, τ_{IM}, from the the analysis in Fig. 6.6a are included. The error bars included for τ_{IM} reflect its variation with different choices of fitting parameters during the analysis shown in Fig. 6.6a. In addition, NMR spin-lattice relaxation times of OD-deuterated 2E1H, τ_{OH}, reflecting the reorientation of hydroxy groups, as well as stimulated-echo time constants, $\tau_{\alpha,\mathrm{NMR}}$, reflecting the α-process from Schildmann et al. [185] are included. To avoid systematic deviations between relaxation times due to differences of the applied model functions, the mean relaxation times $\langle\tau\rangle$ from the respective distributions of relaxation times are considered; except for τ_{IM}, where the peak-maximum time, $\tau = 1/(2\pi\,\nu_{\mathrm{peak}})$ is included. Moreover, systematic temperature deviations between data obtained during the present work and the literature data are ruled out by including fits to relaxation times obtained from $\varepsilon''(\nu)$

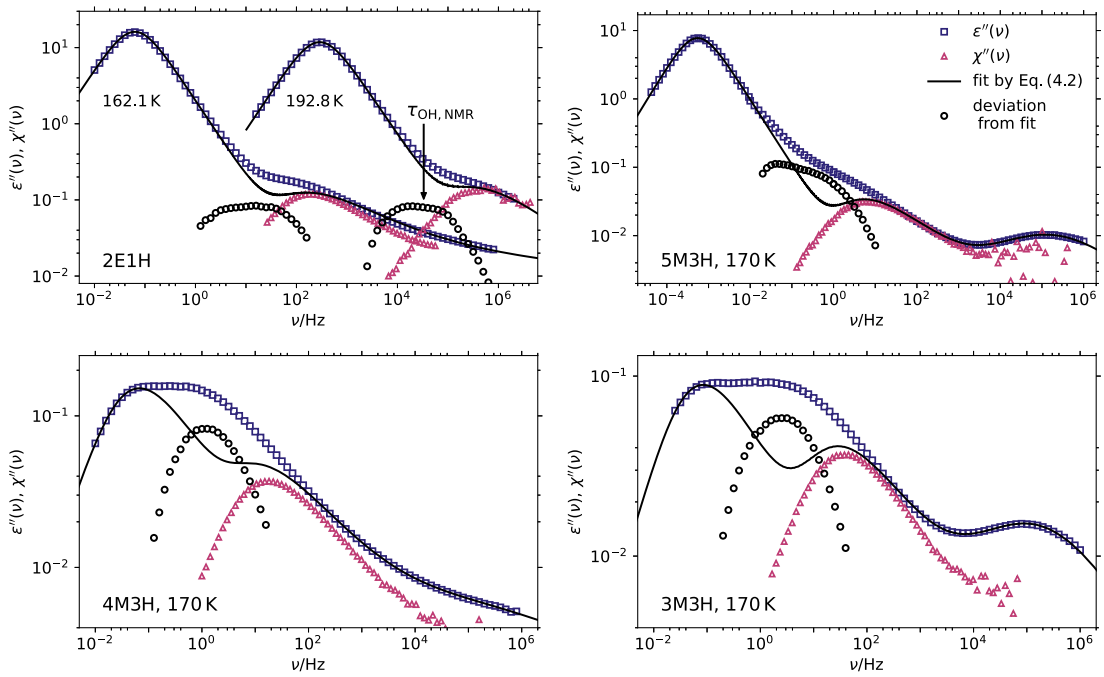

Figure 6.6: Results of quantitative analyses for the data shown in Fig. 6.5 based on Eq. (6.1). $\chi''(\nu)$ was fitted using the model described in Section 3.2.2 with $\alpha = 2$ and $\beta = 0.5$. The relaxation strength $\Delta\varepsilon_{\alpha\beta}$ was determined by fitting the high-frequency part of $\varepsilon''(\nu)$. The relaxation strength of the β-process determined from $\chi''(\nu)$ had to be adapted to fit $\varepsilon''(\nu)$. The contribution $\Delta\varepsilon_{\alpha\beta} \cdot \chi''(\nu)$ is included as the pink symbols.
Subsequently, the low-frequency part of $\varepsilon''(\nu)$ was fitted by the Laplace-transform of the KWW function to model the Debye process. For 2E1H and 5M3H, almost a pure Debye shape ($0.98 < \beta_{KWW} < 1.0$) is found. For 4M3H and 3M3H the exact value of β_{KWW} can not be determined, thus $\beta_{KWW} = 0.65$ is chosen arbitrarily. Qualitatively similar results are obtained for different values of β_{KWW}. Evidently, Eq. (6.1) is insufficient to describe $\varepsilon''(\nu)$ at intermediate frequency. The deviations of $\varepsilon''(\nu)$ from the fit are included as the open black symbols.

from Ref. [185] as dotted lines, which are shown to coincide to the relaxation-times obtained during the present work.

As revealed by Fig. 6.7, τ_{IM} coincides with τ_{OH}, respectively at lower temperatures with the extrapolation of the VFT-fit to τ_{OH}, thus supporting the conjecture that the intermediate relaxation is the dielectric signature of hydroxy-group reorientation. This finding indicates that dielectric relaxation spectra of MAs are more complex than previously thought: In addition to the Debye process, reflecting reorientation of supra structures, and the α-process, reflecting reorientation of single alcohol molecules, a third intermediate time scale reflects the reorientation of hydroxy groups. This observation suggests some degree of intra-molecular decoupling of hydroxy group and carbon backbone. Yet, it is argued below that these observations are mostly conform with the ideas of the transient chain model.

In order to establish a comprehensive picture combining the dielectric and DDLS results, it is essential to discuss how both techniques differ regarding their sensitivity towards different moieties of octanol molecules. Following the discussion in chapter 2.2, DDLS probes the reorientation of the entire octanol molecules and, thus, the signal is dominated by the reorientation of the carbon backbones. By contrast, the dielectric relaxation mostly reflects the reorientation of the C-O-H moieties, more precisely, O-H and C-O bonds contribute almost equally as their

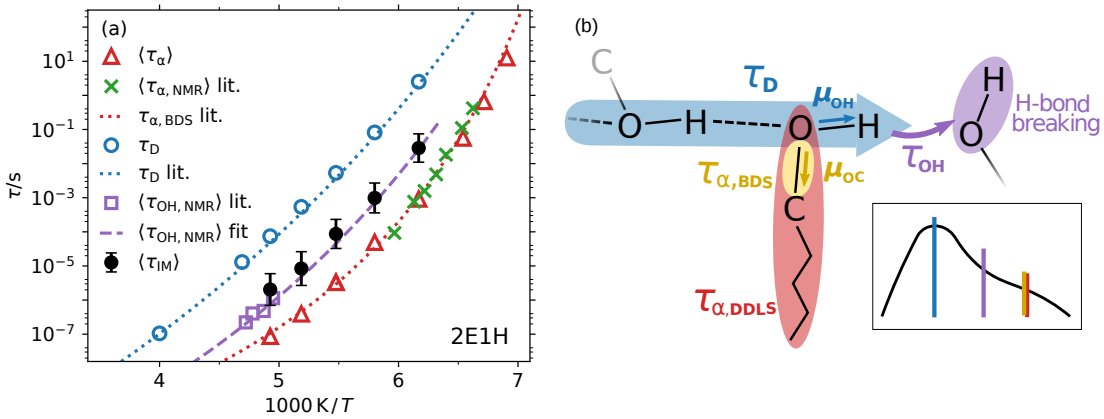

Figure 6.7: (a) Various relaxation time constants of 2E1H as a function of inverse temperature: α-process time constants extracted from $\chi''(\nu)$, $\langle\tau_\alpha\rangle$; from NMR stimulted echo experiments $\langle\tau_{\alpha,\mathrm{NMR}}\rangle$ obtained from Ref. [185]; and from fits to $\varepsilon''(\nu)$, $\tau_{\alpha,\mathrm{BDS}}$, also from Ref. [185]. Debye-process time constants from this work, τ_D; as well as from Ref. [185]. Intermediate time constants determined from NMR spin-lattice relaxation times: $\langle\tau_{\mathrm{OH,NMR}}\rangle$ as well as the respective VFT fit; and from this work: $\langle\tau_\mathrm{IM}\rangle$. Angular brackets indicate that the average relaxation time from the distribution of relaxation times is considered.
(b) Schematic illustration of the possible origin of different relaxation contributions in chain-forming MAs. The colors represent the different motional mechanisms probed by the different techniques. Red: polarizability tensor probed by DDLS; Yellow: Dipole moment of the C-O bond associated with the dielectric α-process ; Purple: Reorientation of O-H bonds due to breaking of H-bonds associated with the intermediate process; Blue: End-to-end dipole moment of supra-structures associated with the Debye process.

respective dipole-moment components μ_OH and μ_CO are of similar magnitude. In particular, if the reorientation of these two bonds decouples and proceeds on different time scales, two distinct contribution to $\varepsilon''(\nu)$ are observed. This seems to be the case for 2E1H according to Fig. 6.7: While the O-H reorientation proceeds on the time scale of the intermediate relaxation, the contributions to $\varepsilon''(\nu)$ on the time scale of the $\chi''(\nu)$ main peak reflect the carbon backbone dynamics. This contribution originates from the reorientation of the C-O bond, as no other bond in the carbon backbone carries any notable dipole moment. Fig. 6.7b illustrates schematically how this dynamic decoupling of hydroxy group and carbon backbone could be understood. Here, a 2E1H molecule bound into a chain-like supra-structure is considered. Due to the H-bonding, the reorientation of the O-H bond is hindered and its orientation is fixed with respect to the supra-structure. By contrast, the carbon backbone (depicted in red) can perform large angle reorientations, as evident from the fact that $\tau_\alpha < \tau_\mathrm{OH}$. While μ_OH is fixed with respect to the orientation of the supra-structure, μ_CO is not fully restricted and therefore, can rotate on a timescale comparable to τ_α (blue). Its dielectric signature is considered to be the dielectric α-process, as its time scale is associated with the glass transition in MAs [148]. The reorientation of the O-H bond can only proceed if either the supra-structure rotates as a whole, or once the molecule under consideration leaves the supra-structure. Evidently, the latter mechanism is predominant, as $\tau_\mathrm{OH} < \tau_\mathrm{D}$ [149]. Consequently, the fact that O-H bonds rotate on an intermediate time scale between Debye- and α-process is a direct manifestation of the transient nature of the supra-structures in chain-forming MAs.

Next, the results for the two ring-forming octanol isomers, 4M3H and 3M3H, are discussed. In previous studies, curve-fitting procedures based on similar models as Eq. (6.1) have been employed to identify the dielectric α-process in 4M3H [148, 181, 182]. However, these results

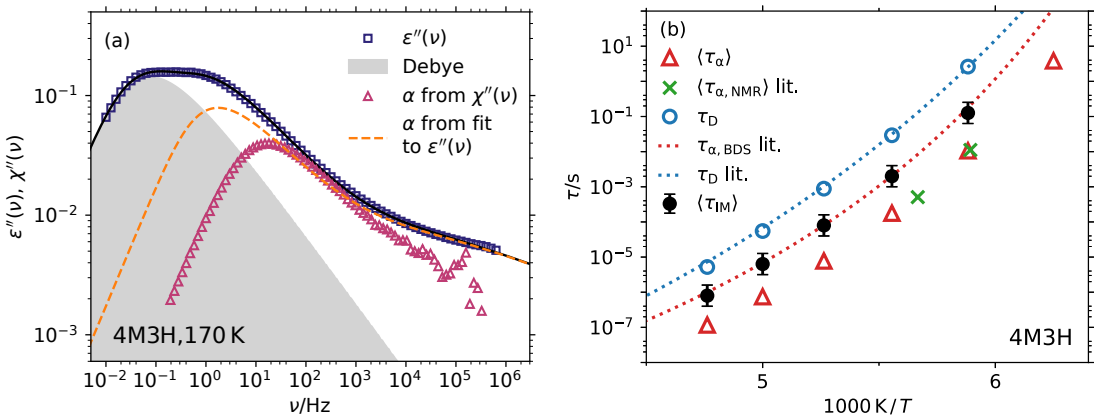

Figure 6.8: (a) Comparison of the literature interpetation [148, 181, 182] of the α-process in 4M3H (dashed orange line) to results from DDLS experiments performed within this work (pink symbols). The solid black line represents a fit to $\varepsilon''(\nu)$ similar to the ones in Refs. [148, 181, 182], which include the Debye- (gray shaded area) and the α-process contribution (orange dashed line).
(b) Relaxation-time constants of 4M3H as a function of temperature: α-process time constants extracted from $\chi''(\nu)$, $\langle\tau_\alpha\rangle$; from NMR experiments $\langle\tau_{\alpha,\mathrm{NMR}}\rangle$ obtained from Ref. [186]; and from fits to $\varepsilon''(\nu)$ using a similar procedure as shown in (a) obtained from Ref. [181]. Debye process time constants from this work, τ_D; as well as from Ref. [181]. Intermediate time constants determined from this work: $\langle\tau_\mathrm{IM}\rangle$. Angular brackets indicate that the average relaxation time from the distribution of relaxation times is considered.

do not agree with the findings from DDLS, as illustrated in Fig. 6.8a, where the dashed orange line represents α-process and β-process identified via fitting a modification of Eq. (6.1) to $\varepsilon''(\nu)$, similar to the procedures in Refs. [148, 181, 182]. The fit implies an average relaxation time of the α-process that is by a factor of ten larger compared to the one probed by DDLS. Fig. 6.8b displays relaxation time constants of the different processes identified in 4M3H as functions of inverse temperature. Evidently, the discrepancy between α-process time constants determined via fits in Ref. [182] (red dashed line) and those probed by DDLS (red triangles) is observed independent of temperature. Moreover, NMR relaxation-time constants from Ref. [186] (green crosses) coincide with the ones from DDLS. At the same time, the time constants determined via fit to $\varepsilon''(\nu)$ coincide with what is identified as the intermediate relaxation in Fig. 6.6. Altogether, these results reveal that the reorientation of the carbon backbone proceeds on a significantly faster time scale compared to what was previously identified as the dielectric α-process in the literature [182]. Most likely, the origin of these discrepancies is the dynamic decoupling of hydroxy group and carbon backbone, analogous to the conclusions drawn for the chain-forming MA 2E1H above. In ring-forming MAs the intermediate relaxation most likely reflects the characteristic time scale of hydroxy groups exiting ring structures.

Intermediate relaxation at elevated temperatures

The above discussed interpretations of the experimental results suggest that the formation of H-bonded structures in octanol isomers induce the dynamic decoupling of hydroxy groups and carbon backbones. Both contribute to the dielectric loss at distinctly different frequencies. As the number of molecules bound into hydrogen bonded structures decreases with increasing

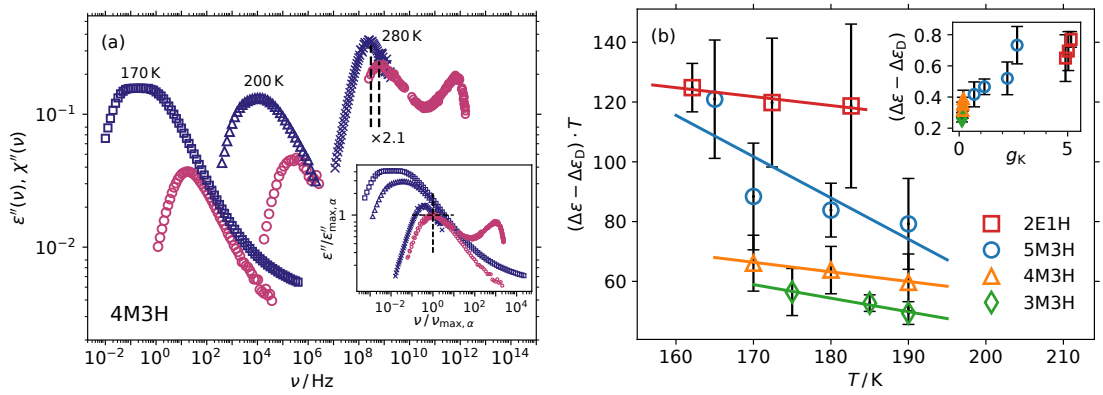

Figure 6.9: (a) Temperature evolution of $\varepsilon''(\nu)$ (blue) and $\chi''(\nu)$-data (pink) of 4M3H from T_g to the liquid regime. The amplitudes of the $\varepsilon''(\nu)$-data reflect the absolute relaxation strength that changes significantly with temperature due to the increase of g_K, cf. Fig. 6.4. The amplitude of $\chi''(\nu)$ is scaled according to analyses like the one shown in Fig. 6.6. In the inset, $\chi''(\nu)$ and $\varepsilon''(\nu)$ are normalized to the peak maximum frequency and amplitude of the DDLS α-process to highlight the decreasing discrepancy between both techniques with increasing temperature.
(b) Relaxation strength excluding the Debye process $(\Delta\varepsilon - \Delta\varepsilon_D)$ multiplied by T to compensate for the trivial Curie temperature dependence. Solid lines represent linear fits to the data. The inset illustrates the correlation between $(\Delta\varepsilon - \Delta\varepsilon_D)$ and g_K.

temperature [148, 187], the degree of dynamic decoupling of different moieties, as well as the relaxation strength of the Debye process, are expected to decrease at elevated temperatures. As a consequence, also the discrepancy between $\varepsilon''(\nu)$ and $\chi''(\nu)$ should decline with increasing temperature. This hypothesis is tested in Fig. 6.9a, comparing data measured at temperatures between 170 K and 280 K. The amplitudes of $\chi''(\nu)$-data are scaled to correspond to the α-process contribution to $\varepsilon''(\nu)$ following an analysis as the ones shown in Fig. 6.6. While the above discussed differences are observed between $\chi''(\nu)$ and $\varepsilon''(\nu)$ at low temperatures, both have a very similar relaxation shape and are separated by only a factor of ~ 2.1 at 280 K. This is also highlighted in the inset, where $\chi''(\nu)$ and $\varepsilon''(\nu)$ are normalized to the respective peak maximum frequencies and amplitudes of $\chi''(\nu)$. Thus, the expected temperature dependence is observed for 4M3H, suggesting that the major part of the discrepancy between $\varepsilon''(\nu)$ and $\chi''(\nu)$ is related to the dynamic signatures of H-bonding, manifested as the Debye process and the dynamic decoupling of molecular sub-units. It is noted that at 280 K a substantial portion of molecules do still form H-bonds, as evident from $g_K(280\,\mathrm{K}) < 1$, thus the discrepancy between $\chi''(\nu)$ and $\varepsilon''(\nu)$ might be reduced even further at higher temperatures.

The effect of dipolar cross-correlations

The different octanol isomers are fundamentally different regarding the degree of static dipolar cross-cross correlations due to the formation of supra-structures. Thus, they are well-suited as model systems to study how dipolar cross-correlations contribute to the dielectric loss. As discussed above, it is well established that dipolar cross-correlations are the origin of the low-frequency Debye process in MAs, while the self-part of dipolar relaxation is observed at higher frequencies. A naive conjecture could be to assume that the Debye process is the only contribution of dipolar cross-correlations on the dielectric loss. As a consequence, the dielectric relaxation strength of self-correlations, $\Delta\varepsilon_{self}$, would be obtained by subtracting the

relaxation strength of the Debye process, $\Delta\varepsilon_{\mathrm{D}}$, from the overall dielectric relaxation strength, $\Delta\varepsilon$, i.e.

$$\Delta\varepsilon_{\mathrm{self}} = \Delta\varepsilon - \Delta\varepsilon_{\mathrm{D}}. \tag{6.3}$$

It is noted that the intermediate relaxation is explicitly considered to be part of the self-correlations, because it is assumed to reflect the reorientation of hydroxy groups. If the assumption leading to Eq. (6.3) were justified, the therein defined $\Delta\varepsilon_{\mathrm{self}}$ multiplied by T should be the same for all octanol isomers according to Onsager's equation [188], as they all share approximately the same dipole density. This conjecture is tested in Fig. 6.9b, where $\Delta\varepsilon_{\mathrm{self}} \cdot T$ is considered as a function of temperature. Contrary to the assumption, significant differences are observed and $\Delta\varepsilon_{\mathrm{self}} \cdot T$ does follow the general trend of the respective g_{K} (2E1H > 5M3H > 4M3H ≈ 3M3H). The correlation between $\Delta\varepsilon_{\mathrm{self}}$ and g_{K} is confirmed in the inset. It is noted that the factor T, which eliminates the trivial Curie-dependence of the dielectric relaxation strength, is not included in the inset, as it is already considered in g_{K}.

The observed correlation between $\Delta\varepsilon_{\mathrm{self}}$ determined via Eq. (6.3) and g_{K} implies that the Debye process is not the only contribution of dipolar cross-correlation to $\varepsilon''(\nu)$. Instead, the results suggest that in addition the self-correlations are weighted by a g_{K}-dependent factor, as suggested earlier for dipolar cross-correlations in polymers by Williams et al. [189]. In conclusion, dipolar cross-correlations contribute to $\varepsilon''(\nu)$ in two ways: First, they lead to the Debye process, an additional contribution on time scales slower than the α-process . Second, they appear as a weighting-factor to the self-correlations. These results imply that the relation between $\Delta\varepsilon_{\mathrm{D}}/\Delta\varepsilon_{\alpha}$ and the average length N of chain-like structures, which was established following the transient chain model [149] could be invalid, as it is based on the assumption that $\Delta\varepsilon_{\alpha}$ is unaffected by dipolar cross-correlations.

Generality of the findings

The above reported results for different octanol isomers suggest three distinct time scales to be relevant for dielectric relaxation in MAs (disregarding any β-processes): τ_{α}, reflecting the reorientation of the carbon backbone, which is the major part of the molecule; $\tau_{\mathrm{IM}} = \tau_{\mathrm{OH}}$, the characteristic time scale of OH-group rotation; and τ_{D}, reflecting the relaxation of H-bonded supra-structures. The fact that $\tau_{\mathrm{OH}} \neq \tau_{\alpha}$ implies that molecules do not rotate as rigid entities, but, instead, pronounced dynamical decoupling between different moieties is observed. Naturally, the question arises as to whether these results are a general feature of MAs. The dynamic decoupling of τ_{OH} and τ_{α} is especially easy to observe in octanol isomers, because in these substances the Debye process is particularly strongly separated from the α-process. This allows to identify an intermediate contribution at the time scale τ_{OH}. Although it is likely that a distinct intermediate contribution to the dielectric loss exists also in other MAs, it would be difficult to disentangle from the Debye process. In this regard NMR experiments can provide unique insights, as probing OD-deuterated compounds allows to directly extract τ_{OH}, which subsequently can be compared to $\varepsilon''(\nu)$. Unfortunately, such NMR-data seem to exists only for a very limited number of MAs, thus making it difficult to draw any general conclusions.

At this point it is worth to mention that very recently the dielectric and rheological response of MAs has been rationalized [122, 190] in terms of a living polymer model [166, 167]. This model explicitly predicts an intermediate relaxation process that is associated with chain-breakage and chain-swapping [190], in analogy to the interpretation of the intermediate contribution provided in this work. Further research in these regards might reveal whether a general quantitative description of MAs can be achieved in terms of the living polymer model.

6.2 POLYHYDRIC ALCOHOLS

For decades, polyhydric alcohols (PAs) have been intensively studied as prototypical glass-formers, due to being easily supercoolable. Especially the homologous series of sugar alcohols (glycerol, threitol, xylitol, sorbitol) has received considerable attention, among other reasons because many fundamental properties of supercooled liquids and glasses, e.g. fragility, vary among the series, thus making PAs perfect model systems to study correlations among these properties. In the context of this work, especially the strong variation of the dielectric relaxation shape along the series is of interest. It is illustrated in Fig. 6.10a, by plotting $\varepsilon''(\nu)$ of different PAs normalized to the peak-maximum frequency of the α-process at temperatures closely above the respective T_g. In the inset the same data are shown, but additionally normalized to their peak-maximum amplitudes. Evidently, increasing molecular weight is associated with broader relaxation shapes and lower values of the high-frequency power-law exponents β. Both observations have been previously interpreted to reflect an increase of dynamic heterogeneity with increasing molecular weight and β of PAs was reported to be correlated with the length scale of dynamic heterogeneity [92] and with fragility [32].

In the context of the results discussed in previous chapters of this work, the conclusions regarding the degree of dynamic heterogeneity drawn from the relaxation shape of PAs raise serious questions: The narrow dielectric relaxation shapes of short chained PAs, glycerol and propylene glycol[1], were shown to originate from dipolar cross-correlation contributions that superimpose the self-correlations Chapter 5. Moreover, the latter were shown to correspond to the generic shape in Chapter 4. On the other hand, the width of the α-process of long-chained PAs exceeds the one of the generic shape; an observation that cannot be understood in terms of cross-correlation contributions. The following sections reports DDLS data for PAs and attempts to resolve the physical origin behind the different relaxation shapes among PAs. The discussed results were previously published in Ref. [191].

Understanding the DDLS relaxation shape of polyhydric alcohols

The DDLS relaxation shapes of different PAs at selected temperatures are shown in Fig. 6.10b. Each spectrum is normalized to its respective peak-maximum frequency and amplitude and the temperatures are the same as in Fig. 6.10a. The generic relaxation shape is included as the black dashed line. As already shown in Chapter 4, DDLS structural relaxation shape of propylene glycol and glycerol correspond to the generic relaxation shape. In contrast, the DDLS structural relaxation shapes of threitol, xylitol and sorbitol follow the generic relaxation shape up to frequencies slightly above the peak-maximum frequency and deviate at higher frequencies. The deviations are systematic in the sense that they increases with increasing molecular weight; the respective values of β equal 0.40, 0.35 and 0.25 ($\pm$0.05 each), respectively.

In order to interpret these observations, it is important to note that previous work on sorbitol observed a quite complex relaxation mechanism involving intra-molecular degrees of freedom. Using ^{2}H-NMR, Döß et al. [193] studied differently isotope-labeled sorbitol samples (-CD_4 and -OD_6) and observed differences regarding average relaxation time and relaxation shape between the samples (cf. Ref. [116] and Fig. 6.36 in Ref. [193]). This result suggests dynamic decoupling of C-H and O-H bonds in deeply supercooled sorbitol. At higher temperatures, ^{13}C-NMR experiments and molecular dynamics simulation studies identified pronounced dynamic decoupling between the different C-H bonds, with the bonds in the center of the

1 Propylene glycol is considered instead ethylene glycol, which is the low molecular weight extension to the homologous series, due to its superior glass-forming ability.

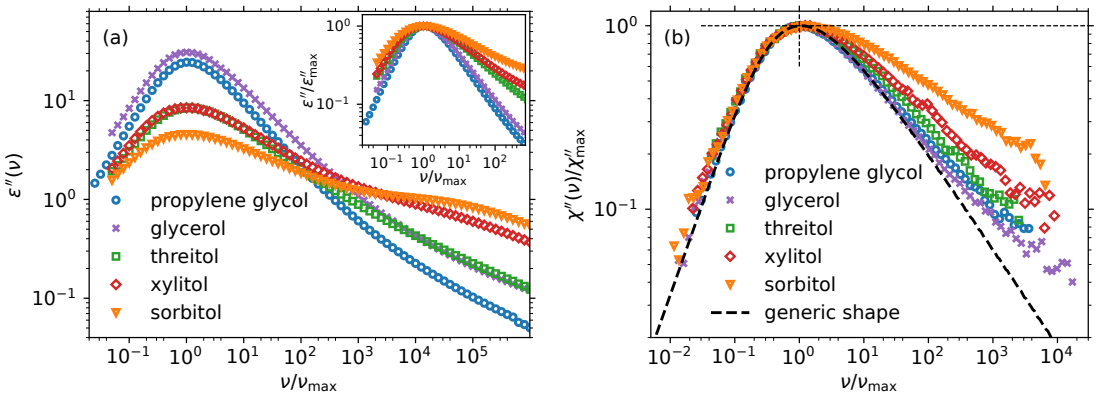

Figure 6.10: Relaxation spectra of different polyhydric alcohols from (a) dielectric spectroscopy, $\varepsilon''(\nu)$, and (b) DDLS, $\chi''(\nu)$. Data are normalized with regard to the respective peak-maximum frequencies, and in panel (b) as well as in the inset of (a) also to the peak-maximum amplitude. The respective temperatures are chosen to be closely above T_g and such that the peak-maximum frequencies ν_{peak} are similar. Temperatures in panel (a) are 180 K, 200 K, 235 K, 255 K and 275 K from propylene glycol to sorbitol in order of increasing molecular mass with $0.5 < \nu_{peak}/\text{Hz} < 1.6$; and in panel (b) 175 K, 200 K, 235 K, 255 K and 277.5 K with $1.0 < \nu_{peak}/\text{Hz} < 3.2$. The generic relaxation shape identified in Chapter 4 is included as the dashed black line.

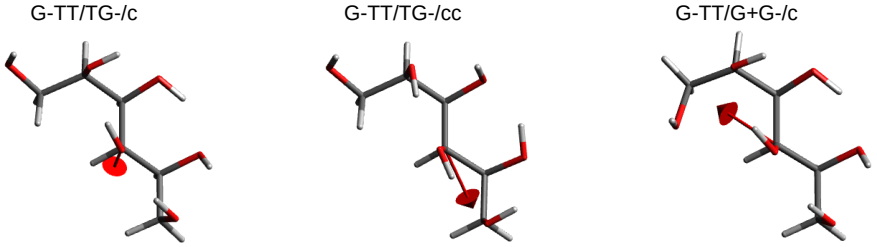

Figure 6.11: Three most stable gas-phase conformers of D-sorbitol (cf. Ref. [192]) and their respective molecular dipole moment vectors (red arrows). Already subtle rotations of a few hydroxy groups alter the magnitude (G-TT/TG-/c: $\mu_1 = 1.00\,\text{D}$; G-TT/TG-/cc: $\mu_2 = 2.01\,\text{D}$; G-TT/G+G-/c: $\mu_3 = 2.07\,\text{D}$), as well as the orientation of the dipole moment vectors ($\sphericalangle(\boldsymbol{\mu}_1, \boldsymbol{\mu}_2) = \sphericalangle_{12} = 38°$; $\sphericalangle_{13} = 73°$; $\sphericalangle_{23} = 110°$ in a molecule-fixed orthonormal frame). Calculations were performed by Yann Cornaton, University of Strasbourg.

molecule having larger rotational relaxation times than to the ones at terminal positions [194, 195]. The fact that different chemical bonds within the sorbitol molecule rotate on different time scales implies that transitions between different conformers proceed on time scales comparable to those of the α-process. In the following, these effects are referred to as *intra-molecular dynamics*. An example emphasizing the importance of considering intra-molecular dynamics is presented in Fig. 6.11, where the three most stable gas-phase conformers of D-sorbitol and their respective dipole-moment vectors are shown. Although the conformation of the carbon backbones are almost identical, the magnitude and the direction of the molecular dipole moment vectors differ drastically between the conformers due to subtle differences regarding the orientations of hydroxy groups. As a consequence, reorientation of molecular dipoles does not exclusively reflect reorientation of entire sorbitol molecules, but also intra-molecular motions, which implies that dielectric spectroscopy experiments are sensitive to intra-molecular dynamics. By contrast, no dynamic decoupling of different chemical bonds

was observed for short-chained PAs like glycerol and therefore, their dipole moment can be assumed to represent a fixed molecular axis in good approximation [193, 196].

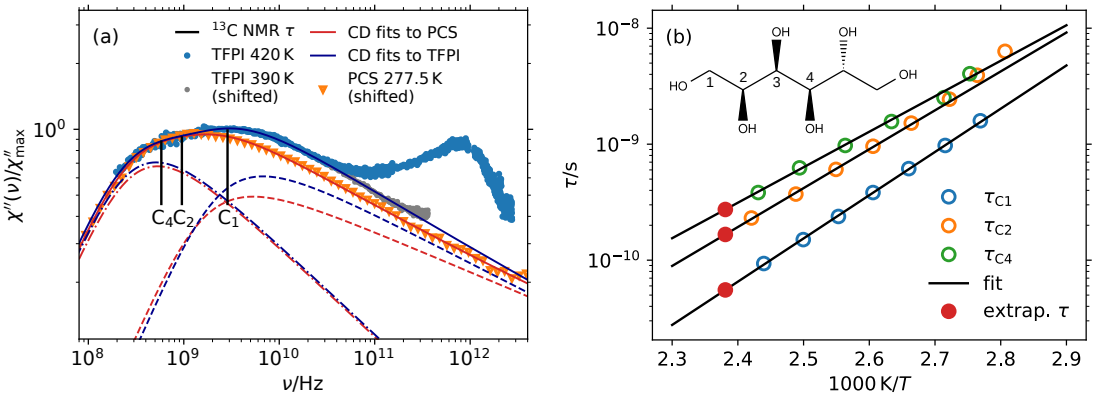

Figure 6.12: (a) $\chi''(\nu)$ data of sorbitol obtained above the melting point at 420 K (blue symbols) using a TFPI. The data are extended to higher frequencies by shifting the spectrum obtained at 390 K (gray symbols). The spectrum is clearly multimodal and can be described by the sum of two processes based on GG distributions of relaxation times (dark blue lines). For comparison, a low temperature spectrum obtained at 277.5 K is included (orange symbols), which appears similarly broad and can be modeled by the same sum of two processes, simply by adjusting the weights (red lines).
(b) Relaxation time constants from ^{13}C-NMR experiments [195], representing the dynamics of C-H bonds at the C_1, C_2 and C_4 carbon atom of sorbitol (see sketched structure formula for assignment). A pronounced intra-molecular dynamic decoupling is observed. The ^{13}C-NMR time constants are extrapolated to 420 K (red circles) via fits by Arrhenius laws (black lines). These time constants are indicated in panel (a) as the vertical black lines. The dynamic decoupling of different carbon atoms within the sorbitol molecule roughly coincides with the observed multimodality of the DDLS spectra.

How intra-molecular dynamics contributes to relaxation spectra of sorbitol is best studied at temperatures around the melting point, because (i) intra-molecular dynamics usually are more pronounced at higher temperatures and (ii) the results can be compared to literature data, e.g. from ^{13}C-NMR. For this purpose, TFPI measurements were performed at 420 K, the results of which are shown in Fig. 6.12a as the blue symbols. Here, the α-process is observed in the GHz region, while microscopic dynamics contribute in the THz region, which, however, are not the focus of this work. Strikingly, the α-process is clearly bi- or even multimodal, resulting in a very broad peak with two clearly distinct shoulders. To visualize the high-frequency behavior of the α-process, which at 420 K is masked by microscopic dynamics, a second TFPI spectrum measured at 390 K is included as the grey symbols and shifted along the frequency axis. The bimodal relaxation shape of the combined TFPI spectrum can only be modeled by the sum of two contributions (here chosen as two (GG) distributions of relaxation times). The sum of both contributions is shown as the solid blue line, while the individual contributions are shown as dashed, res. dashed-dotted blue lines.

To verify whether the observed bimodality is related to intra-molecular dynamics, relaxation time constants of the C_4-H, C_2-H and C_1-H bonds (numbered along the carbon backbone) from ^{13}C-NMR reproduced from Ref. [195] are included as vertical black lines. To obtain relaxation-time constants at exactly 420 K, the data were extrapolated utilizing the fact that their temperature dependence is approximately Arrhenius in the GHz region, as shown in Fig. 6.12b. Evidently, the NMR time constants roughly coincide with the positions of the two shoulders that are observed in the TFPI spectrum. This agreement indicates that the dynamic

decoupling of different molecular moieties leads to the strong broadening and the bimodality of the high-temperature relaxation shape. This is not surprising, as the rotation of the outer parts (C_1 and C_6) of the sorbitol molecule has a significant impact on the optical anisotropy tensor, as they make up a third of the molecule. In addition, also the rotational dynamics of hydroxy groups is markedly heterogeneous [116] and decouples from the dynamics of C-H bonds [193]. Especially the broadening at $\nu > \nu_{C1}$ could reflect hydroxy-group dynamics, as suggested by the very asymmetrically broadened peak observed for OD-labeled sorbitol in ^{2}H-NMR [116].

In addition to high-temperature data, a low-temperature relaxation spectrum of sorbitol measured close to T_g is included in Fig. 6.12 as the orange symbols. It is shifted along the frequency axis such that the ν^1 low-frequency power law of high- and low temperature relaxation spectra coincide. The widths and the high-frequency power-law exponents of both spectra are comparable. Moreover, the comparison reveals that the position of the high-frequency broadening observed for the low-temperature spectrum in Fig. 6.10 coincides with the position of the high frequency shoulder in the TFPI spectrum. This suggests that also at low temperatures, intra-molecular dynamics contributes to the relaxation spectrum of sorbitol. However, the influence of these intra-molecular modes appears to be less prominent in the supercooled regime, as it is commonly observed [116]. The reason for this is probably the onset of cooperative dynamics. Following these ideas, the low-temperature spectrum can be modeled using a similar sum of relaxation contributions as used for the high-temperature spectrum, however, with a reduced amplitude of the fast contribution. The resulting description is included as the dashed, dashed-dotted and solid orange lines in Fig. 6.12, representing both contributions and the sum of both, respectively. It is noted that the description by the sum of two contributions is purely empirical and serves to illustrate the enhanced complexity of the relaxation spectra compared to what is found for low-molecular weight PAs. Obtaining a meaningful quantitative description of these spectra would require an in-depth analysis of relaxation time distributions of different chemical bonds and how these couple to the molecular polarizability tensor or dipole moment. In the future this could possibly be achieved by using ab-initio molecular dynamics simulations. While such simulations have recently been performed for sorbitol [197], so far only the THz region can be covered, due to the high computational cost of these simulations.

It remains to be discussed how the identified contributions of intra-molecular dynamics relate to the concept of the generic relaxation shape. It is found that $\chi''(\nu)$ corresponds to the generic relaxation shape only for short-chained supercooled PAs, which rotate as rigid entities, because conformational transitions are slow with respect to the α-process [196]. As a consequence, the width of their relaxation spectra reflects the inter-molecular dynamic heterogeneity, i.e. the distribution of relaxation times of different molecules. By contrast, intra-molecular dynamics were shown to introduce additional dynamic heterogeneity in sorbitol, resulting in spectra that are broadened compared to the generic relaxation shape. Here, the width of the relaxation spectra reflects inter- as well as intra-molecular dynamic heterogeneity. As both contributions are impossible to disentangle, it cannot be concluded whether the relaxation spectrum of sorbitol reflecting only the inter-molecular dynamic heterogeneity would correspond to the generic relaxation shape. Although no respective NMR or simulation data exist for threitol and xylitol, it is reasonable to assume that some transition occurs between the short- and the long-chain behaviors of PAs. This implies that at chain-lengths between $n = 3$ and $n = 6$, the characteristic timescale of conformational transitions approaches the one of the α-process, thus leading to deviations from the generic shape.

Finally, it should be noted that the majority of supercooled liquids, whose DDLS relaxation spectra were shown to correspond to the generic shape (cf. Chapter 4 and Ref. [94]), have some degree of intra-molecular flexibility. Usually, however, such intra-molecular degrees of freedom are either very fast compared to the α-process and, e.g., appear as a non-Johari-Goldstein β-process [198], or are frozen in the deeply supercooled and cooperative regime as it is found, e.g., for glycerol where molecules are stuck in certain conformations [116]. Thus, the question arises why intra-molecular dynamics and the α-process appear on comparable timescales in long-chained PAs. Two aspects should be considered in this regard:

(i) The potential energy landscape of sorbitol is quite complex, due to the existence of multiple interaction mechanisms and, most importantly, due to the large number of intra- and inter-molecular H-bonds involved [197, 199]. This complexity, presumably, causes several conformational states of sorbitol to have comparable Gibbs energies [192], which could favor transitions between these conformers.

(ii) Due to each sorbitol molecule being involved in several H-bonds with surrounding molecules, the reorientation of the carbon backbone requires several H-bonds at different positions of the molecule to break simultaneously. Thus its reorientation is associated with a comparably large activation energy. Therefore, smaller segments of the molecule are expected to rotate individually and, thus, the α-process in fact occurs via a series of conformational transitions. In such a scenario, bonds at the end of the molecule would rotate slightly faster than the ones in the center and hydroxy-group dynamics could decouple from C-H or C-C bond dynamics, all of which was observed in the case of sorbitol [116, 193, 195].

Slow dipolar cross-correlations in Polyhydric alcohols

Another questions concerns the slow cross-correlation contribution to the dielectric loss spectra of PAs. In this regard, $\varepsilon''(\nu)$- and $\chi''(\nu)$-spectra at supercooled temperatures are compared for the different PAs in Fig. 6.13a-e. As already discussed in Chapter 5, slow dipolar cross-correlations contributions to $\varepsilon''(\nu)$ are identified for the short-chained PAs propylene glycol and glycerol by using a joint analysis of $\varepsilon''(\nu)$- and $\chi''(\nu)$ according to Eq. (5.1); fits of which are included in Fig. 6.13a,b. With respect to the α-process, cross-correlations are stronger and more dynamically separated in PG compared to glycerol. For longer-chained PAs, $\chi''(\nu)$-data at selected temperatures are included in Fig. 6.13 as the black symbols. Qualitative comparison of $\varepsilon''(\nu)$ and $\chi''(\nu)$ reveals that both are very similar with regard to average relaxation times and relaxation shapes. The slight relaxation-time differences most likely originate from small temperature discrepancies, which can have comparably large effects due to the high fragility of long-chained PAs [200].

To rationalize these findings, it has to be noted that slow dipolar cross-correlations can only be observed if orientational correlations of adjacent molecular dipole moments persist to times longer than the α-process time scale. Such behavior could be observed if the reorientation of molecules is to some degree hindered by a hydrogen bonded network, as supposedly the case for glycerol. However, this requires the molecular dipole moment to be fixed within the molecular frame. As this is the case in PG and glycerol, dipolar cross-correlations can persist up to time scales longer than the α-process until they eventually relax. In the case of long-chained PAs, intra-molecular dynamics proceeds on similar, or even faster, timescales than the α-process. As the direction of the molecular dipole moment strongly depends on the conformational state (cf. Fig. 6.11), molecular dipole moments are not fixed within the molecular frame. Thus, even if there were long-lived intermolecular correlations associated with some molecular axis, they would not be reflected by the dipole moment. In such a case, the

contribution of cross-correlations to the dielectric loss cannot be straight-forwardly identified via comparison to DDLS spectra. They should, however, contribute to the static permittivity ε_s. This, however, is difficult to verify quantitatively, as calculation of g_K requires knowledge of the molecular dipole moment, which can only be obtained as the average over the complex conformational space of long-chained PAs. Nakanishi et al. [201] attempted to circumvent this problem by calculating g_K of sorbitol by treating each hydroxy groups as an independent dipole. Their analysis yielded $g_K > 1$, however intra- and inter-molecular orientational correlations of dipoles cannot be distinguished in this approach, making the interpretation of their result difficult. In conclusion, while static dipolar cross-correlations might exist in long-chained PAs, they are not particularly long-lived and do not contribute to the dielectric loss as a separate slow process.

6.3 GENERAL FINDINGS FOR H-BONDING SUPERCOOLED LIQUIDS

The previous sections presented data obtained for various different H-bonding supercooled liquid. One common motive has turned out to be the broad shape-variety of the respective dielectric loss spectra, which reflect the dynamic signatures of supra-structures with various different geometries and sizes. Despite all that, orientational self-correlations, as probed by DDLS, were shown to correspond to the generic structural relaxation shape, similar as found for a broad variety of supercooled liquids. This implies that the α-process of H-bonding supercooled liquids is mostly unaffected by the complexity introduced by structure-formation and seems to reflect the same physics as in less complex structured supercooled liquids.

The second common observation are intra-molecular relaxation mechanisms, which lead to dynamical decoupling of different molecular moieties. Evidently, such mechanisms are relevant in H-bonding systems, because the orientations of hydroxy groups are fixed within supra-structures. Thus, the other parts of the molecule can only relax via mechanisms involving conformational changes. In MAs, this leads to the observation of a relaxation contribution at intermediate time scales between the Debye and the α-process. In longer-chained PAs, the orientations of multiple hydroxy groups are fixed, thus the rotation of entire molecules has to proceed via several rotations of sub-units. As a result, the structural relaxation shape is broadened compared to the generic shape, as it reflects additional intra-molecular dynamic heterogeneity. This observations helps to identify another condition for observing the generic structural relaxation shape in supercooled liquids: Besides cross-correlation contributions needing to be absent, the relaxation shape has to reflect the reorientation of molecule as a whole, i.e. it needs to be associated with the intermolecular distribution of relaxation times.

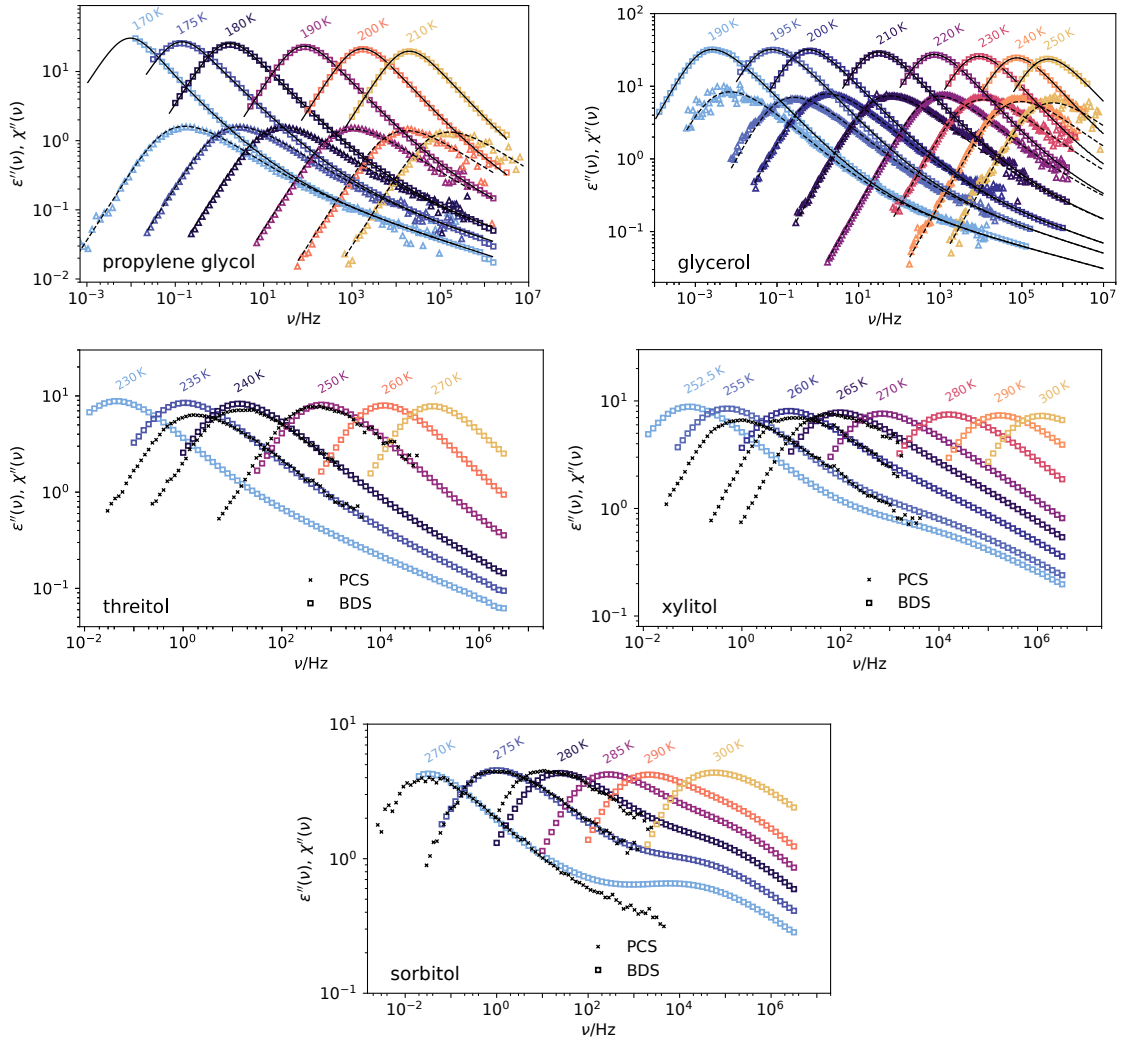

Figure 6.13: Comparison of $\chi''(\nu)$ and $\varepsilon''(\nu)$ data for all five studied PAs. For propylene glycol and glycerol, $\chi''(\nu)$ (triangles) and $\varepsilon''(\nu)$ (squares) are jointly analyzed using Eq. (5.1) as already shown for both substances at one exemplary temperature in Fig. 5.1. Fits are shown as solid and dashed black lines. For the three longer-chained PAs, $\chi''(\nu)$ is shown as the black symbols at some selected temperatures. Here, only a qualitative comparison is performed, due to the similarity of the relaxation shapes and the apparent absence of any slow cross-correlation contribution.

7

RELAXATION IN ASYMMETRIC BINARY MIXTURES

After discussing relaxation spectra of pure molecular liquids in the previous chapters, the following chapter considers supercooled asymmetric binary mixtures. Here, the term 'asymmetric' refers to the fact that the two constituents in their pure form display very different glass transition temperatures, which, upon mixing, leads to dynamic decoupling of fast and slow component. The interest in asymmetric binary mixtures ranges from fundamental science to application-based material science, and covers systems with different levels of complexity ranging from simple models based on disparately sized spheres to application-optimized polymer-plasticizer systems or protein-water mixtures with highly complex solvent-solute interactions. This work is situated somewhere in the middle of this spectrum and aims to gain a fundamental understanding of molecular dynamics in concentrated polymer-solutions. Specifically, the aim is to clarify the origin of apparent slow solvent dynamics, i.e. signatures of solvent molecules that seem to relax on the timescale of the slow component. First, general properties of asymmetric binary mixtures are reviewed in Section 7.1, and subsequently, the results for the concentrated 2-picoline/PMMA mixture are discussed in Section 7.2. The latter were obtained in cooperation with Robin Horstmann, who performed additional computer simulations (see Ref. [202]).

7.1 ASYMMETRIC BINARY MIXTURES: THE GENERAL PICTURE

This section presents a brief review of the characteristics of asymmetric binary mixtures, focusing on general observation instead of specifics. Three common themes are covered, namely *dynamic asymmetry*, *enhanced dynamic heterogeneity* and *intrinsic confinement effects*.

7.1.1 Dynamic asymmetry

Even though many binary mixtures are homogeneously mixed, they do not necessarily exhibit one single structural relaxation process. Experimental evidence was provided by means of differential scanning calorimetry (DSC), probing a sample's heat capacity $c_p(T)$ as a function of temperature. During cooling, the glass transition is associated with a drop of $c_p(T)$ at T_g. By contrast to pure liquids, asymmetric binary mixtures usually display two distinct drops in $c_p(T)$, as was shown, e.g., for oligomers or polymers in solution with low-molecular weight liquids [203–205] or for polymer-polymer blends [206, 207]. Both drops in the DSC curves can be addressed to the dynamics of either solvent or solute, which implies that the two components vitrify at two distinct glass-transition temperatures $T_{g,high}$ and $T_{g,low}$, where $T_{g,high} > T_{g,low}$. The observation of two distinct glass transitions implies that above $T_{g,high}$, both components relax on different timescales and two α-processes are observed. This has been confirmed

experimentally using several techniques, e.g. BDS [203, 205, 208–210], NMR [209, 211] and DLS [208].
Similar separation of timescales was also observed in binary mixtures of two species of non-polymeric molecules, e.g. tristyrene and methyltetrahydrofuran (MTHF) [205], thus the discussed effects are not specific to mixtures containing polymers. Below $T_{g,high}$, the slow component is essentially frozen and and acts as a confinement for the fast component, as discussed in detail below.

7.1.2 Enhanced dynamic heterogeneity

As discussed in Section 3.1, relaxation spectra of pure supercooled liquids appear asymmetrically broadened with low-frequency power law ν^1 high-frequency power law $\nu^{-\beta}$. This shape is associated to spatial dynamic heterogeneity and dynamic facilitation, where the latter leads to a low-frequency cutoff of the distribution of relaxation times. In binary mixtures, strong enhancement of dynamic heterogeneity compared to the pure components is observed. Applying techniques that are sensitive to only one of the components allows to selectively probe the relaxation spectrum of that component. This can be done, e.g., by isotope labeling and performing component-selective NMR experiments or by choosing a non-polar component and preforming dielectric experiments. Such approaches revealed some general features for both, polymer-polymer blends [212, 213] and polymer-solutions [205, 208, 209, 211]: Only subtle broadening of the α-process compared to the pure supercooled liquid is observed for the slow component. By contrast, the fast component displays significantly enhanced dynamic heterogeneity that varies with temperature, leading to strong deviations from TTS, i.e. the width of the distribution of relaxation times is reported to increase linearly with $1/T$ at temperatures below $T_{g,high}$ [209]. Moreover, no ν^1 low-frequency power law is observed for the fast component. From the view of a dynamic-facilitation picture this is not surprising, as the low-frequency cutoff of the distribution of relaxation times is expected to occur upon percolation of fast-relaxing regions, which in asymmetric binary mixtures is hindered by the slow component.

7.1.3 Intrinsic confinement effects in binary mixtures

The dynamic asymmetry in binary mixtures implies that the matrix formed by the slow component effectively acts as a soft confinement for the fast component. These confinement effects significantly alter the dynamic behavior of the fast component. For instance, they enhance dynamic heterogeneity by introducing additional variations of molecular mobilities as a function of distance of solvent molecules from the matrix, local solvent concentration, local density or via additional solvent-solute interactions like hydrogen bonding or steric interactions. Analogous features are observed for low-molecular weight liquids loaded into tube- or sponge-like static confinements [214–217].

Another commonly observed feature in asymmetric binary mixtures is the reappearance of the Arrhenius temperature dependence of solvent-relaxation times, which sometimes is referred to as fragile-to-strong crossover. Within the Adam-Gibbs model, the super-Arrhenius temperature dependence of structural-relaxation times in pure supercooled liquids is rationalized in terms of an increasing dynamic correlation-length with decreasing temperatures. The naive conjecture for confined supercooled liquids is that the increase of the correlation-length is limited by the characteristic length-scale of the confinement and thus, stays constant below some temperature. This should restore the Arrhenius temperature dependence of re-

laxation times, which, indeed, has been observed for some confined liquids [214, 218] and in asymmetric binary mixtures [210]. However, the results might be misleading, because a supercooled liquid in confinement is not guaranteed to be in thermodynamic equilibrium. Due to immobilization upon cooling the local pressure within the pore can be expected to deviate from ambient conditions.

A third observation that has been attributed to reflect the intrinsic confinement is ultra-slow solvent relaxation. Several experimental studies have observed signatures of solvent relaxation several orders of magnitude slower than the solvent α-process and on similar timescales as the solute α-process . This work set out to determine the origin of this phenomenon, which will be discussed in detail in the following section.

7.2 THE ORIGIN OF APPARENT SLOW SOLVENT DYNAMICS

In recent years, experimental effort has increasingly focused on selectively probing the different components of binary mixtures. For instance, Blochowicz et al. [210] studied a 50 wt% mixture composed of the polar solvent 2-methyl tetrahydrofuran (MTHF) and the apolar polymer polystyrene (PS) by combining different experimental techniques. Due to the different polarity of the components, the dielectric response of the mixture only reflects the relaxation of solvent-molecules. It was found that MTHF does not only contribute as a fast process associated with its α-process, but also as a slow contribution with relatively weak relaxation strength and on a same time scale as the solute α-process. This is illustrated in Fig. 7.1a, reproducing some results from Ref. [210] obtained closely above $T_{\mathrm{g,high}}$. In addition to the solvent α-process at high frequencies (dashed lines), which was probed using quasi-elastic neutron scattering, a slow contribution is identified (colored symbols). This observation is intriguing, considering that the slow solvent contribution is up to nine orders of magnitude slower than the solvent α-process. Moreover, the relaxation strength of the slow solvent contribution is observed to increase with decreasing temperature, reaching up to 10% of the total dielectric relaxation strength. These findings were interpreted by the authors in terms of a slow fraction of solvent molecules that becomes immobilized due to their interactions with the polymer matrix, resulting in a bimodal solvent mobility distribution. Similar slow solvent contributions have been observed also for other polymer solutions [219–222], for mixtures containing non-polymeric macromolecules [223] and in aqueous peptide solutions [224, 225].

By contrast, isotope-selective NMR experiments have not been able to confirm the existence of a slow fraction of solvent molecules. This is shown in Fig. 7.1b and c, reporting previously unpublished NMR data for the MTHF-PS mixture studied in Ref. [210]. The ^{2}H NMR spectra in panel (b) selectively access the rotational motion of deuterated MTHF-d_7, by probing the quadrupolar interaction between the nuclear quadrupole moment of the deuteron and the electric field gradient of the C–D chemical bond at the site of the nucleus. Solvent molecules relaxing faster than the inverse quadrupole coupling constant $1/C^* \approx 10^{-6}$ s produce a narrow line in the spectrum, while those slower than $1/C^*$ contribute as a broad line, reflecting the presence and absence of motional averaging, respectively. By fitting the spectra (see the lower spectrum), the fraction of molecules relaxing at times slower than 10^{-6} s can be determined. The results of such an analysis as a function of temperature are shown in panel (c) as the orange symbols. While at low temperatures almost all MTHF molecules relax on timescales slower than $1/C^*$, the slow fraction decreases with increasing temperature until it becomes negligible around 190–200 K. These results can be compared to the fraction of the dielectric

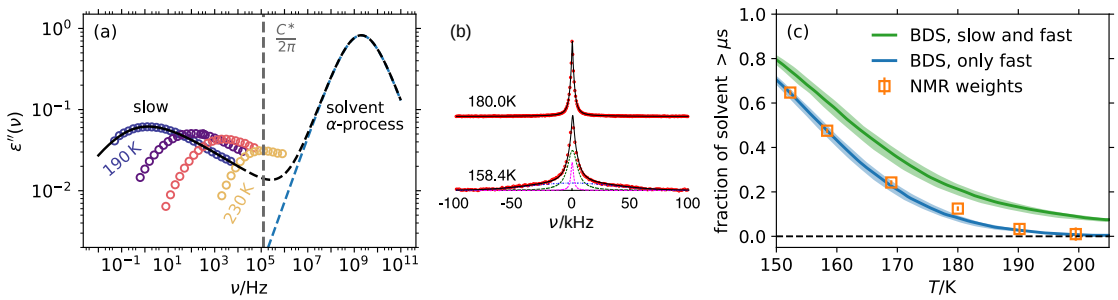

Figure 7.1: Slow solvent relaxation in an MTHF-PS mixture. Some of the data are reproduced from Ref. [210] while the other unpublished part was obtained during earlier work and was finally discussed in Ref. [104] within the present work.
(a) Dielectric relaxation spectra (colored symbols) representing solely the solvent relaxation. While the solvent α-process is observed at GHz, as found by means of quasi-elastic neutron scattering experiments [210], an additional slow solvent contribution is observed at up to nine orders of magnitude slower timescales than the α-process .
(b) ^{2}H NMR spectra specifically probing the isotope labeled MTHF-d$_7$ solvent dynamics. Solvent molecules relaxing faster than the inverse quadrupole coupling constant $1/C^* \approx 10^{-6}$ s produce a narrow line in the spectrum, while those slower than $1/C^*$ contribute as a broad line. Fitting these contribution allows to extract the fraction of solvent molecules slower than $1/C^*$. The associated threshold frequency, $\nu = C^*/2\pi$, is indicated in panel (a) as the gray dashed line.
(c) Comparison of the fraction of solvent relaxation slower than $1/C^*$ as a function of temperature from NMR (orange symbols) and from BDS (green line). A significant discrepancy is observed, which, however, disappears once the slow solvent contribution is disregarded for the analysis of the dielectric data (blue line).

relaxation strength $\Delta\varepsilon$ at $\nu < C^*/2\pi$, res. $\omega < C^*$, which corresponds to the relaxation strength on the left hand side of the gray dashed line in panel (a) and amounts to

$$\frac{\Delta\varepsilon_{\text{slow}}}{\Delta\varepsilon} = \frac{\int_{-\infty}^{\ln(C^*)} \varepsilon''(\omega)\,\mathrm{d}\ln\omega}{\int_{-\infty}^{\infty} \varepsilon''(\omega)\,\mathrm{d}\ln\omega}. \tag{7.1}$$

The obtained fraction of solvent molecules slower than 10^{-6} s according to $\varepsilon''(\nu)$ is included in Fig. 7.1c as the green line, while the green shaded area indicates the uncertainty of the procedure. A significant discrepancy is observed between $\Delta\varepsilon_{\text{slow}}/\Delta\varepsilon$ and the results from NMR. At a given temperature, the fraction of molecules slower than 10^{-6} s probed by NMR is significantly smaller than suggested by $\Delta\varepsilon$. By contrast, the NMR results are well described by the blue line obtained from Eq. (7.1) when the distinct slow relaxation process is ignored and only the solvent α-process is considered, i.e., when the distribution of solvent relaxation times is assumed to be unimodal instead of bimodal. Similar conclusions regarding the absence of a slow contribution were drawn in another NMR study on asymmetric binary mixtures [223]. Moreover, detailed analyses of BDS and NMR results for aqueous ε-polylysine solutions revealed the same discrepancy: While the dielectric analysis yielded a significant slow water contribution [224, 225], ^{2}H NMR measurements did not provide evidence for a slow fraction of water molecules [226].

At least two possible explanations exist for this discrepancy: (i) It originates from the differences between the $\ell = 1$ and $\ell = 2$ ranked correlation functions probed by BDS and NMR, respectively, or (ii) the discrepancy reflects the fact that ^{2}H NMR probes only self-correlations of molecular reorientation, while BDS is also sensitive to cross-correlations, i.e. collective

relaxation modes. The work presented in the following section set out to clarify this open question by studying an asymmetric binary mixture using DDLS, which represents an $\ell = 2$-technique, which at the same time is, at least in principle, sensitive to collective relaxation modes. These experiments were complemented by computer simulations performed by Robin Horstmann, the results of which are published in more details in his PhD thesis [202]. The following discussion covers mainly the complementary picture obtained by combining both techniques, which has been published in Ref. [104].

7.2.1 Broadband DDLS relaxation spectra of an asymmetric binary mixture

In order to study the solvent dynamics using DDLS, a 50 wt% binary mixture of 2-picoline and PMMA with approx. 43 repeat units per molecule was prepared (see sample preparation details in Appendix B). These two components were chosen, because 2-picoline molecules have a large optical anisotropy due to containing a π-electron system and, thus, give a strong depolarized light-scattering signal. PMMA, on the other hand, produces a comparably weak depolarized signal, thus it is expected that the large majority of the intensity fluctuations probed by DDLS reflects the dynamics of 2-picoline molecules [221, 227]. The pure components' glass transition temperatures are $T_{\mathrm{g,picoline}} = 133\,\mathrm{K}$ and $T_{\mathrm{g,PMMA}} \approx 360\,\mathrm{K}$ [228], thus the respective binary mixture is expected to exhibit strongly asymmetric dynamics. This conjecture is confirmed experimentally by performing dielectric experiments, which equally probe the dipole reorientation dynamics of both components due to their comparable polarities. Dielectric-loss spectra of the mixture obtained at various temperatures are shown in Fig. 7.2a. As polymer solutions usually contain significant amount of charge-carriers, the effects of dc conductivity and electrode polarization were removed from these data by considering the approximation

$$\varepsilon''(\nu) \approx \frac{\mathrm{d}\big(\varepsilon'(\nu) - \varepsilon'_{\mathrm{pol}}(\nu)\big)}{\mathrm{d}\ln\nu}, \tag{7.2}$$

where $\varepsilon_{\mathrm{pol.}}$ denotes the electrode polarization contribution, which has been identified by fitting a power law to $\varepsilon'(\nu)$. The approximation (see Eq. (2.39)) achieves accurate results for broad loss peaks, thus is an appropriate approximation for dielectric data of asymmetric binary mixtures [59].

For clarity, data at $T > T_{\mathrm{g,high}}$ are shifted upwards by a factor of ten. At the highest temperatures ($T \geq 213.2\,\mathrm{K}$) only a single relaxation process is identified in the frequency window of the experiment, which is attributed to the segmental dynamics of PMMA. At intermediate temperatures ($162.1\,\mathrm{K} < T < 213.2\,\mathrm{K}$), a second relaxation process is observed at higher frequencies, which is attributed to the relaxation of 2-picoline. Below $T_{\mathrm{g,high}}$ (lower data), only the solvent relaxation is probed, which slows down and undergoes a marked spectral broadening while approaching $T_{\mathrm{g,low}}$ ($T_{\mathrm{g,low}}^{\mathrm{half}} \approx 150\,\mathrm{K}$ as determined from DSC measurements).

Corresponding broadband DDLS spectra are shown in Fig. 7.2a. Although it is to be expected that DDLS mostly probes the relaxation dynamics of the solvent, these data are clearly bimodal. However, before discussing in detail the conclusions that can be drawn from these data, the procedures applied to obtain broadband DDLS data need to be discussed.

$\chi''(\nu)$-data obtained by PCS experiments at various temperatures are shown in Fig. 7.3a. It is important to emphasize that the PCS experiments do not provide an absolute relaxation amplitude for these data, as they are obtained via Laplace transformation of a normalized autocorrelation function. Thus, the temperature evolution of the relaxation amplitudes of the observed processes can not be extracted from these data. By contrast, TFPI experiments can be operated such that an absolute relaxation amplitude is obtained, as they involve measuring

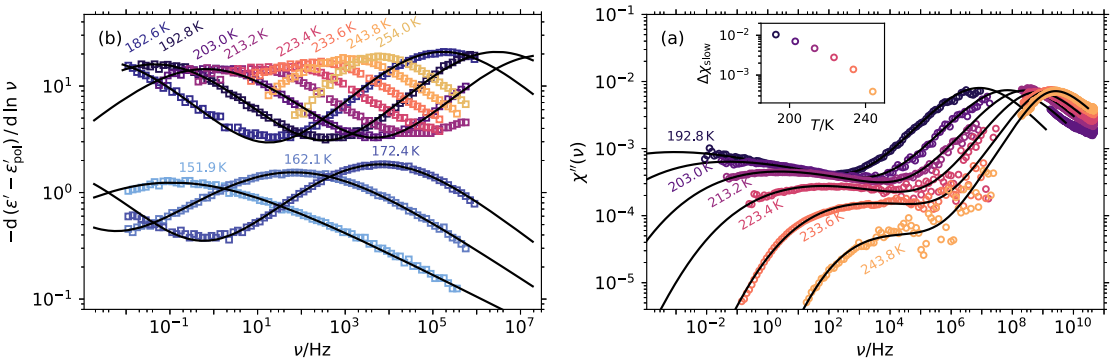

Figure 7.2: Experimental relaxation spectra from (a) dielectric spectroscopy and (b) DDLS obtained at various temperatures. Panel (a) plots the an approximation of the dielectric loss in order to eliminate the influence dc conductivity and electrode polarization. Solute and solvent relaxation are probed equally, due to both being similary polar. The DDLS relaxation spectra in (b) reflect mostly the relaxation of the solvent. Broadband spectra are obtained by combining results from PCS and TFPI (see Fig. 7.3). The inset displays the relaxation strength of the slow solvent contribution as a function of temperature.

absolute scattering intensities. These can be compared across different temperatures as long as the experimental conditions are comparable. $\chi''(\nu)$-data obtained from TFPI measurements at the same and higher temperatures as the PCS data in panel (a) are shown in panel (b). While the PCS experiment accesses the frequency range $10^{-2} > \nu/\mathrm{Hz} > 10^{7}$, the TFPI experiments operates at $3\cdot10^{8} > \nu/\mathrm{Hz} > 10^{11}$, thus the relaxation spectra obtained from both techniques do not overlap. However, as will be discussed in the following, using appropriate model functions does allow to extrapolate the relaxation spectra to obtain a full broadband description.

A single relaxation process contributes to the TFPI-relaxation spectra, which is identified as the solvent α-process and shifts out of the accessible frequency window at $T < 200\,\mathrm{K}$. It can be modeled using the imaginary part of the Havriliak-Negami (HN) equation,

$$\chi''(\nu) = \mathrm{Im}\left[\frac{\Delta\chi}{(1+(i\,2\pi\nu\tau)^{\alpha})^{\beta}}\right], \tag{7.3}$$

which yields a peak with high-frequency power law $\nu^{-\alpha\beta}$ and low-frequency power law ν^{α}. Thus, it is well suited to describe the broadened relaxation spectra commonly observed in asymmetric binary mixtures. At sufficiently low temperatures ($T < 240\,\mathrm{K}$) the low-frequency flank of the solvent α-process can be identified in the PCS relaxation spectra, which allows to approximate the parameter α from Eq. (7.3) by fitting a power law. The results are shown in Fig. 7.3a as the dashed lines. The inset of panel (b) shows the continuous decrease of α with decreasing temperature, the color of the symbols indicating whether the respective value was determined from the TFPI or from the PCS data. The fact that both, TFPI and PCS, probe the solvent α-process , allows to extrapolate the relaxation shape to the intermediate frequency gap between both techniques and to assign an absolute relaxation amplitude to the PCS data. This procedure is illustrated in Fig. 7.3c, where the dashed line indicates the HN equation describing the solvent α-process , the amplitude and relaxation time of which has been fixed via fit to the TFPI data, while α was determined from the PCS data. Subsequently, the amplitude of the PCS-relaxation spectrum is scaled such that it matches the HN equation, which yields the broadband DDLS relaxation spectrum. The same procedure shown in panel (c) can be repeated at various different temperatures, the results of which are shown in Fig. 7.2a.

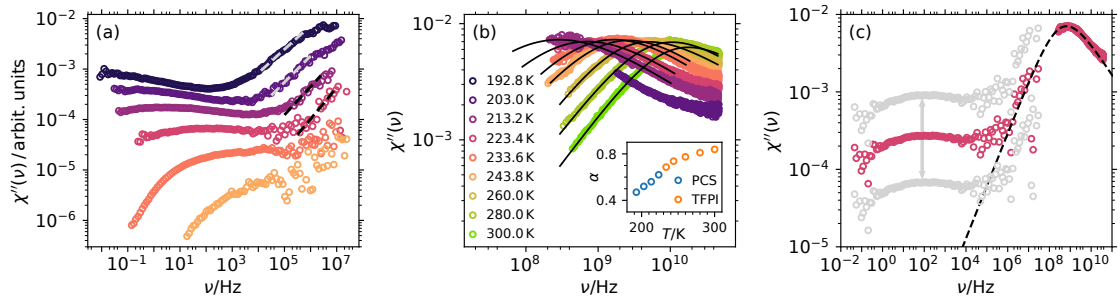

Figure 7.3: Illustration of the procedures to obtain broadband DDLS relaxation spectra. (a) Relaxation spectra from PCS measurements. The dashed lines indicate fits to the low-frequency power law of the solvent α-process . (b) Corresponding TFPI data. Solid lines represent fits by the HN equation. The inset displays the low-frequency power-law exponent α as a function of temperature. Blue symbols indicate temperatures at which α was determined from PCS data, while the orange symbols indicate that it was extracted from fits to the TFPI data. (c) Illustration of the procedure applied to match PCS and TFPI data into broadband DDLS spectra. After having determined the low-frequency power-law exponent of the solvent α-process , the amplitude of the PCS data is scaled such that it corresponds to the HN fit to the TFPI data.

As already mentioned above, a second slow relaxation contribution is observed in the DDLS spectra in addition to the solvent α-process. Strikingly, its relaxation amplitude increases considerably with decreasing temperature, as found by fitting the spectra by the sum of the solvent α-process and a relaxation process based on a GG distribution of relaxation times representing the slow contribution. Plotting the relaxation strength of the slow contribution, $\Delta\chi_{\text{slow}}$, as a function of temperature in the inset of panel (b) reveals an increase of around a factor of 25 upon lowering the temperature from 243.8 K to 192.8 K. This strong temperature dependence indicates that the origin of the slow contribution can not simply be a weak PMMA contribution to the DDLS signal, because the latter would be expected to show an approximately constant relaxation strength, similar to what is found from the dielectric loss spectra. By contrast, the strong increase of $\Delta\chi_{\text{slow}}$ much rather resembles the approximately exponential temperature dependence of the slow solvent-relaxation amplitude observed in a previous study for the MTHF-PS binary mixture [210]. Considering these findings, the slow contribution to the DDLS spectra can be assigned to the relaxation of 2-picoline molecules. The temperature dependence of the peak maximum frequency of the slow solvent contribution and of the dielectric PMMA relaxation approximately coincide, thus suggesting that the slow solvent contribution is in one way or another related to the PMMA matrix relaxation. In contrast to the earlier observation of a slow solvent contribution, the broad frequency range accessible by combining two DDLS techniques allowed to resolve an entire relaxation spectrum containing the solvent α-process and the slow solvent contribution. This allows to precisely analyze the relaxation shape of the slow contribution, revealing a strong broadening on the high-frequency side, creating almost plateau-like relaxation curves, as well as ν^1 low-frequency behavior.

Considering that DDLS spectra reveal an equivalent slow solvent relaxation as previously identified in the dielectric loss spectra of an MTHF-PS binary mixture, it can now be excluded that the absence of the slow contribution in NMR experiments reflects the $\ell = 2$ nature of the orientation correlation function. Instead, it is to be expected that collective solvent relaxation modes, i.e. orientational cross-correlations are the origin of the slow contribution. To confirm the existence of these cross-correlations and to unravel their physical origin,

molecular dynamics (MD) simulation are employed, which allow to readily disentangle self- and cross-correlation contributions.

7.2.2 Combining experiment and computer simulations

In the MD simulations a system consisting of $N = 500$ 2-picoline molecules and 10 PMMA chains, each comprising 50 repeat units, is analyzed. Thus, the 2-picoline concentration is similar in experiment (50 wt%) and in the simulations (48 wt%). Inherently, MD simulations are limited to higher temperatures, where dynamics is sufficiently fast such that the system can be equilibrated within a reasonable time. To minimize the temperature-discrepancy between experiments and simulations, a coarse grained united atom topology was used, which allowed to push the duration of the simulation run to 17.5 µs at the lowest temperature. More details about the MD simulations can be found in the PhD thesis of Robin Horstmann [202].

To unravel the molecular mechanisms behind the slow solvent relaxation, the simulation trajectories are employed to calculate the collective dipole correlation function

$$C_M(t) = \frac{1}{N} \sum_{i,j} \left\langle \boldsymbol{\mu}_i(0) \cdot \boldsymbol{\mu}_j(t) \right\rangle, \tag{7.4}$$

as well as its self-part,

$$C_{\text{self}}(t) = \frac{1}{N} \sum_{i} \left\langle \boldsymbol{\mu}_i(0) \cdot \boldsymbol{\mu}_i(t) \right\rangle, \tag{7.5}$$

of only the solvent molecules. Here, $\boldsymbol{\mu}_i(t)$ denotes the normalized molecular dipole-moment vector of solvent molecule i at time t and the angular brackets $\langle ... \rangle$ denotes averages over multiple time origins. To obtain results that are fully comparable to results from DDLS experiments, a different molecular axis and the $\ell = 2$ correlation should be considered. However, the slow relaxation is weak in the mildly supercooled regime accessible by MD simulations, thus it is exploited that it appears stronger in $\ell = 1$ than in $\ell = 2$ correlation functions. It is shown below, however, that the results obtained for a different molecular axis and the $\ell = 2$ Legendre polynomial are qualitatively similar.

The difference between $C_M(t)$ and $C_{\text{self}}(t)$ are the orientational cross-correlations of solvent molecules

$$C_{\text{cross}}(t) = \frac{1}{N} \sum_{i \neq j} \left\langle \boldsymbol{\mu}_i(0) \cdot \boldsymbol{\mu}_j(t) \right\rangle, \tag{7.6}$$

which are obtained as

$$C_{\text{cross}}(t) = C_M(t) - C_{\text{self}}(t). \tag{7.7}$$

Fig. 7.4 presents the results obtained for the different dipole correlation functions analyzed at various temperatures between 250 K and 500 K. The collective correlation function $C_M(t)$ is found to be dominated by a fast decay that is identified as the solvent α-process. However, unlike in pure liquids, the α-process does not lead to a full decay to zero, but rather leaves a finite correlation value, which is terminated by a second decay at longer timescales. This behavior is qualitatively equivalent to the slow contribution identified in the experimental light-scattering results. This is highlighted in the inset, showing the loss part of the dynamic susceptibility associated $C_M(t)$ as the solid blue line, which was obtained as the Laplace transformation of a fit to $C_M(t)$. Consistent with the DDLS results, the resulting frequency-domain representation of the simulation data features the solvent α-process and a distinct slow relaxation, which occurs on the same timescale as the PMMA segmental reorientation as

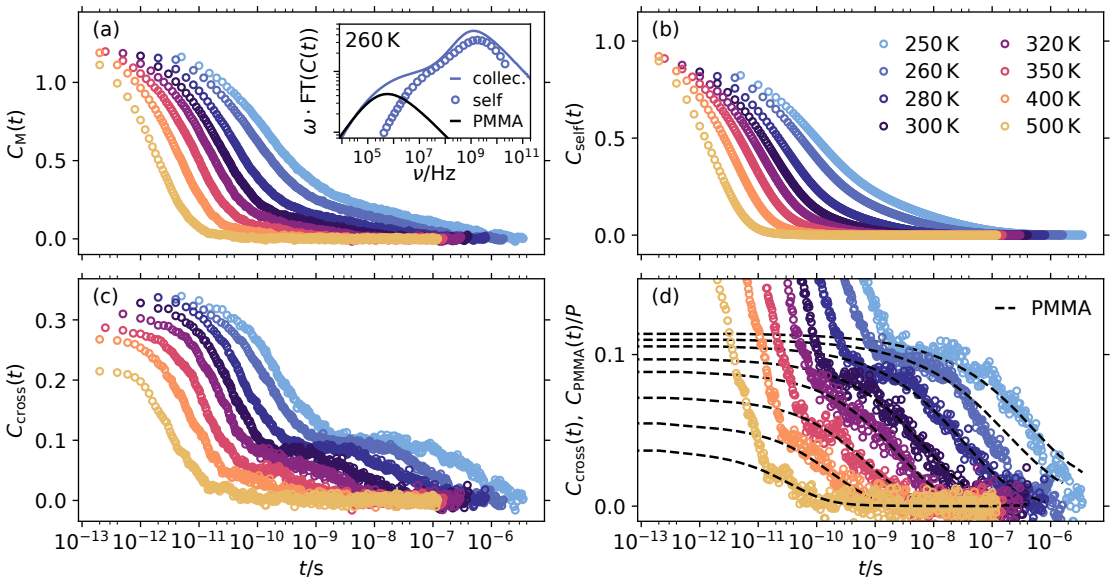

Figure 7.4: Analysis of the solvent dipolar dynamics extracted from MD simulations of the 2-picoline/PMMA mixture at various temperatures. (a) Collective dipole correlation function, $C_M(t)$, (b) self-part of the dipole correlation function, $C_{\text{self}}(t)$ and (c) cross-parts of the dipole correlation function, $C_{\text{cross}}(t)$. Panel (d) compares the slow decay of $C_{\text{cross}}(t)$ to the PMMA dipole correlation function $C_{\text{PMMA}}(t)$ (dashed black lines). Here, $C_{\text{PMMA}}(t)$ was rescaled by a factor P, such that its short-time plateau corresponds to the intermediate plateau of $C_{\text{cross}}(t)$ for better comparison. The inset in panel (a) compares the respective susceptibility representations of the correlation function of the collective (blue line), self (blue symbols) and PMMA (black line) relaxation at 260 K. Again, the amplitude of the susceptibility representation of $C_{\text{PMMA}}(t)$ was rescaled by P for better comparison.

shown by the solid black line. Similar to what is found in the experiment, the intensity of the slow decay in the simulation data increases with decreasing temperature.

By contrast, the self-correlations $C_{\text{self}}(t)$ shown in panel (b) do not display a distinct slow contribution, as evident also from comparing the susceptibility representation obtained at 260 K to the one of $C_M(t)$ in the inset of panel (a). Here, the susceptibility of the self-correlations was directly calculated from the raw data using the Filon algorithm [229]. Only a slight deviation from a power law behavior is observed on the low-frequency side of the main peak, which results from anisotropic ring dynamics (e.g. π-flips) and is not related to the presence of slow solvent molecules. Thus, it can be concluded that, despite the slow contribution to the collective dynamics, no slow species of solvent molecules exists.

Panel (c) displays the solvent cross-correlations $C_{\text{cross}}(t)$, which were calculated from the simulations according to Eq. (7.7). In most pure liquids, cross-correlations decay on time scales close to the one of the α-process. As shown in Chapter 5, slow cross-correlations can persist up to time scales longer than the α-process in certain supercooled liquids, however this involves some form of structure formation via H-bonding, or dipole-dipole interactions and the resulting cross-correlation contribution usually superimposes the α-process. This is not the case for the solvent cross-correlations in the present binary mixture, which feature a distinct finite plateau at times longer than the α-process. Its height increases with decreasing temperature. The final decay of the plateau coincides with the segmental dynamics of PMMA, as confirmed in panel (d), where the self-part of the PMMA dipole correlation functions, $C_{\text{PMMA}}(t)$, at various temperatures are included as the black dashed lines. For better compari-

son, $C_{\mathrm{PMMA}}(t)$ was scaled by the temperature-dependent factor P that describes the height of the long-time plateau of $C_{\mathrm{cross}}(t)$.

Configuration-overlap analysis

To identify the underlying mechanism behind the observed cross-correlations, the overlap of solvent configurations at different times is studied similar to what has been done in some previous approaches [230–232]. At time $t = 0$, the solvent configuration is characterized by a set of spheres of diameter 6 Å around the molecular centers. The diameter value is chosen such that no sphere is occupied by more than one solvent molecule at the majority of times. The self-occupation of sphere i, which has been occupied by solvent molecule i at time $t = 0$, as a function of time is quantified as

$$o_i^{\mathrm{self}}(t) = \begin{cases} 1 & \text{occupied by molecule } i \\ 0 & \text{else.} \end{cases} \tag{7.8}$$

Similarly, the distinct-occupation of sphere i is given by

$$o_i^{\mathrm{dist}}(t) = \begin{cases} 1 & \text{occupied by molecule } j \neq i \\ 0 & \text{else.} \end{cases} \tag{7.9}$$

From $o_i^{\mathrm{self}}(t)$ and $o_i^{\mathrm{dist}}(t)$, the self- and distinct configuration-overlap correlation functions are obtained as

$$O_{\mathrm{self}}(t) = \langle o_i^{\mathrm{self}}(t) \rangle \tag{7.10}$$

and

$$O_{\mathrm{dist}}(t) = \langle o_i^{\mathrm{dist}}(t) \rangle, \tag{7.11}$$

respectively, where the angular brackets $\langle ... \rangle$ indicate average of all spheres as well as over multiple time origins. Simply speaking, $O_{\mathrm{self}}(t)$ quantifies the portion of particles that have not yet moved out of the sphere defined around them at $t = 0$, while $O_{\mathrm{dist}}(t)$ quantifies the portion of particles that, at time t, have moved into *a different* sphere.

$O_{\mathrm{self}}(t)$ and $O_{\mathrm{dist}}(t)$ as a function of t obtained at various temperatures are shown in panels (a) and (b) of Fig. 7.5, respectively. At $t = 0$ one finds $O_{\mathrm{self}}(0) = 1$ and $O_{\mathrm{dist}}(0) = 0$, reflecting the fact that no solvent molecule has moved yet and every molecule sits in the sphere defined around its center of mass at $t = 0$. For $t \to \infty$, $O_{\mathrm{self}}(t)$ decays to zero, which signifies that solvent molecules start to diffuse out of their respective $t = 0$-sphere. Because translation and rotation of solvent molecules are coupled, the decay of $O_{\mathrm{self}}(t)$ qualitatively resembles the one of $C_{\mathrm{self}}(t)$.

$O_{\mathrm{dist}}(t)$ converges to some fixed value $O_{\mathrm{dist}}^{\infty}$ for $t \to \infty$, which represents the average occupation of the set of spheres once all particle positions are randomized. $O_{\mathrm{dist}}^{\infty}$ depends on the average packing density of the defined spheres and is weakly temperature dependent. Strikingly, at intermediate times a distinct maximum is observed for $O_{\mathrm{dist}}(t)$. It signifies an increased probability of solvent molecules being located at positions priorly occupied by other solvent molecules. With decreasing temperature, the maximum value increases compared to $O_{\mathrm{dist}}^{\infty}$, indicating that the solvent molecules increasingly occupy such locations. This observation, which usually is not observed in pure molecular liquids, implies that there exist regions within the binary mixture that are preferably occupied by solvent molecules. The memory of these preferred locations persists over numerous solvent α-process time scales.

In a final step, the average orientational cross-correlation between solvent molecules that have occupied the same sphere at different times, $C_{\mathrm{dist}}(t)$, is determined. For this purpose,

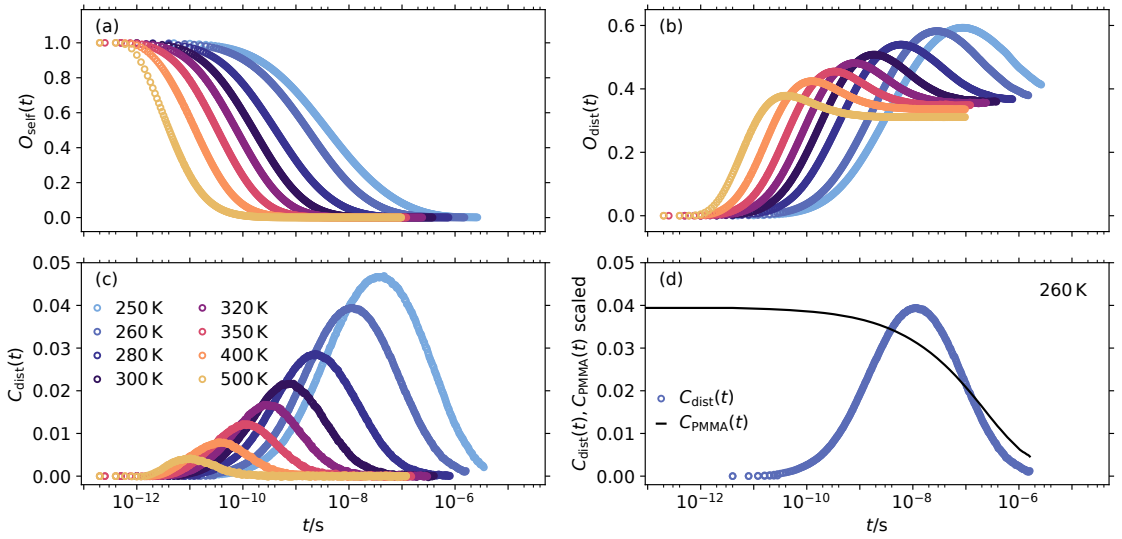

Figure 7.5: Configurational-overlap analysis of solvent molecules. (a) Self-occupation $o_i^{\mathrm{self}}(t)$ of spheres defined around solvent molecules at $t = 0$ as a function of t and (b) distinct-occupation $o_i^{\mathrm{dist}}(t)$ of these spheres. The maximum observed for $o_i^{\mathrm{dist}}(t)$ at intermediate times indicates preferred locations of solvent molecules. (c) Dipole cross-correlations of molecules occupying the same preferred locations at different times, $C_{\mathrm{dist}}(t)$. Values > 0 indicate favored orientations of solvent molecules at preferred locations. (d) Comparison of $C_{\mathrm{dist}}(t)$ and $C_{\mathrm{PMMA}}(t)$ (rescaled). Both decay on similar time scales.

the angle $\varphi(t)$ between the orientation of solvent molecule i in sphere i at $t = 0$ and the orientation of a distinct molecule j located in sphere i at a later time t is defined. $C_{\mathrm{dist}}(t)$ for the normalized dipole moment vectors $\boldsymbol{\mu}$ is then calculated as

$$C_{\mathrm{dist}}(t) = \frac{1}{n} \sum_{\substack{\text{replace-}\\\text{ments}}} \cos\big(\varphi_i(t)\big) = \frac{1}{n} \sum_{\substack{\text{replace-}\\\text{ments}}} \boldsymbol{\mu}_i(0) \cdot \boldsymbol{\mu}_j(t), \tag{7.12}$$

where the summation is performed over all n replacement events, where some molecule j replaced molecule i in sphere i. Thus, the summation also involves averaging over multiple time origins. $C_{\mathrm{dist}}(t)$ quantifies the overall orientational cross-correlations caused by the distinct replacement mechanism.

In a scenario where no preferential orientations exists between solvent molecules that have occupied the same sphere at different times, $C_{\mathrm{dist}}(t) = 0$ should be observed at all t. By contrast, a clear peak is observed for $C_{\mathrm{dist}}(t)$ in panel (c). Its maximum value increases with decreasing temperature and its peak-maximum frequency roughly coincides with the peak observed for $C_{\mathrm{dist}}(t)$. This implies that solvent molecules positioned at the preferred locations identified from $O_{\mathrm{dist}}(t)$ also exhibit a preferred orientation with regard to the dipole-moment vector. In panel (d), $C_{\mathrm{dist}}(t)$ is compared to $C_{\mathrm{PMMA}}(t)$ obtained at 260 K. The comparison reveals that the long-time decay of the peak roughly coincides with the segmental reorientation of PMMA. Thus, it can be concluded that solute molecules imprint preferred locations and orientations onto neighboring solvent molecules, which persist until the solute molecules have rearranged.

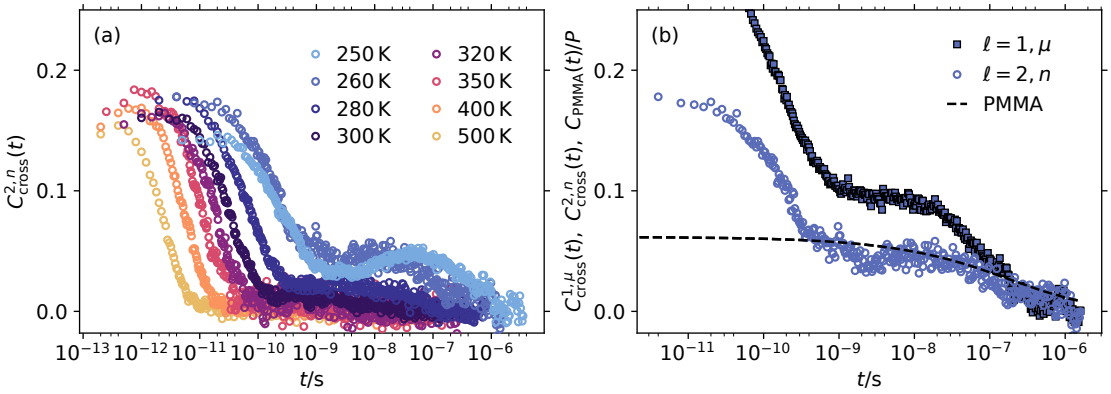

Figure 7.6: (a) Solvent cross-correlations based on the $\ell = 2$ Legendre polynomial and the normal vector of the phenyl ring, $C^{2,\boldsymbol{n}}_{\text{cross}}(t)$. The results qualitatively resemble those in Fig. 7.4c obtained for $\ell = 1$ and the dipole-moment vector, $C^{1,\boldsymbol{\mu}}_{\text{cross}}(t)$. The similarity is confirmed in panel (b) for data obtained at 260 K.

Results for $\ell = 2$ Legendre polynomial and phenyl-ring normal vector

The discussed MD simulation results are based on $\ell = 1$ orientation correlation functions with regard to the 2-picoline dipole moment vector $\boldsymbol{\mu}$. By contrast, DDLS does probe the $\ell = 2$ orientation correlation function of the molecular optical anisotropy tensor. For aromatic molecules, the latter approximately corresponds to the normal vector $\boldsymbol{n}$ of the phenyl ring. Fig. 7.6a considers the orientational cross-correlations of solvent molecules for the $\ell = 2$ orientation correlation function with regard to the vector $\boldsymbol{n}$,

$$C^{2,\boldsymbol{n}}_{\text{cross}}(t) = \frac{1}{N} \sum_{i \neq j} \left\langle P_2\big(\boldsymbol{n}_i(0) \cdot \boldsymbol{n}_j(t)\big) \right\rangle, \tag{7.13}$$

where $P_2(x) = (3x^2 - 1)/2$ is the second rank Legendre polynomial. Similar to what was found for $\ell = 1$ and $\boldsymbol{\mu}$ in Fig. 7.4c, a distinct slow cross-correlation decay is observed. Fig. 7.6b compares $C^{2,\boldsymbol{n}}_{\text{cross}}(t)$ obtained at 260 K to the corresponding $\ell = 1$ cross-correlation function $C^{1,\boldsymbol{\mu}}_{\text{cross}}(t)$ for the dipole moment vector $\boldsymbol{\mu}$. While the slow cross-correlation contribution is found to have a lower amplitude for $\ell = 2$ than for $\ell = 1$, the respective relaxation times are approximately identical and correspond to the decay of $C_{\text{PMMA}}(t)$. It can be concluded that preferred orientations of solvent molecules and the corresponding cross-correlation also exist with regard to the phenyl-ring normal vector and the $\ell = 2$ orientation correlation function, i.e. approximately the correlation function that is probed by DDLS. In this regard, the solvent-solvent cross-correlations in asymmetric binary mixtures do not resemble the cross-correlations in pure supercooled liquids, as the latter have been found to vanish for $\ell = 2$ correlation functions [126, 147]. This also resolves the apparent contradiction as to why DDLS probes exclusively the self-part of molecular dynamics in pure supercooled liquids, whereas cross-correlations do contribute considerably to the DDLS spectra of asymmetric binary mixtures.

Cross-correlation mechanism on the molecular level

The experimental and computational results allow to gain a detailed understanding of the solvent dynamics in asymmetric binary mixtures. Unlike previously assumed [210, 219–223],

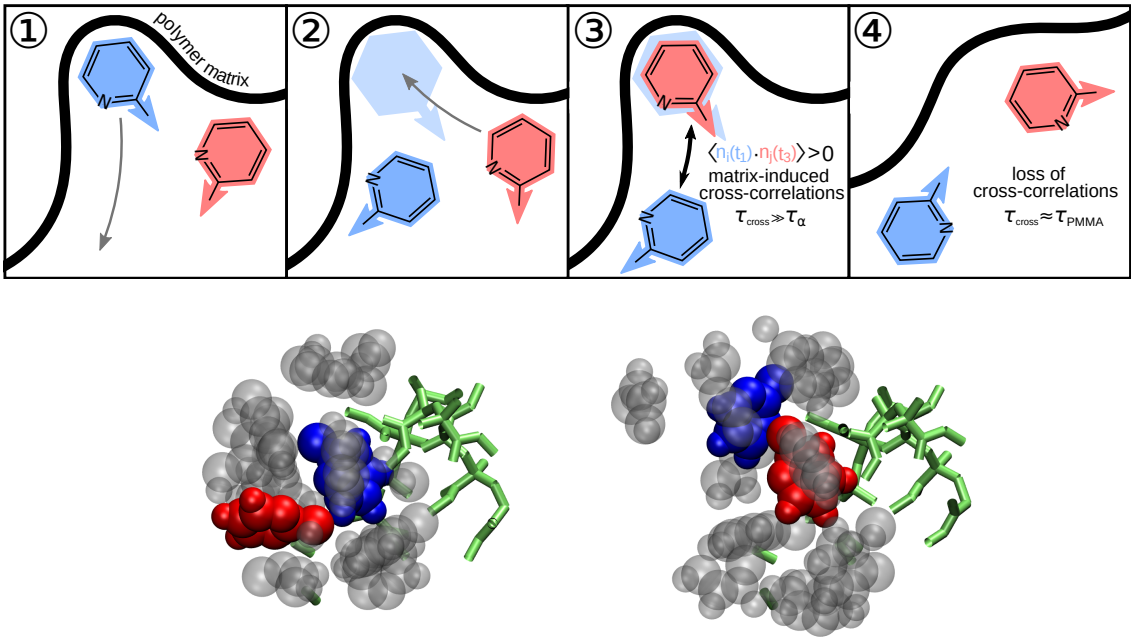

Figure 7.7: Upper panels: Schematic illustration of the cross-correlation mechanism. See text for detailed discussion. Lower Panels: Simulation snapshots showing an ensemble of solvent and solute molecules at different times. The red molecule replaces the blue one and adopts a similar orientation. Simulation snapshots are reproduced from Ref. [202].

there does not exist a distinct slow fraction of solvent molecules. Instead, it was shown that the slow solvent contribution to experimental relaxation spectra can be attributed to the slow decay of solvent-solvent cross-correlations. The upper panels of Fig. 7.7 show a cartoon depicting the underlying molecular mechanism behind these cross-correlations. The fast decay of the solvent self-correlation implies that all solvent molecules, also those located close to the solute, relax on a significantly shorter timescale compared to the surrounding polymer matrix. Thus, the potential energy landscape imposed on the solvent by the polymer matrix can be assumed to behave quasi-static on the time scales of the solvent α-process. At the same time, the interactions with the polymer introduces "preferred" locations, with a larger-than-average occupation by solvent molecules. Once a solvent molecule leaves such a preferred location, it is quickly replaced by another one, as shown in panels ① and ②. This effect is manifested by enhanced distinct-occupations identified in the configuration-overlap analysis shown in Fig. 7.5(b).

Additionally, matrix-solvent interactions at preferred locations cause favored orientations of solvent molecules. Hence, molecules located at preferred locations at different times are orientationally correlated, as was shown in Fig. 7.5(c). This scenario is illustrated in ③, where the contours of the blue and the red molecule roughly coincide with respect to not only their positions but also their orientations. An example of this phenomenon is also depicted in the lower panels of Fig. 7.7 for a snapshot from the simulations, where the red molecule replaces the blue one. With decreasing temperature the relative strength of matrix-solvent interactions increases with respect to the thermal energy, thus the relative amplitude of the orientational cross-correlations grows.

Preferred locations with enhanced orientational correlation only prevail until the energy landscape is significantly altered due to the segmental relaxation of the solute on the charac-

teristic timescale τ_{PMMA}. Consequently, solvent-solvent cross-correlations decay on a similar timescale, i.e. $\tau_{\mathrm{cross}} \approx \tau_{\mathrm{PMMA}}$ as illustrated in ④. On longer timescales, no relevant solvent contributions to experimental relaxation spectra or to the simulation correlation functions are observed.

While BDS and DDLS both access collective solvent dynamics (see Eq. (2.42) and Eq. (2.17)), ^{2}H-NMR is an incoherent technique, thus it does not probe any cross-correlations but only the self-part of molecular dynamics. As evident from Fig. 7.1, any slow solvent contribution probed by NMR experiments is significantly smaller compared to the equivalent contribution to the dielectric loss. The slow contribution to NMR spectra is not zero, because of the enhanced dynamic heterogeneity of the solvent. The latter was identified from the DDLS data, e.g., in terms of the low-frequency power-law exponent α, which was found to be < 1 and decrease significantly with decreasing temperature. An equivalent long-time tail contribution to $C_{\mathrm{self}}(t)$ was identified in the simulations. The origin of the increased dynamic heterogeneity was attributed to local solvent-solute concentration fluctuations in a further detailed analysis of the simulation data discussed above [202]. As a consequence, NMR measurements probe a "slow" contribution as the slowest part of the broad distribution of solvent-relaxation times. However, the latter does not produce a distinct slow contribution and is much smaller than the slow cross-correlation contribution to the dielectric loss.

Obviously, the illustration in Fig. 7.7 is over-simplified. Further analysis of simulation data at the lowest studied temperature revealed that only around half of the cross-correlations can be rationalized in terms of the simple "replacement mechanism". Additionally, the orientations of adjacent solvent molecules close to the solute-surface, i.e. in adjacent preferred locations can be correlated, and also solvent-solute cross-correlations can not be fully neglected.[202]

In his PhD thesis, R. Horstmann extended the analysis of solvent-solvent cross-correlations to several other asymmetric binary mixture. It was found that the occurrence of the above discussed mechanism is independent of the exact interaction mechanisms, i.e. the same effects are found for mixtures involving non-polar solvent and solute molecules and an aqueous peptide solution [202]. For the latter, a distinct slow water relaxation contribution has previously been identified from dielectric loss data [224, 225, 233] and was interpreted in terms of a slow fraction of water molecules, which however could not be observed by recent NMR experiments [226]. Instead, the present results suggest that solvent cross-correlation effects might be the origin of the slow contribution.

Part II

PHYSICAL AGING IN GLASSY SYSTEMS

8

BRIEF INTRODUCTION TO PHYSICAL AGING

Most results discussed in Part I of this work refer to the physics of supercooled liquids in *metastable thermal equilibrium*. Here, the term *metastable* refers to the fact that usually the ordered structure of the crystal represents the state that minimizes free energy, while, however, the formation of the crystal has been suppressed to obtain a supercooled liquid. As it is usually impossible to crystallize the supercooled liquids discussed in the following chapters, the notation *metastable* will not be used hereafter and the term *equilibrium* always refers to the metastable supercooled liquid state.

From a thermodynamic point of view, the equilibrium nature of the supercooled liquid is manifested by the fact that its entropy is constant as a function of time. Out-of-equilibrium states can be obtained by exposing it to some perturbation, e.g. a temperature change. However, as long as the average relaxation time of the supercooled liquid is small, e.g. $\tau \sim$ns closely below the melting point T_m, the relaxation to the new equilibrium state is too fast to be noticed. Because the average relaxation time of a supercooled liquid strongly increases with decreasing temperature, however, its relaxation to the new equilibrium state after a quick change in temperature becomes slow at low temperatures, such that an out-of-equilibrium material, called a *glass*, can be obtained [234, 235]. The slow relaxation of glasses towards the equilibrium supercooled-liquid state is referred to as *physical aging*. Here, the term *physical* indicates that the equilibration process exclusively involves molecular rearrangements and no chemical alterations of the material [5, 35, 36, 236]. In real-life applications where glassy materials like conventional inorganic glasses [38, 237, 238] or plastics [5, 35, 236] are held around room temperature, physical aging typically happens on time scales ranging from days to many years. It usually is observed in terms of very subtle changes of physical properties like, e.g., the refractive index [38, 239, 240] or the mechanical properties of material [5, 35, 238, 241].

From a fundamental science perspective, the best controlled physical aging experiments involve exposing an equilibrium material to a rapid change of temperature. Afterwards, its full relaxation towards equilibrium at a fixed annealing temperature is monitored by continuously measuring some physical property, see e.g. Refs. [37, 242–244]. This process is illustrated in Fig. 8.1a (adapted e.g. from Ref. [35]), where the material's specific volume is plotted as a function of temperature. Equilibrium states are located on the equilibrium line depicted in black. Exposing the material to an instantaneous temperature change of magnitude ΔT results in a deviation of the specific volume from the equilibrium line, as illustrated by the blue and red solid lines for temperature down- and up-jump, respectively. The dashed blue and red lines indicate the slow relaxation towards the equilibrium state during physical aging. It goes along with a slow and gradual change of the specific volume until it converges to its new equilibrium value. This change of the specific volume characterizes the physical aging process and could be probed using an appropriate experiment.

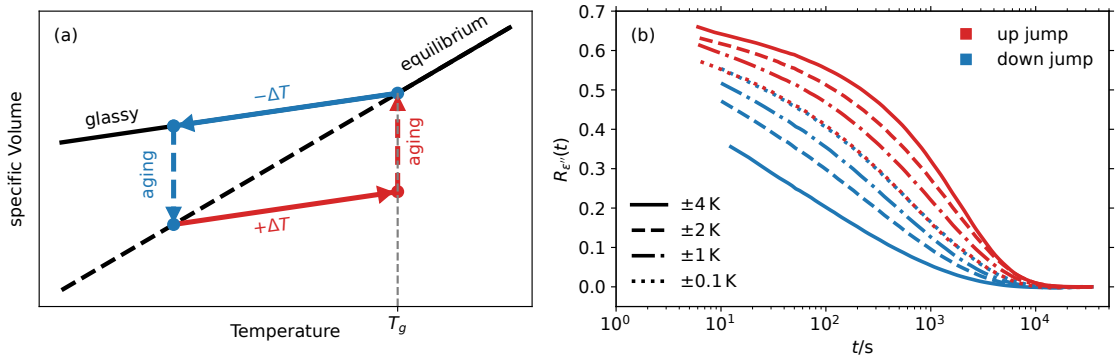

Figure 8.1: (a) Schematic illustration of the evolution of a supercooled liquid in the specific volume-temperature phase space after being exposed to an infinitely fast temperature change. After the temperature change, the system deviates from the equilibrium liquid line (black) and becomes glassy. The system's slow relaxation back to the equilibrium line is referred to as physical aging. (b) The relaxation towards the equilibrium state proceeds vastly different for up- and down-jumps, i.e. normalized relaxation functions obtained for up- and down-jumps of different magnitudes do not collapse, as it would be the case if physical aging was a linear response phenomenon. A brief discussion of the normalized relaxation functions in panel (b) is given in the text, while more details are reported in Section 10.4.1.

From a linear response perspective, the system's response to temperature changes of different magnitudes ΔT should be identical up to some scaling factor $\propto \Delta T$. By contrast, it is commonly found that the system's relaxation towards equilibrium during physical aging differs strongly for temperature jumps of different magnitude, which indicates that physical aging is a highly non-linear phenomenon [36, 37, 242, 245]. This fact is illustrated in Fig. 8.1b, where the time evolution of the imaginary part of the complex dielectric permittivity at 10 kHz, $\varepsilon''(t) \equiv \varepsilon''(t, \nu = 10\,\text{kHz})$ of supercooled 1-phenyl-1-propanol after various different temperature up- and down- jumps to 193 K is presented in terms of the normalized relaxation function [37]

$$R_\varepsilon(t) = \frac{\varepsilon''(t) - \varepsilon''(t \to \infty)}{\varepsilon''(t=0) - \varepsilon''(t \to \infty)}. \tag{8.1}$$

Here, the normalization with regard to the equilibrium values of $\varepsilon''(t)$ before the temperature jump at $t = 0$ and after complete equilibration at $t \to \infty$, $\varepsilon''(t=0)$ and $\varepsilon''(t \to \infty)$, eliminates the trivial scaling factor. Vastly different relaxation behaviors are observed for different temperature jump amplitudes ranging from +4 K to -4 K: The relaxation after down-jumps is visibly more stretched and faster compared to up-jumps. The degree of deviation between up- and down-jump data increases with increasing amplitude of the jumps.

A qualitative explanation of these observations is obtained by considering how the average relaxation rates of the system changes during aging. After a down-jump, the relaxation rate decreases as a function of t, or, as expressed by Kovacs, the jump is "auto retarded" [235], leading to a stretched relaxation towards equilibrium. By contrast, up-jumps are "auto accelerated", thus leading to a slow and compressed relaxation shape.

Narayanaswamy [38] expressed this qualitative idea in terms of a quantitative model by introducing the concept of *material time* $\xi(t)$, which is defined in terms of its clock rate $\gamma(t)$ as

$$\mathrm{d}\xi(t) = \gamma(t)\,\mathrm{d}t. \tag{8.2}$$

$\xi(t)$ can be thought of as measure of time, the clock rate of which itself ages during the aging of the material. The time-dependence of the material-time clock rate $\gamma(t)$ reflects the fact that the system's relaxation rate changes during aging.

The fundamental idea of Narayanaswamy was that the non-linear change of some physical property $X(t)$ is linearized, once it is considered in terms of the material time $\xi(t)$ instead of the conventional time t. That is, for a temperature protocol ending in equilibrium at T_∞, where $X(t \to \infty) = X_\infty$, the change $\Delta X(t) = X(t) - X_\infty$ during physical aging after temperature history $T(t) = T_\infty - \Delta T(t)$ can be expressed in terms of a linear response equation [12, 38]

$$\Delta X(\xi) = C\Delta T(\xi) + \int_{-\infty}^{\xi} M_X(\xi - \xi') \frac{\mathrm{d}\Delta T(\xi')}{\mathrm{d}\xi'} \mathrm{d}\xi'. \tag{8.3}$$

Here, the first term reflects an instantaneous aging contribution, while the second term describes the slow relaxation part that is expressed in terms of a linear convolution integral with a system-specific memory kernel M_X, which importantly is independent of the temperature protocol. For instantaneous temperature jumps at $t = 0$ like discussed above, the second term of Eq. (8.3) yields $\Delta X(\xi) = \Delta T \cdot M_X(\xi(t))$, i.e. the system's response after temperature jumps of different magnitudes as a function of ξ is identical up to a scaling factor. Thus, the material-time concept suggests that the variation of the system's relaxation rate during aging is the only reason for aging being non-linear. More details regarding the material-time concept and its validity will be discussed in Section 10.1.

One major problem for the material-time concept has been that $\xi(t)$ itself has not yet been determined experimentally. An experimental approach would require to probe the structural relaxation within the aging sample *with time-resolution*. This has been an impossible task for almost all experimental techniques, because they require some sort of temporal averaging to obtain these information: In order to probe structural relaxation with average relaxation time τ, these measurements have to average over a multiple of τ. As physical aging of molecular glasses after a temperature jump to T_∞ proceeds on time scales of the order of $\tau(T_\infty)$, any technique requiring substantial temporal averaging is not suitable to approach an experimental determination of the material time.

Multispeckle dynamic light-scattering, however, represents one of the very few experimental techniques that can probe a material's structural relaxation without requiring any temporal averaging. The basic idea is to replace the temporal average by an average over various speckles, i.e. the light and dark spots in the granular interference pattern produced by the light scattered from an aging sample. To utilize the unique advantages multispeckle dynamic light-scattering provides for the experimental investigation of physically aging materials, a respective setup has been built during this work, see Chapter 9. The probed time-resolved intensity autocorrelation functions of the scattered light allow to experimentally determine the material time as a function of t, see Chapter 10. The results allowed to verify the conjecture whether thermal fluctuations of aging materials become statistically time-reversible if they are considered in terms of the material time, see Chapter 11.

9

MULTISPECKLE DDLS EXPERIMENT FOR THE INVESTIGATION OF AGING SAMPLES

The fundamentals of conventional DLS experiments were covered in Section 2.2. In particular, it was discussed that a PCS experiment probes the intensity fluctuations within a single speckle and extensive time-averaging is required to obtain the intensity autocorrelation function $g_2(\Delta t)$ from which the electric field autocorroelation function $g_1(\Delta t)$ can be calculated using the Siegert relation (Eq. (2.23)). In order for $g_1(\Delta t)$ to correctly reflect the microscopic dynamics of the studied sample, significant requirements need to be met: (i) The dynamics needs to be stationary. Due to the temporal averaging, any time-dependence of the dynamics is not considered and, instead, $g_1(\Delta t)$ reflects some average of the time-dependent dynamics. (ii) The sample has to be ergodic on the time scale of the experiment. Erdodicity is the formal requirement for the the temporal averaging to be equivalent to the ensemble average.[246] Many systems in soft matter physics do not fulfill one or both of these requirements. Molecular and colloidal glasses, as well as gels or foams are off-equilibrium systems, thus they behave in a non-stationary manner. For instance, the structural relaxation of a physically aging sample is explicitly time-dependent, thus its analysis requires proper two-time correlation functions, $g_1(t, t+\Delta t)$. In addition, these systems relax on time scales exceeding hours, days or even weeks. Exploring the entire phase space by monitoring a single speckle would require a multiple of these time scales, implying that, within reasonable experimental time scales, glasses and gels usually are non-ergodic when intensity fluctuations are probed within a single speckle.

One solution to these fundamental issues is to no longer limit the experiment to probing a single speckle, but to instead perform a *multispeckle* DLS (msDLS) experiment. These experiments have been introduced in the early nineties [247], using the new CCD technology, and have been improved ever-since alongside advances in imaging technology. Two general approaches can be distinguished: On the one hand, the camera can be positioned in transmission geometry, which allows to study a broad range of different q-vectors at the same time [248, 249]. The second approach, which is the one pursued and discussed in this work, is to study a multitude of speckles at approximately the same q. This procedure allows to replace the temporal average in Eq. (2.22) by a speckle, res. pixel average $\langle ... \rangle_{\mathrm{px}}$,

$$g_2(t, t+\Delta t) = \frac{\left\langle I(t)\, I(t+\Delta t)\right\rangle_{\mathrm{px}}}{\langle I(t)\rangle_{\mathrm{px}} \langle I(t+\Delta t)\rangle_{\mathrm{px}}}. \tag{9.1}$$

The multispeckle approach allows to determine *time-resolved* intensity autocorrelations in samples with dynamics that change as a function of time, e.g. due to physical aging. Over the years various adaptations of the msDLS concept have been developed for various applications in soft matter physics. A brief review of the most important aspects is given in the following.

Especially in the earlier years after the concept was first introduced in 1993, msDLS was limited to the study of ultra-slow dynamics in stationary systems [247, 250, 251], because

the number of speckles that could be probed at once was limited. Here, the idea is to combine temporal- and speckle-averaging to considerably reduce the required measuring time compared to when only a single speckle would be probed in conventional DLS.

Time-resolved correlations became accessible in the earlier 2000s [252–254] and allowed to study various different systems that evolve as a function of time, e.g., aging gels [249, 253–255] and coarsening foams [256–259]. Most of these experiments employ diffusing wave spectroscopy (DWS), i.e. the detected light has been scattered many times within the sample. Recurring observations have been intermittent relaxation events in the form of abrupt loss of intensity correlation [253, 254, 259, 260], which has been associated with rare long-ranged events, e.g. local restructuring in gels [253, 260] and bubble-rearrangements in foams [259]. Moreover, msDLS has been used to study the long-ranged spatial dynamic heterogeneity in foams or gels by considering the temporal fluctuations of time-resolved correlations [256, 257].

Physical aging dynamics of glassy systems probed by means of msDLS have rarely been reported. Noteworthy from the perspective of the present work are the experiments by Viasnoff et al. [261], who investigated the physical aging of a colloidal glass under shear after the shear strain was suddenly turned off. The time-resolved intensity autocorrelations probed by means of multispeckle DWS revealed a continuous slow-down of the colloidal dynamics without the occurrence of any intermittent events.

Various imaging optics can be used to perform msDLS experiments. In the simplest case, a single aperture is sufficient to observe a speckle pattern on a camera chip. In such an approach, light from the entire scattering volume contributes to each speckle. [251] On the other hand, an imaging lens can be adjusted to introduce spatial resolution, in the sense that light detected around a certain position within the speckle pattern originates from some limited spatial subregion of the scattering volume [252, 259]. Such approaches have been referred to as *photon correlation imaging* [259] and allow, e.g., to detect long-range spatial dynamic heterogeneity in foams or gels. In recent years, the concept of photon correlation imaging has been adapted and developed in order to study various different applications, e.g. to investigate material failure [262], local displacement [263] or the yielding transition [264, 265] in materials under mechanical strain or shear. But also more complex approaches exist, e.g., using two lasers and two cameras to perform dynamic speckle holography, in order to obtain a 3d characterization of the flow in a tube [266]. Although the present work focuses on the aging of molecular glasses and does not utilize any spatial resolution, it also employs a photon correlation imaging-like setup, as the latter provides several advantages that will be discussed in the following sections.

Finally, it remains to be noted that msDLS shares several similarities with x-ray photon correlation spectroscopy (XPCS) experiments. In the latter, the speckle pattern formed by x-ray photons scattered from a sample is probed at various different q-vectors. As a consequence, XPCS also allows to determine time-resolved intensity autocorrelations via multispeckle averaging, which was employed to investigate, e.g., the microscopic dynamics during physical aging of metallic glasses. [267–270]

9.1 OPTICAL IMPLEMENTATION

Considering the purpose of studying aging samples of molecular and colloidal glasses, three key requirements can be defined: (i) A high temporal resolution is required. Molecular glasses age on time scales similar to the characteristic time scale of structural relaxation. Thus, substantial changes of the autocorrelations as a function of t proceed on time scales comparable to the decay of the autocorrelations as a function of Δt. Consequently, no substantial tem-

poral averaging should be required to obtain well-resolved autocorrelation functions. This condition can be fulfilled by detecting a large number of speckles, which provides sufficiently large statistical power without requiring any temporal averaging. (ii) Physical aging is best studied at low temperatures where it takes long times for samples to reach a new equilibrium state. Thus, it is necessary to perform long-time measurements over several hours or even days. At the same time, the hard-drive space required for data storage cannot be impractically large. (iii) The intensities scattered from molecular glasses are usually quite low compared to the systems that have been studied in msDLS traditionally, like gels, colloids and foams. Thus, the performance of the setup in this regard needs to be optimized.

Considering points (i) and (ii) defines one key requirement: The size of a single speckle has to be small, such that a comparably small image allows to probe a large number of speckles. At the same time, the average speckle-size should not subceed the size of single pixels, as otherwise many speckles would be probed within a single pixel, which implies substantial loss of information. By performing a photon correlation imaging experiment, the speckle size can easily be controlled by adjusting the imaging optics, which is the reason why such a procedure was utilized within the present work. A photon correlation imaging approach also helps to solve point (iii): The fact that light probed within one speckle originates from some spatially limited area within the sample cell allows to selectively analyze only the light scattered from the sample. Thus, undesired light, e.g. the light scattered from the walls of the sample cell or from any impurities within the sample can be disregarded. If instead a msDLS approach without any spatial resolution would be employed, each speckle would reflect a superposition of light from all the mentioned sources. This would be especially problematic in case the intensity of light scattered from the sample is significantly lower than the intensity of undesired light, which is the case for many molecular glasses.

Fig. 9.1a presents a schematic illustration of the optical setup. All parts positioned between laser and sample cell are identical to setup used for conventional PCS measurements as explained in Section 2.2.2 and, thus, are not discussed herein. Two different sample cells are used for experiments on supercooled liquids and glasses. Both are based on a borosilicate glass tube with 10 mm res. 20 mm outer diameter and 1 mm res. 2 mm wall thickness and will be discussed in further detail in Section 9.3. Scattered light is collected at 90° angle by a home-built imaging optics, a photo and an illustration including dimensions of which is shown in Fig. 9.1. First, the scattered light passes a combination of a spherical and a slit aperture, the size of which can be adjusted. The f =5 cm spherical convex imaging lens is positioned at a distance of 7 cm from the scattering volume. Behind the lens, a second slit aperture of adjustable width is positioned at the focal point of the spherical lens. Afterwards, light passes another Glan-Thompson polarizer from B. Halle (extinction ration 10^{-7}, 12 mm diameter) that can be operated in vertical or horizontal mode, and a 532±2 nm bandpass filter. Finally, the speckle pattern is recorded using a Hamamatsu ORCA-Flash 4.0 V2 SCMOS camera sitting at a distance of 10 cm behind the spherical lens. The camera is equipped with a 2048 px x 2048 px image sensor (the size of single pixels is 6.5 µm x 6.5 µm) and can process a maximum of 100 images per second.

9.2 SPECKLE PATTERNS

Using the optical setup shown in Fig. 9.1 allows to record speckle patterns of various disordered materials, as long as their respective structural relaxation dynamics exceed the minimum temporal resolution of 0.01 s. In the following sections, the static and dynamic properties of

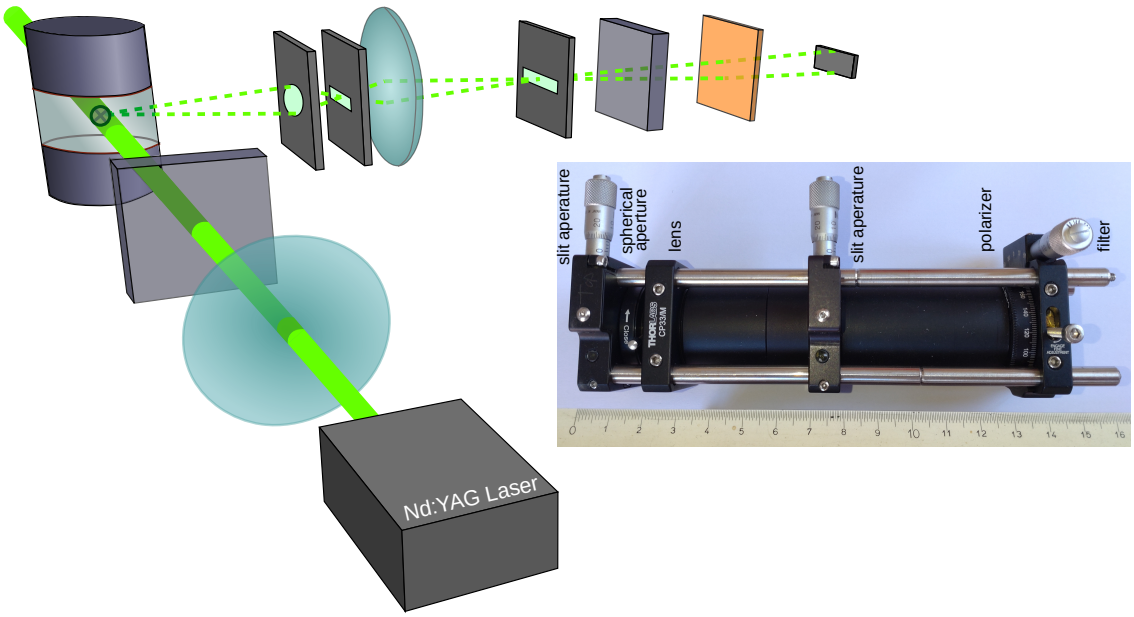

Figure 9.1: Schematic illustration of the optical setup used for the multispeckle detection of scattered light and photo of the imaging optics.

an exemplary movie of speckle images recorded for an equilibrium supercooled sample of 1-phenyl-1-propanol (1P1P) is discussed.

9.2.1 Static properties

An exemplary speckle pattern obtained for the depolarized light scattered from an equilibrium sample of 1P1P closely above T_g is shown in Fig. 9.2a. Due to using an imaging optic, the camera probes a real-space image of the laser beam: A horizontal stripe with a Gaussian intensity profile, as shown in Fig. 9.2b. The imaging setup allows to only use ~6% of the full 2048 x 2048 pixel sensor, while an optical setup based on a single aperture would illuminate the entire chip and each speckle would be significantly larger.

To analyze the spatial dimension of speckles, the average spatial autocorrelation functions [252] of intensity fluctuations $\delta I(x,y,t) = I(x,y,t) - \langle I(x,y)\rangle_t$ are obtained as

$$C(\Delta x) = \frac{\left\langle \delta I(x,y,t)\cdot \delta I(x+\Delta x,y,t)\right\rangle_{x,y,t}}{\sqrt{\left\langle \delta I(x,y,t)^2\right\rangle_{x,y,t}\cdot\left\langle \delta I(x+\Delta x,y,t)^2\right\rangle_{x,y,t}}}. \tag{9.2}$$

Here, $I(x,y,t)$ is the intensity probed at pixel coordinate (x,y) at time t, the angular brackets $\langle ...\rangle_{x,y,t}$ indicate averages over different pixels of the speckle image along x and y-direction as well as temporal averaging over numerous frames of a speckle movie. $\langle I(x,y)\rangle_t$ was determined via temporal averaging of the probed intensities, while at the same time the symmetry of the speckle pattern along the x direction was utilized, i.e. the fact that $\langle I(x_1,y)\rangle_t = \langle I(x_2,y)\rangle_t$ for any x_1, x_2. An procedure equivalent to Eq. (9.2), but along the y-direction yields $C(\Delta y)$.

$C(\Delta x)$ and $C(\Delta y)$ are shown in panels (d) and (e) of Fig. 9.2, respectively. In both cases, a maximum is observed at $\Delta x = 0$, res. $\Delta y = 0$, while the spatial autocorrelations quickly decay to zero for increasing $|\Delta x|$, res. $|\Delta y|$, because adjacent speckles are statistically independent. $C(\Delta x)$ and $C(\Delta y)$ are well-described by Lorentzians (solid black lines), which allows to define the full widths at half maximum w_x and w_y (red lines). w_x and w_y can be interpreted as the

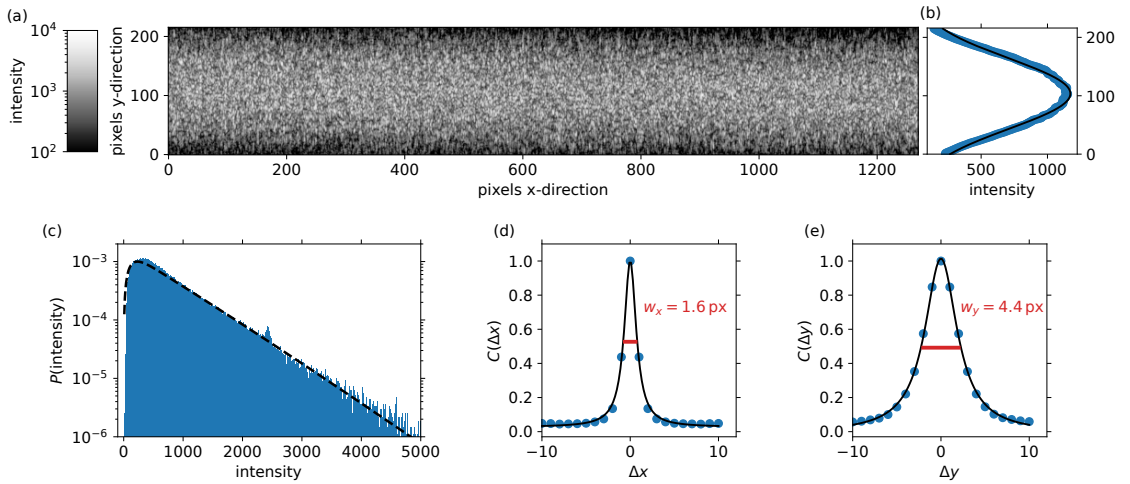

Figure 9.2: Analysis of the static structure of speckle patterns. (a) Exemplary intensity speckle pattern reflecting the depolarized scattered light from an equilibrium sample of 1P1P closely above T_g. The colors indicate the intensity on a logarithmic scale; see colorbar on the left hand side. (b) Along the y-direction, the average intensities follow a Gaussian envelope (solid black line), reflecting the Gaussian beam profile. (c) Probability distribution of speckle intensities. The experimentally probed distribution corresponds well to an approximation of the theoretical prediction for a speckle pattern probed using a finite aperture and a limited spatial resolution (pixels), i.e. Eq. (9.3) as the black dashed line. Eq. (9.3) considers a uniform distribution of average intensities, thus the Gaussian intensity profile was considered, leading to some additional broadening compared to Eq. (9.3). (c),(d) Average spatial intensity autocorrelations $C(\Delta x)$ and $C(\Delta y)$ as functions of Δx and Δy, respectively, obtained via Eq. (9.2). Both are well described by Lorentzians (solid black lines), from which the full widths at half maximum w_x and w_y are extracted (red lines).

average size of the speckles along the x and y-direction in units of pixels (px), respectively. It is found that speckles are elliptically shaped ($w_x \neq w_y$), which is a direct consequence of using a spherical lens to image an elongated scattering volume. Along the x-direction, the average size of a single speckle corresponds to w_x =1.6 px, thus almost the minimal feasible speckle-size is probed. This implies a certain degree of overlap between adjacent speckles. Such effects lead to a reduction of the $\Delta t = 0$-limit of the intensity autocorrelation functions $g_2(t, t+\Delta t)$ as is discussed in Section 9.2.2 below.

The probability distribution of pixel intensities is shown in Fig. 9.2c, revealing an asymmetric distribution with a maximum at $I_0 > 0$. Considering the theoretical treatment of speckle images [271],

$$P(I) = \frac{\left(\frac{m}{I_0}\right)^m I^{m-1} \exp\left(-\frac{mI}{I_0}\right)}{\Gamma(m)} \tag{9.3}$$

is an approximation of the expected probability density of speckle intensities. It considers that the speckle pattern is probed using a limited spatial resolution (pixels), or involves some degree of speckle blurring due to a finite size aperture. Both effects combined are described by the parameter m, which is unity if both are negligible. The dashed black line represents a fit to the data with $m = 2$, where on top the effect of the Gaussian envelope (cf. panel b) is considered, which is not yet taken into account in Eq. (9.3), as it assumes a uniform intensity distribution.

9.2.2 Intensity autocorrelation functions

The dynamics of a movie of speckle images can be quantified in terms of the normalized intensity time autocorrelation function $g_2(t, t+\Delta t)$ that is obtained as a multispeckle/multi-pixel average. Again, the horizontal symmetry of the speckle pattern, $\langle I(x_1, y)\rangle_t = \langle I(x_2, y)\rangle_t$ for any x_1, x_2, is utilized. The symmetry implies that the normalization of the intensity autocorrelation functions is identical for pixels with the same y-coordinates. Thus, the averages along x- and y-direction are calculated independently, which yields

$$g_2(t, t+\Delta t) = \frac{n_x}{n_y} \sum_{y=1}^{n_y} \left[\frac{\sum_{x=1}^{n_x} I(x, y, t) \cdot I(x, y, t+\Delta t)}{\left(\sum_{x=1}^{n_x} I(x, y, t)\right)\left(\sum_{x=1}^{n_x} I(x, y, t+\Delta t)\right)} \right], \tag{9.4}$$

where n_x and n_y denote the number of pixels along the x and y-direction, respectively.

Time-resolved intensity autocorrelation functions $g_2(t, t+\Delta t)$ as a function of Δt are plotted in Fig. 9.3a. The different colors indicate different t. All curves approximately collapse, reflecting that equilibrium dynamics in supercooled liquids is stationary. Thus, the time-averaged intensity autocorrelation function $g_2(\Delta t)$, included as the dashed black line, represents a meaningful description of the stationary dynamics. Slight deviations of the individual time-resolved autocorrelation functions from the average behavior are observed. They reflect an inevitable consequence of probing a finite number of speckles. The main source for these deviations is the imperfect normalization of Eq. (9.4). Thus, the autocorrelation value at short Δt, $g_2^0(t) = \lim_{\Delta t \to 0} g_2(t, t+\Delta)$, is distributed. This fact is visualized in the inset of Fig. 9.3a, showing a zoom into the main panel to illustrate deviations from perfect collapse at short Δt. The dashed gray curve represents the distribution of $g_2^0(t)$ with standard deviation $\Delta g_2^0 = 0.004$, which corresponds to well below 1% deviation from the average. It is noted that performing the same experiments with variations of the imaging optics that result in larger average speckle sizes, i.e. a smaller total number of probed speckles, yields a significantly broader distribution of $g_2^0(t)$. In fact, the distribution's width was minimized during the process of optimize the performance of the imaging optics.

In Fig. 9.3b, the time-averaged intensity autocorrelation function obtained from the multispeckle experiment is compared to the corresponding results from a conventional single-speckle DLS experiment employing an optical fiber optics. Both results are obtained from the same sample, in the same sample environment and at the same temperature. Proper singlespeckle data could only be obtained, because the sample is in equilibrium and at a comparably high temperature, thus dynamics are comparably fast (up to a factor 10^3 faster than in typical aging experiments). It has to be noted, however, that the single-speckle data had to be averaged over 24 h of measurement, while proper multispeckle data could be obtained after the time that it takes for the autocorrelations to decay to zero, i.e. after ~ 100 s. Obviously, the fiber-optical experiment outperforms the multispeckle approach considerably in regards of providing information at short Δt. In addition, the short-Δt limit of the intensity autocorrelations g_2^0 is significantly smaller for the camera-data compared to the fiber-data; the physical origin of this will be discussed below. Apart from that, both experiments provide the same information, as confirmed from the fits to the data (solid black lines) using

$$g_2(\Delta t) - 1 = (g_2^0 - g_2^\infty) \cdot \phi(\Delta t) + g_2^\infty, \tag{9.5}$$

where g_2^∞ is the $\Delta t \to \infty$-limit of $g_2(\Delta t) - 1$, while $\phi(\Delta t)$ is a normalized relaxation function describing the correlation decay of the supercooled liquid, which in this particular case

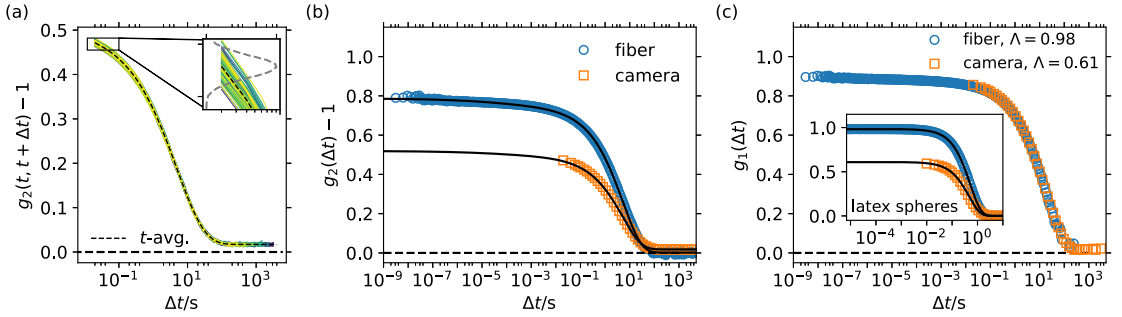

Figure 9.3: Analysis of the intensity and electric-field autocorrelation functions probed using the camera setup. (a) Time-resolved intensity autocorrelations $g_2(t, t+\Delta t)$ of an equilibrium sample of 1P1P. The different colors indicate data obtained at different t, whereas the black dashed line represents the temporal average $g_2(\Delta t) \equiv \langle g_2(t, t+\Delta t)\rangle_t$. The inset shows a zoom into the short-time part of the main panel, revealing that the short-time limit of $g_2(t, t+\Delta t)$, $g_2^0(t)$, is distributed reflecting the finite number of speckles used to normalize the $g_2(t, t+\Delta t)$. The distribution of $g_2^0(t)$-values is shown as the gray dashed line. (b) Comparison of $g_2(\Delta t)$ obtained from measurements using an optical fiber probing a single speckle (blue symbols) and the camera (orange symbols). The solid black lines represent fits by Eq. (9.5), assuming the same relaxation function, but different short and long-time limits for fiber and camera data. (c) The inset shows fiber and camera data obtained for strongly diluted polystyrene spheres dissolved in glycerol. From the short-time plateau, the coherence factor Λ can be determined, which yields $\Lambda_{\text{fiber}} = 0.98$ and $\Lambda_{\text{cam}} = 0.61$. Inserting the respective values into the Siegert relation, Eq. (9.7), and disregarding any heterodyning yields $g_2(\Delta t)$-data of 1P1P for fiber and camera that perfectly overlap (see main panel).

was modeled using a GG distribution of relaxation times for the α-process plus a fast β-process contribution. Both data sets are described using the same relaxation function $\phi(\Delta t)$, the only difference being the choices of values for g_2^0 and g_2^∞.

The significant difference between g_2^0-values observed for fiber and camera data mainly reflects the different speckle selectivities of both techniques, meaning the two experiments are associated with different coherence factors Λ. Generally, g_2^0 is reduced as soon as light from more than one coherence area within the sample is detected, i.e. when the the light probed within the detector area corresponds to more than one speckle. Otherwise, the amplitude of the probed intensity fluctuations decreases compared to the case, where only light from a single speckle is considered.

A direct analysis of this effect based on $g_2(\Delta t)$-data obtained from a supercooled liquid, however, is not straightforward, as two other effects can (potentially) lead to a reduction of g_2^0 below unity. First, molecular dynamics on faster time scales than probed by the detector lead to some unresolved decay of $g_2(\Delta t)$. These contributions could be estimated using high-frequency DLS experiments, e.g. Tandem Fabry-Perot interferometry. Second, detected light that was not scattered from the sample, but, instead, stems from reflections from the sample environment introduces some degree of heterodyning and can reduce g_2^0.

Instead, coherence effects can be isolated by studying the polarized scattered light from a strongly diluted colloidal suspension. Such a system does not show any fast relaxation processes, but only a single exponential decay, the time scale of which depends on the hydrodynamic radius of the colloidal particles and the viscosity of the solvent. Moreover, the very large intensity of the light scattered by the colloidal particles allows to neglect any heterodyning effects, thus for a suitable colloidal suspension $\Lambda = g_2^0$. It has to be noted that the geometry of speckles only depends on the imaging optics and the intensity profile of the laser

beam. Thus, the coherence effects determined from experiments on a colloidal suspension can be assumed to be the same as for any other sample.

The inset of Fig. 9.3c reports $g_2(\Delta t)$-data obtained for 5.5 µm-sized polystyrene particles dissolved in glycerol. The black lines represent fits to the data by the expression

$$g_2(\Delta t) - 1 = \Lambda \cdot \exp\left(-\frac{\Delta t}{\tau}\right), \tag{9.6}$$

which yields $\Lambda_{\text{fiber}} = 0.98$ and $\Lambda_{\text{cam}} = 0.61$. The fact that $\Lambda_{\text{cam}} < \Lambda_{\text{fiber}}$ is no surprise, as an optical fiber has a very strong angle selectivity regarding the transmitted light and, thus, is well suited to obtain Λ-values close to unity. On the other hand, the camera setup has been optimized to achieve small speckle-sizes, which necessarily implies a certain degree of overlap between adjacent speckles and, thus, $\Lambda_{\text{cam}} < 1$.

In a final step it will be shown that, apart from the different coherence factors Λ_{cam} and Λ_{fiber}, the information contained in the autocorrelations probed by both techniques are in fact identical. For this to be the case, the respective electric-field autocorrelations $g_1(\Delta t)$ need to be identical. As discussed in Section 2.2.2, in the most general case, $g_1(\Delta t)$ is related to $g_2(\Delta t)$ as

$$g_2(\Delta t) = \Lambda C^2 g_1(\Delta t)^2 + 2\Lambda C(1-C) g_1(\Delta t) + 1, \tag{9.7}$$

where $C = \langle I_s \rangle / \langle I \rangle$ is the relative intensity of light scattered from the sample and quantifies the degree of heterodyning. For simplicity and because the depolarized scattered intensity of 1P1P is very large, $C_{\text{fiber}} = C_{\text{camera}} = 1$ is assumed. The resulting $g_1(\Delta t)$-data are shown in Fig. 9.3c, where a perfect collapse of fiber and camera data is observed. In addition it is found that the short-time value of the $g_1(\Delta t)$ fiber data corresponds well to the strength of fast dynamics $A_{\text{fast}} \approx 0.13$ estimated from TFPI measurements of 1P1P. This concordance indicates that, most likely, the choice of $C \approx 1$ is justified. It has to be noted, however, that for supercooled liquids with a lower depolarized scattering intensity most likely $C_{\text{camera}} < 1$ has to be chosen in order to collapse $g_1(\Delta t)$-data obtained from fiber- and camera experiments. For 1P1P, however, the collapse of camera and fiber data confirms the consistency of the different DDLS techniques and establishes multispeckle-DDLS as a suitable tool to reliably probe the electric field autocorrelation function $g_1(\Delta t)$ of molecular supercooled liquids and glasses.

9.3 SAMPLE CELLS AND TEMPERATURE CONTROL

Performing physical aging experiments requires to quickly change the sample temperature to a new annealing temperature T_∞. "Quick" in this context means that the variation of the temperature should be much faster than the glass' response to the temperature change. This implies that physical aging can also be studied in a controlled manner in case the temperature change is rather slow, as long as the experiments are performed at sufficiently low temperatures such that the response of the system is even slower. The downside of performing aging experiments at such low temperatures is that also the time required for the system to approach the new equilibrium state becomes very long, i.e. several days or weeks. Consequently, minimizing the time required for changing the temperature of DLS sample cells has been an important task within this work. For the data discussed in the following sections, two sample cells and corresponding temperature-control systems were used: During the first year, aging experiments were performed using an adapted version of an aluminum sample cell, which was originally designed for equilibrium measurements. Here, temperature changes were performed by using an optimized protocol that involves varying the heating current of

the cold-finger cryostat's internal heater at large liquid-nitrogen (LN_2) fluxes. The sample-cell design, as well as the temperature-protocol optimization are discussed in Section 9.3.1. Subsequently, an optimized sample cell for aging experiments was designed, see Section 9.3.2. The optimization involved reducing the size of the previously used sample cell and implementing a Peltier element to allow faster and more precise changes of the sample temperature.

9.3.1 LN_2-controlled sample cell

An illustration of the LN_2- controlled sample cell is shown in Fig. 9.4a. It was originally design by Jan P. Gabriel and is optimized for the investigation of equilibrium supercooled-liquid samples at cryogenic temperatures within an optical Cryovac cold-finger cryostat. Two aspects of the sample cell are optimized in order to reduce the thermal lag between the cold-finger cryostat's heat exchanger and the (supercooled) liquid sample: (i) All parts of the cell, apart from windows and O-rings, are made from aluminum in order to increase the thermal conductivity and to reduce the overall weight of the sample cell. (ii) The aluminum body, consisting of a tube with cavities for optical access in all four directions, passes directly through the liquid sample. The scattering volume is positioned within the tube, thus its distance from the aluminum surfaces is small.

The sample cell is tightened by firmly pressing a Suprasil glass tube (outer diameter 20 mm, wall thickness 2 mm) between a pair of Viton O-rings (thickness 2 mm) via an aluminum ring equipped with an inner thread. Finally, the inner channel of the aluminum body is sealed by a lid and another Viton O-ring. All aluminum parts of the cell are anodized, giving them a matt black surface to reduce the reflection of laser light. To avoid large temperature gradients due to heat input in terms of thermal radiation, the sample cell is surrounded by a gold-plated heat shield coupled to the cold-finger.

When operated in equilibrium-mode, the sample cell achieves high temperature-stability below ±0.01 K. However, despite the implemented optimizations compared to standard DLS sample cells, simply changing the sample temperature from T_0 to T_∞ is rather slow and can take several thousand seconds. Thus, in order to perform physical aging experiments, some optimizations had to be implement during the present work. One first step involved introducing ways of monitoring the sample temperature. Priorly, this could only be done independently from DLS measurements by using an alternative lid equipped with a PT-100 temperature sensor, which could be placed inside the liquid close to the scattering volume. While this procedure allows to precisely monitor the sample temperature, the PT-100 sensor interferes with the laser light, thus probing the sample temperature during DLS measurements was impossible. To solve this issue, another PT-100 temperature sensor was glued inside a drilled channel within the bottom of the aluminum sample cell. Thermal contact between sensor and sample cell was ensured by using thermally conducting epoxy glue (Loctite Stycast 2850FT with hardener CAT 23LV). It was confirmed that the change of temperature probed by the bottom sensor corresponds to the one determined within the supercooled liquid, thus allowing to probe a representation of the sample temperature during DLS measurements.

After having established a procedure to reliably probe the sample temperature, the cooling protocol was optimized to achieve faster temperature down-jumps from T_0 to T_∞. As a first measure, the LN_2-flow through the cold-finger cryostat was increased considerably by setting the nitrogen-pump pressure up to 0.5 bar instead of 0.1 to 0.2 bar typically used for equilibrium measurements. Moreover, instead of simply changing the heat-exchanger settings to T_∞, the basic idea is to cool the heat exchanger below T_∞, i.e. to $T_\infty - \Delta T$. Subsequently the sample is heated back towards T_∞ with constant heating rate h_1 and after some time t_0 the

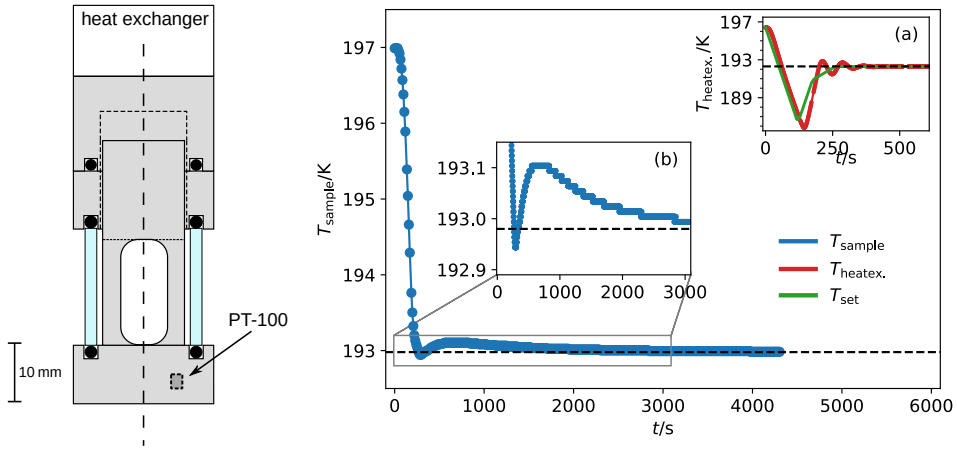

Figure 9.4: Left side: Design of the LN_2-controlled sample cell. See text for details. Right side: Time-evolution of the sample temperature after an optimized down-jump protocol. The main panel shows the sample temperature measured using a PT-100 temperature sensor installed at the bottom of the cell (blue symbols). It was previously shown to reliably reflect the temperature of the supercooled liquid sample, see text for details. Inset (a) shows the temperature of the heat exchanger (red line) and the current set-temperature (green line). Inset (b) is a zoom into the gray rectangle shown in the main panel and illustrates the temperature-overshoot within the sample, which was optimized to be as small as possible.

heating rate is switched to h_2 until T_∞ is reached. This procedure temporarily enhances the temperature gradient between heat exchanger and sample cell, which increases the resulting heat flows. By optimizing the values of ΔT, t_0, h_1 and h_2 it is possible to cool the sample to T_∞ comparably quickly. This is illustrated in Fig. 9.4 for a temperature down-jump from T_0 =197 K to T_∞ =193 K. The main panel displays the sample temperature T_{sample} as a function of the elapsed time t after initiating the jump. T_∞ is reached after $t \approx 200$ s, without any considerable temperature over- or under-shoots as shown in inset (b). Inset (a) displays the temperatures of the heat exchanger T_{heatex} (red line), as well as the set-temperature of the heat exchanger T_{set} (green line) as a function of t. T_{heatex} temporarily reaches 186 K before it is heated back to 193 K. Similar protocols were optimized for temperature jumps of different magnitude. The corresponding aging-data obtained after applying these temperature protocols to the molecular glass 1P1P are discussed in Chapter 10.

9.3.2 Peltier-controlled sample cell

Despite the considerable effort invested into optimizing the performance of the LN_2-controlled sample cell, several issues remain: (i) Taking ~200 s, temperature jumps still are comparably slow. (ii) Operating the setup using large LN_2-flows leads to large LN_2-consumption, which in turn limits the maximum duration of experiments to around two days. (iii) The sample temperature sensitively depends on the LN_2-flow, which makes it almost impossible to perform two consecutive aging experiments ending at exactly the same T_∞. (iv) Optimizing ΔT, t_0, h_1 and h_2 is very time consuming, as it requires repeating temperature jumps several times, mostly because the optimal choice of parameters is different for jumps of different magnitude or to different T_∞ and has to be determined by trial-and-error. (v) The complex temperature protocol combined with jumps being comparably slow makes it difficult to define $t = 0$ of an aging experiment.

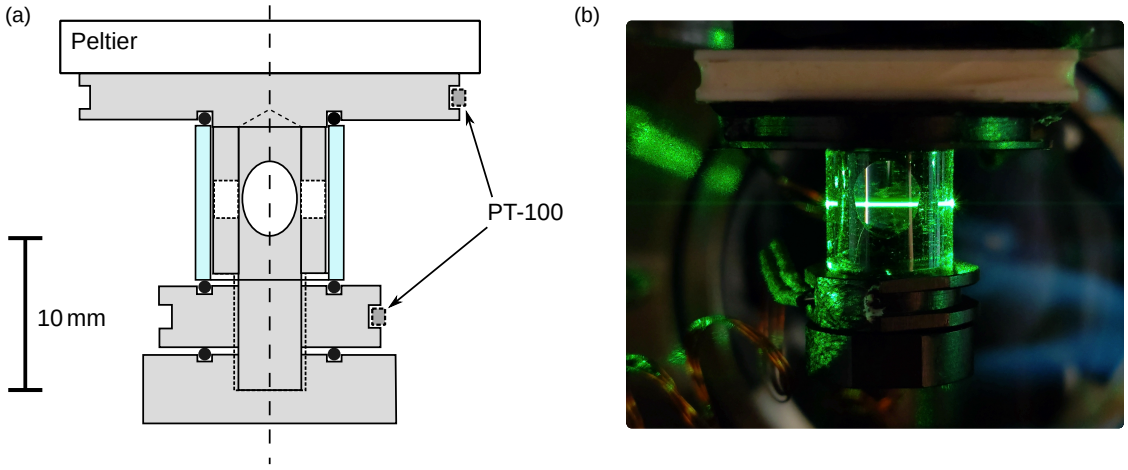

Figure 9.5: Design of the Peltier-controlled sample cell. (a) Construction sketch of the sample cell to scale. See text for details. (b) Photo of the sample cell in operation.

To resolve these issues, a new sample cell optimized for physical aging experiments was developed during the present work, which is illustrated in Fig. 9.5. It represents a downsized version of the LN_2-controlled cell, being approximately a factor five smaller, which is close to the smallest feasible design in order to maintain sufficient optical access and without introducing significant amounts of parasitic stray light. Another important limitation are the dimensions of the glass tube (here: outer diameter 10 mm, wall thickness 1 mm), as further downsizing would introduce significant lensing-effects and, moreover, would complicate the production of the corresponding glass tubes with polished edges. Another optimization compared to the LN_2-controlled cell is the fact that the orientation of the small cell is inverted, such that heat flows into or out-of the sample do not need to pass though any threads, the thermal conductivity of which typically is small compared to solid aluminum.

The most significant innovation, however, is the introduction of a Peltier element to control the sample temperature. The basic concept is adapted from two setups developed within the Glass and Time group at Roskilde university to perform aging experiments using dielectric spectroscopy and neutron scattering, see Refs. [37, 272]. The addition of the Peltier element introduces a "sub-cryostat", in the sense that it allows to change the temperature of a sub-system containing only the sample cell, while all other parts of the cryostat are kept at some constant temperature T_{base} via conventional LN_2-cooling. As the sub-system is much smaller than the entire cold-finger cryostat, its thermal inertia is significantly lower, thus allowing for faster changes of temperatures. In addition, the reduction of the distance between heat bath and sample significantly reduces the thermal lag.

To ensure thermal contact between the Peltier element and the sample cell, as well as between the Peltier element and the cold-finger cryostat, it is glued in-between the two aluminum surfaces by applying a thin layer of Masterbond EP29LPSPAO-1 two-component epoxy glue, which is a thermally conducting epoxy able to withstand cryogenic shocks down to $T = 4$ K. In order to enhance the adhesion of the glue, the Al_2O_3-ceramic surface of the CUI Devices CP402533 Peltier element (25 mm x 25 mm, 4 A) was mechanically roughened by using a file. The Peltier element is controlled via the ± 10 V analog voltage output of a Lakeshore 335 temperature controller, the signal of which is fed into the Huginn Peltier-element driver [272]. The latter was developed and manufactured by the electronic workshop of the Glass and Time group at Roskilde university and supplies the dc current to drive the Peltier element. The

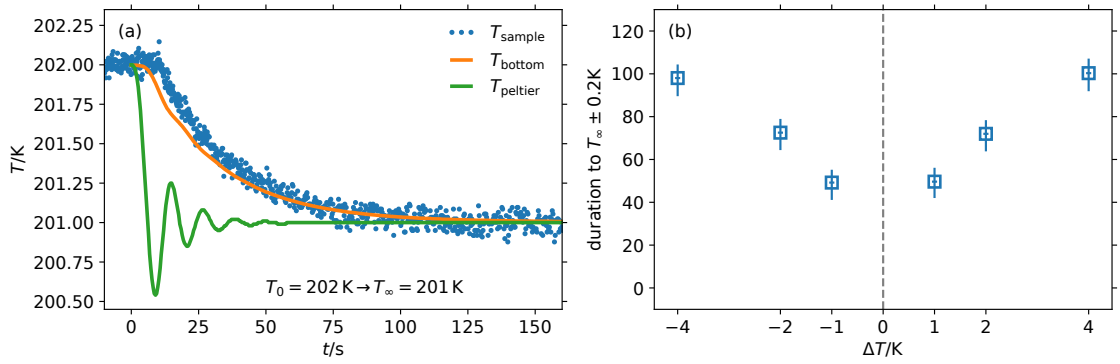

Figure 9.6: (a) Time-evolution of the temperatures probed within the sample cell after performing an instantaneous temperature change from $T_0 = 202\,K$ to $T_\infty = 201\,K$. The temperature probed right below the Peltier element, $T_{peltier}$ (green line), quickly equilibrates, while some thermal lag is observed at the bottom of the cell, T_{bottom} (orange line). Via probing the autocorrelations of the supercooled liquid sample, its temperature T_{sample} is estimated from the relaxation time $\tau(t)$ via Eq. (9.8) (blue symbols). It is found to correspond to T_{sample} in good approximation. (b) Time required for the sample to reach $T_\infty \pm 0.2\,K$ as a function of the temperature-jump amplitude ΔT.

temperature signal fed into the Lakeshore 335 is supplied by 1.2 mm x 1.6 mm sized PT-100 temperature sensor from IST Innovative Sensor Technology, which is glued into a groove carved into the aluminum body of the cell (upper PT-100 in Fig. 9.6). A second identical PT-100 is glued into the bottom part of the sample cell in order to monitor the current sample temperature.

Fig. 9.6a explores the evolution of the sample temperature after an instantaneous temperature jump from $T_0 = 202\,K$ to $T_\infty = 201\,K$ is performed via the Peltier element. Here, the base-temperature of the cold-finger cryostat was set to $T_{base} = 170\,K$ in order to compensate for the heat produced within the Peltier element. While the temperature directly below the Peltier element (green line) equilibrates in only a few seconds, some thermal lag is observed at the bottom of the cell (orange line). T_∞ is reached within approximately 50 s within $\pm 0.2\,K$ accuracy.

To ensure that the temperature probed at the bottom PT-100 sensor does represent the real sample temperature, the temperature of the supercooled-liquid sample was probed indirectly via its relaxation time τ. The procedure is the following: The temperature-range the temperature jump is performed in was chosen such that the equilibrium relaxation times $\tau_0 = \tau(T_0)$ and $\tau_\infty = \tau(T_\infty)$ of the supercooled liquid are as small as possible, while the autocorrelation functions can still be probed via the camera with exposure time 0.01 s. At these temperatures, the system's response to a temperature jump is almost instantaneous, i.e. it fully equilibrates in less than 10 s. Extracting the time-dependent relaxation time $\tau(t)$ as a function of the time t after the jump was initiated allows to indirectly determine the time-dependent sample temperature as

$$T_{sample}(t) = T_\infty + (T_0 - T_\infty)\frac{\log\tau(T) - \log\tau_\infty}{\log\tau_0 - \log\tau_\infty}. \tag{9.8}$$

Here, $\tau \propto \exp T$ is assumed to hold between T_0 and T_∞. $T_{sample}(t)$ is included in Fig. 9.6a as the blue symbols. The observed correspondence to T_{bottom} confirms that the PT-100 at the bottom of the sample cell can be considered to accurately represent the sample temperature. Fig. 9.6b shows the time required for the sample temperature to reach $T_\infty \pm 0.2\,K$ as a function

of the jump amplitude $\Delta T = T_\infty - T_0$. It was determined by repeating the experiment discussed above for different T_0 and T_∞. The required time increases sub-linearly with increasing $|\Delta T|$ and is significantly smaller than for temperature jumps using the LN_2-controlled sample cell. Moreover, the temperature-reproducibility is significantly smaller than 0.05 K, thus making it possible to perform several consecutive jumps to almost exactly the same T_∞. Data obtained using the Peltier-controlled sample cell are discussed in Chapter 12.

10

EXPERIMENTAL DETERMINATION OF THE MATERIAL TIME

The following chapter presents a procedure to experimentally determine the material time $\xi(t)$ from time-resolved intensity autocorrelation functions probed by msDDLS. In Section 10.1, the material time concept and related considerations are discussed in detail. This includes the TNM formalism that allows to obtain models to fit experimental data of, e.g., enthalpy relaxation, the single-parameter aging concept that incorporates the material time in terms of a differential equation, and finally, some general implications of the material time formalism for time autocorrelation functions. Based of the latter, as a first step it is shown in Section 10.2 that the msDDLS intensity autocorrelation functions obey the triangular relation, which suggests the existence of a material time. Subsequently, the procedure of how this material time can be extracted from the intensity autocorrelation functions is discussed in Section 10.3. In a final step, the validity of the determined material time is confirmed in Section 10.4, by showing that it, indeed, linearizes physical aging.

10.1 THE MATERIAL TIME CONCEPT

The material-time concept introduced by Naranayaswamy is phenomenological by postulating the existence of a material time that linearizes physical aging. Neither does it propose what the material time exactly is, nor does it suggest a direct procedure how the concept could be verified experimentally. In order to apply the concept to experimental data and verify its validity, several extensions have been derived, which will be discussed in the following sections. Probably the most famous one is the Tool-Naranayaswamy-Moynihan (TNM) model that combines concepts from all three authors in order to obtain a framework that can be applied, e.g., to model enthalpy relaxation probed in calorimetric experiments. It is also commonly used in industry to optimize the production of glassy materials. While it is very successful with regard to quantitatively describing physical aging, the insights it provides on the underlying physics are limited. By contrast, the single-parameter aging concept introduced by the Glass and time group represents a more direct way of verifying the material-time concept for the simplest case of physical aging, i.e. the relaxation from one equilibrium state to another after a small instantaneous temperature change. Finally, some general implications of the material-time formalism for time autocorrelations that are inherited from the equilibrium state are discussed, i.e. material-time translational invariance and the triangular relation. The latter was first introduced and discussed for the aging of spin glasses, but can also be applied to other physically aging systems.

10.1.1 The Tool-Narayanaswamy-Moynihan formalism

The TNM formalism combines concepts introduced by all three authors, i.e. the material-time concept [38], the concept of a fictive temperature T_f first introduced by Tool et al. in 1931 [273, 274], and additional relations further connecting both concepts by Moynihan [40]. The following discussion gives a brief overview of the TNM formalism. For more details it is referred to the excellent review by Hodge [39] that presents a detailed discussion of enthalpy relaxation in general and the TNM formalism in particular.

The fictive temperature is a concept to describe the structural state of a system subject to physical aging in terms of the temperature T_f at which the equilibrium supercooled liquid would have the same structure as the aging glass [41, 273, 274]. Thus, the difference between the actual physical temperature T and T_f quantifies the system's departure from equilibrium. As it turned out over the years, the idea that the microscopic structure of an aging system with fictive temperature T_f fully resembles the one of an equilibrium supercooled liquid at $T = T_\mathrm{f}$ is not really justified [39, 41]. Nevertheless, T_f remains a useful mathematical tool to quantify the departure of an aging system from equilibrium in terms of structure.

Combining the material-time and the fictive-temperature concepts yields the so-called Tool-Narayanaswamy (TN) formalism that considers T_f as a function of time in terms of a linear convolution integral,

$$T_\mathrm{f}(\xi) = T(\xi) - \int_{-\infty}^{\xi} M_{T_\mathrm{f}}(\xi - \xi') \frac{\mathrm{d}\,\Delta T(\xi')}{\mathrm{d}\,\xi'} \mathrm{d}\xi'. \tag{10.1}$$

Moreover, the material time is derived from the microscopic relaxation time that is assumed to be fully characterized by the physical and fictive temperature, i.e. $\tau(T, T_\mathrm{f})$, which yields

$$\xi(t) = \int_{-\infty}^{t} \tau\left[T(t'), T_\mathrm{f}(t')\right]^{-1} \mathrm{d}\,t' = \int_{-\infty}^{t} \left[A \exp\left(x \frac{\Delta H}{R\,T(t')} + (1-x)\frac{\Delta H}{R\,T_\mathrm{f}(t')}\right)\right]^{-1} \mathrm{d}\,t'. \tag{10.2}$$

Here, the definition of $\tau(T, T_\mathrm{f})$ first suggested by Narayanaswamy [38] and later refined by Moynihan [40] is considered in the third part of the equation. It introduces the non-linearity parameter x that interpolates between $\tau(T, T_\mathrm{f})$ being controlled solely by temperature T ($x = 1$) and solely by its structure, quantified by T_f ($x = 0$) [39, 41]. The prefactor A is a constant and H is the activation energy. Obviously, this relation inevitably fails for fragile systems, as it assumes a purely Arrhenian temperature, res. fictive-temperature dependence of the microscopic relaxation time. To solve this issue, it sometimes is adapted to resemble a VFT dependence [126]. Finally, the kernel M_{T_f} is usually described in terms of a stretched exponential (KWW) function with stretching exponent β.

A conceptually similar and mathematically equivalent formalism has been developed for enthalpy relaxation in polymer glasses in terms of the Kovacs-Aklonis-Hutchinson-Ramos (KAHR) model [275]. Both formalisms yield quantitative models that can, e.g, be used to fit calorimetric data around T_g via the various free parameters [39, 276]. Unfortunately, a general justification for the particular model used to describe $\tau(T, T_\mathrm{f})$, or at least an insightful physical interpretation of the non-linearity parameter x are lacking. In this regard, the TNM model could be considered as phenomenological fit model for the characterization of enthalpy relaxation in glassy materials.

10.1.2 Single-parameter aging

The single-parameter aging approach requires less assumptions and yields a differential equation that describes aging after instantaneous temperature jumps of comparably low amplitude. It was first introduced in 2015 by Hecksher et al. [42] for temperature jumps $T(t)+T_\infty$ to some fixed temperature T_∞. Later it was extended by Roed et al. [277] to consider jumps to different T_∞, and finally shown to be consistent with temperature protocols within the linear response limit by Riechers et al. [43], which allowed to describe arbitrary temperature protocols (as long as the departure from equilibrium is not too large). In the following, a brief overview of the derivation of the key equations used to verify the material-time concept via single-parameter aging is given based on Refs. [42, 43, 277].

Single parameter aging adopts the early ideas of Narayanaswamy, i.e. the existence of a material time $\mathrm{d}\xi = \gamma(t)\mathrm{d}\xi$ that allows to express the change of some quantity $\Delta X(t) = X(t)-X_\infty$ in terms of a linear convolution integral, Eq. (8.3), to make predictions for the normalized aging function

$$R(t)=\frac{\Delta X(t)}{\Delta X(0)}. \tag{10.3}$$

The linear convolution integral for $\Delta X(t)$ implies that there exists a unique function $\phi(x)$ such that

$$R(t)=\phi(\xi). \tag{10.4}$$

$\phi(x)$ can be determined experimentally via small temperature jumps within the linear limit, where $\xi \propto t$ holds to good approximation, as it was convincingly demonstrated recently by Riechers et al. for small temperature jumps with ΔT ranging from 10 to 100 mK [43]. Considering the time derivative of Eq. (10.4) yields

$$\frac{\mathrm{d}R(t)}{\mathrm{d}t}=\frac{\mathrm{d}\phi(\xi)}{\mathrm{d}t}=\frac{\mathrm{d}\phi(\xi)}{\mathrm{d}\xi}\frac{\mathrm{d}\xi}{\mathrm{d}t}=\frac{\mathrm{d}\phi(\xi)}{\mathrm{d}\xi}\gamma(t). \tag{10.5}$$

As according to Eq. (10.4), ξ is a unique function of R, also $\mathrm{d}\phi/\mathrm{d}\xi$ is a unique function of R, which was referred to as $-F[R(t)]$ in Ref. [42], i.e.

$$\frac{\mathrm{d}R(t)}{\mathrm{d}t}=-F[R(t)]\gamma(t). \tag{10.6}$$

Eq. (10.6) is equivalent to Narayanaswamy's linear convolution integral, Eq. (8.3), for instantaneous temperature jumps at $t=0$. The additional assumption of the single-parameter aging approach is that a single unspecified parameter $Q(t)$ controls both $X(t)$, as well as the clock rate $\gamma(t)$. For this to hold true for *any* quantity X, there has to exist a single universal material time that controls the aging of all physical quantities of a glass. Moreover, it is assumed that temperature jumps are sufficiently small such that both, $X[Q(t)]$ and $\ln\gamma[Q(t)]$ can be first-order Taylor expanded in Q, which yields $\Delta X(t) = c_1[Q(t)-Q_\infty]$, as well as $\ln\gamma(t)-\ln\gamma_\infty = c_2[Q(t)-Q_\infty]$. The logarithm is considered for γ to include that γ is controlled by some form of energy barriers.

These assumptions lead to both, an analytical expression for the material-time clock rate,

$$\gamma(t)=\gamma_\infty \exp\left(\frac{\Delta X(0)}{X_\mathrm{const}}R(t)\right), \tag{10.7}$$

as well as, by including Eq. (10.6), a nonlinear differential equation for $R(t)$,

$$\frac{\mathrm{d}R(t)}{\mathrm{d}t}=-\gamma_\infty F(R)\exp\left(\frac{\Delta X(0)}{X_\mathrm{const}}R(t)\right). \tag{10.8}$$

Here, the abbreviation $X_{\text{const}} \equiv c_2/c_1$ was introduced for clarity. It is recalled that the function $F(R)$ is not specified, thus Eq. (10.8) can be rearranged to a form that allows to test its validity without knowledge of $F(R)$, i.e.

$$\ln\left(-\frac{1}{\gamma_\infty}\frac{\mathrm{d}R(t)}{\mathrm{d}t}\right)-\frac{\Delta X(0)}{X_{\text{const}}}R(t)=\ln(F(R)). \tag{10.9}$$

As $F(R)$ is a unique function of R, the left hand side of Eq. (10.9) plotted as a function of R should collapse for data obtained after different temperature jumps, as long as the above discussed assumptions are justified. For different jumps to the same temperature, γ_∞ is constant and can, e.g., be assumed as unity, because the material time is dimensionless. The constant X_{const} can be determined by comparing data from two different temperature jumps to the same temperature T_∞, as will be discussed below.

The validity of Eq. (10.9) has been tested for several different substances and quantities X, i.e. the mechanical resonance frequency, the dielectric loss at a fixed frequency, the dielectric constant at a large fixed frequency such that it represents the density-change of a non-polar liquid, as well as the peak-maximum frequency of the β-process [42, 277]. Deviations have been observed in particular for larger temperature jumps up to 8 K [277].

The uniqueness of $F(R)$ implies that Eq. (10.9) can be applied to obtain a prediction for an unknown relaxation function $R_2(t)$ from an available relaxation function data $R_1(t)$ of a different temperature jump to the same T_∞. $R_1(t)$ is available in terms of measured data-points $\boldsymbol{R}_1=(R_1^1,R_1^2,...,R_1^n)$ at times $\boldsymbol{t}_1=(t_1^1,t_1^2,...,t_1^n)$. Considering that the left hand side of Eq. (10.9) is identical for both jumps, integrating the differential equation yields a time vector $\boldsymbol{t}_2=(t_2^1,t_2^2,...,t_2^n)$ such that $(\boldsymbol{t}_2,\boldsymbol{R}_1)$ is the predicted shape of $R_2(t)$, i.e. [42, 277]

$$t_2=\int_0^{t_1}\exp\left(\frac{\Delta X_1(0)-\Delta X_2(0)}{X_{\text{const}}}R_1(t_1')\right)\mathrm{d}t_1'. \tag{10.10}$$

Performing such an analysis for two known jumps allows to determine X_{const}, which can then be used for all other data.

As already mentioned above, aging in the linear limit has recently been explored by Riechers et al. by probing the subtle changes of the dielectric constant ε' at 10 kHz after small temperature jumps with amplitudes between 10-100 mK [43]. As expected for responses within the linear limit, $R(t)$ for these different jumps collapse, which implies that $\xi(t)\propto t$ for such small temperature changes. As a consequence, the probed $R(t)$ for small temperature jumps correspond to the memory kernel $M_{\varepsilon'}(\xi)$ in the Narayanaswamy's linear convolution integral, Eq. (8.3). Knowledge of $M_{\varepsilon'}(\xi)$ allows to describe more complex temperature protocols within the linear response limit via Boltzmann superposition, which has been confirmed by Riechers et al. for small double temperature jumps and a temperature oscillation protocol. Moreover, by adopting the single-parameter aging result for the material-time clock rate, Eq. (10.7), the description could be extended to different temperature protocols beyond the linear-response limit.[43] This confirms the TN prediction that knowledge of the linear aging response allows to predict nonlinear aging [12, 42]

10.1.3 Material-time translational invariance and the triangular relation

The material-time concept is remarkable by transforming the nonlinear process of aging into a linear phenomenon by replacing time by material time. Following the linear-response spirit,

Dyre established a connection between the material-time concept and time correlations functions [12]. Considering that msDDLS gives access to the intensity time autocorrelation functions during aging, these conclusions provide a valuable basis for applying the material-time formalism to experimental data obtained during the present work. Following Refs. [12] and [278], the following section establishes various predictions for time autocorrelation functions based on the material-time formalism.

Within linear-response theory, time-translational invariance holds, i.e. the linear response does only depend on the elapsed time after some perturbation. Via fluctuation-dissipation relations this characteristic is closely linked to time-translational invariance of time autocorrelation functions. Adopting this concept for the material-time formalism implies material-time translational invariance (MTTI), in the sense that time autocorrelation functions only depend on the elapsed material time, i.e. there exists a function $F_X(x)$ such that

$$\left\langle \Delta X(t_1)\Delta X(t_2)\right\rangle \equiv C_X(t_1,t_2) = F_X\big(\xi(t_1)-\xi(t_2)\big). \tag{10.11}$$

Here, for generality the time autocorrelation functions of the fluctuations of any quantity X are considered, however within the scope of the present work mostly the light-scattering intensity is relevant, i.e. $X(t) = I(t)$. In the following, the abbreviation $C(t_1,t_2)$ instead of $C_X(t_1,t_2)$ and $F(\xi_1-\xi_2)$ instead of $F_X(\xi_1-\xi_2)$ is used for clarity, although obviously the time autocorrelations and, consequently, also the function $F(x)$ generally can depend on the quantity that is considered. Eq. (10.11) can be understood as an extension of the standard time-translational invariance of equilibrium systems, because time-translational invariance directly follows from Eq. (10.11) for $\xi(t) \propto t$. For an aging system, however, only MTTI holds, while time-translational invariance is violated.

Eq. (10.11) allows to determine the material time of an aging system from time-resolved autocorrelation functions. The procedure and results will be discussed in Section 10.3. In the remaining part of this section some consequences of Eq. (10.11) are discussed that represent necessary conditions for deriving the material time from time autocorrelation functions.

A direct consequence of Eq. (10.11) is the *triangular relation*, which for any three times $t_1 < t_2 < t_3$ establishes a relation for the pairwise autocorrelations $C_{12} \equiv C(t_1,t_2)$, $C_{13} \equiv C(t_1,t_3)$ and $C_{23} \equiv C(t_2,t_3)$. Because $F(x)$ monotonically goes to zero for $x \to \infty$ it can be inverted, i.e. there exists $\Phi(x)$ such that

$$\begin{aligned} &\text{(i)} && \xi(t_1)-\xi(t_2) = \Phi(C_{12}) \\ &\text{(ii)} && \xi(t_1)-\xi(t_3) = \Phi(C_{13}) \\ &\text{(iii)} && \xi(t_2)-\xi(t_3) = \Phi(C_{23}). \end{aligned} \tag{10.12}$$

Adding (i) and (iii) yields

$$\xi(t_1)-\xi(t_3) = \Phi(C_{12})+\Phi(C_{23}) = \Phi(C_{13}), \tag{10.13}$$

where in the second step (ii) is used. Φ is monotonous, thus the second part of Eq. (10.13) can be inverted and there exists a function $f(x)$ such that

$$C_{13} = f(C_{12},C_{23}). \tag{10.14}$$

Eq. (10.14) is the triangular relation and implies that knowledge of two of the three pairwise autocorrelations uniquely determines the third one. If MTTI applies, the function $f(x)$ should be the same for *any* temperature protocol.

The triangular relation was originally derived by Cugliandolo and Kurchan via a mean-field description of aging spin glasses after a quench from an infinite to a low temperatur [279].

Mathematically, it was shown that the validity of the triangular relation is a sufficient condition for time-reparametrization invariance, i.e. the existence of functions $h(t)$ and $j(x)$ such that $C(t_1,t_2)=j(h(t_1)-h(t_2))$. In this regard, the time-reparametrization $h(t)$ has the same properties as suggested for the material time by Eq. (10.11), however the interpretation by Cugliandolo and Kurchan refers to a different context and does not consider the most fundamental property of the material time, i.e. that it linearizes aging.

By an analogous procedure as discussed in Ref. [278] it can be derived that the function f in Eq. (10.14) is symmetric: Because $\xi(t)$ is continuous, there exists t_4 such that

$$\xi(t_4)-\xi(t_1)=\xi(t_3)-\xi(t_2), \tag{10.15}$$

which in turn implies that

$$C_{14}=C_{23}. \tag{10.16}$$

At the same time, Eq. (10.15) can be rearranged to

$$\xi(t_3)-\xi(t_4)=\xi(t_2)-\xi(t_1), \tag{10.17}$$

which yields

$$C_{43}=C_{12}. \tag{10.18}$$

By considering that

$$\xi(t_3)-\xi(t_1)=\big(\xi(t_3)-\xi(t_4)\big)+\big(\xi(t_4)-\xi(t_1)\big) \tag{10.19}$$

and that Eq. (10.15) together with $\xi(t)$ being monotonically increasing implies $t_1<t_4<t_3$, one finds

$$C_{13}=f(C_{14},C_{43}), \tag{10.20}$$

which considering Eq. (10.14), Eq. (10.16) and Eq. (10.18) establishes the symmetry of $f(x)$, i.e.

$$C_{13}=f(C_{23},C_{12})=f(C_{12},C_{23}). \tag{10.21}$$

In equilibrium, the symmetry of f follows from time-reversal symmetry. The derivation of this relation and the consequences for non-equilibrium aging samples will be discussed in Chapter 11.

Recently, Douglass et al. [278] verified the validity of the triangular relation for the distances between points in the $3n$-dimensional configuration space that characterize an aging system instead of time autocorrelation functions. These results indicate that the elapsed material time is associated with the distance traveled in configurational space, thus providing a microscopic interpretation of the material time, i.e. as stated by the authors it suggests 'distance as time'. Moreover, it was shown that in this picture the material time is dominated by the distance traveled by the slowest particles of the system.[278]

10.2 CONFIRMING THE EXISTENCE OF A MATERIAL TIME

In this section, time-resolved intensity autocorrelation function data of the scattered light of aging samples of 1P1P are discussed. To maintain the notations from the previous section and in the publication of these data in Ref. [280], in the following the intensity autocorrelations are referred to as

$$C(t,t+\Delta t)=g_2(t,t+\Delta t)-1, \tag{10.22}$$

where $g_2(t,t+\Delta t)$ is determined according to Eq. (9.4). In both panels of Fig. 10.1, $C(t,t+\Delta t)$ is plotted as a function of Δt, while the colors represent different t, with darker colors indicating

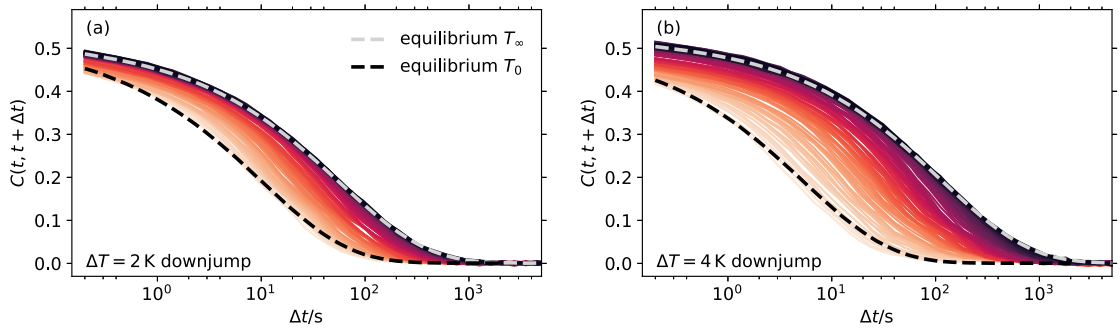

Figure 10.1: Time-resolved intensity autocorrelation functions of an aging sample of 1P1P after a $\Delta T = 2$K (a) and a $\Delta T = 4$K (b) temperature jump to similar temperatures T_∞. The equilibrium autocorrelation functions before the jump and after complete equilibration at T_∞ are shown as the black and the gray dashed lines, respectively. The colors indicate different t, with darker colors indicating larger t. The data shown were obtained using the LN_2-operated sample cell, which is the reason why the annealing temperatures T_∞ are not exactly identical as it would be in the Peltier-driven sample cell.

larger t. Aging is initiated by a temperature down-jump from T_0 to T_∞, starting from an supercooled liquid equilibrated at T_0. Subsequently, the full equilibration of the sample at T_∞ is monitored. The two panels represent data for different $\Delta T = T_\infty - T_0$, i.e. $\Delta T = -2$K in panel (a) and $\Delta T = -4$K in panel (b). Intensity autocorrelations obtained for the equilibrium system at T_0 res. T_∞ are included in Fig. 10.1 as the black and gray dashed lines. During aging, a distinct t- dependence of $C(t, t+\Delta t)$ is observed, i.e. its rate of decay to zero for $\Delta t \to \infty$ slows down with increasing t, until it eventually reaches a stationary equilibrium at T_∞ after several thousand seconds.

The time autocorrelation functions presented in Fig. 10.1 provide a basis to verify the triangular relation equations. To recall and put in simple terms, the considerations in Section 10.1.3 yield three conditions for the triangular relation to be obeyed.

(i) Two pairwise autocorrelations for three points in time predict the value of the third one, Eq. (10.14).

(ii) The underlying relation connecting these pairwise autocorrelations, denoted by $f(x)$ in Eq. (10.14), is the same for all temperature protocols.

(iii) $f(x)$ is symmetric, Eq. (10.21).

In order to test conditions (i) - (iii), C_{12}, C_{23}, and C_{13} were calculated for several million time triplets, $t_1 < t_2 < t_3$, from the speckle-pattern data obtained after the $\Delta T = -2$K and the $\Delta T = -4$K temperature down-jumps and for an equilibrium sample. This was done by choosing 10^3 linearly spaced values of t_1. For each t_1, different $t_2 = t_1 + \tau'$ were constructed for 169 logarithmically equally spaced values τ'. Subsequently, for each combination of t_1 and t_2, different $t_3 = t_2 + \tau''$ were constructed using the same 169 logarithmically equally spaced values for τ''. Combined, this procedure generated $1000 \cdot 169^2 \cong 28.6 \cdot 10^6$ different time triplets. For each of these, the pairwise autocorrelations C_{12}, C_{13} and C_{23} were calculated according to Eq. (9.4), where, e.g., $t = t_1$ and $t + \Delta t = t_2$ for the calculation of C_{12}. Finally, subsets with the same values of C_{12} and C_{23} were binned (with resolution $\Delta C = 0.005$). Each subset yields a distribution of C_{13}-values associated with the respective C_{12} and C_{23}. Finally, from each distribution the mean value, $\overline{C_{13}}(C_{12}, C_{23})$, and the corresponding standard deviation, $\Delta C_{13}(C_{12}, C_{23})$, were calculated. In the following, the $\overline{(...)}$ notation is dropped for clarity and

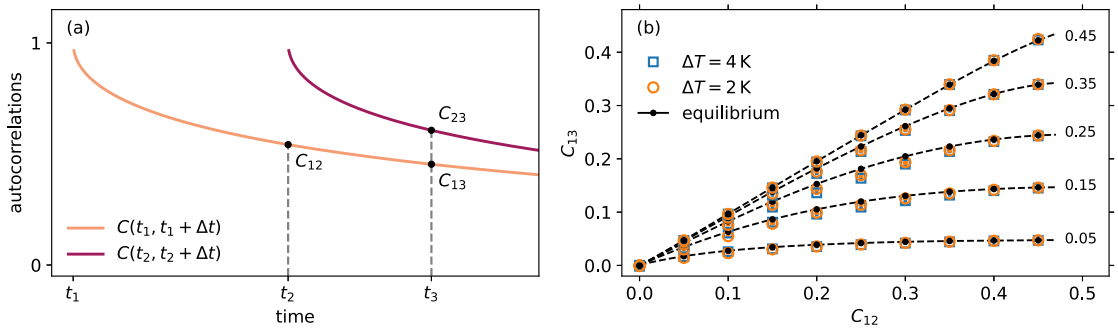

Figure 10.2: Testing the validity of triangular relation. (a) Illustration of how the three pairwise autocorrelation values C_{12}, C_{23}, and C_{13} are defined from two autocorrelation functions, one starting at t_1 (yellow line) and the second from t_2 (red line). The x-axis considers absolute times t instead of relative times Δt as it was done in Fig. 10.1, thus the autocorrelation functions are plotted on a linear time-axis instead of a logarithmic one, leading to a different appearance. (b) Mean values of C_{13} as a function of C_{12} for five fixed C_{23} indicated on the right hand side. The different colors represent data obtained for different temperature protocols, i.e. equilibrium data as black symbols and lines and $\Delta T = -4$ K, res. $\Delta T = -2$ K, temperature down-jump data as blue squares res. orange spheres. Errorbars reflect the standard-deviation values ΔC_{13}, which are much smaller than symbols size. C_{13}-data for the different protocols collapse, confirming that $f(x)$ in Equation (10.14) is independent of the temperature protocol.

$C_{13} \equiv \overline{C_{13}}$ denotes the mean of each distribution. For an illustration of how C_{12}, C_{13} and C_{23} are defined for an exemplary time triplet, see Fig. 10.2.

The results of the triangular-relation analysis are plotted in different representations in Fig. 10.2b and Fig. 10.3, which will be discussed in combination below. In Fig. 10.2b, $C_{13}(C_{12}, C_{23})$ is plotted as a function of C_{12} at five fixed values of C_{23}. The errorbars indicate $\Delta C_{13}(C_{12}, C_{23})$, which, however, are difficult to identify as they are much smaller than the symbol size. Data obtained for both temperature down-jumps and for an equilibrium sample are included. Fig. 10.3 plots data in $2d$-heatmap representation, where x- and y-axes represent C_{12} and C_{23}, respectively. The colors indicate the values of $C_{13}(C_{12}, C_{23})$ (left side panels), $\Delta C_{13}(C_{12}, C_{23})$ (middle panels) and a measure for the deviation from diagonal symmetry of the left side panels, i.e. $|C_{13}(X, Y) - C_{13}(Y, X)|$ for given values of $X = C_{12}$ and $Y = C_{23}$ (ride side panels).

In order for condition (i) to be fulfilled, $\Delta C_{13}(C_{12}, C_{23})$ should be zero at each combination of C_{12} and C_{23}, as the latter uniquely determine C_{13}. Obviously, due to the finite binning resolution and due to experimental noise, $\Delta C_{13} > 0$. To judge whether ΔC_{13}-values obtained for aging samples are sufficiently small in order to conclude that the triangular relation is obeyed, the results are compared to the data obtained in equilibrium, where the triangular relation holds trivially [12]. For both, the down-jump data and the equilibrium data, the errorbars in Fig. 10.2 representing ΔC_{13} are much smaller than the symbol size. Inspecting the middle panels of Fig. 10.3 reveals that for the equilibrium data $\Delta C_{13} \sim 0.003$ for all C_{12} and C_{23}, suggesting the minimum values that can be obtained considered the binning resolution and experimental noise. For the down-jump data, slightly larger values are observed at intermediate C_{12} and C_{23} reaching values up to $\Delta C_{13} \sim 0.006$. While this indicates a slight violation of triangular relation, the deviations are mostly below 1%, indicating that triangular relation can be assumed to hold within good approximation. It has to be noted in this regard that lowering the temperature of a macroscopic sample inevitably leads to some volume contraction and fluxes, which can alter the recorded speckle pattern of scattered light, thus

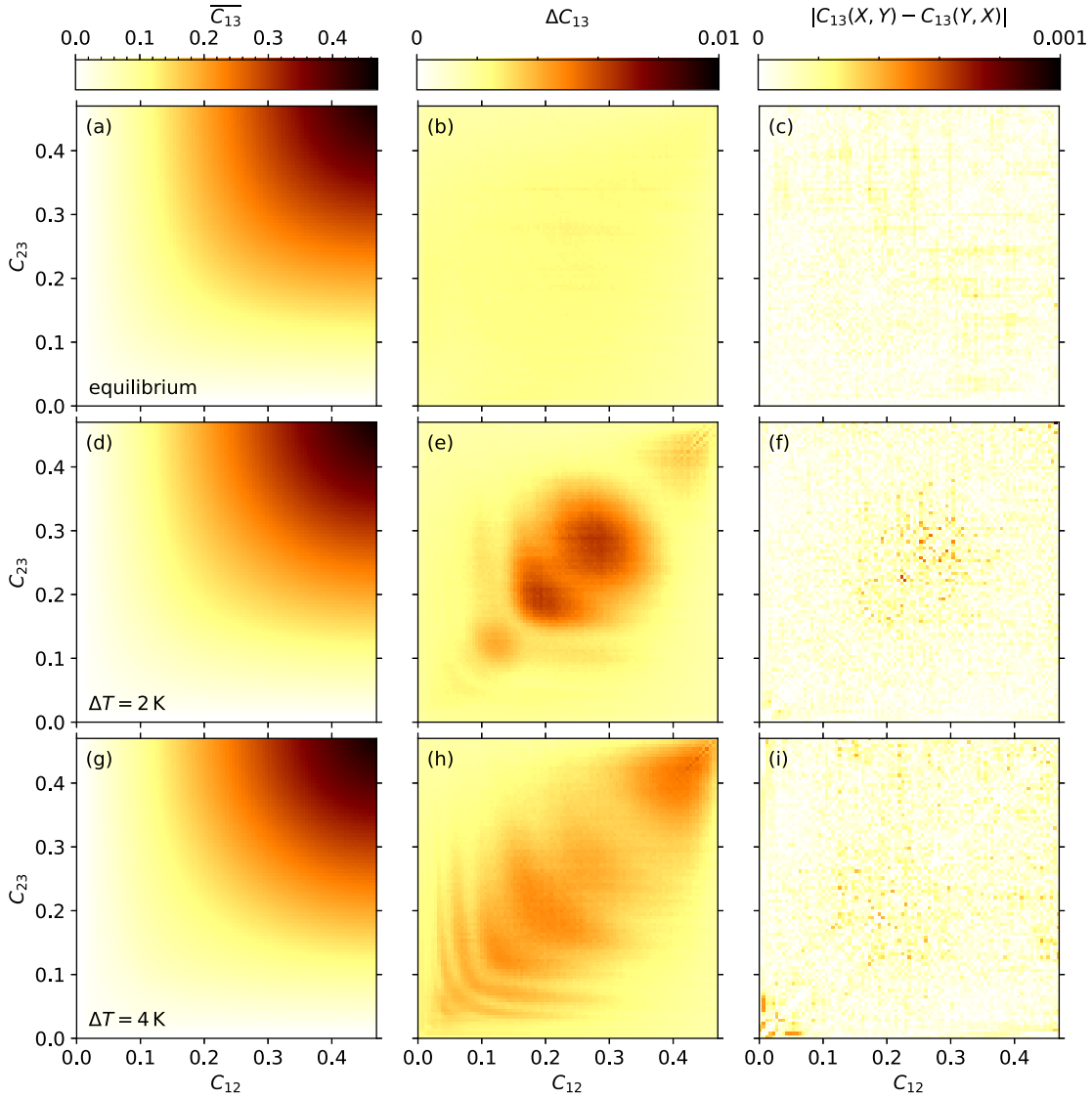

Figure 10.3: Testing the validity of triangular relation. All panels plot data as $2d$ heatmaps, where x- and y-axes represent C_{12} and C_{23}, respectively. The colors reflect mean $C_{13}(C_{12}, C_{23})$ in panels (a), (d) and (g), the standard deviation of C_{13}, $\Delta C_{13}(C_{12}, C_{23})$, in panels (b), (e) and (h), as well the measure of deviation from diagonal symmetry of $C_{13}(C_{12}, C_{23})$, $|C_{13}(X,Y) - C_{13}(Y,X)|$ for given values of $X = C_{12}$ and $Y = C_{23}$, in panels (c), (f), and (i). Each row represents data from one temperature protocol, i.e. in equilibrium (a-c) after the $\Delta T = -2$ K down-jump (d-f) and the $\Delta T = -4$ K down-jump (g-i).

leading to subtle artifacts in the autocorrelation functions. Most likely, these effects lead to some small deviations from triangular relation that do not reflect "real" violations on the microscopic scale.

According to condition (ii), the function $f(x)$ that describes the relation between the three pairwise autocorrelation values, i.e. $C_{13} = f(C_{12}, C_{23})$, should be independent of the temperature protocol. Thus, the heatmaps in the left hand side panels (a), (d) and (g) of Fig. 10.3 should be identical and the data for the different temperature protocols in Fig. 10.2b should collapse. Indeed, this is confirmed in Fig. 10.2b, i.e. $f(x)$ is almost identical for data obtained from both temperature down-jumps and for the equilibrium sample.

Finally, in order for condition (iii) to be valid, the heatmaps in the left hand side panels (a), (d) and (g) of Fig. 10.3 should be symmetrical along the diagonals. To quantify the deviations from perfect symmetry, the measure $|C_{13}(X,Y) - C_{13}(Y,X)|$ for given values of $X = C_{12}$ and $Y = C_{23}$ is considered in the left hand side panels (c), (f) and (i). It reflects the absolute difference between the C_{13} values at some (C_{12}, C_{23})-point and the value at its reflection point through the diagonal axis, (C_{23}, C_{12}). The deviations from perfect symmetry are much smaller than 0.001 for both, equilibrium and temperature down-jump data, thus confirming the symmetry of $f(x)$ independent of the temperature protocol.

To summarize, comparing autocorrelation data of aging and equilibrium samples of 1P1P confirms the validity of the triangular relation. The latter can be considered as a necessary requirement in order to define a material time on the basis of material-time translation invariance, Eq. (10.11). The procedure to extract the material time will be discussed in Section 10.3. Prior to this, Section 10.2.1 presents some artificially generated autocorrelation data constructed to *disobey* triangular relation. These considerations allow to estimate how precisely deviations from triangular relation can be identified using the analysis tools applied in the previous section. It is found that especially deviations from triangular-relation symmetry, quantified by $|C_{13}(X,Y) - C_{13}(Y,X)|$, very sensitively indicate violations of the triangular relation. These results support the conclusions drawn regarding validity of triangular relation in the previous section.

10.2.1 Artificially generated data disobeying triangular relation

In the following, two sets of artificially generated time autocorrelation functions are compared; one defined to obey and the other one defined to disobey MTTI and thus, also triangular relation. Time autocorrelations that obey MTTI are defined as stretched exponential functions of the elapsed material time,

$$C(t_1, t_2) = \exp\left[-\left(\frac{\xi(t_2) - \xi(t_1)}{k}\right)^{\beta}\right], \tag{10.23}$$

where $\beta = 0.5$, k is some constant and $\xi(t)$ is obtained from some predefined function $\gamma(t)$ via integration. Per definition, Equation (10.23) obeys MTTI and, thus, also obeys the triangular relation. Time-resolved autocorrelations $C(t, t+\Delta t)$ obtained from Equation (10.23) are plotted as a function of Δt in Fig. 10.4a. The underlying $\gamma(t)$ as a function of time is shown in the inset of panel (a). It was chosen to resemble the experimentally observed material-time clock rate of a $\Delta T = -2\,\mathrm{K}$ down-jump. According to their definition, the autocorrelations collapse as functions of $\Delta\xi \equiv \xi(t+\Delta t) - \xi(t)$ in panel (b).

A definition similar to Equation (10.23), which, however, disobeys MTTI is given by

$$C(t_1, t_2) = \exp\left[-\left(\frac{\xi(t_2) - \xi(t_1)}{k}\right)^{\beta(t)}\right], \tag{10.24}$$

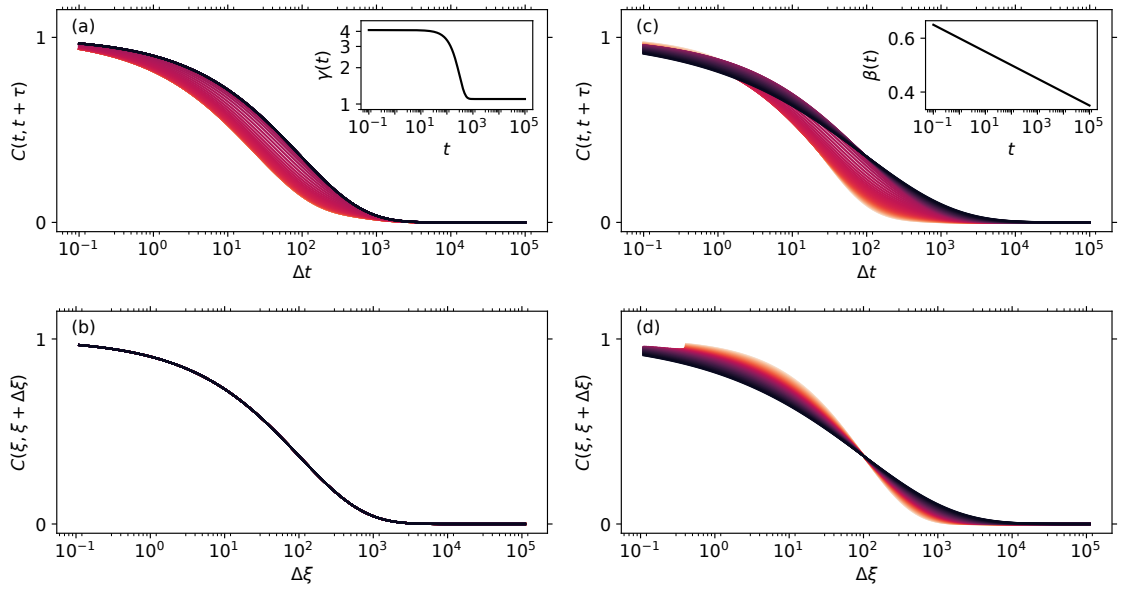

Figure 10.4: Time-resolved autocorrelations defined in Equation (10.23) to obey MTTI (left panels (a) and (b)) and defined in Eq. (10.24) to disobey MTTI. The upper panels (a) and (c) show $C(t, t+\Delta t)$ as functions of Δt, where darker colors indicate larger t. The inset of panel (a) shows the predefined material-time clock rate γ as a function of t, while the inset of panel (c) shows the t-dependence of the stretching exponent β, which was introduced to violate MTTI in Eq. (10.24). The lower panels (b) and (d) show the same data as the upper panels, but as a function of the elapsed material time $\Delta\xi \equiv \xi(t+\Delta t) - \xi(t)$, which collapses the data obeying MTTI in (b), but not the ones disobeying MTTI in (d).

where now an explicit t-dependence of the stretching exponent β is included. Corresponding autocorrelations for the same function $\gamma(t)$ as above are shown in panel Fig. 10.4c. $\beta(t)$ as a function of t is shown in the inset. It is assumed to linearly change from 0.65 to 0.35 as a function of $\log t$. Indeed, the autocorrelations do not collapse as a function of $\Delta\xi$ in panel (d), indicating a violation of MTTI and, consequently, the autocorrelations defined by Eq. (10.24) do not meet the criteria to obey triangular relation.

Triangular relation for both definitions of autocorrelations is tested in Fig. 10.5 by considering the same $2d$ heatmaps as in Figure 10.3. The various time triplets analyzed during the corresponding analysis were determined using an equivalent procedure as for the analysis of experimental data in Section 10.2.

The heatmaps based on autocorrelations defined to obey MTTI (upper panels) can be considered as a representation of the equilibrium heatmap-data from Section 10.2 without any experimental noise. Comparably small values for ΔC_{13} and $|C_{13}(X,Y) - C_{13}(Y,X)|$ are found as for the experimental data above, suggesting that the observed deviations from zero mostly reflect the finite binning resolution. By contrast, large values of ΔC_{13} and $|C_{13}(X,Y) - C_{13}(Y,X)|$ are observed for the autocorrelations defined to disobey MTTI (lower panels) that significantly exceed any of the deviations observed for the experimental data during aging. It is noted that the color scales have been adapted compared to Figure 10.3 in order to include the much larger values of ΔC_{13} and $|C_{13}(X,Y) - C_{13}(Y,X)|$. The upper limits of the color scales used for the analysis of the experimental data are indicated as ticks in the color scales of Fig. 10.5. Especially the deviations from symmetry for the autocorrelations based on Eq. (10.24) exceed the experimentally observed maximum values by much more than a factor ten. This suggests

that $|C_{13}(X,Y) - C_{13}(Y,X)|$ is a very sensitive measure to identify deviations from triangular relation.

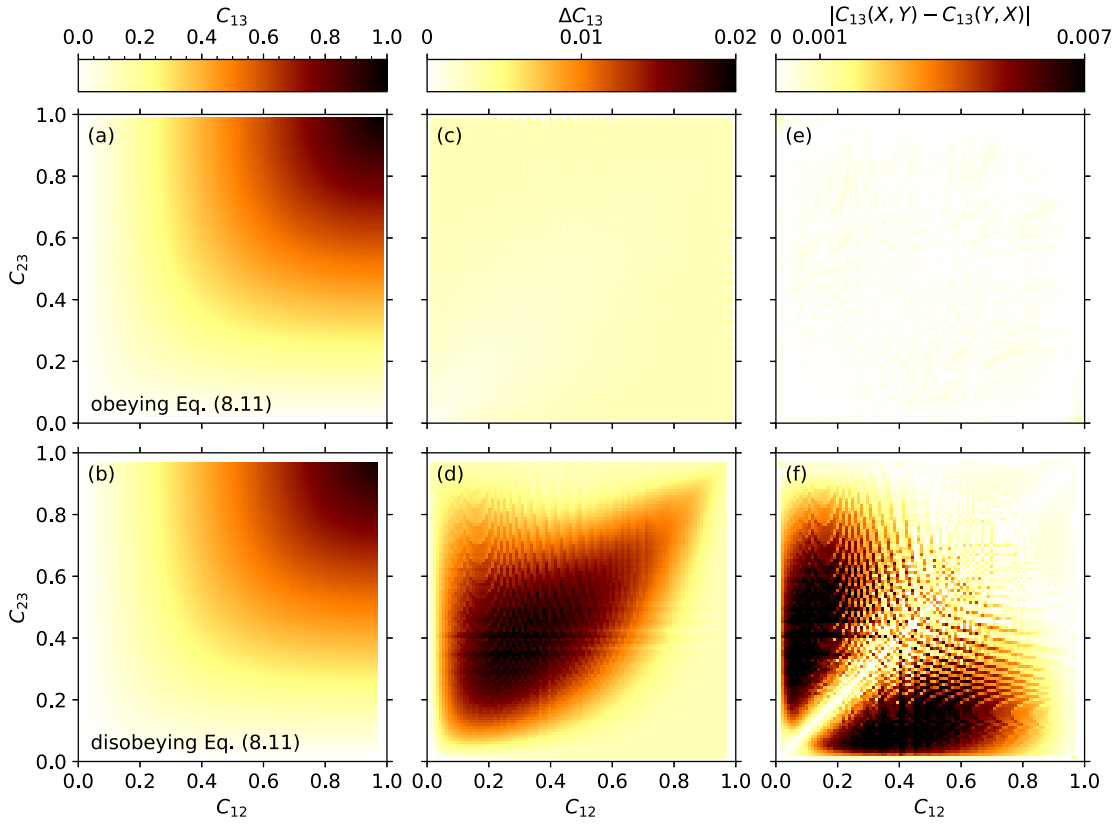

Figure 10.5: Heatmaps for verifying triangular relation equivalent to Fig. 10.3 but for the time autocorrelations shown in Fig. 10.4. Upper panels represent autocorrelations that obey MTTI and triangular relation, while the lower-panel data disobey both.

10.3 DETERMINING THE MATERIAL TIME FROM INTENSITY AUTOCORRELATION FUNCTIONS

The previous sections have confirmed a necessary condition for defining the material time $\xi(t)$ based on MTTI. As discussed in Section 10.1.3, the MTTI relation Eq. (10.11) can be inverted, thus $\Phi(x)$ exists such that

$$\xi(t_1)-\xi(t_2)=\Phi(C(t_1,t_2)). \tag{10.25}$$

As a consequence, once the time autocorrelation function $C(t_1,t_2)$ has decayed to some value, say a, a fixed amount of material time $\Delta\xi$ has elapsed. Thus, $\xi(t)$ can be determined from experimental time autocorrelation functions via an iterative procedure, which is illustrated on a linear time axis in Fig. 10.6. The basic idea is to construct a sequence of points in time, $\boldsymbol{t}=(t_1,t_2,...,t_n)$, such that consecutive elements of the sequence satisfy the criterion

$$C(t_i,t_{i+1})=a. \tag{10.26}$$

Then Eq. (10.25) implies that

$$\xi(t_{i+1})-\xi(t_i)=\Delta\xi\equiv 1, \tag{10.27}$$

i.e. $\boldsymbol{\xi}=(\xi(t_1),\xi(t_2),...,\xi(t_n))=(1,2,...,n)$. Here, it was used that the material time is dimensionless, thus $\Delta\xi\equiv 1$ can be chosen with no loss of generality.

Applying this procedure with $a=0.3$ to the experimental data discussed in Section 10.2 yields the results shown in Fig. 10.7. Panel (a) plots $\xi(t)$ obtained for the different temperature protocols, i.e. $\Delta T=-2\,\mathrm{K}$ (orange line) and $\Delta T=-4\,\mathrm{K}$ (blue line) down-jumps and equilibrium (green line), as a function of t in double-logarithmic representation. While the expected $\xi(t)\propto t$ is confirmed for the equilibrium sample, $\xi(t)$ is a non-linear function of t during physical aging. Panel (b) shows the same data as panel (a) but in linear representation. Here it is found that during aging after a temperature down-jump the material time initially increases quickly at short t, but eventually slows down and reaches a constant slope.

The rate the material time ticks with is obtained via the time-derivative

$$\gamma(t)=\frac{\mathrm{d}\xi(t)}{\mathrm{d}t}, \tag{10.28}$$

which is plotted in double-logarithmic representation for all three data sets in panel (c) and in linear representation in panel (d). These data confirm that following a temperature jump $\gamma(t)$ goes from one value at the shortest times probed to the new equilibrium rate at T_∞. Here, it is noted that the data shown in Figure 10.7 have been obtained before the completion of the Peltier-driven small sample cell and by using the LN_2-cooled large sample cell. As a consequence, T_∞ for the $\Delta T=-2\,\mathrm{K}$ and the $\Delta T=-4\,\mathrm{K}$ temperature jumps were not exactly the same, which was accounted for in Figure 10.7 assuming time-aging-time superposition, the procedure of which will be discussed in Section 10.4.1. Similar data for jumps to exactly the same T_∞ obtained by using the Peltier-driven small sample cell will be shown in Section 12.1.

The data shown in Figure 10.7 have been derived using $a=0.3$, i.e. $\Delta\xi\equiv 1$ elapses while the intensity autocorrelation function decays to 0.3. In fact, the procedure for determining $\xi(t)$ is valid independent of how a is chosen, thus the same results should be obtained for different a. This conjecture is explored in Fig. 10.8, where panels (a) and (b) show $\xi(t)$ and $\gamma(t)$ data as a function of t for $a=0.12...0.38$. While the shape of the curves for different a are very similar, no collapse is observed due to the fact that different choices of a imply different definitions of the material-time base unit $\Delta\xi$. For two choices of a, a_1 and a_2, $\Delta\xi$ elapses while $C(t,t+\Delta t)$ decays to a_1 res. a_2, i.e. the times Δt_1 and Δt_2 that corresponds to $\Delta\xi$ are

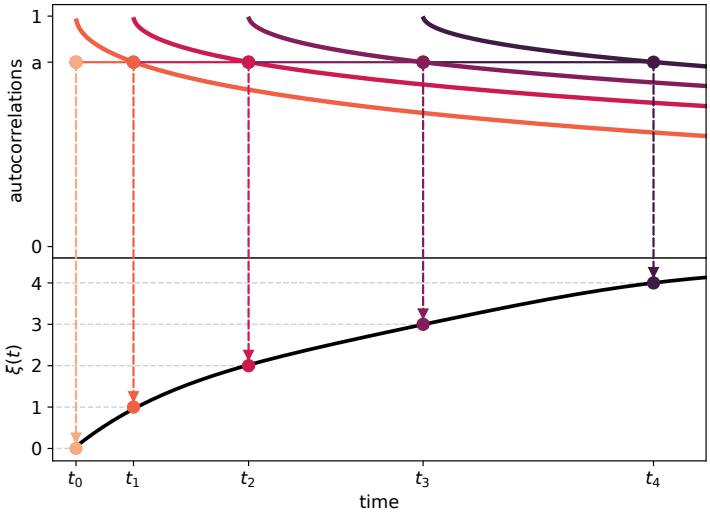

Figure 10.6: Schematic illustration of the procedure used to determine the material time as a function of time, $\xi(t)$, from time autocorrelation functions, plotted as linear function of t in the upper panel. Starting at t_0, $t_1 = t_0 + \Delta t$ is determined such that the function $C(t_0, t_0 + \Delta t)$ (orange line) equals a. Iterative repetition of this procedure yields the vector $\boldsymbol{t} = (t_1, t_2, ..., t_n)$, such that $\boldsymbol{\xi} = (\xi(t_1), \xi(t_2), ..., \xi(t_n)) = (1, 2, ..., n)$, which finally provides the (non-linear) function $\xi(t)$ shown in the lower panel. See text for details.

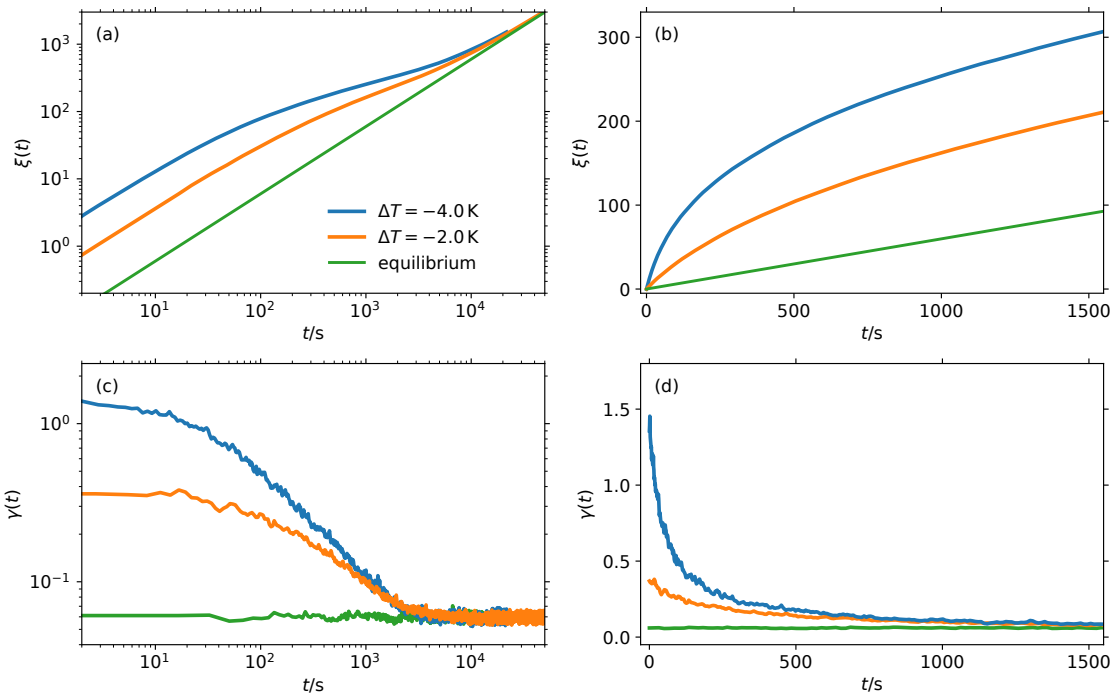

Figure 10.7: Material time $\xi(t)$, panels (a) and (b), and material-time clock rate $\gamma(t)$, panels (c) and (d) obtained from the experimental intensity-autocorrelation data. The different temperature protocols are indicated by the different colors as indicated in the legend. Left hand side panels (a) and (c) use double-logarithmic representation, while the right hand panels (b) and (d) are plotted on a linear scale.

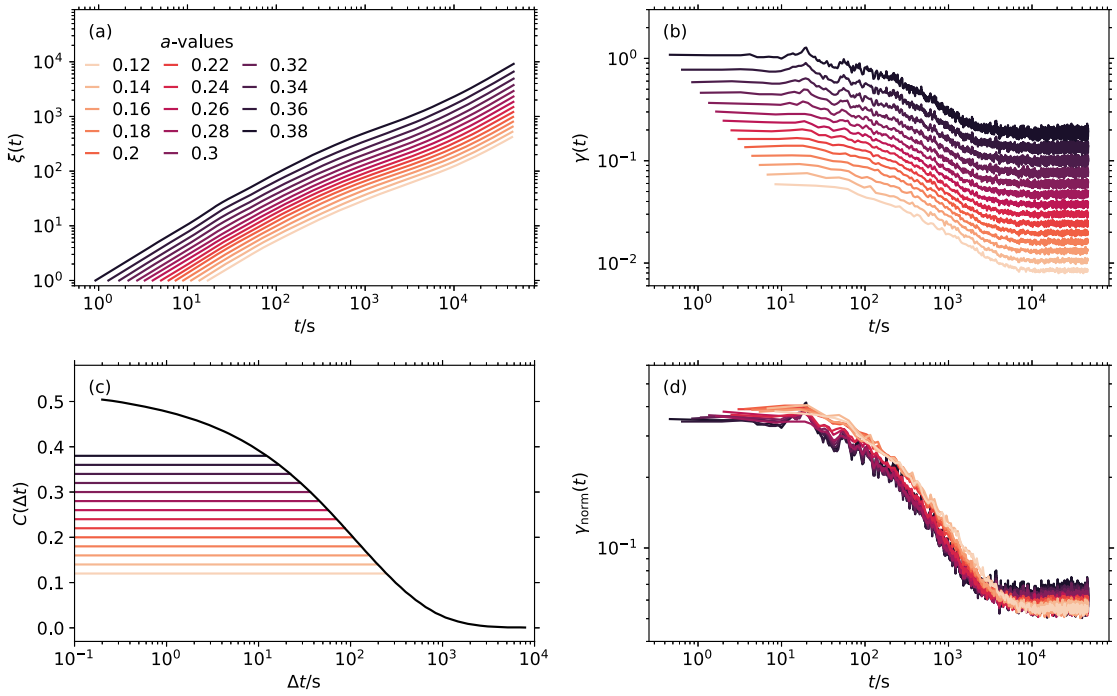

Figure 10.8: Validation that the determined material time is independent of the choice of a in Eq. (10.26). Upper panels consider $\xi(t)$ (a) and $\gamma(t)$ (b) as a function of t for various values of $a = 0.12, ..., 0.38$ indicated by the different colors. While the respective shapes obtained for different a are very similar, the curves do not collapse, due to the different definitions of the material-time base unit. A description with a common definition of the material-time base unit can be obtained by considering the $\Delta t(a)$ as a function of a associated with $\Delta\xi$ for the equilibrium autocorrelation function in panel (c). This is confirmed in panel (d), where all data from panel (b) collapse via Eq. (10.29).

defined as $C(t, t+\Delta t_1) = a_1$ and $C(t, t+\Delta t_2) = a_2$. According to MTTI, the ratio $\Delta t_1/\Delta t_2$ is uniquely defined by the choices of a_1 and a_2, thus can be determined, e.g., from an equilibrium autocorrelation function as illustrated in panel (c). The length of the colored horizontal lines reflects $\Delta t(a)$ that elapses during $\Delta\xi$. $\Delta t(a)$ extracted from the equilibrium autocorrelation function shown in panel (c) allows to calculate representations of $\gamma(t)$ obtained from different values of a that have the same material-time base unit definition as the $a = 0.3$-data shown in Fig. 10.7, i.e.

$$\gamma^a_{\mathrm{norm}}(t) = \frac{\Delta t(a)}{\Delta t(0.3)}\tilde{\gamma}(t), \tag{10.29}$$

where $\tilde{\gamma}(t)$ represents the material-time clock rate determined using $a = 0.3$. Indeed, $\gamma^a_{\mathrm{norm}}(t)$ for various a are shown to collapse in panel (d). Only subtle deviations from a perfect collapse are observed that suggest $\gamma^a_{\mathrm{norm}}(t)$ to relax slightly slower for smaller a, however the validity of this observation is difficult to judge considering the experimental noise. In summary, it was confirmed that the procedure for determining $\xi(t)$ yields equivalent results for different choices of a. For noisy autocorrelation data, small a-values yield less noisy $\gamma(t)$-data, however information is lost at short t. $a = 0.3$ was chosen above as a compromise between these two effects.

10.4 TESTING THE VALIDITY OF THE MATERIAL TIME

Section 10.3 presented the first experimentally determined material-time data for aging molecular glasses, however, so far without any validation that these results represent the correct material time. The following two sections provide such validations. Section 10.4.1 confirms that the determined material time linearizes aging relaxation functions, according to Narayanaswamy's linear convolution integral, Eq. (8.3). Section 10.4.2 tests the validity of MTTI, Eq. (10.11), which, so far, was only confirmed indirectly by showing that the time autocorrelations obey triangular relation in Section 10.2, but can now be tested explicitly with knowledge of the function $\xi(t)$.

10.4.1 Linearizing aging via the material time

In a first step, a relaxation function $R_C(t)$ is determined from the DDLS intensity autocorrelation functions and it is tested whether replacing time by material time linearizes these data. Within the single-parameter aging framework it is assumed that there exists one general material time that controls the aging of any quantity. However, whether the material time that controls the aging of some quantity $X(t)$ does also linearize the change of another quantity $Y(t)$ during aging remains an open question and, in fact, is impossible to test experimentally. As a first attempt to approach this important question, however, it is tested below whether the material time determined from the DDLS intensity autocorrelation functions also linearizes the change of the dielectric loss at a fixed frequency during aging.

DDLS relaxation functions

One popular quantity used to derive a relaxation function from is the dielectric loss $\varepsilon''_\nu(t)$ evaluated at a fixed frequency ν_{fix} along the high-frequency side of the α-process [37, 42, 43, 244, 277, 281–283]. During aging, $\varepsilon''_\nu(t)$ changes as a function of t as the average relaxation time of the sample changes, thus leading to a shift of the α-process . Considering fluctuation-dissipation relations, evaluating a susceptibility spectrum at a fixed frequency is conceptually equivalent to evaluating a time autocorrelation function $C_{\Delta t}(t) \equiv C(t, t+\Delta t)$ at a fixed short lag time Δt. Thus, in this section the relaxation function based on DDLS intensity autocorrelations

$$R_C(t) \equiv \frac{C_{\Delta t}(t) - C_{\Delta t}(t\to\infty)}{C_{\Delta t}(t=0) - C_{\Delta t}(t\to\infty)} \tag{10.30}$$

is analyzed. Finally, this will allow to apply the material time determined from DDLS intensity autocorrelations to relaxation functions obtained within the same experiment.

As a first step, Figure 10.9 explores how $R_C(t)$ depends on the choice of Δt. Intensity autocorrelation functions after a $\Delta T = -4$ K down-jump are shown in panel (a). $R_C(t)$ considers the normalized change of the autocorrelations along the fixed lag times indicated by the colored vertical lines. $C_{\Delta t}(t)$ for the various Δt-values are shown in panel (b), while panel (c) shows the normalized change of $C_{\Delta t}(t)$ during aging, i.e. $R_C(t)$. Quite different behavior is observed for different Δt, i.e. $R_C(t)$ decays steeper and at larger t for large values of Δt. To confirm that this behavior is in-line with the material-time concept, panels (d)-(f) consider the same analyses performed for artificially generated autocorrelation data, similar to the ones in Section 10.2.1 and based on Eq. (10.23), but for a different choice of $\gamma(t)$ to resemble the data shown in Figure 10.9a. Thus, per definition these artificially generated data fully conform to a material time, however the same dependence of $R_C(t)$ on Δt is observed in

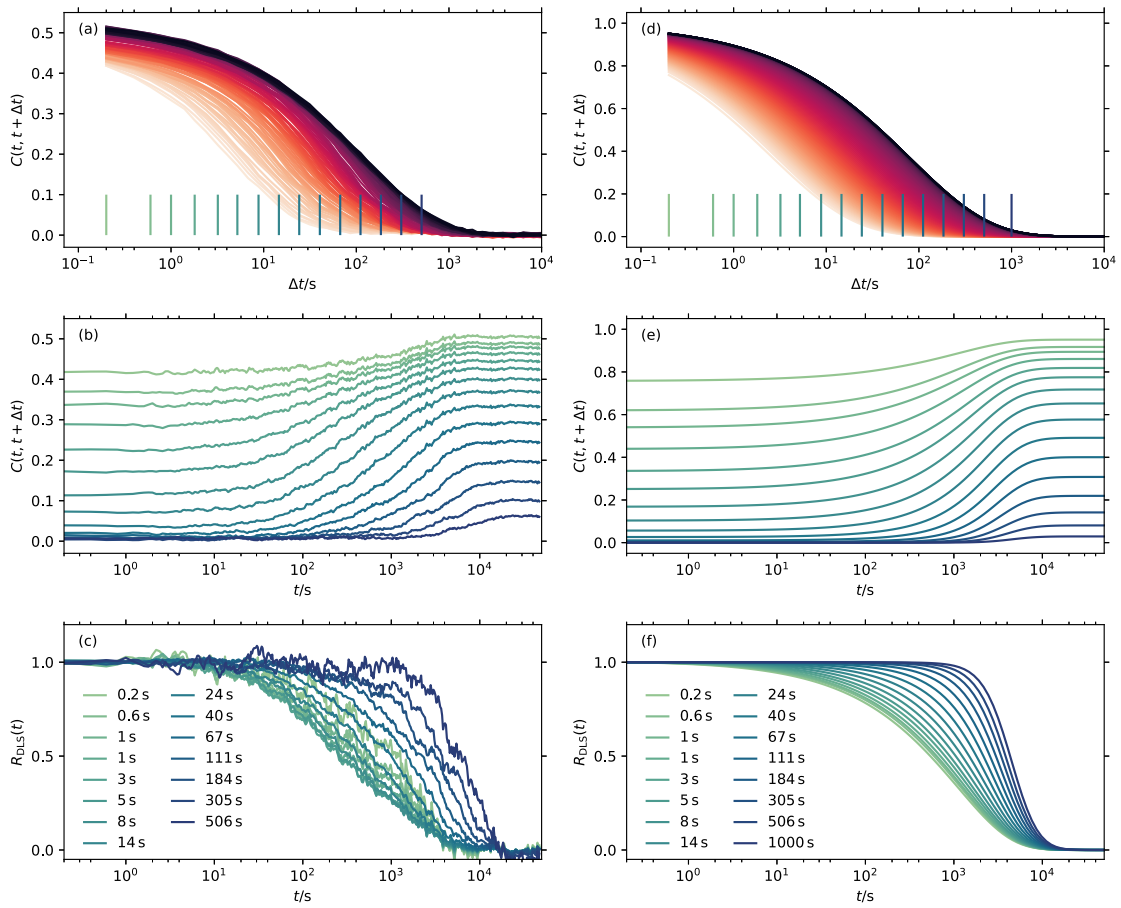

Figure 10.9: Determining the DDLS relaxation function $R_C(t)$. The left-side panels consider experimental data for a $\Delta T = -4\,\mathrm{K}$ down-jump, while the right-side panels considered artificially generated data without any experimental noise based on Eq. (10.23). (a),(d) In order to determine $R_C(t)$, $C(t, t+\Delta t)$ are evaluated at fixed lag times Δt, which are illustrated as vertical colored lines. (b),(e) Raw $C_{\Delta t}(t) \equiv C(t, t+\Delta t)$-data obtained for various choices of Δt between 0.2 and 1000 s. (c),(f) Normalized change of $C_{\Delta t}(t)$, i.e. $R_C(t)$, as a function of time. Different shapes are observed for different choices of δt, reflecting the non-linear weighting of short-time and long-time aging behavior.

panel (f). The quite different behavior for large Δt can be understood by considering that at short t and large Δt, $C_{\Delta t}(t)$ is essentially zero, as the autocorrelations have already fully decayed between t and $t+\Delta t$. As a consequence, almost no change of $C_{\Delta t}(t)$ is detected at short times and only once the decay of the autocorrelations has slowed down considerably such that $C_{\Delta t}(t) > 0$, a relevant contribution is observed for $R_C(t)$. Thus, different choices of Δt essentially weight short- and long-time changes of time autocorrelations differently, leading to considerably different appearances of $R_C(t)$.

In fact, this effect is of quite general relevance: Even though two quantities $X(t)$ and $Y(t)$ obey the same material time, the corresponding relaxation functions $R_X(t)$ and $R_Y(t)$ are not necessarily equal as long as X and Y are different non-linear functions of t. Single-parameter aging does treat this issue by considering small temperature jumps, such that changes of $X(t)$ and $Y(t)$ can be Taylor expanded to first order and, thus, are treated as linear functions of the quantity that controls aging and inherit the corresponding time-dependence, see

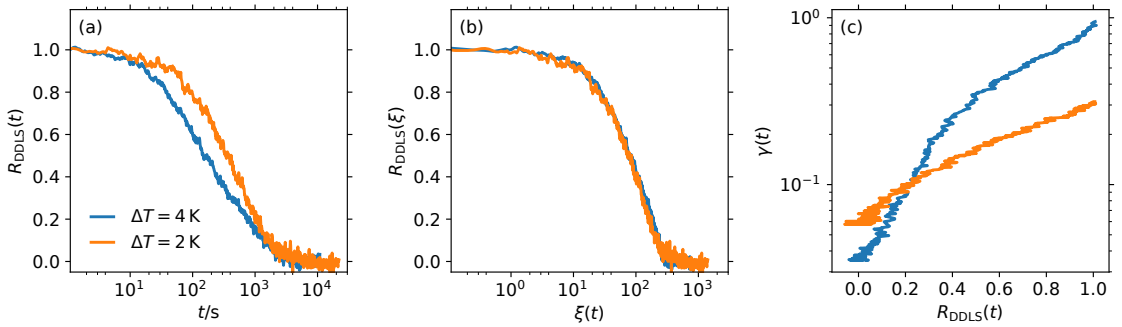

Figure 10.10: (a) $R_C(t)$ for the $\Delta T = -2\,K$ (orange) and the $\Delta T = -4\,K$ (blue) down-jumps are different, reflecting the non-linear nature of physical aging. (b) These data collapse as a function of the material time, i.e. $R_C(\xi)$. (c) Testing the single-parameter aging result that $\gamma \propto \exp(R)$.

Section 10.1.2. Beyond the validity of the first-order Taylor expansion, however, two quantities can obey the same material time, but show different relaxation functions $R_X(t)$ and $R_Y(t)$.

In order to compare $R_C(t)$ quantifying aging after different temperature jumps, small values of Δt should be chosen to ensure that the entire relaxation from one to the other equilibrium state is resolved equally. At the same time, $R_C(t)$ obtained from the shortest obtainable Δt are noisy. As a compromise, $R_C(t)$ obtained from $\Delta t = 6\,s$ are used to verify whether using the material time instead of conventional time linearizes $R_C(t)$ in the second part of this section.

Fig. 10.10a shows $R_C(t)$ obtained for the $\Delta T = -4\,K$ (blue line) and the $\Delta T = -2\,K$ (orange line) down-jump as a function of t. As expected for temperature changes beyond the linear limit, the two relaxation functions do not collapse. Instead, $R_C(t)$ for the larger temperature jump decays earlier and appears more stretched, reflecting a stronger auto-retardation effect compared to the smaller temperature jump.

Plotting these data as a function of material time in panel (b) reveals a perfect collapse, thus confirming the prediction of the Naranayaswamy linear convolution integral. Unfortunately, obtaining $R_C(t)$-data with sufficiently low noise is difficult for smaller temperature jumps, thus it is currently impossible to explore the linear aging regime.

Finally, Fig. 10.10c verifies the single-parameter aging prediction that the material-time clock rate $\gamma(t)$ is an exponential function of the relaxation function $R_C(t)$. If the data would obey the single-parameter aging prediction, plotting $\gamma(t)$ as a function of $R_C(t)$ on a logarithmic y-axis should be linear with a slope proportional to $C_{\Delta t}(t \to \infty) - C_{\Delta t}(0)$. While this, indeed, seems to be the case for the $\Delta T = -2\,K$-data, a distinct deviation from a linear course is observed for the $\Delta T = -4\,K$-data. This deviation could reflect that the non-linear variations of $C_{\Delta t}(t)$ during aging are too strong in order to be Taylor expanded to first order of the underlying single-parameter variable $Q(t)$. Such effects are usually not observed in the standard frequency-domain experiments, because the probed fixed frequency corresponds to much smaller lag-times than 6 s. Thus, the variations of the probed susceptibility during aging are significantly smaller compared to the ones observed for $C_{\Delta t}(t)$, i.e. after a $\Delta T = -4\,K$ down jump, $C_{\Delta t}(t)$ goes from 0.17 to 0.42 (see Figure 10.9b).

Dielectric relaxation functions

To verify whether the material time obtained from the DDLS intensity autocorrelation functions does also linearize the change of some other quantity during aging, dielectric aging experiments have been performed by Jan P. Gabriel in the Glass and Time group at Roskilde

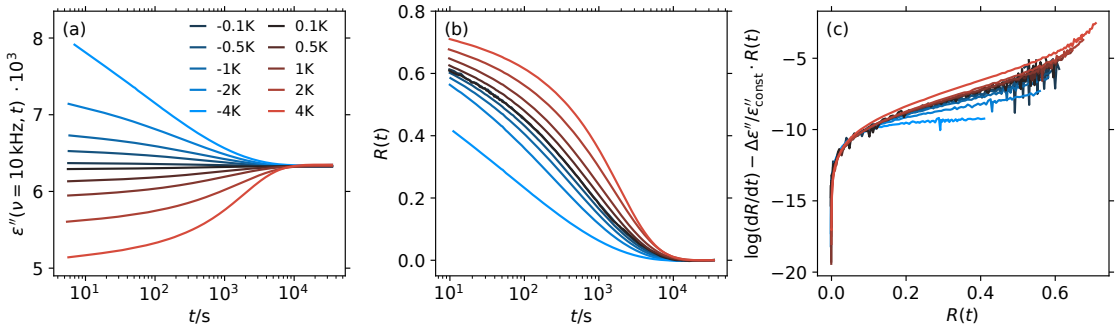

Figure 10.11: (a) Dielectric loss at $\nu = 10\,\mathrm{kHz}$ for aging samples after temperature jumps of different amplitudes to 193 K (b) From these data the dielectric relaxation function $R_\varepsilon(t)$ is derived using Eq. (10.31). No collapse is observed for data obtained after different temperature jumps. (c) Testing single-parameter aging by plotting the left-hand side of Eq. (10.9) as a function of R_ε. Data collapse for smaller jumps, but distinct deviations are observed for the largest jumps, indicating a violation of the single-parameter aging assumptions.

University. The experiments were performed in a custom-built cryostat system that allows to quickly change the sample temperature within a few seconds via a Peltier element [37, 42]. After an equilibrium sample of 1P1P was exposed to a quick temperature change, the complex capacity was measured at the fixed frequency $\nu_0 = 10\,\mathrm{kHz}$, with an Andeen-Hagerling AH 2700A high-precision bridge. From the complex capacity, the time-dependent complex permittivity of 1P1P at 10 kHz was determined and its imaginary part, $\varepsilon''(t) \equiv \varepsilon''(\nu = 10\,\mathrm{kHz}, t)$, was used to calculate the dielectric relaxation function

$$R_\varepsilon(t) = \frac{\varepsilon''(t) - \varepsilon''(t \to \infty)}{\varepsilon''(t=0) - \varepsilon''(t \to \infty)}. \tag{10.31}$$

Fig. 10.11 shows $\varepsilon''(t)$ and $R_\varepsilon(t)$ as a function of t for temperature jumps to 193 K with various different amplitudes ΔT in panels (a) and (b), respectively. Panel (c) shows the results of the single-parameter aging test based on Eq. (10.9), which involves plotting the left-hand side of the equation as a function of $R(t)$. Once the data obey single-parameter aging, all curves should collapse onto a single master curve. Here, the parameter $\varepsilon''_{\mathrm{const}}$ was determined by collapsing $R(t)$ obtained from the $\Delta T = \pm 1\,\mathrm{K}$ temperature jumps onto each other using Eq. (10.10). As is evident from Fig. 10.11c, single-parameter aging breaks down for the $\pm 4\,\mathrm{K}$ data, as it is commonly observed for large-amplitude temperature jumps [42, 277]. This observation might also explain the deviation of the $R_C(t)$-data from the single-parameter aging prediction as shown in Fig. 10.10c.

In a next step, the material time obtained from the DDLS intensity autocorrelations shall be applied to the dielectric relaxation functions. One major issue in this regard is the fact that the two experiments are performed in different laboratories, thus the absolute annealing temperatures of both experiments, $T_{\infty,\mathrm{DDLS}}$ and $T_{\infty,\varepsilon}$, are not the same. Moreover, the DDLS data analyzed in the present chapter were obtained using the LN_2-operated sample cell for which no absolute temperature calibration is available, which introduces further ambiguity. Thus, in order to perform a combined analysis of DDLS and dielectric data, a "retrospective" temperature calibration is required. This can be done by comparing the equilibrium relaxation times at $T_{\infty,\mathrm{DDLS}}$ and $T_{\infty,\varepsilon}$. The DDLS equilibrium relaxation spectrum at $T_{\infty,\mathrm{DDLS}}$ was obtained by Fourier-transforming the electric-field autocorrelation function $g_1(t)$, which was determined from the equilibrium intensity autocorrelation function $g_2(t) = C(\Delta t) + 1$ via the Siegert relation. It is plotted in Fig. 10.12c as the blue triangle symbols and is referred

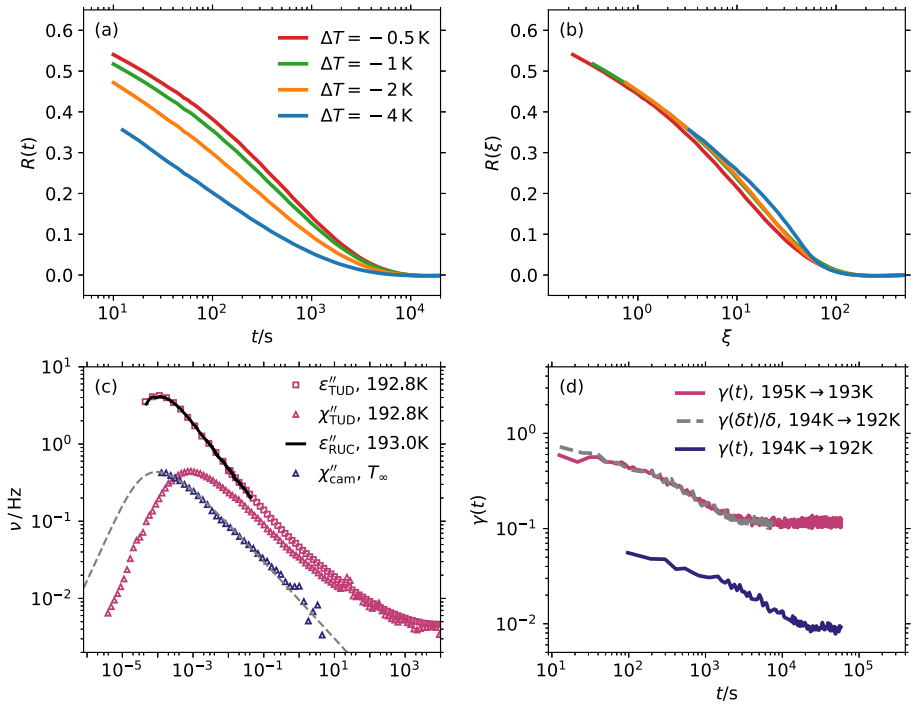

Figure 10.12: R_ε as a function of ξ and related considerations. (a) Selected $R_\varepsilon(t)$-data from Fig. 10.11b for which comparable DDLS-data are available to extract $\xi(t)$. (b) Plotting the same data as $R_\varepsilon(\xi)$ leads to an almost perfect collapse for $\Delta T \leq 2\,\mathrm{K}$ and some subtle deviations for $\Delta T = 4\,\mathrm{K}$. (c) To adapt $\xi(t)$ obtained from DDLS to fit the dielectric experiments, the differences regarding annealing temperatures T_∞ have to be considered. This was done by comparing equilibrium relaxation spectra obtained at the respective T_∞ and priorly presented data from Section 6.1.1. Details can be found in the text. (d) Knowledge of the differences regarding equilibrium relaxation times allows to adapt $\xi(t)$ via TATS, which is confirmed for the material time by comparing data obtained after two $\Delta T = 2\,\mathrm{K}$ temperature jumps. Rescaling by Eq. (10.32) leads to perfect collapse.

to in the legend as χ''_{cam}. An equilibrium dielectric relaxation spectrum of the sample in the Roskilde setup at $T_{\infty,\varepsilon} = 193\,\mathrm{K}$ was obtained using a time-domain experiment. It is included in Fig. 10.12c as the solid black line and is referred to in the legend as $\varepsilon''_{\mathrm{RUC}}$. As discussed in Section 6.1.1, $\chi''(\nu)$ and $\varepsilon''(\nu)$ of 1P1P do not reflect the same aspects of molecular dynamics, as dipolar cross-correlations contribute considerably to the dielectric loss. Thus, χ''_{cam} and $\varepsilon''_{\mathrm{RUC}}$ cannot be compared straightforwardly. To resolve this issue, data from Section 6.1.1 can be used, which provide a connection between $\chi''(\nu)$ and $\varepsilon''(\nu)$ obtained at exactly the same temperatures. One combined data set obtained at $T = 192.8\,\mathrm{K}$ is included in Fig. 10.12c as the pink symbols and referred to in the legend as $\varepsilon''_{\mathrm{TUD}}$, res. χ''_{TUD}. Coincidentally, χ''_{TUD} and $\varepsilon''_{\mathrm{RUC}}$ coincide perfectly, thus χ''_{TUD} can be considered as the representation of the DDLS spectrum one would obtain at $T_{\infty,\varepsilon}$. Comparison of χ''_{cam} and χ''_{TUD} yields $\tau(T_{\infty,\mathrm{DDLS}}) = (8 \pm 1) \cdot \tau(T_{\infty,\varepsilon})$.

The observed difference between the average equilibrium relaxation times at the annealing temperatures implies that the material time $\xi(t)$ obtained from the DDLS intensity autocorrelations cannot be straightforwardly applied to the dielectric aging data. To modify the material time in order for it to be applicable to dielectric aging data, time-aging time superposition (TATS) can be utilized. TATS implies that aging after two temperature jumps with the same amplitudes but to different annealing temperatures, $T_{\infty,1}$ and $T_{\infty,2}$, is identical except for a scaling factor applied to the time-axis that is proportional to the ratio of the equilibrium relax-

ation times at the two temperatures, i.e. proportional to $\delta \equiv \tau(T_{\infty,2})/\tau(T_{\infty,1})$. In addition, it has to be considered that the material-time base unit will be different for the two temperature jumps in an equivalent manner as it has been for different values of a in Fig. 10.8. All together, TATS predicts the material-time clock rates $\gamma_1(t)$ and $\gamma_2(t)$ of the two jumps to $T_{\infty,1}$ and $T_{\infty,2}$, to be related via

$$\gamma_2(t) = \delta\gamma_1(\delta t). \tag{10.32}$$

This conjecture is tested in Fig. 10.12d, where $\gamma(t)$ for two different $\Delta T = -2\,\mathrm{K}$ temperature jumps to different T_∞ is plotted function of t as blue and pink lines, respectively. The dashed gray line represents a rescaled version of the blue curve according to Eq. (10.32). Evidently, the scaling yields a perfect collapse, thus confirming TATS for the material-time clock rate. It has to be noted that in fact, not the temperature-jump amplitudes ΔT need to be identical for both jumps, but rather the ratio of the equilibrium relaxation times before and after the jump, i.e. $\tau(T_{0,1})/\tau(T_{\infty,1})/\tau(T_{0,2})/\tau(T_{\infty,2})$. Obviously, this equation is equivalent to $\Delta T_1 = \Delta T_2$ as long as $\log\tau \propto T$, however discrepancies between both become relevant once the super Arrhenius temperature dependence of relaxation times plays a considerable role, i.e. for large temperature jumps or for largely different T_1 and T_2.

As the ratio of equilibrium relaxation times at the annealing temperatures could be determined via the analysis shown in Fig. 10.12c, Eq. (10.32) allows to obtain a modified version of $\xi(t)$ that compensates for the annealing-temperature discrepancy and thus, can be applied to the dielectric aging data. In addition to the $\Delta T = -2\,\mathrm{K}$ and $-4\,\mathrm{K}$-data shown above, material-time data are available for $\Delta T = -0.5\,\mathrm{K}$ and $-1\,\mathrm{K}$ (similar data for smaller temperature jumps are shown in Section 12.1). The corresponding $R_\varepsilon(t)$-data as a function of t are shown in panel (a) of Fig. 10.12, while the same data as a function of the material time ξ are shown in panel (b). Evidently, the material-time description leads to an almost perfect collapse of the data. Minor deviations from a perfect collapse are observed for the smaller temperature jumps, while slightly larger deviations are observed for the $\Delta T = -4\,\mathrm{K}$-data.

In this regard it has to be kept in mind that the procedure of rescaling the material time via Eq. (10.32) probably is imperfect and discrepancies likely increase for larger jump amplitudes. It remains an open question whether the break-down of single-parameter aging observed for larger temperature jumps in Fig. 10.11c indicates a general break-down of the TN formalism, which would also lead to deviations in Fig. 10.12b, or whether it reflects a violation of the additional single-parameter aging assumptions, which should be irrelevant for the analysis using the experimentally obtained material time in Fig. 10.12b. In this regard it would be insightful to perform DDLS and dielectric aging experiments within the same sample cell. By this, any ambiguities regarding temperature protocols could be ruled out and the results could provide further insight on the limits of single-parameter aging and the TN formalism in general.

Within the scope of the present work, however, it can be concluded that the material time obtained from the DDLS intensity autocorrelations, within the experimental uncertainties, also linearizes data from the dielectric aging experiment. These results can be considered as a first hint towards the existence of one single material time that controls the change of any variable during aging. Obviously, similar tests should be performed for other variables, e.g. for structural ones like density. The latter could be achieved, e.g., by repeating the presented experiments for an unpolar liquid, such that the changes of $\varepsilon'(t)$ at some fixed frequency can be assumed to reflect the change of density. Another approach could be to perform similar experiments using X-rays instead of visible light, which allow to simultaneously probe the dynamics and the structure factor of an aging sample. Computer simulations represent another possibility, as many different variables can be extracted from the trajectories at the

same time and, as will be shown in Section 11.3.3, also the material time can be obtained from computer simulations using an equivalent procedure as shown in Section 10.3.

10.4.2 Confirming material-time translational invariance

Using the experimentally obtained material time $\xi(t)$ allows to verify the initial assumption of material-time translational invariance (MTTI), Eq. (10.11). This is achieved by applying the transformation $t \to \xi(t)$ to the time autocorrelation functions $C(t+\Delta t)$ to obtain the respective material-time autocorrelation functions $C(\xi, \xi+\Delta\xi)$ with $\Delta\xi \equiv \xi(t+\Delta t)-\xi(t)$. Fig. 10.13 plots $C(\xi, \xi+\Delta\xi)$ as a function of $\Delta\xi$ for the same data and using the same color code as in Fig. 10.1. As predicted by MTTI, the autocorrelations are found to collapse as a function of the elapsed material time, with subtle deviations appearing only at small and large $\Delta\xi$. On the one hand, deviations may be caused either by some artifacts that slightly distort the shape of the autocorrelations. On the other hand, the deviations at large $\Delta\xi$ would also be expected in case of a dynamically heterogeneous material time, in the sense that microscopic regions with larger local relaxation times age slower than regions with shorter local relaxation times. This heterogeneous aspect of aging has been discussed previously as a natural implication of the dynamically heterogeneous nature of equilibrium dynamics of supercooled liquids [284–289]. As a matter of fact, no signature of this heterogeneous aging scenario could be identified in some first experiments studying physical aging after exposing a sample to a strong electric field [282]. This observation has been rationalized in terms of rate exchange between slow and fast regions, leading to an average homogeneous behavior [288], or in terms of a lack of correlation between heterogeneous equilibrium dynamics and heterogeneous aging [289]. Recent computer-simulation imply that the homogeneous material time is dominated by the slowest regions within the glass [278]. Further experimental and computational effort is required in these regards and, unfortunately, at the current level of experimental resolution, the DDLS autocorrelation functions cannot provide an unambiguous interpretation on whether aging is heterogeneous or not.

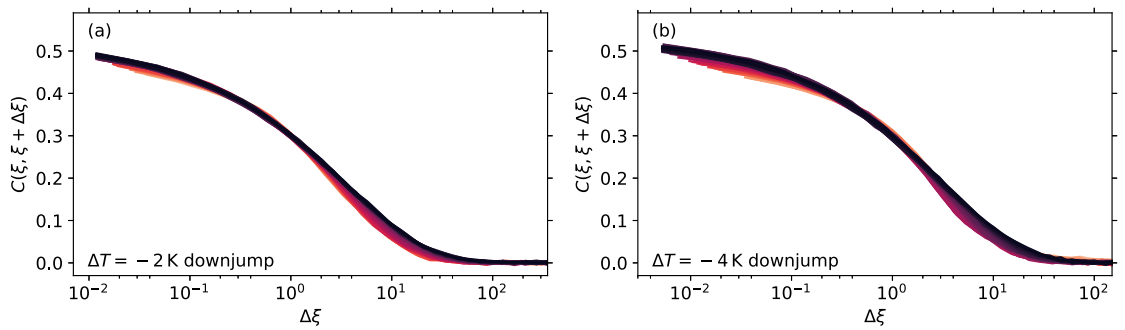

Figure 10.13: Testing MTTI by plotting intensity time autocorrelation functions as a function of the ellapsed material time $\Delta\xi \equiv \xi(t+\Delta t)-\xi(t)$. The panels consider the same data as shown in Fig. 10.1, i.e. data obtained after an $\Delta T = -2$ K down-jump in (a) and a $\Delta T = -4$ K down-jump in (b). Autocorrelations obtained at different t approximately collapse, with small deviations appearing especially at larger $\Delta\xi$.

11

MATERIAL-TIME REVERSIBILITY

Most fundamental laws in physics are time-reversible, i.e. they are invariant under the transformation $t \to -t$. The evident time-irreversibility of everyday live is considered by the second law of thermodynamics, which states that the entropy as a function of time of an isolated system can only increase or stay constant but never decrease. Once a system's entropy increases as a function of time, its time-evolution is no longer invariant under transformation $t \to -t$ and, thus, the system evolution as a function of time is said to be time-irreversible. Supercooled liquids are in thermal equilibrium, i.e. their entropy is constant as a function of time and, thus, their microscopic dynamics are time-reversible. This is reflected, e.g., by the fact that time autocorrelation functions quantifying the microscopic dynamics of supercooled liquids are invariant under time reversal, i.e. under the transformation $t \to -t$.

Interestingly, time-reversal symmetry and time-translational invariance together represent a sufficient condition for the symmetry of the triangular relation: Time-translational invariance, i.e. $C(t_1, t_2) = F(t_2 - t_1)$ for $t_1 < t_2$, and the fact that $F(x)$ is monotonic imply that there exists Φ such that for any $t_1 < t_2 < t_3$, $t_2 - t_1 = \Phi(C_{12})$ and $t_3 - t_2 = \Phi(C_{23})$. Adding these two equations yields

$$t_2 - t_1 - t_2 + t_3 = \Phi(C_{12}) + \Phi(C_{23}) \tag{11.1}$$

$$t_3 - t_1 = f(C_{12}, C_{23}), \tag{11.2}$$

which is the triangular relation, Eq. (10.14). Time-inversion implies that now $-t_3 < -t_2 < -t_1$ and, thus,

$$C_{31} = f(C_{32}, C_{21}), \tag{11.3}$$

which is equivalent to

$$C_{13} = f(C_{23}, C_{12}), \tag{11.4}$$

thus confirming the symmetry of f. It can be concluded that in thermal equilibrium the symmetry of the triangular relation is a trivial consequence of time-reversibility.

Obviously, the evolution of physically aging glasses is not time-reversible: Physical aging involves plasticity, dissipation, entropy production and the time autocorrelation functions as well as the characteristic length scale of dynamical heterogeneity explicitly evolve as a function of time [290]. Despite all that, the validity of triangular relation and its symmetry during physical aging are "inherited" from thermal equilibrium, which in turn implies time-reparametrization invariance as shown by Cugliandolo and Kurchan [279]. Also the TN formalism recovers thermal-equilibrium physics for aging samples by describing aging in terms of a linear convolution integral when time is replaced by material time. Together, these considerations lead to the conjecture of *material-time reversibility*. The basic idea is that the irreversible thermal fluctuations during aging recover the properties of equilibrium fluctuations, meaning they become reversible, when they are considered in terms of material time instead of time.

The following chapter attempts to verify this idea by applying time-series analysis concepts to intensity fluctuations probed by DLS. As the latter reflect fluctuations of molecular orientations res. position within the sample, they can be considered as a proxy for the thermal fluctuations of an aging sample. Section 11.1 presents a brief introduction to time-series analyses, in particular for detecting reversibility, before discussing the main analysis tool used in what remains of the present chapter, i.e. the visibility-graph algorithm. In Section 11.2 material-time reversibility is confirmed for the fluctuations of aging 1P1P samples, while Section 11.3 finally attempts to extend material-time reversibility to other amorphous systems, i.e. an aging colloidal glass, a polymerizing epoxy and a computer-simulated model glass.

11.1 TEST FOR TIME-REVERSIBILITY: VISIBILITY-GRAPH ALGORITHM

Generally speaking, a time series (TS) is a sequence of measurement results at a discrete set of equally spaced points in time. For measurements of some (physical) quantity X with time resolution Δt at points in time $(t_n) = (n \cdot \Delta t, n \in \mathbb{N})$, the TS is given by $(X_n) = (X(t_1), X(t_2), ...)$. Obviously, real-life time series are finite, thus they have some final element $X_N = X(t_N)$.

The concept of TS is universally applied in various scientific fields ranging from physics over statistics and finance to ecological science. Hence, there exist a multitude of statistical tools for TS analysis for various applications. The particular field relevant for the present work is time-reversibility analysis. Here, the aim is to judge as to whether there are statistical differences between a TS $(X_n) = (X_1, X_2, ..., X_N)$ and its own time-reversed counterpart $(X_n^-) = (X_N, X_{N-1}, ..., X_1)$, i.e. under transformation $t \rightarrow -t$. For an excellent review discussing TS analysis tools for testing time-reversibility it is referred to the work of Zanin et al. [291]. Generally speaking, for an irreversible process the probability that some line of events takes place depends on whether the data are analyzed along or against the arrow of time, while it is identical for both directions for a reversible process [292, 293]. Statistical tests attempt to detect these, often subtle, differences via a multitude of approaches ranging from quite simple procedures that, e.g., compare the bicovariances of (X_n) and (X_n^-) [294], to more complicated algorithms for identifying repeating patterns on various different scales and comparing their appearance along and against the arrow of time [295–299]. With recent advances in artificial intelligence, also machine-learning approaches for detecting time-(ir)reversibility have emerged [300].

Many tests for detecting time-irreversibility either focus on small-scale irreversibility, i.e. asymmetry of "local" time-series patterns under time-reversal, or require the user to specify some scale on which irreversibility should be considered, thus introducing additional free parameters. By contrast, irreversibility during physical aging most likely appears on a broad range of more "global" scales. For instance, the irreversible evolution of the time autocorrelations as a function of time proceeds over hundreds or thousands of seconds, while fluctuations might appear to be (almost) reversible on shorter time scales. One family of tests that is suited for the analysis of such global aspects of irreversibility are based on visibility graphs (VG). Here, a TS is mapped onto a directed graph that "inherits" the structure of the TS. The following brief discussion of VGs and related reversibility tests follows Refs. [301–303] by Lacasa et al., who have established the VG as a general tool for TS analysis in 2008 and for reversibility-testing in 2012.

Considering again the real-valued TS $(X_n) = (X_1, X_2, ..., X_N)$, the corresponding VG is composed of N nodes, each of which represents one element of the TS. Two nodes $i < j$ are

connected by a directed edge if element i of the TS can "see" element j in a plot where (X_n) is plotted over (t_n), i.e. one can draw a line from i to j that does not intersect with any other element in between. This visibility criterion is illustrated in the left side panels of Fig. 11.1 for a TS with six elements, the VG of which is shown below. Trivially, each node i has an outgoing node to the subsequent node $i+1$, as no in-between nodes exist. On a longer scale, node 1 is connected to node 4, while node 2 is *not* connected to node 4 because visibility is "blocked" by node 3. Mathematically, the visibility criterion can be formulated as a convex criterion, i.e. an outgoing edge from i to j with $i < j$ exists if

$$X_k < X_i + \frac{k-i}{j-i}(X_j - X_i), \quad \forall k: \; i < k < j. \tag{11.5}$$

Here, the direction of the arrow of time is considered by the restriction to $i < j$. Inverting the arrow of time is equivalent to inverting this criterion, or, alternatively, inverting the direction of any edge, i.e. outgoing edges become incoming ones and vice versa. The basic idea of the VG-based reversibility test is that if the TS (X_n) is time-reversible, the two VGs constructed from (X_n) and (X_n^-) have the same properties.

Typically, the property considered in this regard is the degree distribution of the VG, i.e. the probability $P(k)$ that a randomly chosen node of the graph has exactly k edges. Because VGs considered for testing reversibility are directed, each VG is, in fact, associated with two degree distributions $P_{\text{in}}(k)$ and $P_{\text{out}}(k)$, which reflect the probabilities that a randomly chosen node has k incoming, res. outgoing edges. Considering that time-reversal inverts the direction of each edge, it can be derived [303] that the incoming and outgoing degree distributions of a time-reversible TS are asymptotically identical for $n \to \infty$, i.e.

$$P_{\text{in}}(k) = P_{\text{out}}(k). \tag{11.6}$$

This is illustrated in the right side panels of Fig. 11.1 for a correlated Gaussian random process, i.e. an Ornstein-Uhlenbeck process without drift-term [304]. By definition, it is time-reversible. $P_{\text{in}}(k)$ and $P_{\text{out}}(k)$ are shown to be (almost) identical in the lower panel, both averaged over 10^4 equivalent TS obtained from the same random process to reduce noise. VGs are determined from the TS data by using the TS2VG python package [305], which is based on the algorithm proposed by Lan et. al [306].

The TS shown in Fig. 11.1 is finite like any other real-life TS. Thus, Eq. (11.6) does not apply exactly leading to minor differences between $P_{\text{in}}(k)$ and $P_{\text{out}}(k)$ reflecting the finite statistical power. To quantify such discrepancies, a measure for the dissimilarity of $P_{\text{in}}(k)$ and $P_{\text{out}}(k)$ can be considered. One possible realization is the Kullback-Leibler (KL) divergence [307]

$$D_{\text{KL}}\big(P_{\text{in}}||P_{\text{out}}\big) = \sum_k P_{\text{in}}(k) \ln \frac{P_{\text{in}}(k)}{P_{\text{out}}(k)}, \tag{11.7}$$

which can be considered as a statistical distance between the two probability distributions $P_{\text{in}}(k)$ and $P_{\text{out}}(k)$. $D_{\text{KL}}(P_{\text{in}}||P_{\text{out}}) = 0$ for $P_{\text{in}} = P_{\text{out}}$ and > 0 in any other case. D_{KL} is not symmetric, i.e. $D_{\text{KL}}(P_{\text{in}}||P_{\text{out}}) \neq D_{\text{KL}}(P_{\text{out}}||P_{\text{in}})$. To obtain a symmetric version of the KL divergence, the Jensen-Shannon (JS) divergence [308]

$$D_{\text{JS}}(P_{\text{in}}||P_{\text{out}}) = \frac{1}{2}\Big(D_{\text{KL}}\big(P_{\text{in}}||\bar{P}\big) + D_{\text{KL}}\big(P_{\text{out}}||\bar{P}\big)\Big), \tag{11.8}$$

with $\bar{P} = (P_{\text{in}} + P_{\text{out}})/2$, can be considered instead. In order to apply Eq. (11.8) to experimental data it has to be considered how to deal with k where $P_{\text{in}}(k) = 0$ or $P_{\text{out}}(k) = 0$, as these would

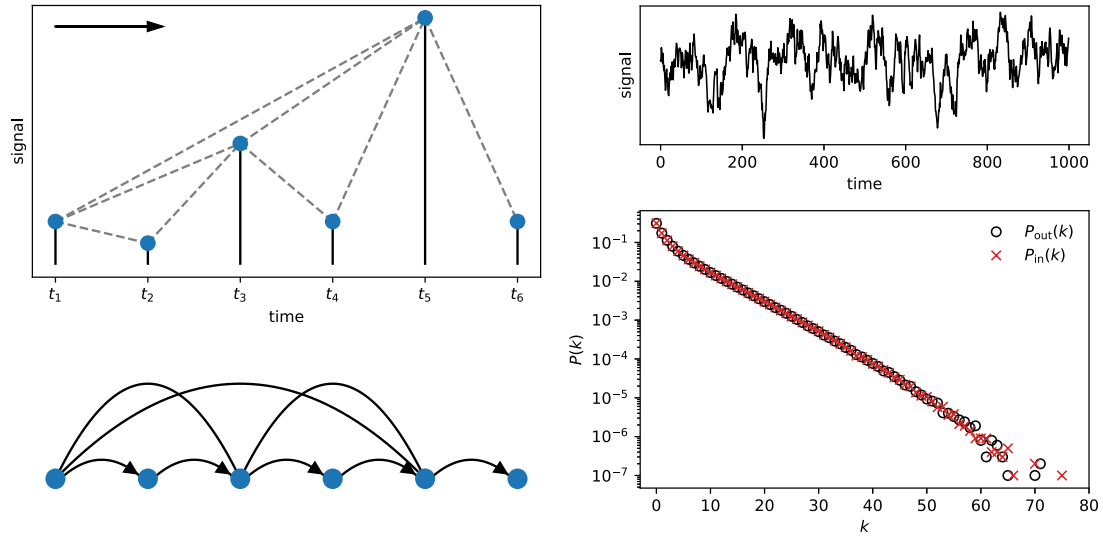

Figure 11.1: The visibility-graph formalism and the related test for TS-reversibility.
Left side: The upper panels illustrates how the "visibility criterion" Eq. (11.5) applies to an exemplary TS with six elements , $(X(t_1),...,X(t_6))$. Visibility is assessed along the arrow of time, i.e. in direction of increasing time-index. The gray dashed line between two elements $X(t_i)$ and $X(t_j)$ indicates "visibility", i.e. the view from $X(t_i)$ to $X(t_j)$ is not "blocked" by another datum in-between. The corresponding VG is shown in the lower panel. It contains a node for each TS element, while nodes are connected by a directed edge in case of visibility. Here, the direction of the edge goes along the arrow of time. Note that for clarity arrow-heads are only included for selected edges.
Right side: The VG formalism is applied to an exemplary TS (upper panel) obtained from a correlated Gaussian random process, which is fully time-reversible. As a consequence, the incoming and outgoing degree distributions $P_{in}(k)$ (black symbols) and $P_{out}(k)$ (red symbols) as a function of k collapse in the lower panel. Deviations between both would be observed in case of time-irreversibility.

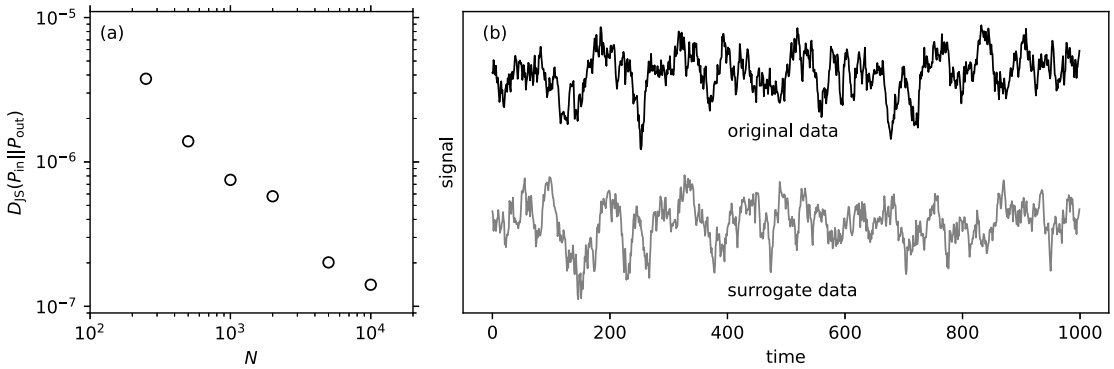

Figure 11.2: (a) D_{JS} obtained for TS that reflect a correlated Gaussian random process (see Fig. 11.1) as a function of the TS length N. Here, the VG-degree distributions P_{in} and P_{out} are averaged over 10^4 TS to reduce noise. $D_{JS} \to 0$ while $N \to \infty$ is observed, as it is expected for a reversible process like a Gaussian random process. Despite the process being reversible, $D_{JS} > 0$ for finite N. A way for determining the lowest possible values D_{JS} that could be obtain for a certain TS if it were fully reversible are surrogates. Surrogates are defined to resemble the TS they are based on in various aspects, however, are, per definition, reversible. Panel (b) shows a surrogate (gray line) determined based on the original data (black line) using the iAAFT algorithm.

imply division by zero in Eq. (11.7). To avoid such instances, it is a standard procedure to add a small bias to P_{in} or P_{out} [303], e.g. here, $P_{\text{in}} + 10^{-10}$ is analyzed instead of P_{in}. Before the VG-based test for reversibility is applied to experimentally obtained intensity TS, a few general aspects are discussed.

First of all, the degree of a certain node can, in principle, reflect the properties of a quite large portion of the TS, which is the reason why the VG-based reversibility test is said to assess "global" aspects of reversibility [302, 303]. In reality, of course, each node has a limited "visual range", as reflected by the fact that nodes with large degrees become very rare, see the lower right panel of Fig. 11.1. This implies that a VG has some effective accessible "time scale" on which reversibility can be judged, which, however, depends on the exact properties of the TS, e.g. how fast are the fluctuations or how are the TS values distributed. In principle, this effective accessible time scale can be slightly varied by changing the number of elements of the TS, e.g., by introducing some degree of averaging, which will also be applied for the experimental data discussed below.

As already mentioned, fully-reversible but finite TS never have exactly identical incoming and outgoing degree distributions, thus $D_{\text{JS}}(P_{\text{in}}||P_{\text{out}}) > 0$. Reasons for this are the finite size effects at the beginning and the end of the TS, as well as limited statistical power. In fact, the lowest value of D_{JS} that could be obtained for a finite TS with N elements is inversely proportional to N, because finite size effects become less relevant at large N [302, 303]. An illustration of this is given in Fig. 11.2, where D_{JS} of the Gaussian random process is considered as a function of the number of elements N of each TS. Again, the degree distributions are averaged over 10^4 TS to reduce statistical noise. Evidently, $D_{\text{JS}} \to 0$ for $N \to \infty$, as it is expected for a reversible process like a Gaussian random process.

The fact that $D_{\text{JS}}(P_{\text{in}}||P_{\text{out}}) > 0$ even for reversible but finite TS poses a problem: How can an irreversible TS be distinguished from a reversible one if both yield values larger zero? For mathematically defined TS, the solution to this problem is to perform an analysis of the N-dependence in order to verify whether $D_{\text{JS}} \to 0$ for $N \to \infty$ [303]. Obviously, this is usually impossible to test for real-life TS, as the amount of available data is limited. Thus, another solution is to construct surrogates of the experimentally obtained TS. A surrogate is constructed as a stationary Gaussian linear stochastic process that resembles the original TS in certain basic feature, i.e. it has the same distribution of TS values and the same power spectrum [309]. However, the fact that the surrogate is obtained from a Gaussian process implies that it is, per definition, time-reversible. Thus, comparing the D_{JS}-values obtained for the surrogate, $D_{\text{JS}}^{\text{surro}}$, provides a lower "reversibility limit" for D_{JS}. It reflects the lowest possible values of D_{JS} that one could obtain for a TS with the given characteristics, thus, for finite TS $D_{\text{JS}} > D_{\text{JS}}^{\text{surro}}$ can be considered as the new criterion for irreversibility. In the present work, surrogates are constructed using the iterated Amplitude Adjusted Fourier Transform (iAAFT) algorithm [310] implemented in the IAAFT python package [311].

Finally, it remains to be noted that the large majority of statistical tests for reversibility, including VG-based tests, deal with the issue that usually only a single or a few equivalent TS are available that reflect some stochastic process, e.g. in finance [312] or climate science [313]. This usually requires to use some form of hypothesis testing under the null-hypothesis of reversibility. In the present work, thousands of intensity TS are available via the msDLS approach, thus the distribution of D_{JS}-values can be approximated and compared without requiring any hypothesis testing.

11.2 APPLICATION TO EXPERIMENTAL DATA

The discussed VG-based test for reversibility is now applied to intensity TS obtained for physically aging and equilibrium samples of 1P1P in order to verify the conjecture of material-time reversibility. The following two results are required in order to confirm material-time reversibility:

(i) Intensity TS sampled equidistantly in time, (I_t), are found to be *irreversible*. This observation confirms that the VG-based test for TS reversibility can, in principle, detect the irreversibility of thermal fluctuations during aging.

(ii) Intensity TS sampled equidistantly in material time, (I_ξ), are found to be *reversible*. This could be confirmed by showing that the obtained "degree of irreversibility" in the form of D_{JS} is comparable to the one for intensity TS obtained from equilibrium samples. The latter are assumed to be time- and material-time reversible.

In a first step, corresponding intensity TS (I_t) and (I_ξ) have to be extracted from the recorded speckle patterns. This procedure is explained in Section 11.2.1. A necessary requirement for material-time reversibility is material-time stationarity, which is tested for in Section 11.2.2. Finally, material-time reversibility is verified in Section 11.2.3.

11.2.1 Obtaining intensity time-series

The recorded speckle-pattern movies are sampled with a fixed exposure time of Δt =0.2 s and comprise approx. $4 \cdot 10^5$ pixels. To obtain reliable results from the VG-based reversibility test, it has turned out to be favorable to average over 10^4 statistically independent TS reflecting the same process. Therefore, a set of 10^4 uniformly spaced pixels within the speckle images is chosen from which intensity TS are extracted. Here, the uniform spacing of the pixels ensures that the corresponding intensity fluctuations can be assumed to be statistically independent. In order to obtain a distribution of the reversibility-test result in order to extract an uncertainty for D_{JS}, the analysis is repeated for a total of ten different sets of 10^4 uniformly spaced pixels. In the following, the procedure for extracting (I_t) and (I_ξ) from the intensity raw-data of a single pixel is described, which was analogously applied to the combined number of 10^5 analyzed pixel within the ten different sets of 10^4 pixels each.

The intensity TS are constructed from the raw $I(t)$-data within the time interval $[0, t_{\mathrm{f}}]$, where t_{f} is chosen such that significant changes of the material-time clock rate are observed within the entire interval, i.e. such that $|\mathrm{d}\gamma(t)/\mathrm{d}t| > 0$. Later times are excluded, as here the sample is very close to thermal equilibrium and, thus, the reversibility of thermal fluctuations holds trivially. To obtain intensity TS (I_t) res. (I_ξ) of length N, the interval $[0, t_{\mathrm{f}}]$ is divided into N sub-intervals, the lengths of which are chosen to either be constant in units of time t, or res. constant in units of material time ξ. Within each sub-interval, the average intensity is calculated from the raw $I(t)$-data. Finally, the intensity TS are constructed such that the j^{th} element of the TS is given by the average intensity obtained from the respective j^{th} sub-interval.

The discussed procedure for constructing TS may be thought of as measuring the scattered intensity using a camera with an exposure time which is chosen to either be constant in units of t, as it is done in conventional cameras, or in units of ξ. For aging samples, the latter implies that the exposure time is explicitly time-dependent in units of t. While this is rather uncommon for conventional cameras, it would be well-possible to obtain (I_ξ) directly from an experiment by accordingly programming the camera to use a time-dependent exposure time

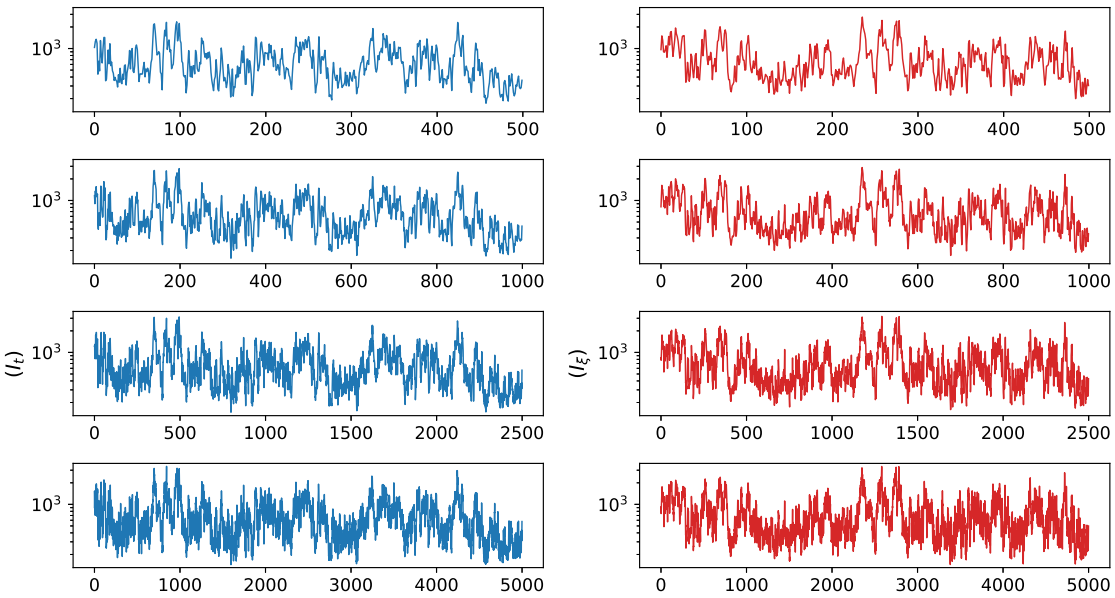

Figure 11.3: Intensity TS reflecting the intensity fluctuations within one exemplary pixel after the $\Delta T = -4\,\mathrm{K}$ temperature down-jump. The TS are sampled equidistantly in time, (I_t) (left side panels), and in material time, (I_ξ) (right side panels), respectively. Each row reports TS-data with a different number of elements $N = 500, 1000, 2500, 5000$ (from top to bottom).

and to normalize the data with regard to the exposure time, such that an intensity instead of an absolute photon-count is obtained. Of course, choosing the exposure times requires preceding knowledge of $\xi(t)$, which could be realized by repeating a temperature protocol twice for the same sample. While there obviously is no reason to do this, because the post-experimental data-treatment is much simpler, these considerations are meant to show that the construction of (I_ξ) does not involve any "unnatural" data treatment.

In order to ensure that the qualitative results are independent of the number of TS elements N, the procedure discussed above is performed for various different $N = 500, 1000, 2500, 5000$. Fig. 11.3 presents (I_t) (left side) and (I_ξ) (right side) for different N (rows) obtained from the same exemplary pixel and after the $\Delta T = -4\,\mathrm{K}$ down-jump. Evidently, the choice of N does not affect the low-frequency intensity fluctuations, while high-frequency fluctuations are suppressed for smaller N due to the enhanced degree of averaging. While differences between (I_t) and (I_ξ) are visible, their (ir)reversibility is difficult to judge by bare eye.

11.2.2 Time-series stationarity

A necessary condition for TS reversibility is TS stationarity [291, 292]. The exact definition of stationarity is that two TS $(X(t_1), ..., X(t_N))$ and $(X(t_1 + l), ..., X(t_N + l))$ have the same joint probability distributions for all lag times l. Obviously, this definition is impossible to confirm for real-life TS, such that weaker definitions of stationarity are commonly used. One example is weak stationarity, which is defined as the mean value $\mu(t)$ and the autocovariance $\mathrm{cov}(t, t+\Delta t)$ being independent of t. Instead of analyzing $\mathrm{cov}(t, t+\Delta t)$ of a TS, equivalently its spectral density can be considered, which is the Fourier transform of $\mathrm{cov}(t, t+\Delta t)$. [314].

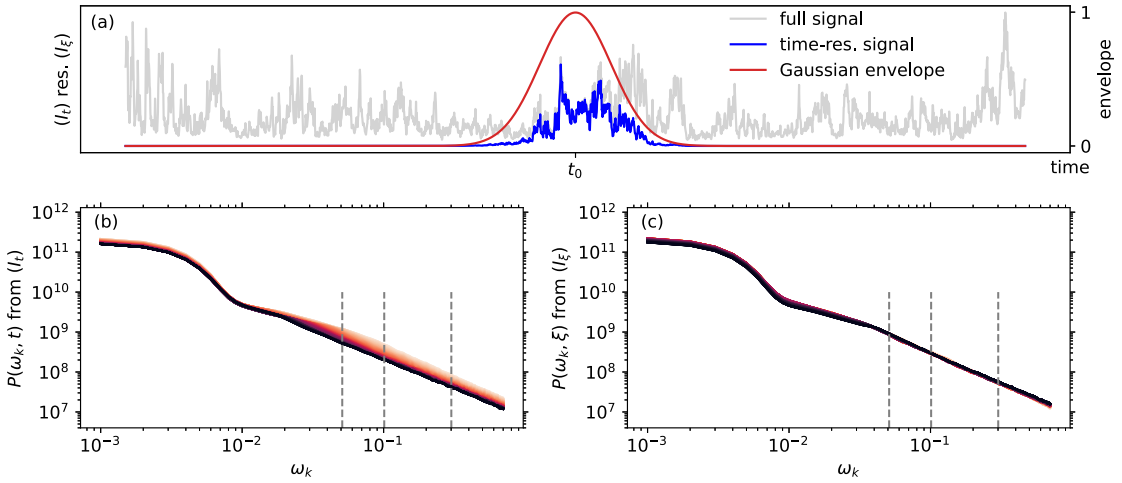

Figure 11.4: Time-resolved Fourier analysis of intensity TS to assess stationarity. (a) Illustration of the procedure to obtain a time-resolved res. material-time-resolved representation of an intensity TS by multiplication with a Gaussian envelope with mean t_0, res. ξ_0 (red). The result is a time-resolved wavelet representation (blue) of the original TS (I_t) res. (I_ξ) (gray). Repeating this procedure for different t_0 allows to obtain time-resolved res. material-time-resolved periodograms $P(\omega_k, t)$ and $P(\omega_k, \xi)$. Panels (b) and (c) show these periodograms as a function of ω_k for different t res. ξ. The latter are indicated by the colors ranging from light to dark for increasing t res. ξ. The dashed gray lines indicate the discrete Fourier frequencies ω_k the periodograms are analyzed at in Fig. 11.5.

This section presents a time-resolved analysis of the the spectral densities of (I_t) and (I_ξ). Here, from the discrete Fourier transform of the TS,

$$A_k = \sum_{n=0}^{N-1} X_n \cdot \exp(-i\omega_k n) \text{ with } \omega_k = 2\pi k/N, \tag{11.9}$$

which is calculated using the fast-Fourier transform (FFT) algorithm, the periodogram

$$P(\omega_k) = |A_k|^2 \tag{11.10}$$

is determined and used as an estimator for the spectral density $f(\omega)$ [314]. It is noted that the scaling factor between the temporal frequencies ω and the discrete Fourier frequencies ω_k is not considered below, as it does not affect any of the results.

To introduce temporal resolution, only short sub-sequences of the intensity TS (I_t) and (I_ξ) are analyzed, which yields time-resolved periodograms $P(\omega_k, t)$ and material-time resolved periodograms $P(\omega_k, \xi)$. As, however, cutting out a short sub-sequence of a TS using a rectangular envelope introduces significant artifacts to the discrete Fourier transform, time-resolution is implemented by multiplying the TS by a Gaussian function with mean t_0 (res. ξ_0). This procedure is illustrated in Fig. 11.4a, where an original intensity TS (gray) is multiplied by an Gaussian envelope with mean t_0 (red), which yields a time-resolved wavelet representation of the TS around $t = t_0$, res. $\xi = \xi_0$ (blue).

Time-resolved periodograms of (I_t) and (I_ξ) as a function of ω_k are shown in panels (b) and (c) of Fig. 11.4, respectively. The colors indicate different t, res. ξ similar to the time-resolved autocorrelations in Fig. 10.1. The low-frequency contribution to $P(\omega_k, t)$ res. $P(\omega_k, \xi)$ represents the Fourier-transform contribution of the Gaussian envelope, while the data at higher frequencies reflect the spectral density of the intensity fluctuations associated with

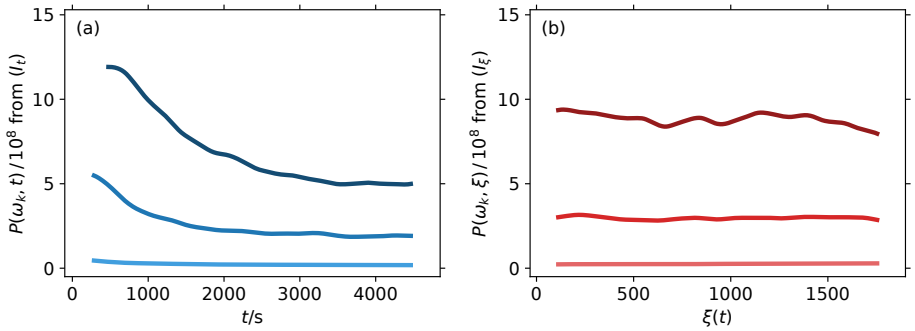

Figure 11.5: Analyzing the stationarity of (a) (I_t) and (b) (I_ξ) by considering the spectral density, estimated by the periodograms $P(\omega_k, t)$ and $P(\omega_k, \xi)$, at three fixed discrete Fourier frequencies ω_k (different colors). These three frequencies are indicated in Fig. 11.4 by the dashed gray lines. While $P(\omega_k, t)$ is explicitly t-dependent and, thus, non-stationary, $P(\omega_k, \xi)$ is constant as a function of ξ, confirming material-time stationarity of the intensity fluctuations.

the microscopic dynamics within the sample. Evidently, (I_t) is non-stationary, as the spectral density explicitly depends on t. By contrast, the periodograms obtained from (I_ξ) collapse for different ξ_0, thus (I_ξ) can be considered being stationary. The same conclusions are drawn from Fig. 11.5, where $P(\omega_k, t)$ res. $P(\omega_k, \xi)$ are plotted at three fixed ω_k, which are indicated in Fig. 11.4 by the vertical dashed lines. While the spectral density evaluated at fixed frequencies is explicitly time-dependent for (I_t), it is approximately constant for (I_ξ). To summarize, while intensity TS during aging and sampled equidistantly in t are non-stationary, they are found to be stationary when sampled equidistantly in material time. The latter observation is a necessary condition for material-time reversibility to be valid, which will be verified in the following section. Finally, it remains be noted that stationarity of intensity TS sampled equidistantly in material time is equivalent to MTTI, due to the one-to-one relation between the spectral density and the autocorrelation function.

11.2.3 Time-series reversibility

The conjecture of material-time reversibility is tested for intensity TS with $N = 2500$ obtained in thermal equilibrium and during physical aging after the $\Delta T = -2\,\mathrm{K}$ and the $\Delta T = -4\,\mathrm{K}$ down-jump. The main results of this section are summarized in Fig. 11.6, where $D_{\mathrm{JS}}(P_{\mathrm{in}}||P_{\mathrm{out}})$ is plotted as a function of ΔT. It can be considered to quantify the "degree of irreversibility" of a TS. Red symbols indicate results for TS sampled equidistantly with regard to material time and blue refer to TS sampled equidistantly in time. Each point reflects the average $D_{\mathrm{JS}}(P_{\mathrm{in}}||P_{\mathrm{out}})$-value obtained from ten equivalent analysis of 10^4 TS each (for details see Section 11.2.1), while the error bars indicate the corresponding standard deviations. In addition, the "reversibility limit" of these TS was determined via a surrogate analysis. It is indicated by the gray area, which corresponds to the σ-interval obtained for the distribution of $D_{\mathrm{JS}}(P_{\mathrm{in}}||P_{\mathrm{out}})$-values of surrogates and can be interpreted as the range of values for which the TS can be considered reversible.

As a first result, Fig. 11.6 rightfully indicates equilibrium intensity TS ($\Delta T = 0$) to be reversible. This finding can be regarded as a consistency requirement for applying the VG-based reversibility test to assess the reversibility of intensity TS. Unsurprisingly, the same

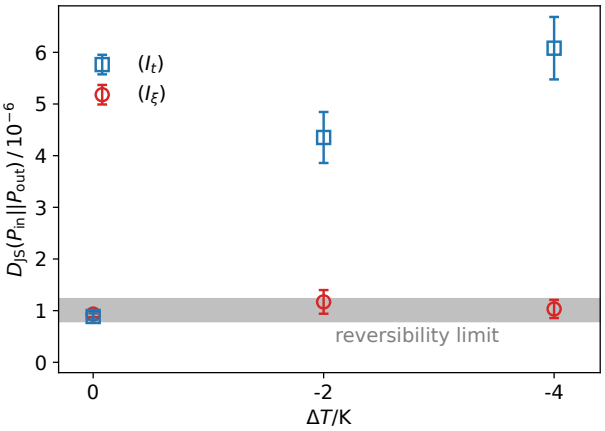

Figure 11.6: Analyzing the reversibility of (I_t) and (I_ξ) obtained for equilibrium and aging samples of 1P1P using the VG-based test for TS-reversibility, see Section 11.1. The Jensen-Shannon divergence D_{JS} obtained for (I_t) (blue symbols) and (I_ξ) (red symbols) is plotted as a function of the temperature-jump amplitude ΔT after which the TS data were obtained. $\Delta T = 0$ refers to a sample in thermal equilibrium. The error bars reflect the standard deviation of the distribution of D_{JS}, which was estimated by repeating the reversibility analysis for ten different sets of intensity TS. The reversibility limit was determined via a surrogate analysis, see Section 11.1, and is illustrated by the gray shaded area, the width of which was determined using an equivalent procedure as for the determining the error bars.

$D_{JS}(P_{in}||P_{out})$-values are obtained for (I_t) and (I_ξ), because in equilibrium $t \propto \xi$ and thus, $(I_t) \approx (I_\xi)$ except for small deviations due to experimental noise.

By contrast, significantly different $D_{JS}(P_{in}||P_{out})$-values are obtained for (I_t) and (I_ξ) for the aging samples: While the results for (I_ξ) are found to be within the reversibility limit and close to the ones obtained for the equilibrium TS, the degree of irreversibility obtained for (I_t) significantly exceeds the reversibility limit by up to a factor six. To summarize, these results confirm material-time reversibility according to the criteria formulated in the beginning of the present section: Irreversible (I_t) confirm that the applied reversibility-test is capable of resolving the irreversibility of thermal fluctuations during aging. Moreover, intensity fluctuations considered as a function of material time are equally reversible as corresponding equilibrium fluctuations and surrogates. Before verifying the validity of material-time reversibility for other aging systems, the remainder of the present section reports some additional details about the test for material-time reversibility, namely a comparison of the full degree distributions and a confirmation that the results presented in Fig. 11.6 are obtained independent of the number of TS elements N.

To obtain a more in-depth understanding how the different $D_{JS}(P_{in}||P_{out})$-values shown in Fig. 11.6 result from the respective degree distributions, Fig. 11.7 presents a detailed analysis of $P_{in}(k)$ and $P_{out}(k)$ as a function of the degree k for equilibrium intensity TS (left side panels) and for TS obtained after the $\Delta T = -4\,\mathrm{K}$ down-jump (right side panels). For equilibrium TS in panel (a), $P_{in}(k)$ and $P_{out}(k)$ are found to collapse for (I_t) (blue and green color) as well as (I_ξ) (red and orange color). Note that for clarity, the degree distributions obtained for (I_ξ) are shifted relative to those for (I_t) along the k axis. Otherwise all data would collapse. Subtle deviations between $P_{in}(k)$ and $P_{out}(k)$ are observed especially at large k for (I_t) of an aging sample in panel (b), while those for (I_ξ) show no visible deviation.

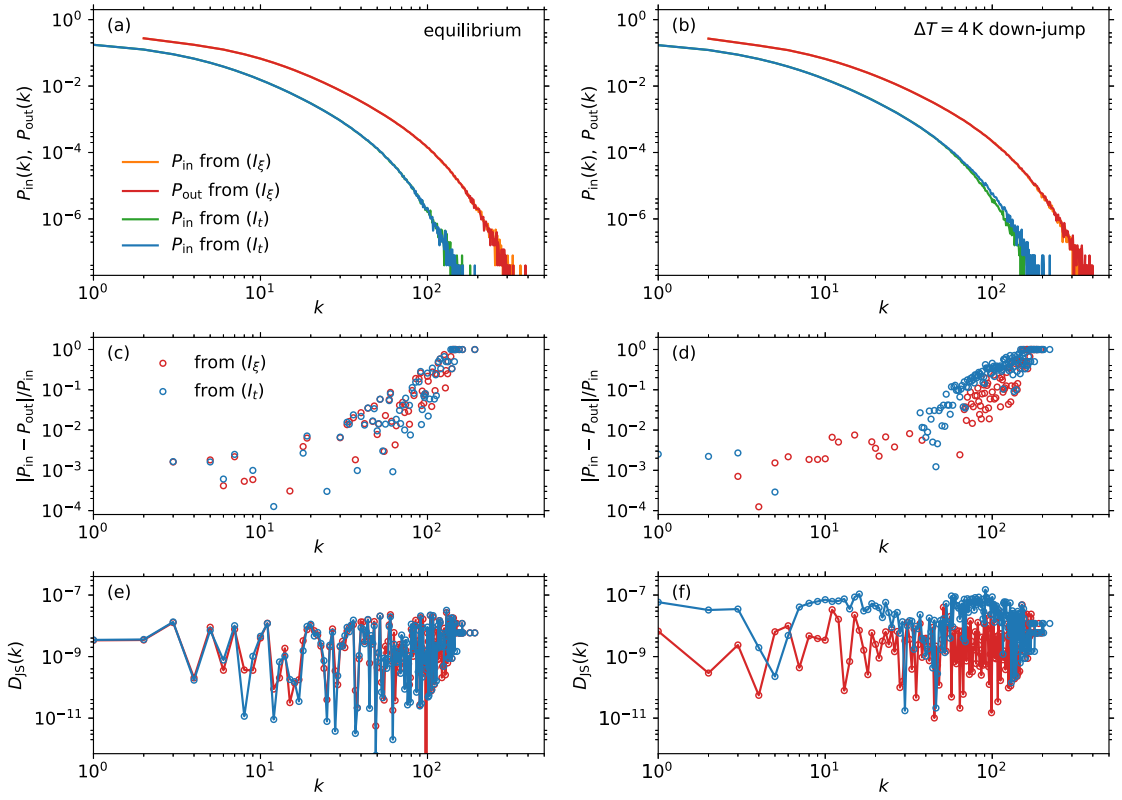

Figure 11.7: Detailed analysis of the VG-degree distributions obtained from (I_t) (blue and green colors) and (I_ξ) (red and orange colors) in equilibrium (left side) and after the $\Delta T = 4\,\mathrm{K}$ down-jump (right side). (a) and (b) Incoming and outgoing degree distributions P_{in} and P_{out} as a function of the degree k. (c) and (d) Relative deviations between P_{in} and P_{out}, Eq. (11.11). (e) and (f) Per-degree contribution, $D_{\mathrm{JS}}(k)$, to the total Jensen-Shannon divergence, D_{JS}.

As discrepancies between $P_{\mathrm{in}}(k)$ and $P_{\mathrm{out}}(k)$ are difficult to identify in panels (a) and (b), panels (c) and (d) report the relative deviation between both, i.e.

$$\Delta P(k) = \frac{|P_{\mathrm{in}}(k) - P_{\mathrm{out}}(k)|}{P_{\mathrm{in}}(k)}. \tag{11.11}$$

The largest relative deviations are found for the degree distributions reflecting (I_t) of the aging sample, as evident in panel (d). All other data show similarly small relative deviations. To indicate how these deviations contribute to D_{JS}, the the contribution to D_{JS} at each k

$$D_{\mathrm{JS}}(k) = P_{\mathrm{in}}(k) \ln \frac{P_{\mathrm{in}}(k)}{\tilde{P}(k)} + P_{\mathrm{out}}(k) \ln \frac{P_{\mathrm{out}}(k)}{\tilde{P}(k)} \tag{11.12}$$

such that

$$D_{\mathrm{JS}} = \sum_k D_{\mathrm{JS}}(k) \tag{11.13}$$

is considered in panels (e) and (f). It is found for (I_t) in panel (f) that the excess contributions to D_{JS} are observed at almost all k. Small k are usually associated with nodes that probe the TS quite locally due to having very limited "visibility" of later portions of the TS, while, following similar arguments, large k assess more global aspects of reversibility. Thus, it can be concluded that thermal fluctuations during aging are irreversible on various different scales. Remarkably, replacing time by material time yields reversible fluctuations on all these different scales.

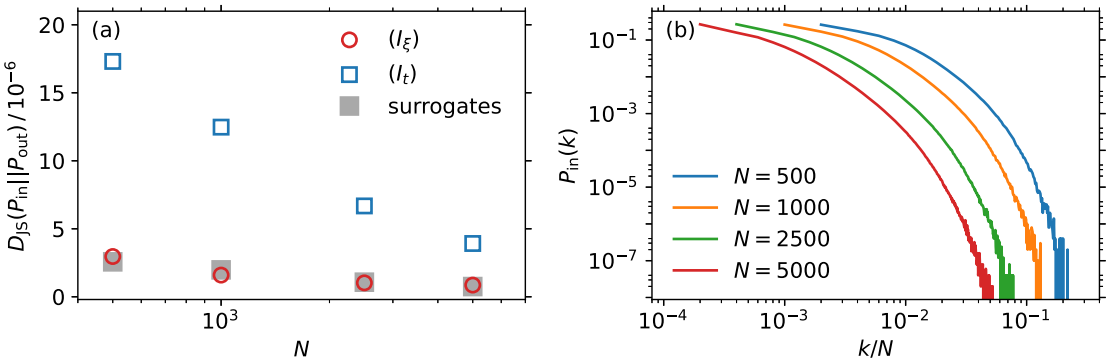

Figure 11.8: Analyzing how the reversibility analysis of (I_t) and (I_ξ) obtained after the $\Delta T = 4\,\mathrm{K}$ down-jump depends on the number of TS elements N. (a) D_{JS} obtained for (I_t) (blue), (I_ξ) (red) and corresponding surrogates (gray) as a function of N. The irreversibility of (I_t) is best observed for small N, which can be rationalized in terms of the degree distributions plotted as a function of the relative degree k/N in panel (b). VGs obtained for TS with smaller N assess (ir)reversibility on a more global scale than for larger N, which helps to detect the global aspects of irreversibility during aging.

Finally, it is confirmed that material-time reversibility discussed in the context of Fig. 11.6 for intensity TS with $N = 2500$ elements is observed independently of the particular choice of N. Fig. 11.8a shows D_{JS} for (I_t), (I_ξ) and corresponding surrogates obtained for the $\Delta T = -4\,\mathrm{K}$ down-jump as a function of N. Indeed, the qualitative findings discussed above are the same for all N, i.e. (I_t) is found to be irreversible, while (I_ξ) is reversible. The observed discrepancy between D_{JS} for (I_t) and (I_ξ) increases for decreasing N, which can be rationalized in terms of the degree distributions $P_{in}(k)$ res. $P_{in}(k)$. The latter are plotted as a function of k/N in panel (b), i.e. the degree is considered relative to the total number of TS elements res. nodes of the corresponding VG graph. Evidently, the average node is connected to a large portion of the VG graph for smaller N, thus more global aspects of reversibility are assessed for smaller N. As the irreversibility during aging is of global nature due to the gradual change of the material-time clock rate as a function of time, the irreversibility of (I_t) is detected more strongly for small N. Material-time reversibility is, however, detected independent of N.

11.3 RESULTS FOR OTHER AMORPHOUS SYSTEMS

After having established material-time reversibility for the physical aging of an organic molecular glass, the following sections explore how the concept translates to other aging amorphous systems. So far, physical aging was studied starting from and ending in an equilibrium supercooled-liquid state. By contrast, an aging colloidal solution that gradually solidifies into a colloidal glass without reaching an equilibrium state on any accessible time scale is considered. Subsequently results for a chemically aging system, i.e. a polymerizing epoxy that transforms from a monomeric liquid state into a polymeric glassy state are discussed. Despite the distinct differences compared to the aging molecular glass discussed above, material-time reversibility is equally observed for both of these systems. Finally, a computer-simulated model glass is considered that ages after an instantaneous temperature change. Instead of using the DLS intensity autocorrelations, here the material time time is extracted from the per-particle potential energy autocorrelations. The presented analyses employ the same tools as explained above, thus the procedures are only discussed briefly.

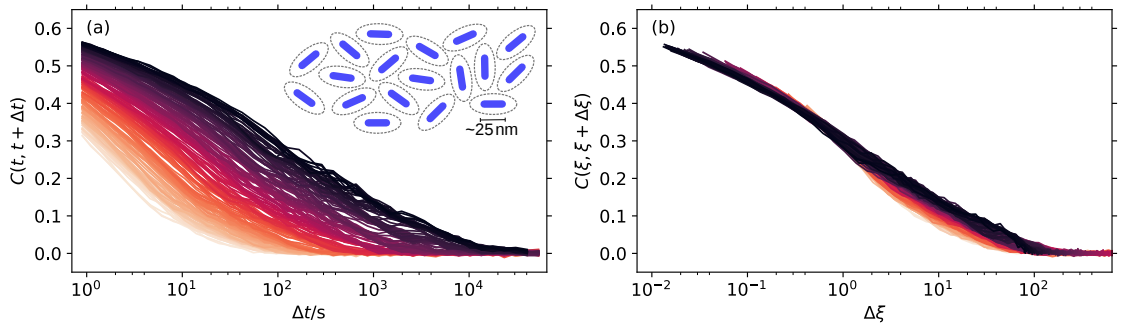

Figure 11.9: Intensity autocorrelation functions $C(t, t+\Delta)$ obtained for a physically aging Laponite suspension (3 wt%) in deionized water of pH 10. (a) Autocorrelations as a function of Δt, where colors indicate different t and (b) as a function of the elapsed material time $\Delta\xi$. The material time ξ was determined using the procedure discussed in Section 10.3 using $a = 0.3$.

11.3.1 Laponite

Laponite is synthetic clay that, once suspended in water, ages and gradually solidifies into different arrested states, i.e. into a colloidal gel, a colloidal glassy state or a nematic phase, depending on the exact experimental conditions. Its rich variety of amorphous states lead to Laponite being investigated in a fundamental-science context [315–324], as well as with regard to various applications as a rheology-modifier [325, 326] or as nanomaterial in biology or medicine [327].

Laponite-particles are disk-shaped with $\sim 25\,\text{nm}$ radius and $\sim 1\,\text{nm}$ thickness and attain positive electric charge on the edges and a negative charge on the surface in deionized water. Depending on the salt-content of the water and the mass-concentration of the colloid, these charges lead to anisotropic inter-particle interactions, which finally support the formation of different structures. A comprehensive review of the state-diagram of Laponite suspensions has been published by Ruzicka et al. [323] based on various previous works (see references therein).

From a physical aging perspective, Laponite is interesting as it allows to study the aging of a colloidal glass. Typically, colloidal glasses are formed by preparing colloidal suspensions with very large packing fractions, such that the colloidal particles experience caging effects similar to the ones in molecular glasses, which lead to an extreme slowing-down of the colloidal dynamics [10, 11]. The parameter that controls the colloidal glass transition is the volume fraction ϕ, thus the straight-forward way to study physical aging would be to perform an instantaneous change of the volume fraction. While this is possible in specially designed colloids with a thermo-responsive diameter [328, 329], it is almost impossible to realize experimentally in conventional colloids. Alternatively, mechanical shear can be used as an additional parameter that controls the colloidal dynamics, i.e. aging can be observed after an external shear is switched off [261]. However, such a procedure has been shown to lead to different aging behavior than changes of the volume fraction [330]. Laponite is quite different in this regard, as its metastable equilibrium state is a glass already at comparably low volume factions. The reason for this are the long-ranged electrostatic interactions that result in an "effective" interaction diameter of Laponite particles that is much larger than $\sim 25\,\text{nm}$ [323]. For instance, Bonn et al. estimated that while typical "true" volume fractions are as low as $\phi \sim 0.014$, the "effective" volume fraction considering the Debye screening length can be $\phi \sim 0.43$ [331], which is close to typical volume fractions at the colloidal glass-transition [10,

11]. Such a phase is referred to as Wigner glass [332] in analogy to the Wigner crystal, i.e. a crystal formed via electrostatic interactions [333].

Within the present work, using Laponite as the model-system to study physical aging of colloidal glasses has two main advantages: (i) Physical aging is initiated simply by suspending Laponite in water. Subsequently, the system slowly solidifies into a Wigner glass (as long as the correct experimental conditions are met, see discussion below). (ii) Due to the low "true" volume fraction, the Wigner-glass state of Laponite is optically transparent. This allows to perform DLS experiments within the single-scattering limit.

Key aspects of the sample preparation follow the review by Ruzicka et al. [323]. The arrested state the Laponite suspension evolves towards depends critically on the salt concentration and the pH-value of water, as well as the Laponite concentration. A Wigner glass is formed in pH 10 water with ionic strength $I = 10^{-4}$ at 2-3 wt% of Laponite. To ensure that the Laponite powder does not contain any residual water with other salt-concentration and pH, it was dried in vacuum (1 mbar) for one week. Subsequently, 3 wt% Laponite were added to milli-Q water, the pH of which was set to 10 by adding the appropriate amount of NaOH. The mixture was stirred for 24 h and finally filtered using a 450 nm syringe filter. The filtering procedure has been identified being important in previous work [320, 323], as it destroys any previously formed aggregates of Laponite particles and defines $t = 0$ of the aging process.

The aging of the Laponite suspension was monitored at room temperature by msDLS operated in polarized (VV) mode. Here, it has to be considered that, in contrast to molecular liquids and glasses, rotational and translational dynamics of Laponite particles proceed on comparable time scales [334]. However, as the depolarized signal is much weaker than the polarized one, VV can be considered to reflect mostly the translational dynamics of Laponite particles. The respective intensity autocorrelation functions as a function of Δt are reported in Fig. 11.9a, where the strong slowing-down of the (structural) translation dynamics can be observed with increasing time t over the course of two days. It is important to note that only a selection of autocorrelation functions is considered: At earlier times the dynamics are much faster and are barely resolved by the camera operated with an exposure time of 0.1 s; the slow-down continues indefinitely at later times, where the autocorrelations are dominated by artifacts.

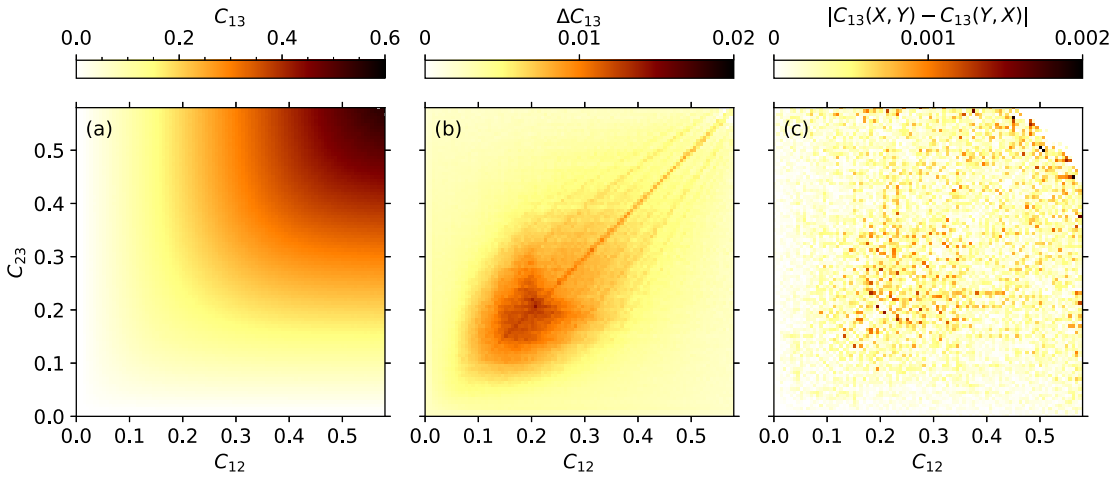

Figure 11.10: Validating the triangular relation for the intensity autocorrelation functions of Laponite (see Fig. 11.9). Equivalent plots for 1P1P and a detailed discussion of the plotted quantities can be found in Fig. 10.3.

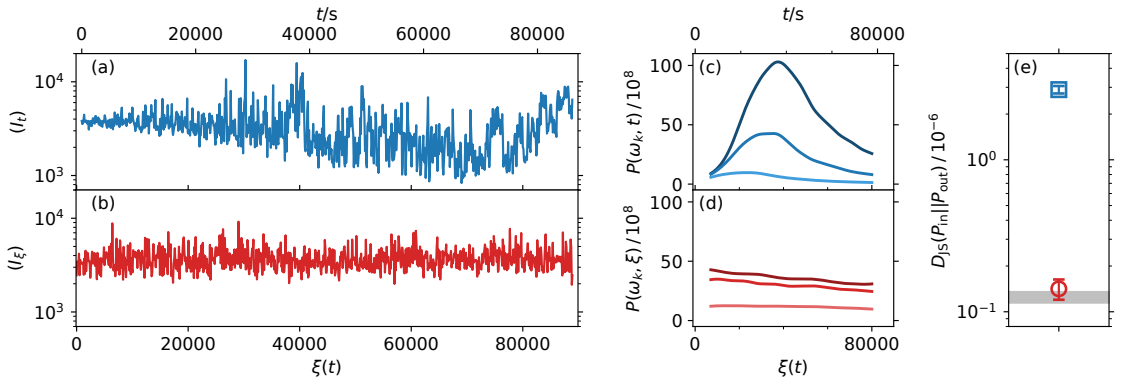

Figure 11.11: Testing stationarity and reversibility of intensity TS (I_t) and (I_ξ) obtained for an aging Laponite suspension. (a) and (b) show exemplary TS sampled equidistantly in t (a) and ξ (b). Stationarity is verified in (c) and (d) by analyzing the corresponding periodograms at three fixed frequencies, revealing pronounced non-stationarity of (I_t) that is vastly reduced for (I_ξ). Material-time reversibility is demonstrated in (e).

By using an analogous procedure as discussed in Section 10.3, the material time ξ as a function of t is extracted from the Laponite intensity autocorrelation functions using $a = 0.3$. Fig. 11.9b plots the same data as in panel (a), but as a function of $\Delta\xi$, thus testing MTTI. The data approximately collapse, showing some deviations at large $\Delta\xi$. Triangular relation is tested in Fig. 11.10, revealing slightly larger values of ΔC_{13} and stronger deviations from symmetry compared to 1P1P, which however are still of the order of one percent and one promille, respectively. In this regard, it has to be noted that a slowing-down of structural relaxation times by more than two orders of magnitude is analyzed for Laponite, thus introducing more potential for deviations from MTTI. To summarize, the aging of Laponite is reasonably well controlled by a material time.

Material-time stationarity and reversibility of intensity TS are tested in Fig. 11.11. Exemplary data for (I_t) and (I_ξ) are shown in panels (a) and (b). Here, it is immediately clear that (I_t) is irreversible, due to showing a distinct t-dependence of the fluctuation amplitude and frequency. (I_ξ), on the other hand, does not show any of these features. To understand why the amplitude of intensity fluctuations is different between (I_t) and (I_ξ), it is important to consider that probing fluctuations with a comparably low sampling rate leads to a reduction of the fluctuation amplitude due to temporal averaging. As thermal fluctuations in Laponite are fast at short t and become very slow at large t, sampling with a fixed exposure time Δt implies that the degree of temporal averaging changes as a function of t. This is not the case when using an exposure time that is fixed in units of ξ, thus leading to a t-independent degree of temporal averaging and to intensity fluctuations with constant amplitude. In principle, the same effect applies for any aging sample, however it is particular pronounced in the case of Laponite, where the strongest change of the relaxation time is observed during aging.

Stationarity of (I_t) and (I_ξ) is tested in panels (c) and (d), confirming the expectation that (I_t) is strongly non-stationary. Replacing t by ξ vastly reduces the non-stationarity, however, in line with the observations in Figs. 11.9 and 11.10, some minor residual non-stationarity remains that does not conform to ξ. Similarly, the reversibility analysis in panel (e) suggests that the material-time description considerably reduces the degree of irreversibility observed for (I_t). While the average D_{JS} obtained for (I_ξ) slightly exceeds the reversibility-limited defined by surrogates, the discrepancy is not significant considering the corresponding standard deviations. It has to be noted that no comparison to TS obtained from the equilibrium state is

possible for Laponite, as the equilibrium state is not reached within the experiments. Previous work suggests that the aging of Laponite suspensions continues for hundreds of days [320], thus it is not clear whether an equilibrium state would be reached eventually.

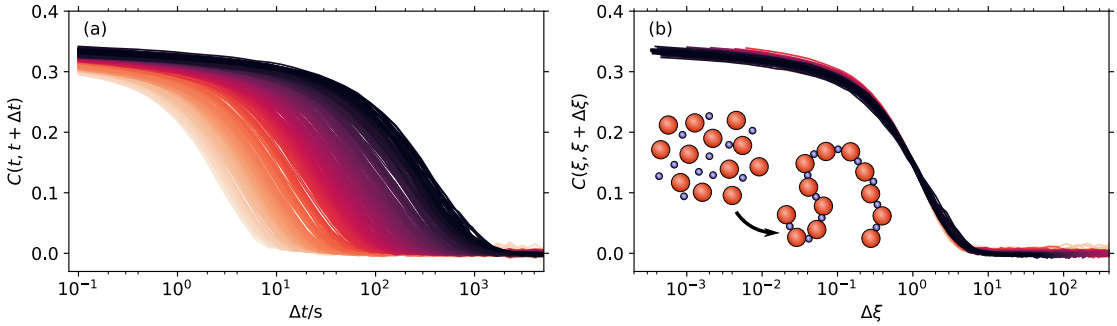

Figure 11.12: Intensity autocorrelation functions $C(t, t+\Delta)$ obtained for an chemically aging epoxy based on bisphenol A diglycidyl ether resin. (a) Autocorrelation functions as a function of Δt, where colors indicate different t (darker colors indicate longer t), and (b) same data as a function of the elapsed material time $\Delta\xi$. The material time ξ was determined using the procedure discussed in Section 10.3 using $a = 0.15$.

11.3.2 Polymerizing epoxy

The existence of a material time that controls aging and the related concept of material-time reversibility seems to apply for most *physically* aging materials. By contrast, no such concepts are predicted to hold during chemical aging, i.e. changes of material properties due to gradual chemical reactions. Thus, searching for a counter example for material-time reversibility, the gradual slow-down of the microscopic dynamics within a polymerizing epoxy is analyzed. Polymerization proceeds via the reaction of the epoxy-groups of bisphenol A diglycidyl ether resin with the amine groups of hardener molecules upon mixing both components, as visualized schematically in Fig. 11.12. Details about the sample preparation can be found in Appendix B. The molecular geometry of the chosen hardener results in chain-like structures being formed, i.e. the final product is a melt containing mostly linear-chained polymers. During polymerization, the sample gradually solidifies from a low-viscosity liquid into a rigid plastic. Fig. 11.12a shows the corresponding slowing-down of the intensity autocorrelation functions as a function of Δt. The latter have been obtained in depolarized (VH) mode and reflect the dynamics of resin-hardener concentration fluctuations. As for Laponite, the full equilibration of the sample can not be monitored, as for large t the decay of the autocorrelation functions becomes so slow that it is dominated by artifacts. Also autocorrelation functions at small t, where the relaxation time is fast, are not considered in the subsequent analysis, as here the material time can not be extracted reliably.

In an analogous procedure as described in Section 10.3, the material time is extracted from the intensity autocorrelation functions using $a = 0.15$. MTTI is tested in Fig. 11.12b, revealing an almost perfect collapse of autocorrelation functions as a function of $\Delta\xi$. Correspondingly, negligible deviations from triangular relation are observed in Fig. 11.13 and the symmetry of the triangular relation once again suggests material-time reversibility.

Intensity TS are analyzed in Fig. 11.14, confirming material-time stationarity in panel (d) and material-time reversibility in panel (e), while (I_t) is found to be non-stationary and irreversible. Thus, surprisingly the chemical aging of a polymerizing epoxy is found to be well described in

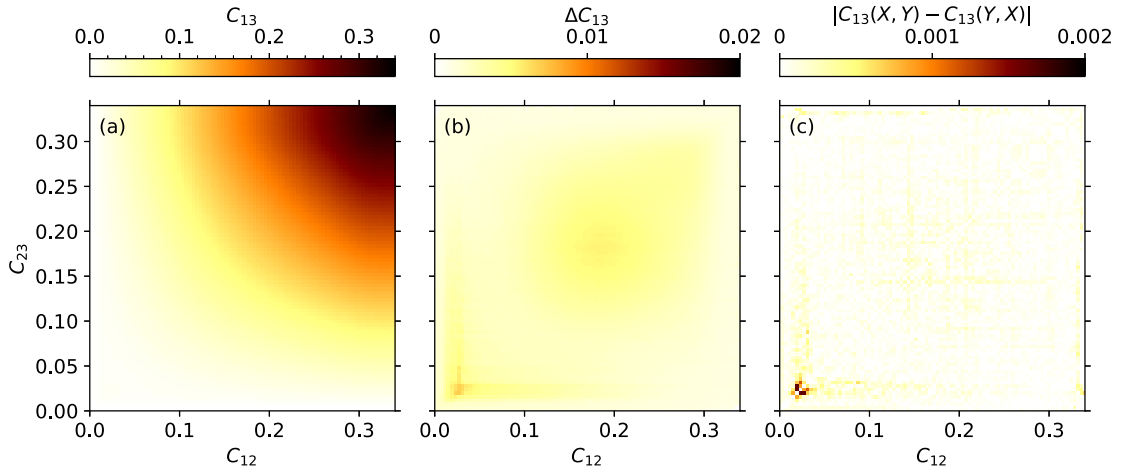

Figure 11.13: Validating the triangular relation for the intensity autocorrelation functions of a chemically aging epoxy. Equivalent plots for 1P1P and a detailed discussion of the plotted quantities can be found in Fig. 10.3.

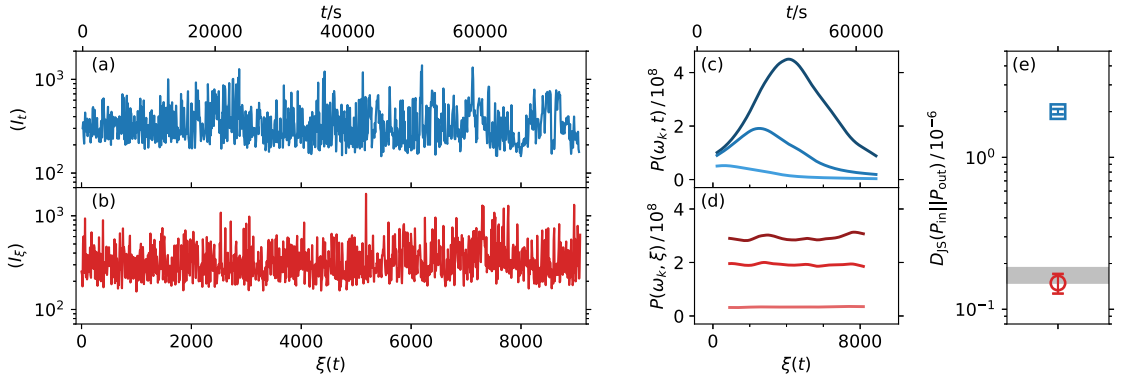

Figure 11.14: Testing stationarity and reversibility of intensity TS (I_t) and (I_ξ) obtained for a chemically aging epoxy. (a) and (b) show exemplary TS sampled equidistantly in t (a) and ξ (b). Stationarity is verified in (c) and (d) by analyzing the corresponding periodograms at three fixed frequencies, revealing pronounced non-stationarity of (I_t) that is vastly reduced for (I_ξ). Material-time reversibility is demonstrated in (e).

terms of a material time and in this regard displays no notable differences compared to an aging colloidal glass that also does not approach thermal equilibrium. It remains to be noted, however, that material-time reversibility might not be generalizable to any chemically aging system and it remains an open question to what extent the material-time concept does apply to other chemically aging systems. One aspect that should be considered in this regard are reaction kinetics, i.e. it should be verified whether chemical aging does conform to a material time once the chemical reactions proceeds with a much faster rate. For the above discussed epoxy system, the average microscopic relaxation time τ changes very slowly as a function of t, i.e. $\mathrm{d}\tau/\mathrm{d}t \ll 1$, thus, the decay of the autocorrelation functions shifts towards larger Δt very slowly.

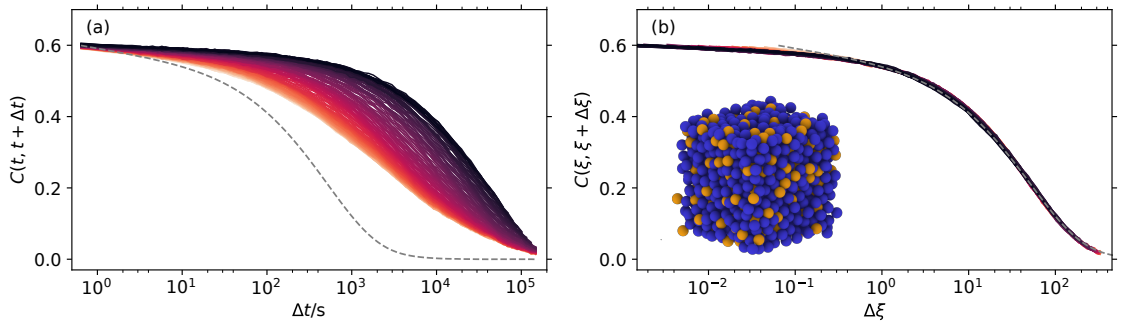

Figure 11.15: Time-resolved autocorrelation functions reflecting the per-particle potential-energy fluctuations (Eq. (11.14)) in a LJ glass during aging after a temperature jump from $T_0 = 0.48$ to $T_\infty = 0.40$. (a) $C(t, t+\Delta t)$ as a function of Δt for various t indicated by the colors. $C(t, t+\Delta t)$ obtained for an equilibrium sample at $T_0 = 0.48$ is included as the gray dashed line. (b) Same data but plotted as $C(\xi, \xi+\Delta\xi)$ as a function of $\Delta\xi$ (obtained using $a = 0.54$). Replacing time by material time leads to a collapse of the autocorrelation functions, thus confirming MTTI.

11.3.3 Computer-simulated Lennard-Jones glass

The third system is a computer-simulated model glass, which was analyzed to confirm that material-time reversibility does not only apply for fluctuations of the scattered intensity, which were considered as a proxy for thermal fluctuations of microscopic molecular positions and orientations, but also for the fluctuations of a system's potential energy. Molecular dynamics (MD) simulations have long been a popular way of studying physical aging [278, 284, 290, 335–341], as (i) time-resolved autocorrelations can be extracted quite easily compared to most experimental approaches and (ii) instantaneous changes of, e.g., temperature to initiate aging can be implemented straightforwardly.

For this work, the Kob-Andersen binary Lennard-Jones (LJ) system [342, 343] was studied, the interaction potential of which was modified to counteract crystallization according to Ref. [344]. The simulations were performed by Lorenzo Costigliola from the Glass and Time group at Roskilde University using the GPU-optimized software RUMD [345] and the resulting data have been analyzed in the present work. A system consisting of 8000 particles (6400 type A particles and 1600 type B particles, see snapshot in Fig. 11.15b) was equilibrated at temperature $T_0 = 0.48$ and density $\rho = 1.20$. Subsequently, the temperature was instantaneously changed to $T_\infty = 0.40$ and the system's evolution at the new temperature was monitored for $1.68 \cdot 10^5$ LJ time units with a time step of 0.005 (see Appendix for more details on the specific simulation procedures). The potential energy of each particle was saved every 128 time steps, corresponding to 0.64 LJ time-units. To obtain sufficient statistical power in order to determine time-resolved potential-energy autocorrelation functions, simulations were performed for a total of 30 independent starting configurations. Thus, in total, the simulations provided per-particle potential-energy data as a function of time for $N = 192.000$ particles of type A (particles of type B were not considered in the analysis below).

Time-resolved per-particle potential-energy autocorrelation functions are obtained as

$$C(t, t+\Delta t) = \frac{\left\langle \Delta u_i(t) \Delta u_i(t+\Delta t) \right\rangle_N}{\sqrt{\left\langle \left(\Delta u_i(t)\right)^2 \right\rangle_N \left\langle \left(\Delta u_i(t+\Delta t)\right)^2 \right\rangle_N}}, \tag{11.14}$$

where $\langle ... \rangle_N$ indicates the average over all particles and $\Delta u_i(t) = u_i(t) - \overline{u}(t)$ denotes the potential-energy fluctuations of particle i with respect to the time-dependent average per-particle potential energy $\overline{u}(t) = \langle u_i(t) \rangle_N$.

$C(t, t+\Delta t)$ as a function of Δt at various t are shown in Fig. 11.15a, where also the autocorrelation function obtained for the equilibrium system at $T_0 = 0.48$ is included as the dashed line. It is noted that the amplitude of the equilibrium autocorrelation function was slightly rescaled to compensate for the temperature dependence of the intermediate-time plateau value of $C(t, t+\Delta t)$ (the short-time microscopic relaxation is almost unresolved in Fig. 11.15a).

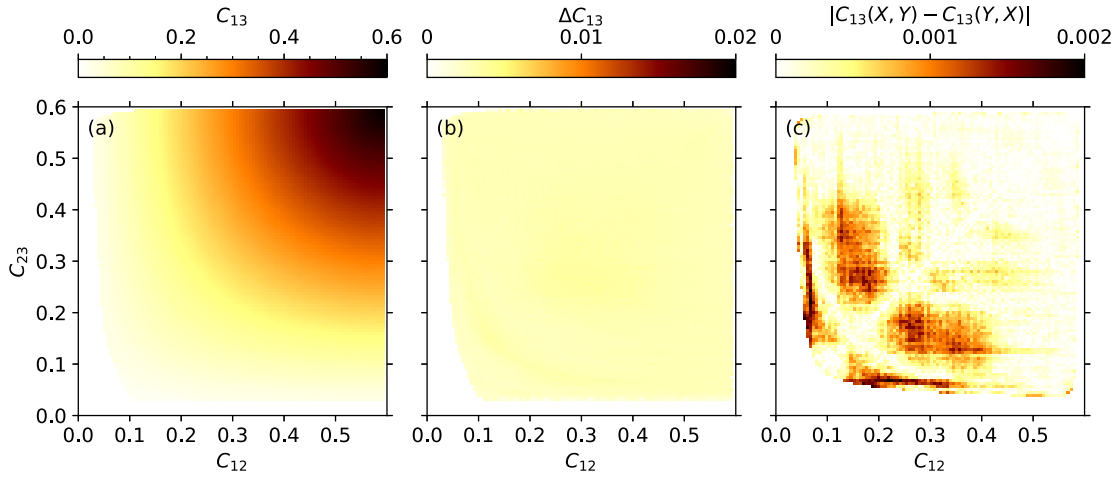

Figure 11.16: Testing triangular relation for the per-particle potential-energy autocorrelation functions (Eq. (11.14)) of a LJ glass during aging after a temperature jump from $T_0 = 0.48$ to $T_\infty = 0.40$. The plotted quantities are equivalent to the ones in Fig. 10.3.

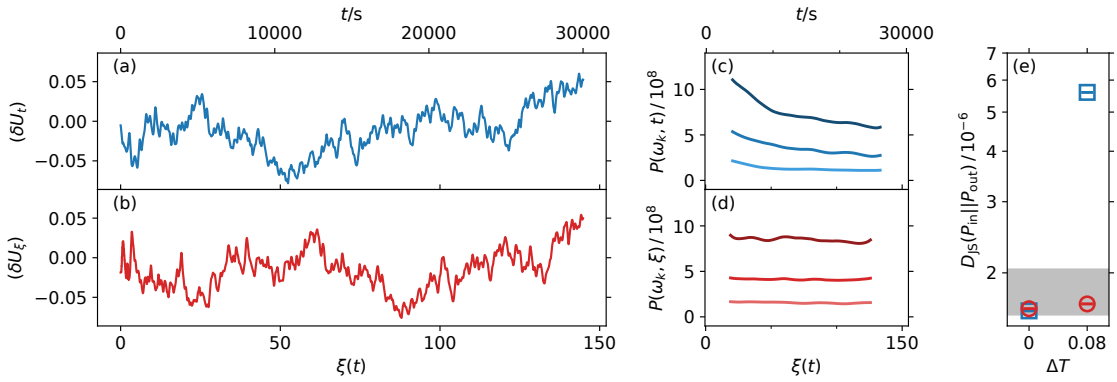

Figure 11.17: Verifying material-time reversibility and stationarity for the per-particle potential-energy fluctuations of a LJ glass during aging after a temperature jump from $T_0 = 0.48$ to $T_\infty = 0.40$. The exemplary TS in panels (a) and (b) are obtained using an Gaussian-weighter averaging procedure (see text). Stationarity is verified in (c) and (d) by analyzing the corresponding periodograms at three fixed frequencies, revealing pronounced non-stationarity of $\langle \delta U_t \rangle$ and stationarity of $\langle \delta U_\xi \rangle$. Material-time reversibility is demonstrated in (e).

The material time is extracted using the same procedure as applied to the intensity autocorrelation functions before ($a = 0.54$). It is applied in Fig. 11.15b to confirm MTTI by plotting the potential-energy autocorrelation functions as a function of $\Delta\xi$, which collapses all data shown

in panel (a). Small deviations are only observed at very short $\Delta\xi$, where slight contributions from the microscopic relaxation are observed. It is not surprising that the micropscopic relaxation does not conform to the material time, as its temperature-dependence is weak and thus, it does not age. Consequently, those thermal fluctuations that reflect the micropscopic relaxation are approximately stationary and time-reversible as a function of t, even during aging, such that replacing time by material time does in fact introduces additional non-stationarity and irreversibility with regard to the microscopic fluctuations. However, this almost never plays a role for experimental studies of physical aging, as at temperatures close to T_g any microscopic relaxation processes are dynamically separated from the structural relaxation process by many orders of magnitude and, thus, are not resolved. To summarize, microscopic relaxations do not conform to the material-time formalism, however this mainly plays a role for the aging of computer-simulated glasses, as these are studied at elevated temperatures.

The observed collapse of potential-energy autocorrelation functions when considered in terms of the material time in Fig. 11.15b is especially convincing, considering that the shapes of the autocorrelation functions during aging in panel (a) are clearly stretched compared to the shape of the equilibrium autocorrelation function. The stretched shape reflects the decay of the autocorrelation proceeding on a similar time scale as the change of the material-time clock rate, and is, thus, fully compensated for by using material time instead of time in panel (b). In principle, the same effects apply for the experimental data discussed above, however, there, the autocorrelation functions decay faster with respect to the change of the material-time clock rate and the stretching of the autocorrelation functions during aging compared to the ones obtained for the equilibrium system is hardly noticeable.

Triangular relation is verified in Fig. 11.16. Although no large values of ΔC_{13} are observed in harmony with the perfect collapse of autocorrelations in Fig. 11.15b, subtle deviations from perfect triangular-relation symmetry are identified in panel (c). So far, the origin of these deviations is not clear. They might reflect contributions from the microscopic relaxation, which, in principle, should violate triangular relation. However, strikingly, the deviations from symmetry are observed at small C_{12} and C_{23}, whereas the naive expectation would be that the microscopic relaxation leads to deviations at large C_{12} and C_{23}.

Fig. 11.17 presents an analysis of TS reflecting potential-energy fluctuations δU, examples of which are included in panels (a) and (b) as a function of t and ξ, respectively. Each TS is obtained as the sum of potential-energy fluctuations of 200 randomly chosen particles, thus the results in Fig. 11.17 are obtained as an average of a total of $192.000/200 = 960$ independent TS. The procedure for obtaining (δU_t) and (δU_ξ) is very similar to the one applied to intensity TS described in Section 11.2.1, except that instead of averaging over discrete binning intervals, a Gaussian weighted time-average at times chosen to be constant in time, res. material time is performed. The width of the Gaussian filter is chosen proportional to the time clock rate (which is constant), res. to the material-time clock rate. This procedure yields very similar results as binning, but is able to filter out microscopic fluctuations more efficiently. Material-time stationarity and reversibility for the obtained TS are confirmed in panels (c)-(e). As in contrast to Laponite and the epoxy, the equilibrium state of the LJ system can be explored, D_{JS} obtained for (δU_ξ) during aging is compared to D_{JS} of equilibrium TS at $T = 0.48$ in panel (e). The comparison confirms that (δU_ξ) is as reversible as equilibrium TS. It has to be noted that a subtle degree of irreversibility remains when (δU_ξ) is determined using the binning procedure instead of the Gaussian weighted time-average, reflecting that the degree to which the microscopic relaxation contributes to (δU_ξ) varies as a function of ξ.

11.4 SUMMARIZING DISCUSSION

Chapters 10 and 11 presented analyses of four different amorphous materials, which all are subject to aging, i.e. slow and gradual evolutions of material properties as a function of time. The focus has been the proposed procedure of extracting the material time postulated within the TN formalism from time autocorrelation functions based on the underlying assumption of material-time translational invariance (MTTI). The latter can be considered to be inherited from thermal equilibrium as a logical consequence of the TN conjecture that aging becomes a linear-response phenomenon by replacing time with material time [12]. A necessary condition for defining a material time based on MTTI was discussed in terms of the triangular relation, which has been proposed in a different context for aging spin-glasses by Cugliandolo and Kurchan [279, 346]. Validity of the triangular relation has been shown to imply time-reparametrization invariance, which is conceptually similar to MTTI, although time-reparametrization invariance does not consider aging as a linear phenomenon like it is done within the TN formalism. Verifying the triangular relation is possible without explicit knowledge of the material time as a function of time, thus it could be confirmed for the different aging systems without any underlying assumptions. For the molecular glass 1P1P, the extracted material time was confirmed to linearize aging relaxation functions $R(t)$ by showing that $R(\xi(t))$ obtained for different temperature protocols collapse, i.e. correspond to the linear-response prediction.

The triangular relation is symmetrical, which in thermal equilibrium is associated with the time-reversibility of thermal fluctuations. In a similar spirit, the conjecture of material-time reversibility for aging samples has been proposed, i.e. the prediction that time-irreversible thermal fluctuations during aging become reversible when they are considered in terms of the material time. Using a statistical test for time-series reversibility, material-time reversibility could be confirmed for the intensity fluctuations of the light scattered from aging samples, which are used as proxies for thermal fluctuations on the microscopic scale. Applying the same concepts used to analyze experimental data to results for a computer-simulated LJ model glass allowed to demonstrate material-time reversibility also for the fluctuations of the per-particle potential energies, thus confirming that it, indeed, applies at the shortest length-scales.

In summary, material-time reversibility is observed during physical aging of a molecular glass (1P1P), a colloidal glass (Laponite) and a computer-simulated LJ glass, as well as for the chemical aging of a polymerizing epoxy. The nature of these systems, as well as the aspects of the dynamics that have been probed in the experiments and simulations, are quite different as it becomes clear from the following paragraph from Ref. [280]: "1P1P and epoxy are molecular while Laponite is colloidal; 1P1P, Laponite and LJ age physically while epoxy ages chemically; Laponite and epoxy do not converge to equilibrium within the window of observation while 1P1P and LJ do. Moreover, our experiments probed dynamics on different length scales: while reorientation of the optical anisotropy on a molecular scale is probed in VH light scattering of 1P1P, in the case of VV scattering on Laponite density fluctuations are probed on the scale of the optical wavelength. In VH scattering of the curing epoxy, it is mainly hardener/resin concentration fluctuation effects that are probed. Finally, similar to 1P1P, the computer simulations access the single-particle scale."

The validity of material-time reversibility in various different contexts suggests it to be of quite broad generality for amorphous systems and it remains a task for future work to determine the exact scope of its validity. In this regard it would be important to identify system's that explicitly disobey the material-time formalism in general or material-time reversibility

specifically. Promising in this regard are recent observations of extremely heterogeneous aging after large temperature up-jumps from a glassy state of low fictive temperature, involving the formation of liquid droplets within a glassy matrix [347, 348]. Intuitively, one might expect the material-time formalism to fail in such cases, as liquid droplets and glassy matrix, most likely, do not conform to a single material time and, instead, the material time might be heterogeneous in space.

The previous analyses in chapters 10 and 11 mostly assessed the *existence* of a material time and how it relates to the aspects of linear response as well as stationarity and reversibility of thermal fluctuations. A whole other field of questions concerns how exactly the material-time clock rate changes as a function of time for different materials. The following chapter provides a brief introduction to these issues and suggests a model that predicts how the material-clock rate changes as a function of time after small temperature changes.

12

TIME-EVOLUTION OF THE DYNAMICS DURING AGING

The following chapter discusses how the material-time clock rate $\gamma(t)$ changes as a function of t during aging based on results obtained for 1P1P. Due to how $\gamma(t)$ is defined in Chapter 10, it is directly related to the relaxation time $\tau(t)$ as $\gamma(t)=\tau(t)^{-1}$, if $\tau(t)$ is defined as $C(t,t+\tau)=a$, as it is commonly done in computer simulation studies for $a=\lim_{\Delta t\to 0} C(t,t+\Delta t)/2$. As a consequence, the results obtained for $\gamma(t)$ within the present chapter can be straightforwardly compared to literature results for $\tau(t)$.

First, Section 12.1 considers the evolution of $\gamma(t)$ after small temperature jumps, which is dominated by the cross-over into the new equilibrium state. A simple model is proposed that is able to describe the sigmoidal shape of $\gamma(t)$ in terms of a simple logistic differential equation. Second, Section 12.2 considers larger temperature jumps deep into the glassy state, such that the glass does not equilibrate on any experimentally accessible time scale. Here, the evolution of $\gamma(t)$ conforms neither to the proposed differential equation, nor to what is predicted by the simplest version of trap models.

12.1 DIFFERENTIAL EQUATION FOR SMALL TEMPERATURE JUMPS

Exposing an equilibrium supercooled liquid to a temperature jump from T_0 to T_∞ and waiting sufficiently long such that the new equilibrium at T_∞ is reached leads to a gradual evolution of the material-time clock rate $\gamma(t)$ from its equilibrium value at T_0, γ_0, to the new equilibrium value at T_∞, γ_∞. One of the simplest models that potentially could describe $\gamma(t)$ is the logistic differential equation

$$\frac{\mathrm{d}}{\mathrm{d}t}\gamma(t) = -E\,\gamma(t)\big(\gamma(t)-\gamma_\infty\big) \quad \text{with} \quad \gamma(0)=\gamma_0. \tag{12.1}$$

Eq. (12.1) assumes that the change of $\gamma(t)$ as a function of t is proportional to $\gamma(t)$ itself, i.e. the current relaxation rate, its distance from the equilibrium relaxation rate, $(\gamma(t)-\gamma_\infty)$, and some constant E that can be interpreted as the efficiency of the relaxation mechanism. Eq. (12.1) can be solved analytically, which yields

$$\gamma(t) = \frac{\gamma_\infty\gamma_0\exp\big(E\,\gamma_\infty\,t\big)}{\gamma_\infty-\gamma_0+\gamma_0\exp\big(E\,\gamma_\infty\,t\big)}. \tag{12.2}$$

The material time is obtained via integration, i.e.

$$\xi(t) = \int_0^t \gamma(t')\,\mathrm{d}t' = \frac{\log\big(\gamma_\infty+\gamma_0\big(\exp\big(E\gamma_\infty\,t\big)-1\big)\big)-\log\big(\gamma_\infty\big)}{E}. \tag{12.3}$$

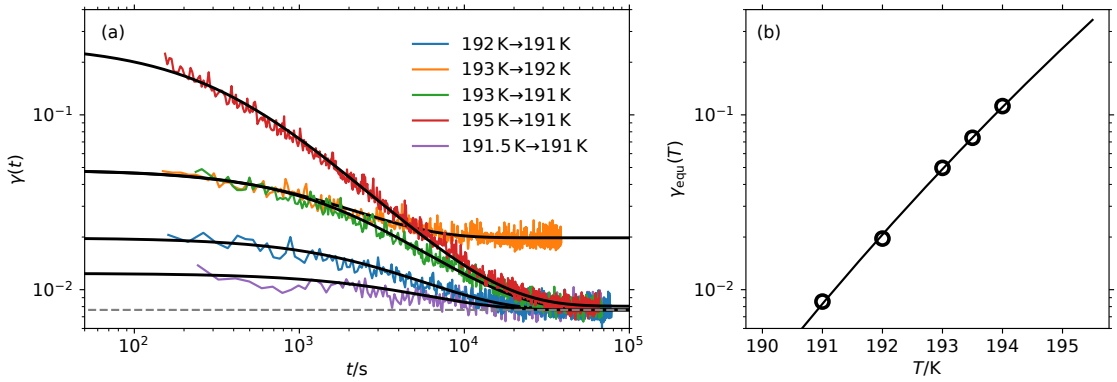

Figure 12.1: Testing the logistic differential-equation description of the material-time clock rate for 1P1P. (a) Material-time clock rate as a function of time after various temperature down-jumps. All shown data were obtained using the Peltier-controlled sample cell. Black solid lines represent the solution of Eq. (12.1) with γ_0 and γ_∞ being determined from the respective equilibrium states at T_0 and T_∞, while E was treated as a free parameter. (b) Equilibrium clock-rates as a function of sample temperature. The solid line is a fit by the VFT equation, which is also used to interpolate data at temperatures where no equilibrium measurement has been performed. It is noted that T is defined in terms of the PT-100 installed at the bottom of the sample cell, thus the temperatures do not exactly coincide with the ones obtained within the LN_2-controlled sample cell (data shown in Chapter 10).

γ_0 and γ_∞ are predefined through the equilibrium states at T_0 and T_∞, thus the only free parameter of Eq. (12.2) is E. It is a simple scaling factor along the time-axis, thus does not affect the shape of $\gamma(t)$. Fig. 12.1a explores whether Eq. (12.2) is able to describe the experimentally obtained data after various temperature down-jumps with amplitudes ΔT between -0.5 K and -4 K. All included data were obtained using the Peltier-controlled sample cell, thus T_0 and T_∞ could reproduced very precisely. In addition, time zero for each temperature jump can be determined more precisely than it has been possible with the LN_2-controlled sample cell.

The solid lines represent the description in terms of Eq. (12.2), which in all cases agrees well with the data. γ_0 and γ_∞ are extracted from equilibrium measurements performed at T_0 to T_∞, or in some cases are interpolated by using a VFT description of the equilibrium material-time clock rates $\gamma(T)$, see panel (b). The values of E vary slightly as a function of ΔT, i.e. E ranges from 0.018 to 0.011 for ΔT between -0.5 K and -4 K.

The presented results suggest that $\gamma(t)$ can be described in terms of a simple differential equation. This is surprising considering that physical aging is a highly non-linear phenomenon, which has been the reason why previous attempts of describing aging in terms of a differential equation of, e.g., the fictive temperature have turned out to be insufficient [35]. However, because the variation of $\gamma(t)$ as a function of t itself is the origin of the mentioned non-linearity, it might be just the right quantity to consider in a differential-equation approach. It has to be noted, however, that all data considered in Fig. 12.1 represent physical aging after temperature-jump protocols, thus only the fictive temperature T_f changes as a function of t, while T is constant. Following the TNM-assumption of γ being a function of both T and T_f, the scenario analyzed above is an especially simple case of physical aging. It might well be that Eq. (12.1) does not describe data obtained during more complex temperature protocols, during which both T and T_f evolve as a function of t. Unfortunately, this conjecture has been difficult to verify using the Peltier-controlled sample cell, as the evolution of $\gamma(t)$ during slow changes of T most probably is affected by the t-dependence of temperature gradients within the sample cell. Future experiments should aim at disentangling these different effects, in order to study

physical aging during more complex temperature protocols, which, from a purely technical point of view, can easily be implemented.

12.2 SUB-AGING AFTER DEEP QUENCHES

Although studying physical aging from one equilibrium state to another evidently is very insightful from a fundamental-science perspective, it is hardly the scenario relevant with regard to the typical applications of glassy materials. During production of inorganic or polymeric glasses, liquid or supercooled-liquid melts are usually cooled to room temperature, i.e. very far below their respective glass-transition temperatures. Consequently, these systems do not reach an equilibrium state for a very long time, or possibly never at all, because their relaxation rate becomes extremely slow. Clarifying how the relaxation rate changes as a function of time after a quench deep into the glassy state is important in order to predict how material properties evolve after their production.

Pioneering work in this regard was carried out and published in 1978 by Struik [35], who analyzed the mechanical properties of aging plastics as a function of the annealing time after a deep quench. He found that the creep compliance obtained after different annealing times t could be collapsed by shifting the curves along the time axis by a factor $\propto t^{-\mu}$ [35], or expressed in terms of time autocorrelation functions [20]

$$C(t, t+\Delta t) = C(\Delta t / t^{-\mu}). \tag{12.4}$$

From a material-time perspective, Eq. (12.4) implies that $\gamma(t) \propto t^{-\mu}$, res. $\tau(t) \propto t^{\mu}$. Struik obtained $\mu \sim 1$ for many different polymers, however also values below unity have been reported.

In later years, a characterization of aging behavior in terms of μ has been established, i.e. $\mu = 1$ is referred to as simple aging, $\mu < 1$ is called sub-aging and the quite rare case of $\mu > 1$ is denoted as hyper-aging [341]. This classification is not only used for polymer glasses [35, 349, 350], but also for spin glasses [9, 351, 352] and structural glasses [341, 353].

In an insightful computer-simulation study, Warren et al. [353] showed for an LJ model-system that simple aging is the "true" aging behavior after deep quenches, while sub-aging is an "artifact" of the crossover to an equilibrium state, meaning the system does not reach $\tau(t) \propto t^1$, because it crosses into a stationary equilibrium state where $\tau = \text{const}$. In such a crossover scenario, the authors do not observe a constant power-law exponent $\mu < 1$ over a broad t-interval, but instead $\tau(t)$ has a sigmoidal shape with varying logarithmic slope.

Theoretical models of aging after quenches into the glassy state have been formulated in terms of "trap models", where it is assumed that the system explores an energy landscape within configurational space by hopping between different minima. The minima states are modeled as sites arranged on a hypercubic lattice with energies E drawn from some distribution $\rho(E)$. Early trap models assumed the hopping rate to depend only on the energy of the current state, which yields a scaling law according to $\mu = 1$, i.e. simple aging behavior [354, 355]. Later, these models have been extended by an additional parameter that allows the hopping rate to depend on both, the energy of the current and of the target site. This approach requires to assume quenched disorder instead of treating the system in terms of a mean-field model. The extensions of the trap-model were shown to introduce sub-aging behavior, the power law exponent of which depends on the choice of the different parameters assumed to model the hopping rate. The authors rationalized the observation of sub-aging by the fact that quenched disorder and the adapted hopping rate allow the system to revisit low-energy states, which is not possible in a mean-field treatment [356, 357].

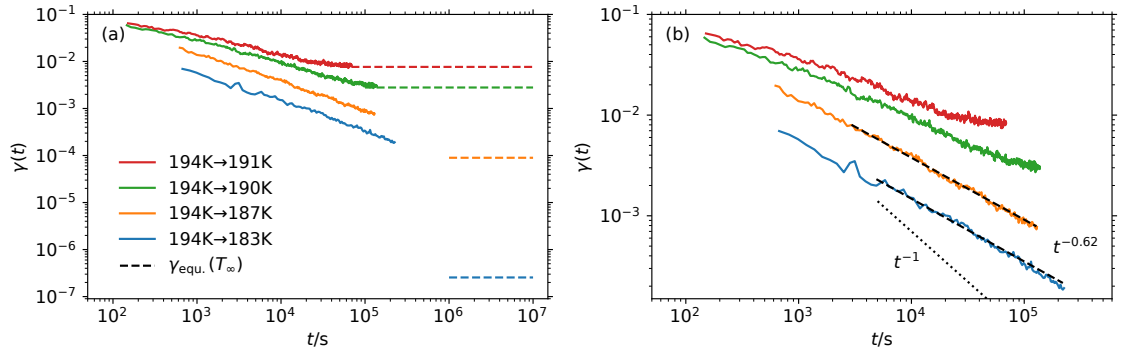

Figure 12.2: Exploring the time evolution of the material-time clock rate of 1P1P after down-jumps with different amplitudes from 194 K to T_∞ indicated in the legend. (a) The equilibrium clock rates at T_∞ are included as the dashed colored lines, from which it becomes clear that a cross-over to equilibrium is observed for the two smaller jumps, while the system's aging is studied far away from equilibrium for the two larger jumps. Panel (b) explores the respective t-dependencies in more detail, revealing a sigmoidal shape for the two smaller jumps and an inverse power-law behavior with exponent $\mu = 0.62$ for the two larger jumps. The black dotted line indicates the power law expected for simple aging, i.e. $\mu = 1$.

Simple aging is also predicted by the differential equation, Eq. (12.1), because after a quench to some low temperature $\gamma(t) - \gamma_\infty \approx \gamma(t)$, which yields

$$\frac{\mathrm{d}}{\mathrm{d}t}\gamma(t) = -E\,\gamma(t)^2 \tag{12.5}$$

with solution $\gamma(t) = \gamma_0/(1 + E\gamma_0 t)$ proportional to t^{-1} for large t.

In order to determine the t-dependence of $\gamma(t)$ after large temperature down-jumps into the glassy state, a sample of 1P1P was first equilibrated at $T_0 = 194$ K and subsequently cooled to T_∞ ranging from 191 K to 183 K with a cooling rate of 1 K/min. Larger jumps or faster cooling rates are difficult to achieve, as they enhance internal stresses within the glass, leading to the formation of cracks, the light scattered from which makes it impossible to perform DDLS experiments. However, no cooling-rate dependence has been observed for jumps with smaller amplitudes, suggesting that the same is to be expected for larger jumps.

The results are summarized in Fig. 12.2. Panel (a) displays $\gamma(t)$ as a function of t and includes the interpolated equilibrium clock rates at T_∞ as the dashed lines. While a cross-over to the equilibrium state is observed after the jumps to 191 K and 190 K, the system is far away from its equilibrium state after jumps to 187 K and 183 K; even after annealing for up to three days. Thus, it can be assumed that no cross-over to equilibrium does occur for the two largest down-jumps. The t-dependencies of $\gamma(t)$ are explored in detail in panel (b). It is found that $\gamma(t)$ evolves proportional to $t^{-0.62}$ after jumps deep into the glassy state. This observations seems to be independent of T_∞, as long as no cross-over into the equilibrium state is observed. Considering that the same power law behavior is observed over more than two orders of magnitude of t, it is unlikely that a transition to $\mu = 1$ would be observed at larger t.

To summarize, sub-aging behavior is observed for the molecular glass 1P1P after quenches deep into the glassy state. These results seem to contradict earlier computer-simulation studies suggesting that sub-aging is an artifact due to the cross-over to an equilibrium state [353]. One reason for this apparent discrepancy might be that the temperatures considered in the computer simulations are much higher than the ones considered in the presented experiments, thus the geometry of the energy landscape the systems explore in both approaches might be fundamentally different. Instead, the results obtained during this work support theoretical

predictions of sub-aging behavior for certain trap-models defined to mimic hopping in an energy landscape with quenched disorder [356, 357]. It remains to be confirmed that the same sub-aging behavior is observed after even larger and faster down-jumps. Experience shows that the temperature below T_g at which cracks form in a glass depend on the exact substance that is studied, thus exploring other molecular glass formers might help to obtain data for even deeper quenches.

13

SUMMARY

Part I of this work dealt with relaxation spectra of various different (equilibrium) supercooled liquids. The main focus has been the relaxation shape of the α-process in pure molecular supercooled liquids, the asymmetric broadening of which has been shown before to be associated with dynamic heterogeneity in numerous studies [25–29]. Previous experimental effort aiming at identifying universal characteristics of the α-process relaxation shape in supercooled liquids mostly focused on data obtained from dielectric spectroscopy (DS) [32–34]. Although a predominant high-frequency powerlaw of $\nu^{-1/2}$ has been identified based on DS-data in some previous studies [33, 93], the general consensus has been that for the majority of molecular supercooled liquids the high-frequency power law exponent β depends on the molecular structure and is distributed between 0.3 and 1 [32, 34]. Contrasting results from depolarized dynamic light scattering (DDLS) were discussed in Chapter 4, parts of which have already been presented in previous work by Florian Pabst [44]. There, a $\nu^{-1/2}$ high-frequency behavior is observed for a broad variety of supercooled liquids with different molecular structures and interaction mechanisms. Moreover, selected supercooled liquids were shown to obey time-temperature superposition, i.e. the relaxation shape of the α-process does not change as a function of temperature within the deeply supercooled regime. Finally, the implications of the generic $\nu^{-1/2}$ high-frequency behavior were discussed, which, following recent computer-simulation results [30, 86], might reflect general characteristics of dynamic facilitation, e.g. with regard to the rate at which mobile clusters emerge or the number of those clusters as a function of waiting time.

The origin of the discrepancies between the structural relaxation shapes obtained by means of DS and DDLS was discussed in Chapter 5, again building on earlier work [44]. It was shown that dielectric loss spectra of various supercooled liquids can be described by the superposition of the DDLS relaxation spectrum and a slow Debye-shaped contribution. The latter was argued to reflect the relaxation of dipolar cross-correlations. So far, cross-correlation effects have mostly been ignored in the interpretation of dielectric loss spectra, although it is well-established that they substantially contribute to the static dielectric constant. The conjecture was shown to be supported by multiple recently published results within the field; among other things computer-simulation studies that unambiguously identify a slow dipolar cross-correlation contribution in a polar model-liquid [147] and glycerol [126]. Moreover, it was demonstrated based on literature data of glycerol that inhibiting the formation of hydrogen-bonds by applying large hydrostatic pressures or by hyper-quenching from the liquid phase recovers the DDLS structural relaxation shape, because dipolar cross-correlations are largely suppressed. Finally, a quantitative relation was established between the high-frequency power law exponent β and the degree of dipolar cross-correlations, which was quantified in terms of the Kirkwood correlation factor g_K [156]. Both were shown to be correlated for 25 different supercooled liquids, i.e. the dielectric loss spectra of supercooled liquids with larger g_K tend

to feature a steeper high-frequency power law, $\beta \approx 0.5$ was identified once dipolar cross-correlations were absent ($g_K = 1$). The results support the recent theory of Dejardin at al. [109] that predicts an additional slow cross-correlation contribution to the dielectric loss as soon as $g_K > 1$. Finally, joint DS and DDLS-analyses allowed to demonstrate that most supercooled liquids do not obey the micro-macro relations predicted by Kivelson and Madden, which relate macroscopic and microscopic dipolar relaxation times while taking into account dipolar cross-correlations [138, 139].

Due to dynamic signatures of hydrogen-bonded supra-structures with different geometries, the dielectric responses of many hydrogen-bonding liquids are known to be especially complex. In Chapter 6, the dielectric loss spectra of hydrogen-bonding supercooled liquids were disentangled through comparison to respective DDLS relaxation spectra. The focus was to study the influence of the molecular architecture on the dynamics of hydrogen-bonded supra-structures along isomeric or homologous series. First, it was shown for an isomeric series of phenyl propanols that, contrary to previous notions [161, 171, 172], the steric hindrance introduced by a phenyl-ring does not generally suppress the formation of hydrogen-bonded structures in monohydroxy alcohols. Instead, the geometry of these structures shifts from predominantly chain-like to coexisting ring-like and chain-like structures being formed upon decreasing the distance between hydroxy and phenyl group. Similar effects have been observed previously for octanol isomers [132–135, 158–160, 179], which were also analyzed within the present work. Here, combined DS and DDLS analyses revealed an intermediate relaxation contribution to the dielectric loss at frequencies between the α-process and the Debye-process, in accordance to results from shear rheology [183, 184]. Comparisons to NMR results from the literature revealed that the intermediate contribution reflects the orientation of hydroxy groups, which decouple from the remaining molecule due to being incorporated into supra-structures. Finally, it was found for the homologous series of polyhydric alcohols (PAs) that dielectric loss-spectra of short-chained PAs are dominated by dipolar cross-correlations. By contrast, longer-chained PAs become more and more flexible, such that relaxation spectra are dominated by intra-molecular relaxation mechanisms. Consequently, no contributions of slow dipolar cross-correlation are observed, because intra-molecular flexibility leads to the dipole moment vectors not being fixed within the molecular frames. Despite the evident complexity regarding structure-formation, the α-process probed by DDLS was found to correspond to the generic relaxation shape for most investigated supercooled liquids.

Finally, Chapter 7 attempted to shed light on the physical origin of slow solvent relaxation in asymmetric binary mixtures, which is the commonly obsered scenario that solvent-contributions are observed on the time scale of the solute-relaxation [210, 219–225]. By analyzing a 2-picolin/PMMA binary mixture by means of broadband DDLS, solvent relaxation was monitored over 13 orders of magnitude in frequency. The treatment allowed for a detailed characterization of the slow solvent relaxation, the relaxation strength of which was found to sharply decrease with decreasing temperature. Computer-simulation performed by Robin Horstmann [202] for the same mixture revealed slow solvent relaxation is caused by long-lived solute induced solvent-solvent cross-correlations, which reflect favored orientations of solvent molecules in the vicinity of the quasi-static solute matrix. Combined, the presented results suggest that slow solvent relaxation in asymmetric binary mixtures is not associated with a bimodal distribution of solvent mobilities, but reflects the complex interaction mechanisms between solvent and solute.

Part II focused on physical aging in non-equilibrium glassy systems and its description in terms of a material time as postulated by Narayanaswamy [38]. Although the material-time formalism has been applied to describe enthalpy relaxation in glasses for decades [39, 41,

276], open questions remain, because it so far had been impossible to explicitly determine the material time in experiments. The present work provides a way forward in this regard by proposing a procedure to extract the material time from time-resolved autocorrelation functions. In experiments, such data can be obtained by applying multispeckle dynamic light-scattering (msDLS). Chapter 9 presented and characterized the msDLS experiment developed within this work, which allowed to determine time-resolved intensity autocorrelations of molecular glasses for the first time. In addition, studying physical aging requires to quickly change sample temperatures, thus a Peltier-controlled DLS sample cell was constructed, which considerably outperforms conventional sample-cell designs in terms of temperature-variation capability.

Chapter 10 verified the material-time description of msDLS data obtained for the molecular glass 1-phenyl-1-propanol (1P1P) after temperature down-jumps of different amplitudes. First, a necessary condition for the existence of a material time was confirmed to be obeyed by the autocorrelation-data, i.e. the triangular relation originally proposed for spin glasses by Cugliandolo and Kurchan [279]. After having established the existence of a material time that controls the aging of 1P1P, it was extracted from the intensity autocorrelation functions via an iterative procedure. This is based on the assumption of material-time translational invariance (MTTI), meaning that time-autocorrelations can be expressed as a unique function of the elapsed material time. As proposed by Dyre [12, 278], MTTI is assumed to be inherited from time translational invariance in thermal equilibrium, following Narayanaswamy's idea that the material-time description recovers equilibrium characteristics for physically aging samples. The extracted material time was shown to linearize the changes of the dielectric loss probed at a fixed frequency during aging. Furthermore, MTTI could be verified explicitly.

Physical aging is a non-stationary and time-irreversible process. It could be shown, however, that the triangular relation equations are symmetric, which in thermal equilibrium is associated with time-reversal symmetry. Building on this observation, Chapter 11 explored the conjecture of material-time reversibility, meaning that thermal fluctuations during aging become reversible if considered as a function of the material time. Indeed, this notion was confirmed by applying statistical tests for time-series reversibility to intensity fluctuations of the light scattered from aging samples. In addition, material-time reversibility was confirmed for three other disordered materials, namely the physically aging colloidal glass Laponite, a poylmerizing epoxy that is subject to chemical aging, as well as a computer-simulated model glass. For the latter, material-time reversibility was confirmed for potential-energy fluctuations. The broad validity of material-time reversibility suggests that the irreversibility of physical aging originates solely from the evolution of the system's relaxation rate as a function of time.

While chapters 10 and 11 explored as to whether a material time exists that controls physical aging and how it relates to thermal fluctuations, Chapter 12 explicitly considered how the material-time clock rate evolves during aging. Two distinct scenarios were considered: Physical aging from one to another equilibrium state after small temperature changes, and physical aging after deep quenches into the glassy state, after which the system does not equilibrate within any experimentally accessible time period. For aging after small temperature changes it was shown that the sigmoidal-shaped material-time clock rate as a function of time is described in terms of a simple logistic differential equation. Here it is assumed that the change of the clock rate is proportional to the clock rate itself, i.e. the system's current relaxation rate, as well as to the difference of the clock rate with respect to its equilibrium value. For deep quenches into the glassy state, a common notion is that the clock rate evolves as t^{-1} [353], which is referred to as simple-aging behavior. Instead, experimental results obtained within

this work suggest a much weaker t-dependence of $t^{-0.62}$. Such a sub-linear aging scenario does not conform to predictions from simple mean-field trap models, which assume that the system explores the rugged potential-energy landscape in phase space [354, 355]. Instead, it is explicitly predicted for trap-models that involve quenched disorder and, thus, allow the system to revisit low-energy states [356, 357].

Part III

APPENDIX

A

PARAMETERS FOR CALCULATING g_K

The following discussion is adopted from the SI of Ref. [105]. All parameters used to determine g_K are listed in table A.1. In most cases, density data measured at several temperatures were taken from the literature and extrapolated to supercooled temperatures using the linear expression (see e.g. Ref. [358] for an example of the validity of this procedure)

$$\rho(T) = \rho_0 - \delta \cdot T. \tag{A.1}$$

To calculate the temperature dependent refractive index $n(T)$, the Lorentz-Lorenz equation

$$\frac{n(T)^2 - 1}{n(T)^2 + 2} = \frac{N_A \rho(T) \alpha}{3\varepsilon_0 M} \tag{A.2}$$

was used, where α is the molecular polarizability. No explicit knowledge of α is required to solve Eq. (A.2). Instead, the literature value for the refractive index at 25°C, n_{25}, the density at 25°C, ρ_{25}, and $\rho(T)$ are used to obtain

$$n(T) = \sqrt{\frac{2(n_{25}^2 - 1)\rho(T) + (n_{25}^2 + 2)\rho_{25}}{(n_{25}^2 + 2)\rho_{25} - 2(n_{25}^2 - 1)\rho(T)}}. \tag{A.3}$$

For some liquids (indicated in table A.1) the density is only reported at one single temperature. In these cases the opposite procedure as Eq. (A.3) was applied, i.e. $\rho(T)$ was calculated from $n(T)$, which was measured at several temperatures using an Abbe refractometer (see Ref. [44]) and extrapolated linearly to lower temperatures.

Table A.1: g_K, β, μ, parameters ρ_0 and δ from Eq. (A.1) and n_{25} at 25°C of all investigated liquids. The citation behind the substance names refers to an earlier publication of the dielectric data. [a] Due to structure formation of phosphates with benzene and carbon tetrachloride, data determined in solution with alkanes are used. [b] For MAs, the dipole moment of the C-O-H bond, $\mu_{COH} = 1.68$ D, is used. [c] Determined via refractive index. [d] Data are for 2-methyl-2-hexanol. [e] Determined by combining ρ(20°C) [359] and temperature dependence of N,N-dimethylacetamide [360]. [f] Determined from room temperature data due to problems with partial crystallization at low temperatures.

supercooled liquid	g_K	β	μ/D	$\rho_0/(\mathrm{g\,cm^{-3}})$	$\delta/(10^{-4}\,\mathrm{g\,cm^{-3}K^{-1}})$	n_{25}	studied T / K
diethylphthalate	0.80 (8)	0.48	2.73 [361]	1.37338 [362]	8.7088	1.50	192-220
dibuthylphthalate	0.82 (8)	0.50	2.82 [361]	1.28348 [363]	8.1045	1.49	183-210
dioctylphthalate	0.83 (8)	0.47	2.84 [361]	1.20026 [362]	7.3896	1.49	185-189
triethyl phospate	1.98 (20)	0.61	2.86 [364] [a]	1.36609 [365]	9.9886	1.41	138-142
tripropyl phosphate	1.61 (16)	0.66	2.93 [364] [a]	1.27859 [366]	9.267	1.4136	140-160
tributhyl phosphate [102]	1.74 (18)	0.62	2.76 [364] [a]	1.22584 [362]	8.4999	1.42	147-178
triphenyl phosphite	0.70 (7)	0.49	1.51 [367]	1.44297 [368]	8.7143	1.56	206-208
methyl-m-toluate	0.76 (8)	0.51	1.97 [369]	1.29303 [370]	7.85	1.52	175-185
m-toluidine [371]	0.99 (10)	0.45	1.45 [372]	1.23679[373]	8.46	1.568	192-202
toluene [108]	0.90 (21) [f]	0.44	0.38 [369]	1.14090[374]	9.35	1.494	119-122
buthyl methacrylate	0.58 (6)	0.51	2.15 [361]	1.17547 [375]	9.5582	1.43	137-150
2-methyltetrahydrofuran	0.91 (9)	0.50	1.58 [376]	1.1545 [377]	10.285	1.41	97-102
propylene carbonate	1.09 (11)	0.62	4.55 [361]	1.50832 [378]	10.42	1.4218	159-177
N,N-diethylacetamide	2.05 (21)	0.72	3.68 [379]	1.16188 [e]	8.480 [e]	1.4385	165-180
propylene glycol [191]	2.92 (30)	0.66	2.25 [380]	1.24892 [381]	7.2503	1.43	175-210
glycerol [121]	2.48 (25)	0.59	2.67 [382]	1.42982 [381]	5.7469	1.47	204-234
phenyl salicate (salol) [383]	0.62 (6)	0.48	2.27 [384]	1.45381 [385]	8.652143	1.62	230-235
eugenol	1.08 (11)	0.56	2.49 [386]	1.30571 [387]	8.5018	1.54	199-204
1-phenyl-1-propanol [103]	1.59 (16)	0.59	1.68 [b]	1.19326 [c]	6.7363	1.5266	199-234
1-phenyl-2-propanol	3.39 (34)	0.68	1.68 [b]	1.19326 [c]	6.7363	1.5191	208-240
2-phenyl-1-propanol [103]	3.30 (33)	0.67	1.68 [b]	1.20365 [c]	6.7949	1.5266	203-234
3-phenyl-1-propanol [103]	3.52 (36)	0.74	1.68 [b]	1.20365 [c]	6.7949	1.5266	190-223
1-propanol [168]	4.56 (46)	0.92	1.68 [b]	1.03393 [381]	7.8577	1.3862	113-125
5-methyl-2-hexanol	4.07 (41)	0.86	1.68 [b]	1.04563 [388] [d]	7.95	1.4312	156-215
2-ethyl-1-hexanol [169]	4.93 (50)	0.94	1.68 [b]	1.04941 [389]	7.39	1.4325	170-220

B

SAMPLE PREPARATION DETAILS

Details about the preparation of various samples analyzed within this work are summarized in the subsequent sections.

Various supercooled liquids analyzed with regard to dipolar cross-correlations

All liquids were prepared as received from the vendor in a standard home-built dielectric sample cell. The samples were quenched by exposing the entire sample holder to LN_2. Subsequently, the samples were progressively heated from T_g to room temperature, while the dielectric spectrum was probed at various temperatures in-between.

Phenyl Propanols

1-phenyl-1-propanol (Acros Organics, 99%), 2-phenyl-1-propanol (Aldrich, 97%) and 3-phenyl-1-propanol (Alfa Aesar, 99%) were filtered into a PCS sample-cell by using a 200 nm hydrophilic syringe filter. The samples for DS were used without further purification.[103]

Octanol isomers

2-ethyl-1-hexanol (2E1H, Sigma Aldrich, 99%), 5-methyl-3-heptanol (5M3H, TCI Chemicals, 98%), 4-methyl-3-heptanol (4M3H, Alfa Aesar, 99%) and 3-methyl-3-heptanol (3M3H, TCI Chemicals, 98%) were filtered into PCS sample-cells using 200 nm hydrophobic syringe filters. The dielectric samples were prepared without further purification. A broad temperature range was analyzed in PCS and DS, except for 5M3H, where in PCS only temperatures below 170 K could be measured, due to turbidity of the sample. At low temperatures, turbidity could be avoided by rapidly cooling from high temperatures to a temperature just below T_g with cooling rates > 6 K/min. At these temperatures the sample stayed transparent for >24 h.[170]

Polyhydric alcohols

Propylene glycol (PG, 1,2-propanediol, Alfa Aesar, 99.5%), DL-threitol (Sigma Aldrich, 97%), xylitol (Acros Organics, 99%) and D-sorbitol (Acros Organics, 97%) were measured in DS and PCS. The data of glycerol were already published and discussed in Ref.[121]. PG was used in this study, since ethylene glycol, the next smaller element of the homologous series after Glycerol, tends to crystallized and is not easily supercoolable. For the DS measurements PG and glycerol were used as received. For PCS both substances were filtered using a 400 nm hydrophilic syringe filter. The other PAs were received as a white powder. For DS the powder

was first filled into a sample cell, then dried at 1 mbar and room temperature for one hour, and finally melted and once again dried at 150°C and 1 mbar for three hours. The PCS samples were prepared using the same drying and melting procedure, however carried out with the powder filled into a glass syringe. A stainless steel filter holder in combination with 450 nm Nylon membrane filters was used to fill the liquid sample into the PCS sample cell at 150°C. This procedure was repeated several times until a sufficiently large sample volume was obtained. Finally, the sample was again dried in the vacuum oven for more than three hours.[191]

2-picoline/PMMA mixture

2-picoline (Aldrich, 98%) and Poly(methyl methacrylate) (PSS, Mw = 4300 Da, PDI= 1.05, atactic) were mixed with a solvent concentration of 50 wt%. The mixture was sealed and stored at 70°C for four weeks to ensure complete mixing. Afterwards, a DS sample cell was prepared without further purification and the remainder of the sample was filtered into a light-scattering sample cell using a 450 nm Nylon syringe filter. To ensure the high-viscosity liquid to pass through the filter, the latter was flooded with 2-picoline before the filtering process. The slight increase of concentration was estimated to be 2-3% by weight.[104]

Laponite

Laponite powder (Laponite-RD from BYK) was dried for one week at 1 mbar to remove all residual water. Water with pH 10 and ionic strength $I < 10^{-4}$ M was obtained by adding an appropriate amount of NaOH to milli-Q water. Subsequently, 2.98 wt% of Laponite was added and the mixture was stirred for 24 h. Finally, the sample was filtered into a glass cylinder using a 450 nm syringe filter, which may have led to a slight reduction of the Laponite concentration. Physical aging starts directly after the mixture is filtered; however for the first few hours the colloidal dynamics is too fast to be captured by the camera. The camera measurement with exposure time 0.1 s was started several minutes after filtration, and the scattered light was monitored in VV (polarized) geometry over 1,500,000 frames (∼ 42 h). Laponite was studied at room temperature.[280]

Epoxy

The epoxy system is based on bisphenol A diglycidyl ether resin (Alfa Aesar). As polymerization agent N,N,N',N'-tetraethyldiethylenetriamine (Sigma Aldrich, 90%) was used. This specific agent induces a linear polymerization; thus the mixture was prepared with a 1:1 molar ratio. Before mixing, the resin was dried and degassed in a vacuum oven. Afterwards, it was filled into a glass syringe equipped with a stainless steel filter holder containing a 450 nm nylon membrane filter suitable for operation at high temperatures. The syringe was then heated to 150 °C to decrease the viscosity of the resin, which allowed us to filter the resin into a dust-free sample glass. The appropriate amount of hardener was added, again, using a syringe filter. Subsequently, the mixture was magnetically stirred at 400 rpm for 10 min and filled into a dust-free cylindrical glass sample holder. Air-bubbles were removed by exposing the mixture to vacuum for 15 min. Finally, the glass tube was sealed and placed inside a suitable sample oven preheated to 310 K, and the camera measurement in VH geometry with exposure time 0.1 s was started for 2,000,000 frames (∼56 h).[280]

LJ system

The data for the binary Lennard-Jones (LJ) system were produced using the GPU-optimized software RUMD [345]. The interaction potential used is the modification of the standard Kob-Andersen potential introduced in Ref. [344] to counteract crystallization. Jumps from temperature 0.48 to 0.40 at density 1.20 for a system of $N = 8000$ particles (6400 A particles and 1600 B particles) were simulated for $1.68 \cdot 10^5$ LJ time units with a time step of 0.005. The simulations ran in the *NVT* ensemble using a standard Nosé-Hoover thermostat with relaxation time of 0.2 in LJ units. Velocities were re-scaled at the start of the simulation to temperature 0.40 in order to avoid nonphysical behavior of the thermostat. The potential energy of each particle was saved every 128 time steps (corresponding to 0.64 LJ time units). Simulations from 30 independent starting configurations were run. The data analyzed in Section 11.3.3 refer to the A particles only and consider a total of 192,000 particles in order to obtain time-resolved autocorrelations with minimal statistical noise. Starting configurations were obtained from an equilibrium simulation at density 1.20 and temperature 0.48, separated in time by $4.2 \cdot 10^4$ LJ units (roughly corresponding to 80 relaxation times).[280]

1P1P in the Peltier-controlled sample cell

Due to the small volume of the Peltier-controlled sample cell, the sample can not be prepared as usual by drop-wisely filtering the liquid into the cell, due to the surface tension of the liquid. To resolve this issue, first a cannula was cleaned with filtered 2-butanone and, subsequently, it was inserted into the sample cell to fill it with filtered 1P1P. A second issue that has to be considered are residual air-bubbles that remain inside of the sample cell after sealing it, which would interfere with the laser beam during measurement. Thus, a teflon plug is used to avoid air from the thread at the lid to enter the sample cell after it has been attached to the cold-finger.

BIBLIOGRAPHY

[1] P. G. Debenedetti and F. H. Stillinger, *Supercooled liquids and the glass transition*, Nature **410**, 259–267 (2001) (cit. on p. 1).

[2] G. Greaves and S. Sen, *Inorganic glasses, glass-forming liquids and amorphizing solids*, Adv. Phys. **56**, 1–166 (2007) (cit. on p. 1).

[3] A. K. Varshneya, *Fundamentals of inorganic glasses* (Elsevier, 2013) (cit. on p. 1).

[4] D. Cangialosi, *Dynamics and thermodynamics of polymer glasses*, J. Phys.: Condens.Matter **26**, 153101 (2014) (cit. on p. 1).

[5] I. M. Hodge, *Physical aging in polymer glasses*, Science **267**, 1945–1947 (1995) (cit. on pp. 1, 3, 89).

[6] A. L. Greer, *Metallic glasses*, Science **267**, 1947–1953 (1995) (cit. on p. 1).

[7] C. A. Angell, *Formation of glasses from liquids and biopolymers*, Science **267**, 1924–1935 (1995) (cit. on pp. 1–2).

[8] K. H. Fischer and J. A. Hertz, *Spin glasses*, 1 (Cambridge University Press, 1993) (cit. on p. 1).

[9] E. Vincent, J. Hammann, M. Ocio, et al., *Slow dynamics and aging in spin glasses*, in Complex behaviour of glassy systems: proceedings of the xiv sitges conference sitges, barcelona, spain, 10–14 june 1996 (Springer, 2007), pp. 184–219 (cit. on pp. 1, 153).

[10] F. Sciortino and P. Tartaglia, *Glassy colloidal systems*, Adv. Phys. **54**, 471–524 (2005) (cit. on pp. 1, 141).

[11] G. L. Hunter and E. R. Weeks, *The physics of the colloidal glass transition*, Rep. Prog. Phys. **75**, 066501 (2012) (cit. on pp. 1, 141).

[12] J. C. Dyre, *Narayanaswamy's 1971 aging theory and material time*, J. Chem. Phys. **143**, 114507 (2015) (cit. on pp. 1, 91, 110–111, 114, 149, 159).

[13] J.-P. Hansen and I. R. McDonald, *Theory of simple liquids: with applications to soft matter* (Academic press, 2013) (cit. on pp. 2, 8).

[14] H. Vogel, *Das temperaturabhangigkeitsgesetz der viskositat von flüssigkeiten*, Phys. Z. **22**, 645–646 (1921) (cit. on p. 2).

[15] G. S. Fulcher, *Analysis of recent measurements of the viscosity of glasses*, J. Am. Ceram. Soc. **8**, 339–355 (1925) (cit. on p. 2).

[16] G. A. Tammann and W. Hesse, *Die abhängigkeit der viscosität von der temperatur bie unterkühlten flüssigkeiten*, Z. Anorg. Allg. Chem. **156**, 245–257 (1926) (cit. on p. 2).

[17] T. Hecksher, A. I. Nielsen, N. B. Olsen, et al., *Little evidence for dynamic divergences in ultraviscous molecular liquids*, Nat. Phys. **4**, 737–741 (2008) (cit. on p. 2).

[18] Y. S. Elmatad, D. Chandler, and J. P. Garrahan, *Corresponding states of structural glass formers*, J. Phys. Chem. B **113**, 5563–5567 (2009) (cit. on p. 2).

[19] A. Cavagna, *Supercooled liquids for pedestrians*, Phys. Rep. **476**, 51–124 (2009) (cit. on p. 2).

[20]L. Berthier and G. Biroli, *Theoretical perspective on the glass transition and amorphous materials*, Rev. Mod. Phys. **83**, 587–645 (2011) (cit. on pp. 2, 153).

[21]J. C. Dyre, *Colloquium: the glass transition and elastic models of glass-forming liquids*, Rev. Mod. Phys. **78**, 953–972 (2006) (cit. on p. 2).

[22]C. Rainone, E. Bouchbinder, and E. Lerner, *Pinching a glass reveals key properties of its soft spots*, Proc. Natl. Acad. Sci. **117**, 5228–5234 (2020) (cit. on p. 2).

[23]G. Kapteijns, D. Richard, E. Bouchbinder, et al., *Does mesoscopic elasticity control viscous slowing down in glassforming liquids?*, The Journal of Chemical Physics **155**, 074502 (2021) (cit. on p. 2).

[24]M. P. Ciamarra, W. Ji, and M. Wyart, *Local vs. cooperative: unraveling glass transition mechanisms with seer*, 2024 (cit. on p. 2).

[25]R. Böhmer, *Nanoscale heterogeneity if glass-forming liquids: experimental advances*, Curr. Opin. Solid State Mater. Sci. **3**, 378–385 (1998) (cit. on pp. 2, 23–24, 157).

[26]H. Sillescu, *Heterogeneity at the glass transition: a review*, J. Non-Cryst. Solids **243**, 81–108 (1999) (cit. on pp. 2, 23, 157).

[27]M. D. Ediger, *Spatially heterogeneous dynamics in supercooled liquids*, Annu. Rev. Phys. Chem. **51**, 99–128 (2000) (cit. on pp. 2–3, 23–24, 157).

[28]R. Richert, *Heterogeneous dynamics in liquids: fluctuations in space and time*, J. Phys.: Condens. Matter **14**, R703 (2002) (cit. on pp. 2–3, 23–24, 157).

[29]R. Richert, N. Israeloff, C. Alba-Simionesco, et al., *Experimental approaches to heterogeneous dynamics*, in *Dynamical Heterogeneities in Glasses, Colloids, and Granular Media* (Oxford University Press, July 2011) (cit. on pp. 2, 23, 157).

[30]C. Scalliet, B. Guiselin, and L. Berthier, *Thirty milliseconds in the life of a supercooled liquid*, Phys. Rev. X **12**, 041028 (2022) (cit. on pp. 3, 25, 35, 157).

[31]J. C. Dyre, *Solid-that-flows picture of glass-forming liquids*, J. Phys. Chem. Lett. **15**, 1603–1617 (2024) (cit. on pp. 3, 35).

[32]R. Böhmer, K. L. Ngai, C. A. Angell, et al., *Nonexponential relaxations in strong and fragile glass formers*, J. Chem. Phys. **99**, 4201–4209 (1993) (cit. on pp. 3, 31, 66, 157).

[33]A. I. Nielsen, T. Christensen, B. Jakobsen, et al., *Prevalence of approximate t relaxation for the dielectric α process in viscous organic liquids*, J. Chem. Phys. **130**, 154508 (2009) (cit. on pp. 3, 29, 31–33, 45, 157).

[34]M. Paluch, J. Knapik, Z. Wojnarowska, et al., *Universal behavior of dielectric responses of glass formers: role of dipole-dipole interactions*, Phys. Rev. Lett. **116**, 025702 (2016) (cit. on pp. 3, 31, 44–47, 157).

[35]L. C. E. Struik et al., *Physical aging in amorphous polymers and other materials*, Vol. 106 (Citeseer, 1978) (cit. on pp. 3, 89, 152–153).

[36]G. Scherer, *Relaxation in glass and composites*, A Wiley-Interscience publication (Wiley, 1986) (cit. on pp. 3, 89–90).

[37]T. Hecksher, N. B. Olsen, K. Niss, et al., *Physical aging of molecular glasses studied by a device allowing for rapid thermal equilibration*, J. Chem. Phys. **133**, 174514 (2010) (cit. on pp. 3, 89–90, 103, 122, 125).

[38]O. S. Narayanaswamy, *A model of structural relaxation in glass*, J. Am. Ceram. Soc. **54**, 491–498 (1971) (cit. on pp. 3, 89–91, 108, 158).

[39]I. Hodge, *Enthalpy relaxation and recovery in amorphous materials*, J. Non-Cryst. Solids **169**, 211–266 (1994) (cit. on pp. 3, 108, 158).

[40]C. T. Moynihan, A. J. Easteal, M. A. De Bolt, et al., *Dependence of the fictive temperature of glass on cooling rate*, J. Am. Ceram. Soc. **59**, 12–16 (1976) (cit. on pp. 3, 108).

[41]J. C. Mauro, R. J. Loucks, and P. K. Gupta, *Fictive temperature and the glassy state*, J. Am. Ceram. Soc. **92**, 75–86 (2009) (cit. on pp. 3, 108, 158).

[42]T. Hecksher, N. B. Olsen, and J. C. Dyre, *Communication: Direct tests of single-parameter aging*, J. Chem. Phys. **142**, 241103 (2015) (cit. on pp. 3, 109–110, 122, 125).

[43]B. Riechers, L. A. Roed, S. Mehri, et al., *Predicting nonlinear physical aging of glasses from equilibrium relaxation via the material time*, Sci. Adv. **8**, eabl9809 (2022) (cit. on pp. 3, 109–110, 122).

[44]F. Pabst, *Understanding the relaxation spectra of neat and mixed ionic liquids*, PhD thesis (Technische Universität, Darmstadt, 2022) (cit. on pp. 4, 13, 19, 32, 37–41, 157, 163).

[45]N. Wiener, *Generalized harmonic analysis*, Acta Math. **55**, 117–258 (1930) (cit. on p. 8).

[46]A. Khintchine, *Korrelationstheorie der stationären stochastischen prozesse*, Math. Ann. **109**, 604–615 (1934) (cit. on p. 8).

[47]F. Kremer and A. Schönhals, *Broadband dielectric spectroscopy* (Springer Science & Business Media, 2002) (cit. on pp. 8, 16).

[48]J. Gabriel, F. Pabst, A. Helbling, et al., *Depolarized dynamic light scattering and dielectric spectroscopy: two perspectives on molecular reorientation in supercooled liquids*, in *The scaling of relaxation processes* (Springer, 2018), pp. 203–245 (cit. on pp. 8, 16, 18, 55).

[49]B. Berne and R Pecora, *Dynamic light scattering* (Wiley, New York, 1976) (cit. on p. 9).

[50]A. Siegert, *On the fluctuations in signals returned by many independently moving scatterers* (Radiation Laboratory, Massachusetts Institute of Technology, 1943) (cit. on p. 12).

[51]L. G. B. Bremer, L. Deriemaeker, R. Finsy, et al., *Fiber optic dynamic light scattering, neither homodyne nor heterodyne*, Langmuir **9**, 2008–2014 (1993) (cit. on p. 13).

[52]F. Pabst, J. Gabriel, P. Weigl, et al., *Molecular dynamics of supercooled ionic liquids studied by light scattering and dielectric spectroscopy*, Chem. Phys. **494**, 103–110 (2017) (cit. on p. 13).

[53]E. Hecht, *Optik* (Walter de Gruyter GmbH & Co KG, 2023) (cit. on p. 14).

[54]J. Sandercock, *Tandem fabry-perot interferometer tfp-1*, Scientific Instruments (Mettmenstetten, Switzerland) (cit. on pp. 14–16).

[55]T. Blochowicz, *Broadband dielectric spectroscopy in neat and binary molecular glass formers* (Logos Verlag Berlin, Berlin, Germany, Aug. 2003) (cit. on pp. 16, 19, 27).

[56]R. de L. Kronig, *On the theory of dispersion of x-rays*, J. Opt. Soc. Am. **12**, 547–557 (1926) (cit. on p. 17).

[57]H. Kramers, *La diffusion de la lumière par les atomes* (1928) (cit. on p. 17).

[58]P. Steeman and J Van Turnhout, *A numerical kramers-kronig transform for the calculation of dielectric relaxation losses free from ohmic conduction losses*, Colloid Polym. Sci. **275**, 106–115 (1997) (cit. on p. 17).

[59]M. Wübbenhorst and J. van Turnhout, *Analysis of complex dielectric spectra. i. one-dimensional derivative techniques and three-dimensional modelling*, J. Non-Cryst. Solids **305**, 40–49 (2002) (cit. on pp. 17, 77).

[60]P.-M. Déjardin, *Kinetic yvon-born-green theory of the linear dielectric constant and complex permittivity of isotropic polar fluids*, Phys. Rev. E **105**, 024109 (2022) (cit. on pp. 18, 39–40).

[61]A. Rivera, T. Blochowicz, C. Gainaru, et al., *Spectral response from modulus time domain data of disordered materials*, J. Appl. Phys. **96**, 5607–5612 (2004) (cit. on p. 19).

[62]R. Böhmer, R. Chamberlin, G. Diezemann, et al., *Nature of the non-exponential primary relaxation in structural glass-formers probed by dynamically selective experiments*, J. Non-Cryst. Solids **235-237**, 1–9 (1998) (cit. on p. 23).

[63]G. Hinze, *Geometry and time scale of the rotational dynamics in supercooled toluene*, Phys. Rev. E **57**, 2010–2018 (1998) (cit. on p. 23).

[64]G. Hinze, G. Diezemann, and H. Sillescu, *Four-time rotational correlation functions*, Europhys. Lett. **44**, 565 (1998) (cit. on p. 23).

[65]A. Heuer, M. Wilhelm, H. Zimmermann, et al., *Rate memory of structural relaxation in glasses and its detection by multidimensional nmr*, Phys. Rev. Lett. **75**, 2851–2854 (1995) (cit. on p. 23).

[66]M. T. Cicerone and M. D. Ediger, *Relaxation of spatially heterogeneous dynamic domains in supercooled ortho-terphenyl*, J. Chem. Phys. **103**, 5684–5692 (1995) (cit. on p. 23).

[67]C.-Y. Wang and M. D. Ediger, *How long do regions of different dynamics persist in supercooled o-terphenyl?*, J. Phys. Chem. B **103**, 4177–4184 (1999) (cit. on p. 24).

[68]B. Schiener, R. Böhmer, A. Loidl, et al., *Nonresonant spectral hole burning in the slow dielectric response of supercooled liquids*, Science **274**, 752–754 (1996) (cit. on p. 24).

[69]R. Richert and M. Richert, *Dynamic heterogeneity, spatially distributed stretched-exponential patterns, and transient dispersions in solvation dynamics*, Phys. Rev. E **58**, 779–784 (1998) (cit. on p. 24).

[70]K. Paeng, H. Park, D. T. Hoang, et al., *Ideal probe single-molecule experiments reveal the intrinsic dynamic heterogeneity of a supercooled liquid*, Proc. Natl. Acad. Sci. **112**, 4952–4957 (2015) (cit. on p. 24).

[71]H. Wendt and R. Richert, *Heterogeneous relaxation patterns in supercooled liquids studied by solvation dynamics*, Phys. Rev. E **61**, 1722–1728 (2000) (cit. on p. 24).

[72]R. Chamberlin, B Schiener, and R Böhmer, *Slow dielectric relaxation of supercooled liquids investigated by nonresonant spectral hole burning*, MRS Online Proc. Libr. **455**, 117 (1996) (cit. on p. 24).

[73]T. Blochowicz and E. A. Rössler, *Nonresonant dielectric hole burning in neat and binary organic glass formers*, J. Chem. Phys. **122**, 224511 (2005) (cit. on p. 24).

[74]A. Heuer, U. Tracht, S. C. Kuebler, et al., *The orientational memory from three-time correlations in multidimensional nmr experiments*, J. Mol. Struct. **479**, 251–259 (1999) (cit. on p. 24).

[75]L. Berthier, *Self-induced heterogeneity in deeply supercooled liquids*, Phys. Rev. Lett. **127**, 088002 (2021) (cit. on p. 24).

[76]D. Diaz Vela and D. S. Simmons, *The microscopic origins of stretched exponential relaxation in two model glass-forming liquids as probed by simulations in the isoconfigurational ensemble*, J. Chem. Phys. **153**, 234503 (2020) (cit. on p. 24).

[77]U. Tracht, M. Wilhelm, A. Heuer, et al., *Length scale of dynamic heterogeneities at the glass transition determined by multidimensional nuclear magnetic resonance*, Phys. Rev. Lett. **81**, 2727–2730 (1998) (cit. on p. 24).

[78]E Vidal Russell and N. Israeloff, *Direct observation of molecular cooperativity near the glass transition*, Nature **408**, 695–698 (2000) (cit. on p. 24).

[79]S. A. Reinsberg, X. H. Qiu, M. Wilhelm, et al., *Length scale of dynamic heterogeneity in supercooled glycerol near Tg*, J. Chem. Phys. **114**, 7299–7302 (2001) (cit. on p. 24).

[80]E. R. Weeks, J. C. Crocker, A. C. Levitt, et al., *Three-dimensional direct imaging of structural relaxation near the colloidal glass transition*, Science **287**, 627–631 (2000) (cit. on p. 24).

[81]W. K. Kegel, and A. van Blaaderen, *Direct observation of dynamical heterogeneities in colloidal hard-sphere suspensions*, Science **287**, 290–293 (2000) (cit. on p. 24).

[82]C. K. Mishra, A. Rangarajan, and R. Ganapathy, *Two-step glass transition induced by attractive interactions in quasi-two-dimensional suspensions of ellipsoidal particles*, Phys. Rev. Lett. **110**, 188301 (2013) (cit. on p. 24).

[83]Z. Zheng, R. Ni, F. Wang, et al., *Structural signatures of dynamic heterogeneities in monolayers of colloidal ellipsoids*, Nat. Commun. **5**, 3829 (2014) (cit. on p. 24).

[84]A. Ninarello, L. Berthier, and D. Coslovich, *Models and algorithms for the next generation of glass transition studies*, Phys. Rev. X **7**, 021039 (2017) (cit. on p. 24).

[85]S. C. Glotzer, *Spatially heterogeneous dynamics in liquids: insights from simulation*, J. Non-Cryst. Solids **274**, 342–355 (2000) (cit. on p. 25).

[86]B. Guiselin, C. Scalliet, and L. Berthier, *Microscopic origin of excess wings in relaxation spectra of supercooled liquids*, Nat. Phys **18**, 468–472 (2022) (cit. on pp. 25, 35, 157).

[87]T. Blochowicz, C. Tschirwitz, S. Benkhof, et al., *Susceptibility functions for slow relaxation processes in supercooled liquids and the search for universal relaxation patterns*, J. Chem. Phys. **118**, 7544–7555 (2003) (cit. on pp. 27–28, 44).

[88]G. Williams, D. C. Watts, S. B. Dev, et al., *Further considerations of non symmetrical dielectric relaxation behaviour arising from a simple empirical decay function*, Trans. Faraday Soc. **67**, 1323–1335 (1971) (cit. on p. 28).

[89]J. C. Dyre, *Ten themes of viscous liquid dynamics*, J. Phys.: Condens.Matter **19**, 205105 (2007) (cit. on p. 31).

[90]P. K. Gupta and J. C. Mauro, *Two factors governing fragility: stretching exponent and configurational entropy*, Phys. Rev. E **78**, 062501 (2008) (cit. on p. 31).

[91]K. Ngai, *Universal properties of relaxation and diffusion in complex materials: originating from fundamental physics with rich applications*, Prog. Mater. Sci. **139**, 101130 (2023) (cit. on p. 31).

[92]X. Qiu and M. D. Ediger, *Length scale of dynamic heterogeneity in supercooled d-sorbitol: comparison to model predictions*, J. Phys. Chem. B **107**, 459–464 (2003) (cit. on pp. 31, 66).

[93]N. B. Olsen, T. Christensen, and J. C. Dyre, *Time-temperature superposition in viscous liquids*, Phys. Rev. Lett. **86**, 1271–1274 (2001) (cit. on pp. 32–33, 157).

[94]F. Pabst, J. P. Gabriel, T. Böhmer, et al., *Generic Structural Relaxation in Supercooled Liquids*, J. Phys. Chem. Lett. **12**, 3685–3690 (2021) (cit. on pp. 32, 37–40, 44, 70).

[95]D. L. Sidebottom, *Generic α relaxation in a strong GeO2 glass melt*, Phys. Rev. E **107**, L012602 (2023) (cit. on p. 33).

[96]D. Sidebottom, *Dynamic light scattering study of the non-exponential α-relaxation in sodium germanate glass melts*, J. Non-Cryst. Solids **627**, 122819 (2024) (cit. on p. 33).

[97] J. C. Dyre, *Solidity of viscous liquids. iii. α relaxation*, Phys. Rev. E **72**, 011501 (2005) (cit. on p. 35).

[98] J. C. Dyre, *Solidity of viscous liquids. iv. density fluctuations*, Phys. Rev. E **74**, 021502 (2006) (cit. on p. 35).

[99] I. Pihlajamaa, C. C. L. Laudicina, and L. M. C. Janssen, *Influence of polydispersity on the relaxation mechanisms of glassy liquids*, Phys. Rev. Res. **5**, 033120 (2023) (cit. on p. 35).

[100] M. Ozawa, Y. Iwashita, W. Kob, et al., *Creating bulk ultrastable glasses by random particle bonding*, Nature Communications **14**, 113 (2023) (cit. on p. 35).

[101] M. Ozawa, J.-L. Barrat, W. Kob, et al., *Creating equilibrium glassy states via random particle bonding*, J. Stat. Mech.: Theory Exp. **2024**, 013303 (2024) (cit. on p. 35).

[102] F. Pabst, A. Helbling, J. Gabriel, et al., *Dipole-dipole correlations and the debye process in the dielectric response of nonassociating glass forming liquids*, Phys. Rev. E **102**, 010606 (2020) (cit. on pp. 37, 40–41, 164).

[103] T. Böhmer, J. P. Gabriel, T. Richter, et al., *Influence of Molecular Architecture on the Dynamics of H-Bonded Supramolecular Structures in Phenyl-Propanols*, J. Phys. Chem. B **123**, 10959–10966 (2019) (cit. on pp. 37, 55–56, 164–165).

[104] T. Böhmer, R. Horstmann, J. P. Gabriel, et al., *Origin of apparent slow solvent dynamics in concentrated polymer solutions*, Macromolecules **54**, 10340–10349 (2021) (cit. on pp. 37, 76–77, 166).

[105] T. Böhmer, F. Pabst, J. P. Gabriel, et al., *Dipolar order controls dielectric response of glass-forming liquids*, Phys. Rev. Lett. **132**, 206101 (2024) (cit. on pp. 37, 163).

[106] J. E. Anderson and R. Ullman, *Molecular Relaxation in a Fluctuating Environment*, J. Chem. Phys. **47**, 2178–2184 (1967) (cit. on p. 39).

[107] S. Shahriari, A. Mandanici, L.-M. Wang, et al., *Dynamics of glass-forming liquids. VIII. Dielectric signature of probe rotation and bulk dynamics in branched alkanes*, J. Chem. Phys. **121**, 8960–8967 (2004) (cit. on pp. 39–40).

[108] A. Kudlik, S. Benkhof, T. Blochowicz, et al., *The dielectric response of simple organic glass formers*, J. Mol. Struct. **479**, 201–218 (1999) (cit. on pp. 39–40, 164).

[109] P.-M. Déjardin, S. V. Titov, and Y. Cornaton, *Linear complex susceptibility of long-range interacting dipoles with thermal agitation and weak external ac fields*, Phys. Rev. B **99**, 024304 (2019) (cit. on pp. 39, 158).

[110] P.-M. Déjardin, F. Pabst, Y. Cornaton, et al., *Temperature dependence of the kirkwood correlation factor and linear dielectric constant of simple isotropic polar fluids*, Phys. Rev. E **105**, 024108 (2022) (cit. on pp. 39–40).

[111] S. Hensel-Bielowka, S. Pawlus, C. M. Roland, et al., *Effect of large hydrostatic pressure on the dielectric loss spectrum of type-a glass formers*, Phys. Rev. E **69**, 050501 (2004) (cit. on p. 41).

[112] C. Gainaru, H. Nelson, J. Huebinger, et al., *Suppression of orientational correlations in the viscous-liquid state of hyperquenched pressure-densified glycerol*, Phys. Rev. Lett. **125**, 065503 (2020) (cit. on p. 41).

[113] M. Naoki and S. Katahira, *Contribution of hydrogen bonds to apparent molecular mobility in supercooled d-sorbitol and some polyols*, J. Phys. Chem. **95**, 431–437 (1991) (cit. on p. 41).

[114] R. L. Cook, H. E. King, and D. G. Peiffer, *Pressure-induced crossover from good to poor solvent behavior for polyethylene oxide in water*, Phys. Rev. Lett. **69**, 3072–3075 (1992) (cit. on p. 41).

[115]T. Körber, R. Stäglich, C. Gainaru, et al., *Systematic differences in the relaxation stretching of polar molecular liquids probed by dielectric vs magnetic resonance and photon correlation spectroscopy*, J. Chem. Phys. **153**, 124510 (2020) (cit. on p. 42).

[116]M. Becher, T. Körber, A. Döß, et al., *Nuclear Spin Relaxation in Viscous Liquids: Relaxation Stretching of Single-Particle Probes*, J. Phys. Chem. B **125**, 13519–13532 (2021) (cit. on pp. 42, 66, 69–70).

[117]M. Becher, A. Lichtinger, R. Minikejew, et al., *NMR Relaxometry Accessing the Relaxation Spectrum in Molecular Glass Formers*, Int. J. Mol. Sci. **23**, 5118 (2022) (cit. on pp. 42, 58).

[118]C. Gainaru, R. Figuli, T. Hecksher, et al., *Shear-modulus investigations of monohydroxy alcohols: evidence for a short-chain-polymer rheological response*, Phys. Rev. Lett. **112**, 098301 (2014) (cit. on pp. 42, 55).

[119]M. Mikkelsen, J. P. Gabriel, and T. Hecksher, *Dielectric and shear mechanical spectra of propanols: the influence of hydrogen-bonded structures*, J. Phys. Chem. B **127**, 371–377 (2023) (cit. on pp. 42, 58).

[120]S. Arrese-Igor, A. Alegría, and J. Colmenero, *Signature of hydrogen bonding association in the dielectric signal of polyalcohols*, J. Mol. Liq. **318**, 114215 (2020) (cit. on p. 42).

[121]J. P. Gabriel, P. Zourchang, F. Pabst, et al., *Intermolecular cross-correlations in the dielectric response of glycerol*, Phys. Chem. Chem. Phys. **22**, 11644–11651 (2020) (cit. on pp. 42, 164–165).

[122]S. Patil, R. Sun, S. Cheng, et al., *Molecular mechanism of the debye relaxation in monohydroxy alcohols revealed from rheo-dielectric spectroscopy*, Phys. Rev. Lett. **130**, 098201 (2023) (cit. on pp. 42, 55, 65).

[123]K. Moch, P. Münzner, R. Böhmer, et al., *Molecular cross-correlations govern structural rearrangements in a nonassociating polar glass former*, Phys. Rev. Lett. **128**, 228001 (2022) (cit. on p. 42).

[124]S. Arrese-Igor, A. Alegría, and J. Colmenero, *Non-simple flow behavior in a polar van der Waals liquid: Structural relaxation under scrutiny*, J. Chem. Phys. **158**, 174504 (2023) (cit. on p. 42).

[125]M. Paluch, K. Koperwas, and Z. Wojnarowska, *Determination of self and cross contributions to the dipole–dipole correlations function from analysis of dielectric measurements*, J. Mol. Liq. **382**, 121907 (2023) (cit. on pp. 42, 58).

[126]M. Hénot, P.-M. Déjardin, and F. Ladieu, *Orientational dynamics in supercooled glycerol computed from md simulations: self and cross contributions*, Phys. Chem. Chem. Phys. **25**, 29233–29240 (2023) (cit. on pp. 43, 49, 84, 108, 157).

[127]S. Carlson, F. N. Brünig, P. Loche, et al., *Exploring the absorption spectrum of simulated water from mhz to infrared*, J. Phys. Chem. A **124**, 5599–5605 (2020) (cit. on p. 43).

[128]C. Hölzl, H. Forbert, and D. Marx, *Dielectric relaxation of water: assessing the impact of localized modes, translational diffusion, and collective dynamics*, Phys. Chem. Chem. Phys. **23**, 20875–20882 (2021) (cit. on p. 43).

[129]F. Alvarez, A. Arbe, and J. Colmenero, *The Debye's model for the dielectric relaxation of liquid water and the role of cross-dipolar correlations. A MD-simulations study*, J. Chem. Phys. **159**, 134505 (2023) (cit. on p. 43).

[130]T. Fukasawa, T. Sato, J. Watanabe, et al., *Relation between dielectric and low-frequency raman spectra of hydrogen-bond liquids*, Phys. Rev. Lett. **95**, 197802 (2005) (cit. on p. 43).

[131]J. S. Hansen, A. Kisliuk, A. P. Sokolov, et al., *Identification of structural relaxation in the dielectric response of water*, Phys. Rev. Lett. **116**, 237601 (2016) (cit. on p. 43).

[132]G. Johari and W Dannhauser, *Dielectric study of intermolecular association in sterically hindered octanol isomers*, J. Phys. Chem. **72**, 3273–3276 (1968) (cit. on pp. 44, 54, 57–58, 158).

[133]W Dannhauser, *Dielectric study of intermolecular association in isomeric octyl alcohols*, J. Chem. Phys. **48**, 1911–1917 (1968) (cit. on pp. 44, 54, 57–58, 158).

[134]L. P. Singh and R. Richert, *Watching hydrogen-bonded structures in an alcohol convert from rings to chains*, Phys. Rev. Lett. **109**, 167802 (2012) (cit. on pp. 44, 58, 158).

[135]L. P. Singh, C. Alba-Simionesco, and R. Richert, *Dynamics of glass-forming liquids. xvii. dielectric relaxation and intermolecular association in a series of isomeric octyl alcohols*, J. Chem. Phys. **139**, 144503 (2013) (cit. on pp. 44, 58, 158).

[136]F Fairbrother, *Determination of dipole moments in solution*, Nature **134**, 458–459 (1934) (cit. on p. 44).

[137]T. G. Scholte, *Determination of dipole moments from measurements on diluted solutions*, Recl. Trav. Chim. Pays-Bas **70**, 50–56 (1951) (cit. on p. 44).

[138]D. Kivelson and P. Madden, *Theory of dielectric relaxation*, Mol. Phys. **30**, 1749–1780 (1975) (cit. on pp. 48, 158).

[139]P. Madden and D. Kivelson, *A consistent molecular treatment of dielectric phenomena*, Adv. Chem. Phys., 467–566 (1984) (cit. on pp. 48, 158).

[140]T. Keyes, *Microscopic theory of collective anisotropic molecular reorientation*, Mol. Phys. **23**, 737–743 (1972) (cit. on p. 48).

[141]P. Bordewijk, *The Application of the Memory-Function Formalism to Dielectric Relaxation*, Z. Naturforsch. A **35**, 1207–1217 (1980) (cit. on p. 48).

[142]D. V. Matyushov and R. Richert, *From single-particle to collective dynamics in supercooled liquids*, J. Phys. Chem. Lett. **14**, 4886–4891 (2023) (cit. on p. 48).

[143]A. Volmari and H. Weingärtner, *Cross terms and kirkwood factors in dielectric relaxation of pure liquids*, J. Mol. Liq. **98-99**, 295–303 (2002) (cit. on p. 48).

[144]H. Weingärtner, H. Nadolny, A. Oleinikova, et al., *Collective contributions to the dielectric relaxation of hydrogen-bonded liquids*, J. Chem. Phys. **120**, 11692–11697 (2004) (cit. on p. 48).

[145]D. Braun, S. Boresch, and O. Steinhauser, *Transport and dielectric properties of water and the influence of coarse-graining: Comparing BMW, SPC/E, and TIP3P models*, J. Chem. Phys. **140**, 064107 (2014) (cit. on p. 48).

[146]T. Samanta and D. V. Matyushov, *Nonlinear dielectric relaxation of polar liquids*, J. Mol. Liq. **364**, 119935 (2022) (cit. on p. 48).

[147]K. Koperwas and M. Paluch, *Computational evidence for the crucial role of dipole cross-correlations in polar glass-forming liquids*, Phys. Rev. Lett. **129**, 025501 (2022) (cit. on pp. 49, 84, 157).

[148]R Böhmer, C Gainaru, and R Richert, *Structure and dynamics of monohydroxy alcohols—milestones towards their microscopic understanding, 100 years after debye*, Phys. Rep. **545**, 125–195 (2014) (cit. on pp. 49, 53–54, 62–64).

[149]C Gainaru, R Meier, S Schildmann, et al., *Nuclear-magnetic-resonance measurements reveal the origin of the debye process in monohydroxy alcohols*, Phys. Rev. Lett. **105**, 258303 (2010) (cit. on pp. 49, 54–55, 60, 62, 65).

[150]C. Gainaru, *Spectral shape simplicity of viscous materials*, Phys. Rev. E **100**, 020601 (2019) (cit. on p. 49).

[151]P. Debye, *Polar molecules*, J. Soc. Chem. Ind. **48**, 1036–1037 (1929) (cit. on p. 53).

[152]P. J. W. Debye, *Zur theorie der anomalen dispersion im gebiete der langwelligen elektrischen strahlung* (Druck von Friedr. Vieweg & Sohn, 1913) (cit. on p. 53).

[153]G. W. Stewart and R. M. Morrow, *X-ray diffraction in liquids: primary normal alcohols*, Phys. Rev. **30**, 232–244 (1927) (cit. on p. 54).

[154]P. Girard, *Dipole association in pure liquids*, Trans. Faraday Soc. **30**, 763–772 (1934) (cit. on p. 54).

[155]G. Oster and J. G. Kirkwood, *The Influence of Hindered Molecular Rotation on the Dielectric Constants of Water, Alcohols, and Other Polar Liquids*, J. Chem. Phys. **11**, 175–178 (1943) (cit. on p. 54).

[156]J. Kirkwood, *The dielectric polarization of polar liquids*, J. Chem. Phys. **7**, 911 (1939) (cit. on pp. 54, 157).

[157]H Fröhlich, *Theory of dielectrics* (Clarendon Press, Oxford, 1958) (cit. on p. 54).

[158]W Dannhauser, *Dielectric relaxation in isomeric octyl alcohols*, J. Chem. Phys. **48**, 1918–1923 (1968) (cit. on pp. 54, 57–58, 158).

[159]G. Johari and W Dannhauser, *Evidence for structural transformation in liquid octyl alcohols from pvt studies*, J. Chem. Phys. **48**, 3407–3408 (1968) (cit. on pp. 54, 58, 158).

[160]G. P. Johari and W. Dannhauser, *Viscosity of isomeric octyl alcohols as a function of temperature and pressure*, J. Chem. Phys. **51**, 1626–1631 (1969) (cit. on pp. 54, 58, 158).

[161]G. P. Johari and W. Dannhauser, *Dielectric properties of isomeric phenyl propanols*, Phys. Chem. Liq. **3**, 1–11 (1972) (cit. on pp. 54–55, 57, 158).

[162]P. Girard and P. Abadie, *B. theory of relaxation times. experimental curves of losses and of anomalous dispersion as a basis of a spectral method*, Trans. Faraday Soc. **42**, A040–A047 (1946) (cit. on p. 54).

[163]C. Hansen, F. Stickel, T. Berger, et al., *Dynamics of glass-forming liquids. III. Comparing the dielectric α- and β-relaxation of 1-propanol and o-terphenyl*, J. Chem. Phys. **107**, 1086–1093 (1997) (cit. on p. 54).

[164]H. Huth, L.-M. Wang, C. Schick, et al., *Comparing calorimetric and dielectric polarization modes in viscous 2-ethyl-1-hexanol*, J. Chem. Phys. **126**, 104503 (2007) (cit. on p. 54).

[165]K. Adachi and T. Kotaka, *Dielectric normal mode relaxation*, Prog. Polym. Sci. **18**, 585–622 (1993) (cit. on p. 55).

[166]M. E. Cates, *Reptation of living polymers: dynamics of entangled polymers in the presence of reversible chain-scission reactions*, Macromolecules **20**, 2289–2296 (1987) (cit. on pp. 55, 65).

[167]M. Cates, *Dynamics of living polymers and flexible surfactant micelles: scaling laws for dilution*, J. Phys. France **49**, 1593–1600 (1988) (cit. on pp. 55, 65).

[168]J. Gabriel, F. Pabst, and T. Blochowicz, *Debye process and β -relaxation in 1-propanol probed by dielectric spectroscopy and depolarized dynamic light scattering*, J. Phys. Chem. B **121**, 8847–8853 (2017) (cit. on pp. 55, 57, 164).

[169]J. Gabriel, F. Pabst, A. Helbling, et al., *Nature of the Debye-Process in Monohydroxy Alcohols: 5-Methyl-2-Hexanol Investigated by Depolarized Light Scattering and Dielectric Spectroscopy*, Phys. Rev. Lett. **121**, 10.1103/PhysRevLett.121.035501 (2018) (cit. on pp. 55, 164).

[170]T. Böhmer, T. Richter, J. P. Gabriel, et al., *Revealing complex relaxation behavior of monohydroxy alcohols in a series of octanol isomers*, J. Chem. Phys. **159**, 054501 (2023) (cit. on pp. 55, 58, 165).

[171]G. P. Johari, O. E. Kalinovskaya, and J. K. Vij, *Effects of induced steric hindrance on the dielectric behavior and H bonding in the supercooled liquid and vitreous alcohol*, J. Chem. Phys. **114**, 4634–4642 (2001) (cit. on pp. 55, 57, 158).

[172]O. E. Kalinovskaya, J. K. Vij, and G. P. Johari, *Mechanism of the major orientation polarization in alcohols, and the effects of steric hindrance-, and dilution-induced decrease on h-bonding*, J. Phys. Chem. A **105**, 5061–5070 (2001) (cit. on pp. 55, 57, 158).

[173]M. Tarnacka, A. Czaderna-Lekka, Z. Wojnarowska, et al., *Nature of dielectric response of phenyl alcohols*, J. Phys. Chem. B **127**, 6191–6196 (2023) (cit. on p. 58).

[174]J. P. Gabriel, E. Thoms, and R. Richert, *High electric fields elucidate the hydrogen-bonded structures in 1-phenyl-1-propanol*, J. Mol. Liq. **330**, 115626 (2021) (cit. on p. 58).

[175]A. Nowok, K. Jurkiewicz, M. Dulski, et al., *Influence of molecular geometry on the formation, architecture and dynamics of h-bonded supramolecular associates in 1-phenyl alcohols*, J. Mol. Liq. **326**, 115349 (2021) (cit. on p. 58).

[176]A. Nowok, M. Dulski, K. Jurkiewicz, et al., *Molecular stiffness and aromatic ring position – crucial structural factors in the self-assembly processes of phenyl alcohols*, J. Mol. Liq. **335**, 116426 (2021) (cit. on p. 58).

[177]J. Grelska, K. Jurkiewicz, A. Nowok, et al., *Computer simulations as an effective way to distinguish supramolecular nanostructure in cyclic and phenyl alcohols*, Phys. Rev. E **108**, 024603 (2023) (cit. on p. 58).

[178]C. Dugue, J. Emery, and R. A. Pethrick, *Ultrasonic and 13 C N.M.R. studies of isomeric octanols*, Mol. Phys. **41**, 703–713 (1980) (cit. on p. 58).

[179]T Hecksher and B Jakobsen, *Communication: supramolecular structures in monohydroxy alcohols: insights from shear-mechanical studies of a systematic series of octanol structural isomers*, J. Chem. Phys. **141**, 101104 (2014) (cit. on pp. 58, 158).

[180]A. Young-Gonzales and R Richert, *Field induced changes in the ring/chain equilibrium of hydrogen bonded structures: 5-methyl-3-heptanol*, J. Chem. Phys. **145**, 074503 (2016) (cit. on p. 58).

[181]S. Bauer, H. Wittkamp, S. Schildmann, et al., *Broadband dynamics in neat 4-methyl-3-heptanol and in mixtures with 2-ethyl-1-hexanol*, J. Chem. Phys. **139**, 134503 (2013) (cit. on pp. 59, 62–63).

[182]S. Pawlus, M. Wikarek, C. Gainaru, et al., *How do high pressures change the debye process of 4-methyl-3-heptanol?*, J. Chem. Phys. **139**, 064501 (2013) (cit. on pp. 59, 62–63).

[183]S Arrese-Igor, A Alegría, and J Colmenero, *Multimodal character of shear viscosity response in hydrogen bonded liquids*, Phys. Chem. Chem. Phys. **20**, 27758–27765 (2018) (cit. on pp. 60, 158).

[184]S Arrese-Igor, A Alegría, A Arbe, et al., *Insights into the non-exponential behavior of the dielectric debye-like relaxation in monoalcohols*, J. Mol. Liq. **312**, 113441 (2020) (cit. on pp. 60, 158).

[185]S Schildmann, A Reiser, R Gainaru, et al., *Nuclear magnetic resonance and dielectric noise study of spectral densities and correlation functions in the glass forming monoalcohol 2-ethyl-1-hexanol*, J. Chem Phys. **135**, 174511 (2011) (cit. on pp. 60–62).

[186]S. Bauer, *Assoziationsgleichgewichte und dynamische prozesse in glasbildenden debye-flüssigkeiten*, PhD thesis (Technische Universität Dortmund, Mar. 2015) (cit. on p. 63).

[187]S. Bauer, K. Burlafinger, C. Gainaru, et al., *Debye relaxation and 250 k anomaly in glass forming monohydroxy alcohols*, J. Chem. Phys. **138**, 094505 (2013) (cit. on p. 64).

[188]L. Onsager, *Electric moments of molecules in liquids*, J. Am. Chem. Soc. **58**, 1486–1493 (1936) (cit. on p. 65).

[189]G. Williams, M. Cook, and P. J. Hains, *Molecular motion in amorphous polymers. consideration of the mechanism for α, β and ($\alpha\beta$) dielectric relaxations*, J. Chem. Soc., Faraday Trans. 2 **68**, 1045–1050 (1972) (cit. on p. 65).

[190]S. Cheng, S. Patil, and S. Cheng, *Hydrogen bonding exchange and supramolecular dynamics of monohydroxy alcohols*, Phys. Rev. Lett. **132**, 058201 (2024) (cit. on p. 65).

[191]T. Böhmer, J. P. Gabriel, R. Zeißler, et al., *Glassy dynamics in polyalcohols: intermolecular simplicity vs. intramolecular complexity*, Phys. Chem. Chem. Phys. **24**, 18272–18280 (2022) (cit. on pp. 66, 164, 166).

[192]E. R. Alonso, I. León, L. Kolesniková, et al., *The Structural Signs of Sweetness in Artificial Sweeteners: A Rotational Study of Sorbitol and Dulcitol*, ChemPhysChem **19**, 3334–3340 (2018) (cit. on pp. 67, 70).

[193]A. Döß, *Relaxationsuntersuchungen in unterkuhlten und glasig erstarrten polyalkoholen mittels dielektrischer und nmr-spektroskopie*, PhD thesis (Mainz Univ., Diss., 2001) (cit. on pp. 66, 68–70).

[194]M. M. Margulies, B Sixou, L David, et al., *Molecular mobility of sorbitol and maltitol: a 13 c nmr and molecular dynamics approach*, Eur. Phys. J. E **3**, 55–62 (2000) (cit. on p. 67).

[195]B. Sixou, L. David, M. M. Margulies, et al., *Condensed State Molecular Dynamics in Sorbitol and Maltitol: Mobility Gradients and Conformation Transitions*, Mol. Simul. **27**, 243–265 (2001) (cit. on pp. 67–68, 70).

[196]M Becher, T Wohlfromm, E. A. Rössler, et al., *Molecular dynamics simulations vs field-cycling NMR relaxometry: Structural relaxation mechanisms in the glass-former glycerol revisited*, J. Chem. Phys. **154**, 124503 (2021) (cit. on pp. 68–69).

[197]M. Krynski, F. Mocanu, and S. Elliott, *Elucidation of the Nature of Structural Relaxation in Glassy d -Sorbitol*, J. Phys. Chem. B **124**, 1833–1838 (2020) (cit. on pp. 69–70).

[198]E. Kaminska, K. Kaminski, M. Paluch, et al., *Additive property of secondary relaxation processes in di-n-octyl and di-isooctyl phthalates: signature of non-johari-goldstein relaxation*, J. Chem. Phys. **126**, 174501 (2007) (cit. on p. 70).

[199]M. T. Ruggiero, M. Krynski, E. O. Kissi, et al., *The significance of the amorphous potential energy landscape for dictating glassy dynamics and driving solid-state crystallisation*, Phys. Chem. Chem. Phys. **19**, 30039–30047 (2017) (cit. on p. 70).

[200]A. Döß, M. Paluch, H. Sillescu, et al., *From Strong to Fragile Glass Formers: Secondary Relaxation in Polyalcohols*, Phys. Rev. Lett. **88**, 095701 (2002) (cit. on p. 70).

[201] M. Nakanishi and R. Nozaki, *Dynamics and structure of hydrogen-bonding glass formers: Comparison between hexanetriol and sugar alcohols based on dielectric relaxation*, Phys. Rev. E **81**, 041501 (2010) (cit. on p. 71).

[202] R. Horstmann, *On the glass transition of bulk and confined polyamorphic liquids: a molecular dynamics simulations study*, PhD thesis (Technische Universität, Darmstadt, 2023) (cit. on pp. 73, 77, 80, 85–86, 158).

[203] K. Adachi and Y. Ishida, *Effect of diluent on molecular motion and glass transition in polymers. iv. the system poly(methyl acrylate)—toluene*, Polym. J. (Tokyo, Jpn.) **11**, 233–239 (1979) (cit. on pp. 73–74).

[204] D. A. Savin, A. M. Larson, and T. P. Lodge, *Effect of composition on the width of the calorimetric glass transition in polymer–solvent and solvent–solvent mixtures*, J. Polym. Sci., Part B: Polym. Phys. **42**, 1155–1163 (2004) (cit. on p. 73).

[205] T. Blochowicz, S. A. Lusceac, P. Gutfreund, et al., *Two glass transitions and secondary relaxations of methyltetrahydrofuran in a binary mixture*, J. Phys. Chem. B **115**, 1623–1637 (2011) (cit. on pp. 73–74).

[206] T. P. Lodge, E. R. Wood, and J. C. Haley, *Two calorimetric glass transitions do not necessarily indicate immiscibility: the case of peo/pmma*, J. Polym. Sci., Part B: Polym. Phys. **44**, 756–763 (2006) (cit. on p. 73).

[207] A. N. Gaikwad, E. R. Wood, T. Ngai, et al., *Two calorimetric glass transitions in miscible blends containing poly(ethylene oxide)*, Macromolecules **41**, 2502–2508 (2008) (cit. on p. 73).

[208] G. Floudas, W. Steffen, E. W. Fischer, et al., *Solvent and polymer dynamics in concentrated polystyrene/toluene solutions*, J. Chem. Phys. **99**, 695–703 (1993) (cit. on p. 74).

[209] T. Blochowicz, C. Karle, A. Kudlik, et al., *Molecular dynamics in binary organic glass formers*, J. Phys. Chem. B **103**, 4032–4044 (1999) (cit. on p. 74).

[210] T. Blochowicz, S. Schramm, S. Lusceac, et al., *Signature of a type-a glass transition and intrinsic confinement effects in a binary glass-forming system*, Phys. Rev. Lett. **109**, 035702 (2012) (cit. on pp. 74–76, 79, 84, 158).

[211] D. Bingemann, N. Wirth, J. Gmeiner, et al., *Decoupled dynamics and quasi-logarithmic relaxation in the polymer-plasticizer system poly(methyl methacrylate)/tri-m-cresyl phosphate studied with 2d nmr*, Macromolecules **40**, 5379–5388 (2007) (cit. on p. 74).

[212] J. Colmenero and A. Arbe, *Segmental dynamics in miscible polymer blends: recent results and open questions*, Soft Matter **3**, 1474–1485 (2007) (cit. on p. 74).

[213] I. Cendoya, A. Alegría, J. M. Alberdi, et al., *Effect of blending on the pvme dynamics. a dielectric, nmr, and qens investigation*, Macromolecules **32**, 4065–4078 (1999) (cit. on p. 74).

[214] M. Uhl, J. K. H. Fischer, P. Sippel, et al., *Glycerol confined in zeolitic imidazolate frameworks: the temperature-dependent cooperativity length scale of glassy freezing*, J. Chem. Phys. **150**, 024504 (2019) (cit. on pp. 74–75).

[215] P Medick, T Blochowicz, M Vogel, et al., *Comparing the dynamical heterogeneities in binary glass formers and in a glass former embedded in a zeolite – a 2h nmr study*, J. Non-Cryst. Solids **307-310**, 565–572 (2002) (cit. on p. 74).

[216] J. Schüller, R. Richert, and E. W. Fischer, *Dielectric relaxation of liquids at the surface of a porous glass*, Phys. Rev. B **52**, 15232–15238 (1995) (cit. on p. 74).

[217] J. K. H. Fischer, P. Sippel, D. Denysenko, et al., *Metal-organic frameworks as host materials of confined supercooled liquids*, J. Chem. Phys. **143**, 154505 (2015) (cit. on p. 74).

[218] M. Arndt, R. Stannarius, H. Groothues, et al., *Length scale of cooperativity in the dynamic glass transition*, Phys. Rev. Lett. **79**, 2077–2080 (1997) (cit. on p. 75).

[219] P. J. Hains and G. Williams, *Molecular motion in polystyrene-plasticizer systems as studied by dielectric relaxation*, Polymer **16**, 725–729 (1975) (cit. on pp. 75, 84, 158).

[220] G. Fytas, A. Rizos, G. Floudas, et al., *Solvent mobility in polystyrene/aroclor solutions by depolarized rayleigh scattering*, J. Chem. Phys. **93**, 5096–5104 (1990) (cit. on pp. 75, 84, 158).

[221] G. Floudas, G. Fytas, and W. Brown, *Solvent Mobility in Poly(methyl methacrylate)/toluene Solutions by Depolarized and Polarized Light Scattering*, J. Chem. Phys. **96**, 2164–2174 (1992) (cit. on pp. 75, 77, 84, 158).

[222] R. Kahlau, D. Bock, B. Schmidtke, et al., *Dynamics of asymmetric binary glass formers. i. a dielectric and nuclear magnetic resonance spectroscopy study*, J. Chem. Phys. **140**, 044509 (2014) (cit. on pp. 75, 84, 158).

[223] B. Pötzschner, F. Mohamed, C. Bächer, et al., *Non-polymeric asymmetric binary glass-formers. i. main relaxations studied by dielectric, 2h nmr, and 31p nmr spectroscopy*, J. Chem. Phys. **146**, 164503 (2017) (cit. on pp. 75–76, 84, 158).

[224] S. Cerveny, I. Combarro-Palacios, and J. Swenson, *Evidence of coupling between the motions of water and peptides*, J. Phys. Chem. Lett. **7**, 4093–4098 (2016) (cit. on pp. 75–76, 86, 158).

[225] S. Cerveny and J. Swenson, *Water dynamics in the hydration shells of biological and non-biological polymers*, J. Chem. Phys. **150**, 234904 (2019) (cit. on pp. 75–76, 86, 158).

[226] M. Weigler, I. Combarro-Palacios, S. Cerveny, et al., *On the microscopic origins of relaxation processes in aqueous peptide solutions undergoing a glass transition*, J. Chem. Phys. **152**, 234503 (2020) (cit. on pp. 76, 86).

[227] A. C. Ouano and R. Pecora, *Rotational Relaxation of Chlorobenzene in Poly(methyl methacrylate). 1. Temperature and Concentration Effects*, Macromolecules **13**, 1167–1173 (1980) (cit. on p. 77).

[228] K O'Driscoll and R. A. Sanayei, *Chain-length dependence of the glass transition temperature*, Macromolecules **24**, 4479–4480 (1991) (cit. on p. 77).

[229] L. N. G. Filon, *Iii.—on a quadrature formula for trigonometric integrals*, Proc. R. Soc. Edinburgh **49**, 38–47 (1930) (cit. on p. 81).

[230] L. Berthier and W. Kob, *Static point-to-set correlations in glass-forming liquids*, Phys. Rev. E **85**, 011102 (2012) (cit. on p. 82).

[231] F. Klameth, P. Henritzi, and M. Vogel, *Static and dynamic length scales in supercooled liquids: insights from molecular dynamics simulations of water and tri-propylene oxide*, J. Chem. Phys. **140**, 144501 (2014) (cit. on p. 82).

[232] R. Horstmann, E. P. Sanjon, B. Drossel, et al., *Effects of confinement on supercooled tetrahedral liquids*, J. Chem. Phys. **150**, 214704 (2019) (cit. on p. 82).

[233] S. Capaccioli, L. Zheng, A. Kyritsis, et al., *The dynamics of hydrated proteins are the same as those of highly asymmetric mixtures of two glass-formers*, ACS Omega **6**, 340–347 (2021) (cit. on p. 86).

[234] F. Simon, *ber den zustand der unterkühlten flüssigkeiten und gläser*, Z. anorg. allg. Chem. **203**, 219–227 (1931) (cit. on p. 89).

[235]A. J. Kovacs, *Applicability of the free volume concept on relaxation phenomena in the glass transition range*, Rheol. Acta **5**, 262–269 (1966) (cit. on pp. 89–90).

[236]H. Stuart, *Physikalische ursachen der alterung von kunststoffen*, Angew. Chem. **79**, 877–884 (1967) (cit. on p. 89).

[237]M. Micoulaut, *Relaxation and physical aging in network glasses: a review*, Rep. Prog. Phys. **79**, 066504 (2016) (cit. on p. 89).

[238]R. C. Welch, J. R. Smith, M. Potuzak, et al., *Dynamics of glass relaxation at room temperature*, Phys. Rev. Lett. **110**, 265901 (2013) (cit. on p. 89).

[239]C. G. Robertson and G. L. Wilkes, *Refractive index: a probe for monitoring volume relaxation during physical aging of glassy polymers*, Polymer **39**, 2129–2133 (1998) (cit. on p. 89).

[240]N. Tanio and T. Nakanishi, *Physical aging and refractive index of poly (methyl methacrylate) glass*, Polym. J. **38**, 814–818 (2006) (cit. on p. 89).

[241]G. Odegard and A. Bandyopadhyay, *Physical aging of epoxy polymers and their composites*, J. Polym. Sci., Part B: Polym. Phys. **49**, 1695–1716 (2011) (cit. on p. 89).

[242]G. B. McKenna, Y. Leterrier, and C. R. Schultheisz, *The evolution of material properties during physical aging*, Polym. Eng. Sci. **35**, 403–410 (1995) (cit. on pp. 89–90).

[243]S. Kolla and S. L. Simon, *The -effective paradox: new measurements towards a resolution*, Polymer **46**, 733–739 (2005) (cit. on p. 89).

[244]P. Lunkenheimer, R. Wehn, U. Schneider, et al., *Glassy aging dynamics*, Phys. Rev. Lett. **95**, 055702 (2005) (cit. on pp. 89, 122).

[245]G. B. McKenna and S. L. Simon, *50th anniversary perspective: challenges in the dynamics and kinetics of glass-forming polymers*, Macromolecules **50**, 6333–6361 (2017) (cit. on p. 90).

[246]B. J. Berne and R. Pecora, *Dynamic light scattering: with applications to chemistry, biology, and physics* (Courier Corporation, 2000) (cit. on p. 93).

[247]A. P. Y. Wong and P. Wiltzius, *Dynamic light scattering with a CCD camera*, Rev. Sci. Instrum. **64**, 2547–2549 (1993) (cit. on p. 93).

[248]L. Cipelletti and D. A. Weitz, *Ultralow-angle dynamic light scattering with a charge coupled device camera based multispeckle, multitau correlator*, Rev. Sci. Instrum. **70**, 3214–3221 (1999) (cit. on p. 93).

[249]L. Cipelletti, S. Manley, R. C. Ball, et al., *Universal aging features in the restructuring of fractal colloidal gels*, Phys. Rev. Lett. **84**, 2275–2278 (2000) (cit. on pp. 93–94).

[250]L. Cipelletti and L. Ramos, *Slow dynamics in glassy soft matter*, J. Phys.: Condens.Matter **17**, R253 (2005) (cit. on p. 93).

[251]S. Kirsch, V. Frenz, W. Schärtl, et al., *Multispeckle autocorrelation spectroscopy and its application to the investigation of ultraslow dynamical processes*, J. Chem. Phys. **104**, 1758–1761 (1996) (cit. on pp. 93–94).

[252]V. Viasnoff, F. Lequeux, and D. J. Pine, *Multispeckle diffusing-wave spectroscopy: A tool to study slow relaxation and time-dependent dynamics*, Rev. Sci. Instrum. **73**, 2336–2344 (2002) (cit. on pp. 94, 96).

[253]H. Bissig, S. Romer, L. Cipelletti, et al., *Intermittent dynamics and hyper-aging in dense colloidal gels*, PhysChemComm **6**, 21–23 (2003) (cit. on p. 94).

[254]L. Cipelletti, H Bissig, V Trappe, et al., *Time-resolved correlation: a new tool for studying temporally heterogeneous dynamics*, J. Phys.: Condens.Matter **15**, S257 (2002) (cit. on p. 94).

[255]L. Ramos and L. Cipelletti, *Ultraslow dynamics and stress relaxation in the aging of a soft glassy system*, Phys. Rev. Lett. **87**, 245503 (2001) (cit. on p. 94).

[256]P. Mayer, H. Bissig, L. Berthier, et al., *Heterogeneous dynamics of coarsening systems*, Phys. Rev. Lett. **93**, 115701 (2004) (cit. on p. 94).

[257]A. Duri, H. Bissig, V. Trappe, et al., *Time-resolved-correlation measurements of temporally heterogeneous dynamics*, Phys. Rev. E **72**, 051401 (2005) (cit. on p. 94).

[258]R. Höhler, S. Cohen-Addad, and D. J. Durian, *Multiple light scattering as a probe of foams and emulsions*, Curr. Opin. Colloid Interface Sci. **19**, 242–252 (2014) (cit. on p. 94).

[259]A. Duri, D. A. Sessoms, V. Trappe, et al., *Resolving long-range spatial correlations in jammed colloidal systems using photon correlation imaging*, Phys. Rev. Lett. **102**, 085702 (2009) (cit. on p. 94).

[260]Z. Filiberti, R. Piazza, and S. Buzzaccaro, *Multiscale relaxation in aging colloidal gels: from localized plastic events to system-spanning quakes*, Phys. Rev. E **100**, 042607 (2019) (cit. on p. 94).

[261]V. Viasnoff and F. m. c. Lequeux, *Rejuvenation and overaging in a colloidal glass under shear*, Phys. Rev. Lett. **89**, 065701 (2002) (cit. on pp. 94, 141).

[262]S. Aime, L. Ramos, and L. Cipelletti, *Microscopic dynamics and failure precursors of a gel under mechanical load*, Proc. Natl. Acad. Sci. **115**, 3587–3592 (2018) (cit. on p. 94).

[263]J. Ju, L. Cipelletti, S. Zoellner, et al., *Multispeckle diffusing wave spectroscopy as a tool to study heterogeneous mechanical behavior in soft solids*, J. Rheol. **66**, 1269–1283 (2022) (cit. on p. 94).

[264]S. Aime and L. Cipelletti, *Probing shear-induced rearrangements in fourier space. i. dynamic light scattering*, Soft Matter **15**, 200–212 (2019) (cit. on p. 94).

[265]S. Aime, D. Truzzolillo, D. J. Pine, et al., *A unified state diagram for the yielding transition of soft colloids*, Nat. Phys. **19**, 1673–1679 (2023) (cit. on p. 94).

[266]S. Aime, M. Sabato, L. Xiao, et al., *Dynamic speckle holography*, Phys. Rev. Lett. **127**, 088003 (2021) (cit. on p. 94).

[267]B. Ruta, Y. Chushkin, G. Monaco, et al., *Atomic-scale relaxation dynamics and aging in a metallic glass probed by x-ray photon correlation spectroscopy*, Phys. Rev. Lett. **109**, 165701 (2012) (cit. on p. 94).

[268]Z. Evenson, B. Ruta, S. Hechler, et al., *X-ray photon correlation spectroscopy reveals intermittent aging dynamics in a metallic glass*, Phys. Rev. Lett. **115**, 175701 (2015) (cit. on p. 94).

[269]V. Giordano and B Ruta, *Unveiling the structural arrangements responsible for the atomic dynamics in metallic glasses during physical aging*, Nat. Comm. **7**, 10344 (2016) (cit. on p. 94).

[270]A. Cornet, G. Garbarino, F. Zontone, et al., *Denser glasses relax faster: enhanced atomic mobility and anomalous particle displacement under in-situ high pressure compression of metallic glasses*, Acta Mater. **255**, 119065 (2023) (cit. on p. 94).

[271]J. W. Goodman, *Statistical properties of laser speckle patterns*, in *Laser speckle and related phenomena*, edited by J. C. Dainty (Springer Berlin Heidelberg, Berlin, Heidelberg, 1975), pp. 9–75 (cit. on p. 97).

[272]B. Jakobsen, A. T. Holmes, T. Rasmussen, et al., *Huginn: a peltier-based sub-cryostat for neutron scattering*, J. Neutron Res. **21**, 47–57 (2019) (cit. on p. 103).

[273]A. Q. Tool and C. G. Eicitlin, *Variations caused in the heating curves of glass by heat treatment*, J. Am. Ceram. Soc. **14**, 276–308 (1931) (cit. on p. 108).

[274]A. Q. Tool, *Relation between inelastic deformability and thermal expansion of glass in its annealing range*, J. Am. Ceram. Soc. **29**, 240–253 (1946) (cit. on p. 108).

[275]A. J. Kovacs, J. J. Aklonis, J. M. Hutchinson, et al., *Isobaric volume and enthalpy recovery of glasses. ii. a transparent multiparameter theory*, J. Polym. Sci., Part B: Polym. Phys. **17**, 1097–1162 (1979) (cit. on p. 108).

[276]J. Málek, *Structural relaxation rate and aging in amorphous solids*, J. Phys. Chem. C **127**, 6080–6087 (2023) (cit. on pp. 108, 158).

[277]L. A. Roed, T. Hecksher, J. C. Dyre, et al., *Generalized single-parameter aging tests and their application to glycerol*, J. Chem. Phys. **150**, 044501 (2019) (cit. on pp. 109–110, 122, 125).

[278]I. M. Douglass and J. C. Dyre, *Distance-as-time in physical aging*, Phys. Rev. E **106**, 054615 (2022) (cit. on pp. 111–112, 128, 146, 159).

[279]L. F. Cugliandolo and J Kurchan, *On the out-of-equilibrium relaxation of the sherrington-kirkpatrick model*, J. Phys. A: Math. Gen. **27**, 5749 (1994) (cit. on pp. 111, 129, 149, 159).

[280]T. Böhmer, J. P. Gabriel, L. Costigliola, et al., *Time reversibility during the ageing of materials*, Nature Physics **20**, 637–645 (2024) (cit. on pp. 112, 149, 166–167).

[281]R. Richert, P. Lunkenheimer, S. Kastner, et al., *On the derivation of equilibrium relaxation times from aging experiments*, J. Phys. Chem. B **117**, 12689–12694 (2013) (cit. on p. 122).

[282]B. Riechers and R. Richert, *Structural recovery and fictive variables: the fictive electric field*, Thermochim. Acta **677**, 54–59 (2019) (cit. on pp. 122, 128).

[283]T. Hecksher, N. B. Olsen, and J. C. Dyre, *Fast contribution to the activation energy of a glass-forming liquid*, Proc. Natl. Acad. Sci. **116**, 16736–16741 (2019) (cit. on p. 122).

[284]H. E. Castillo and A. Parsaeian, *Local fluctuations in the ageing of a simple structural glass*, Nat. Phys. **3**, 26–28 (2007) (cit. on pp. 128, 146).

[285]A. Parsaeian and H. E. Castillo, *Equilibrium and nonequilibrium fluctuations in a glass-forming liquid*, Phys. Rev. Lett. **102**, 055704 (2009) (cit. on p. 128).

[286]K. E. Avila, H. E. Castillo, and A. Parsaeian, *Mapping dynamical heterogeneity in structural glasses to correlated fluctuations of the time variables*, Phys. Rev. Lett. **107**, 265702 (2011) (cit. on p. 128).

[287]R. Richert, *Physical aging and heterogeneous dynamics*, Phys. Rev. Lett. **104**, 085702 (2010) (cit. on p. 128).

[288]R. Richert, J. P. Gabriel, and E. Thoms, *Structural relaxation and recovery: a dielectric approach*, J. Phys. Chem. Lett. **12**, 8465–8469 (2021) (cit. on p. 128).

[289]R. Richert, *On the origin of time-aging-time superposition*, J. Chem. Phys. **160**, 024501 (2024) (cit. on p. 128).

[290]A. Parsaeian and H. E. Castillo, *Growth of spatial correlations in the aging of a simple structural glass*, Phys. Rev. E **78**, 060105 (2008) (cit. on pp. 129, 146).

[291]M. Zanin and D. Papo, *Algorithmic approaches for assessing irreversibility in time series: review and comparison*, Entropy **23**, 1474 (2021) (cit. on pp. 130, 135).

[292]A. J. Lawrance, *Directionality and reversibility in time series*, Int. Stat. Rev. **59**, 67–79 (1991) (cit. on pp. 130, 135).

[293]E. Roldán, I. Neri, M. Dörpinghaus, et al., *Decision making in the arrow of time*, Phys. Rev. Lett. **115**, 250602 (2015) (cit. on p. 130).

[294]J. B. Ramsey and P. Rothman, *Time irreversibility and business cycle asymmetry*, J. Money Credit Bank. **28**, 1–21 (1996) (cit. on p. 130).

[295]C. S. Daw, C. E. A. Finney, and M. B. Kennel, *Symbolic approach for measuring temporal "irreversibility"*, Phys. Rev. E **62**, 1912–1921 (2000) (cit. on p. 130).

[296]W. Yao, W. Yao, J. Wang, et al., *Quantifying time irreversibility using probabilistic differences between symmetric permutations*, Phys. Lett. A **383**, 738–743 (2019) (cit. on p. 130).

[297]J. H. Martínez, J. L. Herrera-Diestra, and M. Chavez, *Detection of time reversibility in time series by ordinal patterns analysis*, Chaos **28**, 123111 (2018) (cit. on p. 130).

[298]M. Zanin, A. Rodríguez-González, E. Menasalvas Ruiz, et al., *Assessing time series reversibility through permutation patterns*, Entropy **20**, 665 (2018) (cit. on p. 130).

[299]C. Cammarota and E. Rogora, *Time reversal, symbolic series and irreversibility of human heartbeat*, Chaos, Solitons Fractals **32**, 1649–1654 (2007) (cit. on p. 130).

[300]A. Seif, M. Hafezi, and C. Jarzynski, *Machine learning the thermodynamic arrow of time*, Nat. Phys. **17**, 105–113 (2021) (cit. on p. 130).

[301]L. Lacasa, B. Luque, F. Ballesteros, et al., *From time series to complex networks: the visibility graph*, Proc. Natl. Acad. Sci. **105**, 4972–4975 (2008) (cit. on p. 130).

[302]L. Lacasa, A. Nunez, É. Roldán, et al., *Time series irreversibility: a visibility graph approach*, Eur. Phys. J. B **85**, 1–11 (2012) (cit. on pp. 130, 133).

[303]L. Lacasa and R. Flanagan, *Time reversibility from visibility graphs of nonstationary processes*, Phys. Rev. E **92**, 022817 (2015) (cit. on pp. 130–131, 133).

[304]G. E. Uhlenbeck and L. S. Ornstein, *On the theory of the brownian motion*, Phys. Rev. **36**, 823–841 (1930) (cit. on p. 131).

[305]C. Bergillos, *Ts2vg: time series to visibility graphs*, `https://github.com/CarlosBergillos/ts2vg`, 2021 (cit. on p. 131).

[306]X. Lan, H. Mo, S. Chen, et al., *Fast transformation from time series to visibility graphs*, Chaos **25**, 083105 (2015) (cit. on p. 131).

[307]S. Kullback and R. A. Leibler, *On information and sufficiency*, Ann. Math. Stat. **22**, 79–86 (1951) (cit. on p. 131).

[308]J. Lin, *Divergence measures based on the shannon entropy*, IEEE Trans. Inf. Theory **37**, 145–151 (1991) (cit. on p. 131).

[309]T. Schreiber and A. Schmitz, *Surrogate time series*, Phys. D **142**, 346–382 (2000) (cit. on p. 133).

[310]V. Venema, F. Ament, and C. Simmer, *A stochastic iterative amplitude adjusted fourier transform algorithm with improved accuracy*, Nonlinear Process. Geophys. **13**, 321–328 (2006) (cit. on p. 133).

[311]B. Goswami, *Iterated amplitude adjusted fourier transform time series surrogates*, `https://github.com/mlcs/iaaft`, 2021 (cit. on p. 133).

[312]M. D. Vamvakaris, A. A. Pantelous, and K. M. Zuev, *Time series analysis of sp 500 index: a horizontal visibility graph approach*, Phys. A **497**, 41–51 (2018) (cit. on p. 133).

[313]D. Zhao, X. Yang, W. Song, et al., *Visibility graph analysis of the sea surface temperature irreversibility during el niño events*, Nonlinear Dyn. **111**, 17393–17409 (2023) (cit. on p. 133).

[314]P. J. Brockwell and R. A. Davis, *Introduction to time series and forecasting* (Springer, 2002) (cit. on pp. 135–136).

[315]M. Kroon, G. H. Wegdam, and R. Sprik, *Dynamic light scattering studies on the sol-gel transition of a suspension of anisotropic colloidal particles*, Phys. Rev. E **54**, 6541–6550 (1996) (cit. on p. 141).

[316]D. Bonn, H. Kellay, H. Tanaka, et al., *Laponite: what is the difference between a gel and a glass?*, Langmuir **15**, 7534–7536 (1999) (cit. on p. 141).

[317]T. Nicolai and S. Cocard, *Light scattering study of the dispersion of laponite*, Langmuir **16**, 8189–8193 (2000) (cit. on p. 141).

[318]B. Ruzicka, L. Zulian, and G. Ruocco, *Routes to gelation in a clay suspension*, Phys. Rev. Lett. **93**, 258301 (2004) (cit. on p. 141).

[319]S. Jabbari-Farouji, G. H. Wegdam, and D. Bonn, *Gels and glasses in a single system: evidence for an intricate free-energy landscape of glassy materials*, Phys. Rev. Lett. **99**, 065701 (2007) (cit. on p. 141).

[320]H. Z. Cummins, *Liquid, glass, gel: the phases of colloidal laponite*, J. Non-Cryst. Solids **353**, 3891–3905 (2007) (cit. on pp. 141–142, 144).

[321]B. Ruzicka, L. Zulian, R. Angelini, et al., *Arrested state of clay-water suspensions: gel or glass?*, Phys. Rev. E **77**, 020402 (2008) (cit. on p. 141).

[322]S. Jabbari-Farouji, H. Tanaka, G. H. Wegdam, et al., *Multiple nonergodic disordered states in laponite suspensions: a phase diagram*, Phys. Rev. E **78**, 061405 (2008) (cit. on p. 141).

[323]B. Ruzicka and E. Zaccarelli, *A fresh look at the laponite phase diagram*, Soft Matter **7**, 1268–1286 (2011) (cit. on pp. 141–142).

[324]B. Ruzicka, E. Zaccarelli, L. Zulian, et al., *Observation of empty liquids and equilibrium gels in a colloidal clay*, Nat. Mater. **10**, 56–60 (2011) (cit. on p. 141).

[325]J. L. Dávila and M. A. d'Ávila, *Laponite as a rheology modifier of alginate solutions: physical gelation and aging evolution*, Carbohydr. Polym. **157**, 1–8 (2017) (cit. on p. 141).

[326]S. Samimi Gharaie, S. M. H. Dabiri, and M. Akbari, *Smart shear-thinning hydrogels as injectable drug delivery systems*, Polymers **10**, 1317 (2018) (cit. on p. 141).

[327]H. Tomás, C. S. Alves, and J. Rodrigues, *Laponite®: a key nanoplatform for biomedical applications?*, Nanomedicine **14**, 2407–2420 (2018) (cit. on p. 141).

[328]X. Di, X. Peng, and G. B. McKenna, *Dynamics of a thermo-responsive microgel colloid near to the glass transition*, J. Chem. Phys. **140**, 10.1063/1.4863327 (2014) (cit. on p. 141).

[329]Q. Li, X. Peng, and G. B. McKenna, *Physical aging and compressed exponential behaviors in a model soft colloidal system*, Soft Matter **15**, 2336–2347 (2019) (cit. on p. 141).

[330]X. Peng and G. B. McKenna, *Comparison of the physical aging behavior of a colloidal glass after shear melting and concentration jumps*, Phys. Rev. E **90**, 050301 (2014) (cit. on p. 141).

[331]D. Bonn, H Tanaka, G Wegdam, et al., *Aging of a colloidal "wigner" glass*, Europhys. Lett. **45**, 52 (1999) (cit. on p. 141).

[332]J. Bosse and S. D. Wilke, *Low-density ionic glass*, Phys. Rev. Lett. **80**, 1260–1263 (1998) (cit. on p. 142).

[333]E. Wigner, *Effects of the electron interaction on the energy levels of electrons in metals*, Trans. Faraday Soc. **34**, 678–685 (1938) (cit. on p. 142).

[334]S. Jabbari-Farouji, R. Zargar, G. H. Wegdam, et al., *Dynamical heterogeneity in aging colloidal glasses of laponite*, Soft Matter **8**, 5507–5512 (2012) (cit. on p. 142).

[335]W. Kob and J.-L. Barrat, *Aging effects in a lennard-jones glass*, Phys. Rev. Lett. **78**, 4581–4584 (1997) (cit. on p. 146).

[336]J.-L. Barrat and W. Kob, *Fluctuation-dissipation ratio in an aging lennard-jones glass*, Europhys. Lett. **46**, 637 (1999) (cit. on p. 146).

[337]W. Kob and J.-L. Barrat, *Fluctuations, response and aging dynamics in a simple glass-forming liquid out of equilibrium*, Eur. Phys. J. B **13**, 319–333 (2000) (cit. on p. 146).

[338]L. Berthier and G. Biroli, *Glasses and aging, a statistical mechanics perspective on*, in *Encyclopedia of complexity and systems science*, edited by R. A. Meyers (Springer New York, New York, NY, 2009), pp. 4209–4240 (cit. on p. 146).

[339]D. El Masri, L. Berthier, and L. Cipelletti, *Subdiffusion and intermittent dynamic fluctuations in the aging regime of concentrated hard spheres*, Phys. Rev. E **82**, 031503 (2010) (cit. on p. 146).

[340]S. Mehri, T. S. Ingebrigtsen, and J. C. Dyre, *Single-parameter aging in a binary Lennard-Jones system*, J. Chem. Phys. **154**, 094504 (2021) (cit. on p. 146).

[341]L. F. Elizondo-Aguilera, T. Rizzo, and T. Voigtmann, *From subaging to hyperaging in structural glasses*, Phys. Rev. Lett. **129**, 238003 (2022) (cit. on pp. 146, 153).

[342]W. Kob and H. C. Andersen, *Testing mode-coupling theory for a supercooled binary lennard-jones mixture i: the van hove correlation function*, Phys. Rev. E **51**, 4626–4641 (1995) (cit. on p. 146).

[343]S. Toxvaerd, U. R. Pedersen, T. B. Schrøder, et al., *Stability of supercooled binary liquid mixtures*, J. Chem. Phys. **130**, 224501 (2009) (cit. on p. 146).

[344]T. B. Schrøder and J. C. Dyre, *Solid-like mean-square displacement in glass-forming liquids*, J. Chem. Phys. **152**, 141101 (2020) (cit. on pp. 146, 167).

[345]N. P. Bailey, T. S. Ingebrigtsen, J. S. Hansen, et al., *RUMD: a general purpose molecular dynamics package optimized to utilize GPU hardware down to a few thousand particles*, Scipost Phys. **3**, 038 (2017) (cit. on pp. 146, 167).

[346]C. Chamon and L. F. Cugliandolo, *Fluctuations in glassy systems*, J. Stat. Mech.: Theory Exp. **2007**, P07022 (2007) (cit. on p. 149).

[347]A. Vila-Costa, M. Gonzalez-Silveira, C. Rodríguez-Tinoco, et al., *Emergence of equilibrated liquid regions within the glass*, Nat. Phys. **19**, 114–119 (2023) (cit. on p. 150).

[348]C. Herrero, C. Scalliet, M. Ediger, et al., *Two-step devitrification of ultrastable glasses*, Proc. Natl. Acad. Sci. **120**, e2220824120 (2023) (cit. on p. 150).

[349]G. B. McKenna, *Mechanical rejuvenation in polymer glasses: fact or fallacy?*, J. Phys.: Condens.Matter **15**, S737 (2003) (cit. on p. 153).

[350]K. Chen and K. S. Schweizer, *Molecular theory of physical aging in polymer glasses*, Phys. Rev. Lett. **98**, 167802 (2007) (cit. on p. 153).

[351] L. Berthier, *Sub-aging in a domain growth model*, Eur. Phys. J. B **17**, 689–692 (2000) (cit. on p. 153).

[352] L. Berthier and J.-P. Bouchaud, *Geometrical aspects of aging and rejuvenation in the ising spin glass: a numerical study*, Phys. Rev. B **66**, 054404 (2002) (cit. on p. 153).

[353] M. Warren and J. Rottler, *Quench, equilibration, and subaging in structural glasses*, Phys. Rev. Lett. **110**, 025501 (2013) (cit. on pp. 153–154, 159).

[354] J.-P. Bouchaud and D. S. Dean, *Aging on parisi's tree*, J. Phys. I **5**, 265–286 (1995) (cit. on pp. 153, 160).

[355] P. Le Doussal, C. Monthus, and D. S. Fisher, *Random walkers in one-dimensional random environments: exact renormalization group analysis*, Phys. Rev. E **59**, 4795–4840 (1999) (cit. on pp. 153, 160).

[356] B. Rinn, P. Maass, and J.-P. Bouchaud, *Multiple scaling regimes in simple aging models*, Phys. Rev. Lett. **84**, 5403–5406 (2000) (cit. on pp. 153, 155, 160).

[357] B. Rinn, P. Maass, and J.-P. Bouchaud, *Hopping in the glass configuration space: subaging and generalized scaling laws*, Phys. Rev. B **64**, 104417 (2001) (cit. on pp. 153, 155, 160).

[358] I. V. Blazhnov, N. P. Malomuzh, and S. V. Lishchuk, *Temperature dependence of density, thermal expansion coefficient and shear viscosity of supercooled glycerol as a reflection of its structure*, J. Chem. Phys. **121**, 6435–6441 (2004) (cit. on p. 163).

[359] M. I. Kabachnik, T. A. Mastryukova, and A. E. Shipov, *Reaction of phosphoramidites of phosphonamidites with acid anhydrides*, Zh. Obshch. Khim. **33**, 320–1 (1963) (cit. on p. 164).

[360] A. G. Peshwe, B. R. Arbad, and S. P. Pachaling, *Volumetric and viscometric studies on n, n-dimethylacetamide and methanol binary mixtures at different temperatures*, Int. J. Chem. Sci. **7**, 1505–1517 (2009) (cit. on p. 164).

[361] C. L. Yaws and P. K. Narasimhan, *Chapter 19 - dipole moment—organic compounds*, in *Thermophysical properties of chemicals and hydrocarbons*, edited by C. L. Yaws (William Andrew Publishing, Norwich, NY, 2009), pp. 672–682 (cit. on p. 164).

[362] L. De Lorenzi, M. Fermeglia, and G. Torriano, *Density, refractive index, and kinematic viscosity of diesters and triesters*, J. Chem. Eng. Data **42**, 919–923 (1997) (cit. on p. 164).

[363] A. I. Kemppinen and N. A. Gokcen, *Density of dibutyl phthalate*, J. Phys. Chem. **60**, 126–127 (1956) (cit. on p. 164).

[364] D. M. Petkovic, B. A. Kezele, and D. R. Rajic, *Dipole moments of some neutral organic phosphates*, J. Phys. Chem. **77**, 922–924 (1973) (cit. on p. 164).

[365] J. Wang, C. Li, C. Shen, et al., *Towards understanding the effect of electrostatic interactions on the density of ionic liquids*, Fluid Phase Equilib. **279**, 87–91 (2009) (cit. on p. 164).

[366] D. P. Evans, W. C. Davies, and W. J. Jones, *Clxvii.—the lower trialkyl orthophosphates. part i*, J. Chem. Soc., 1310–1313 (1930) (cit. on p. 164).

[367] M. J. Aroney, L. H. L. Chia, R. J. W. Le Fèvre, et al., *568. molecular polarisability. the dipole moments, molar kerr constants, and conformations of eleven phosphate and phosphite triesters as solutes in benzene*, J. Chem. Soc., 2948–2954 (1964) (cit. on p. 164).

[368] M. F. Mole, W. S. Holmes, and J. C. McCoubrey, *986. temperature-dependence of the liquid viscosities of some phosphorus compounds*, J. Chem. Soc., 5144–5149 (1964) (cit. on p. 164).

[369]N. V. Sidgwick, *Appendix. a table of dipole moments*, Trans. Faraday Soc. **30**, B00i–Blxxxvi (1934) (cit. on p. 164).

[370]L. Tommila E an Brehmer and H Elo, *Kinetic studies of ester hydrolysis. ix. alkaline hydrolysis of several new substituted benzoic acid esters*, Ann. Acad. Sci. Fenn., Ser. A2 **16**, 14 pp. (1945) (cit. on p. 164).

[371]A. Mandanici, M. Cutroni, and R. Richert, *Dynamics of glassy and liquid m-toluidine investigated by high-resolution dielectric spectroscopy*, J. Chem. Phys. **122**, 084508 (2005) (cit. on p. 164).

[372]G. Barclay, R. Le Fevre, and B. Smythe, *The variation of dipole moment with state for n-propyl-and n-butyl-amines. with notes on the apparent moments in solution of certain other amines*, Trans. Faraday Soc. **47**, 357–365 (1951) (cit. on p. 164).

[373]S. P. Sulthana, M Gowrisankar, S. Babu, et al., *Binary mixtures of 2-ethyl-1-hexanol with various functional groups (benzyl chloride, 3-methylaniline, 3-methoxyaniline and 2, 6-dimethylcyclohexanone)*, SN Appl. Sci. **2**, 1–11 (2020) (cit. on p. 164).

[374]S. Song, S. Xia, P. Ma, et al., *Densities and viscosities of n-formylmorpholine + benzene, + toluene at different temperatures and atmospheric pressures*, J. Chem. Eng. Data **52**, 591–595 (2007) (cit. on p. 164).

[375]J. Wisniak, G. Cortez, R. Peralta, et al., *Some thermodynamic properties of the binary systems of toluene with butyl methacrylate, allyl methacrylate, methacrylic acid and vinyl acetate at 20, 30 and 40 ∘ c*, J. Solution Chem. **36**, 997–1022 (2007) (cit. on p. 164).

[376]M. G. Faizullin, R. V. Galeev, and A. K. Mamleev, *Microwave spectrum of 2-methyltetrahydrofuran*, Russ. J. Phys. Chem. A **91**, 2275–2278 (2017) (cit. on p. 164).

[377]R. Francesconi, A. Bigi, K. Rubini, et al., *Molar heat capacities, densities, viscosities, and refractive indices of poly(ethylene glycols) + 2-methyltetrahydrofuran at (293.15, 303.15, and 313.15) k*, J. Chem. Eng. Data **52**, 2020–2025 (2007) (cit. on p. 164).

[378]D. S. Wankhede, N. N. Wankhede, M. K. Lande, et al., *Ultrasonic velocities and refractive indices of binary mixtures of propylene carbonate + n-alkanols*, Indian J. Pure Appl. Phys. **44**, 909–916 (2006) (cit. on p. 164).

[379]F. I. Mopsik, *Chapter ii tables of dielectric constants, dipole moments, and dielectric relaxation times*, in Digest of literature on dielectrics, Vol. 27 (IEEE, 1963), pp. 23–56 (cit. on p. 164).

[380]S. Weinstein and R. Richert, *Nonlinear features in the dielectric behavior of propylene glycol*, Phys. Rev. B **75**, 064302 (2007) (cit. on p. 164).

[381]C. M. Romero, M. S. Páez, and D. Pérez, *A comparative study of the volumetric properties of dilute aqueous solutions of 1-propanol, 1,2-propanediol, 1,3-propanediol, and 1,2,3-propanetriol at various temperatures*, J. Chem. Thermodyn. **40**, 1645–1653 (2008) (cit. on p. 164).

[382]Y. E. Ryabov, Y. Hayashi, A. Gutina, et al., *Features of supercooled glycerol dynamics*, Phys. Rev. B **67**, 132202 (2003) (cit. on p. 164).

[383]R. Casalini, M. Paluch, and C. M. Roland, *Dynamics of salol at elevated pressure*, J. Phys. Chem. A **107**, 2369–2373 (2003) (cit. on p. 164).

[384]C. S. Copeland and M. W. Rigg, *Determination of the dipole moments of some derivatives of hydroxybenzoic acid*, J. Am. Chem. Soc. **73**, 3584–3588 (1951) (cit. on p. 164).

[385]F. B. Marti, *Methods and equipment used at the bureau of physicochemical standards. iii. physicochemical properties of some organic compounds which are solid at ordinary temperature*, Bull. Soc. Chim. Belg. **39**, 590–626 (1930) (cit. on p. 164).

[386]W. G. Scaife, *The effects of temperature and pressure on the complex dielectric permittivity of liquid eugenol and glycerol*, J. Phys. D: Appl. Phys. **9**, 1489 (1976) (cit. on p. 164).

[387]M. G. Kim, *Viscoelastic relaxation in supercooled eugenol*, J. Chem. Soc. **71**, 415–425 (1975) (cit. on p. 164).

[388]T. Shinomiya, *Dielectric relaxation and intermolecular association for various secondary and tertiary alcohols*, Bull. Chem. Soc. Jpn. **62**, 3636–3642 (1989) (cit. on p. 164).

[389]S. C. Bhatia, J. Sangwan, R. Rani, et al., *Densities, viscosities, speeds of sound, and refractive indices of binary mixtures of 2-ethyl-1-hexanol with benzene and halobenzenes*, Int. J. Thermophys. **34**, 2076–2088 (2013) (cit. on p. 164).

LIST OF PUBLICATIONS

T. Böhmer, F. Pabst, J.P. Gabriel, T. Blochowicz
Dipolar order controls dielectric response of glass-forming liquids
Physical Review Letters **132**, 206101 (2024)
10.1103/PhysRevLett.132.206101

T. Böhmer, J.P. Gabriel, L. Costigliola, J.N. Kociok, T. Hecksher, J.C. Dyre, T. Blochowicz
Time reversibility during the aging of materials
Nature Physics **20**, 637–645 (2024)
10.1038/s41567-023-02366-z

T. Böhmer, T. Richter, J.P. Gabriel, R. Zeißler, P. Weigl, F. Pabst, T. Blochowicz
Revealing complex relaxation behavior of monohydroxy alcohols in a series of octanol isomers
Journal of Chemical Physics **159**, 054501 (2023)
10.1063/5.0160894

R. Zeißler, F. Pabst, **T. Böhmer**, T. Blochowicz
Influence of intramolecular dynamics on the relaxation spectra of simple liquids
Physical Chemistry Chemical Physics **25**, 16380-16388 (2023)
10.1039/D3CP01172K

T. Böhmer, J.P. Gabriel, R. Zeißler, T. Richter, T. Blochowicz
Glassy dynamics in polyalcohols: Intermolecular simplicity vs. intramolecular complexity
Physical Chemistry Chemical Physics **24**, 18272-18280 (2022)
10.1039/D2CP01969H

T. Böhmer, R. Horstmann, J.P. Gabriel, F. Pabst, M. Vogel, T. Blochowicz
Origin of apparent slow solvent dynamics in concentrated polymer solutions
Macromolecules **54**, 22, 10340–10349 (2021)
10.1021/acs.macromol.1c01414

F. Pabst, J.P. Gabriel, **T. Böhmer**, P. Weigl, A. Helbling, T. Richter, P. Zourchang, T. Walther, T. Blochowicz
Generic structural relaxation in supercooled liquids
Journal of Physical Chemistry Letters **12**, 14, 3685–3690 (2021)
10.1021/acs.jpclett.1c00753

J.P. Gabriel, P. Zourchang, F. Pabst, A. Helbling, P. Weigl, **T. Böhmer**, T. Blochowicz
Intermolecular cross-correlations in the dielectric response of glycerol
Physical Chemistry Chemical Physics **22**, 11644-11651 (2020)
10.1039/C9CP06344G

T. Böhmer, J.P. Gabriel, T. Richter, F. Pabst, T. Blochowicz
Influence of molecular architecture on the dynamics of H-bonded supramolecular structures in phenyl-propanols
Journal of Physical Chemistry B **123**, 51, 10959–10966 (2019)
10.1021/acs.jpcb.9b07768

J. Gabriel, F. Pabst, A. Helbling, **T. Böhmer**, T. Blochowicz
Nature of the Debye-process in monohydroxy alcohols: 5-methyl-2-hexanol investigated by depolarized light scattering and dielectric spectroscopy
Physical Review Letters **121**, 035501 (2018)
10.1103/PhysRevLett.121.035501

J. Gabriel, F. Pabst, A. Helbling, **T. Böhmer**, T. Blochowicz
Depolarized dynamic light scattering and dielectric spectroscopy: Two perspectives on molecular reorientation in supercooled liquids
The Scaling of Relaxation Processes. Advances in Dielectrics. Springer, Cham. (2018)
10.1007/978-3-319-72706-6_7

CONFERENCE CONTRIBUTIONS

Viscous liquids and the glass transition. XX. (2024), Roskilde, Denmark
Time evolution of the material time during physical aging (talk)

9th Int. Disc. Meeting on Relaxations in Complex Systems (2023), Chiba, Japan
Time-Reversibility during the Aging of Materials (talk)

Viscous liquids and the glass transition. XIX. (2023), Holbæk, Denmark
Time-Reversibility during the Aging of Materials (talk)

11th BDS Conference (2022), Donostia-San Sebastián, Spain
The Material Time of Physical Aging (talk)

11th BDS Conference (2022), Donostia-San Sebastián, Spain
The Origin of the Apparent Slow Solvent Dynamics in Binary Mixtures (poster)

International Dielectric Society Online Workshop (2021)
The Origin of the Apparent Slow Solvent Dynamics in Binary Mixtures (talk)

Deutsche Physikalische Gesellschaft - Spring Meeting (2017), Berlin, Germany
Secondary Relaxation Dynamics Observed by Photon-Correlation Spectroscopy (talk)

ACKNOWLEDGMENTS

Zuletzt möchte ich denjenigen danken, die zur Entstehung dieser Arbeit beigetragen haben.

Ein großer Dank gilt zunächst Thomas Blochowicz, der mich über sieben Jahre lang auf meinem wissenschaftlichen Weg begleitet hat und stets ein offenes Ohr für jegliche Fragen und Probleme hatte. Besonders zu schätzen weiß ich die große Freiheit zum Verfolgen eigener Forschungsideen, die mir gelassen wurde sowie die Möglichkeiten internationale Konferenzen zu besuchen. Beides hat mir in meiner bisherigen wissenschaftlichen Laufbahn sehr weitergeholfen.

Many thanks also go to Jeppe C. Dyre for being so closely involved with our research over the last two years. Your great interest in the light-scattering results has motivated me very much and our numerous discussions have sparked my interest for physical aging and more theoretical approaches to our recent research. I'm looking forward to working with you in the near future.

Außerdem möchte ich mich bei Michael Vogel als Zweitgutachter dieser Arbeit sowie für die Zusammenarbeit im Rahmen der binären Mischungen bedanken. Auch Benno Liebchen und Thomas Halfmann gilt Dank für die Bereitschaft als Prüfer an meiner Disputation teilzunehmen.

Großer Dank gebührt meinen vielen Kollegen der letzten Jahre: Zunächst Jan, der mich erst in Bachelor- und Masterarbeit betreut hat und dadurch zu einem wichtigen Kollegen und Freund wurde. Ich erinnere mich gerne an vieles zurück und hoffe, dass wir auch weiterhin so produktiv zusammenarbeiten werden. Außerdem Flo und Rolf für die gute Zusammenarbeit, die angenehmen Gespräche und zuletzt auch für das Korrekturlesen meiner Arbeit. Auch bei Peter und Robin möchte ich mich für die angenehme Zusammenarbeit bedanken. Dank gilt außerdem Parvaneh, Timo und Jen, die ich während meiner Promotion betreuen durfte und deren großes Interesse an unseren gemeinsamen Forschungsthemen mir immer viel Spaß bereitet hat. Außerdem auch dem Rest der Vogelgruppe für die vielen Kaffeepausen und die angenehme Atmosphäre im Institut.

Bedanken möchte ich mich außerdem bei Harald, Ibrahim und Klaus für die Zusammenarbeit bei der Planung von Probenzellen und für das viele spontane Helfen bei kleinen und großen Problemen, bei Barbara für die viele Unterstützung bei Organisatorischem, sowie bei Markus für die Hilfe mit verschiedensten Rechnern.

I also want to thank Pierre-Michel, for the fruitful discussions about dielectric and physics in general, as well as Tina and Lorenzo for the collaboration.

Großer Dank gebührt auch meinen Freunden Philipp, Janina, Max, Basti und Kai, die mich seit dem ersten Semester durchs ganze Studium und die Promotion begleitet haben. Unsere gemeinsamen Abende, Mittagessen, Kaffeepausen etc. waren die Highlights vieler Tage.

Zuletzt gilt ein großer Dank meinen Eltern und meiner Schwester für die jahrelange Unterstützung bei allem denkbaren. Besonders dankbar bin ich euch auch für das Wecken meines Interesses daran die Dinge zu verstehen zu wollen und zu hinterfragen; ohne gäbe es diese Arbeit vermutlich nicht. Zuletzt gilt ein riesiger Dank meiner Freundin Luisa: Für deine große Unterstützung beim Erreichen meiner Ziele seit dem Bachelorstudium und während meiner ganzen Promotionszeit. Aber auch für das Aushalten von langen Arbeitszeiten, die manchmal auch Zuhause nicht enden wollten und für die willkommene Ablenkung und die Freizeit, die

wir meistens zusammen verbracht haben und die ich mir alleine nicht immer ausreichend genommen hätte.

ERKLÄRUNG LAUT PROMOTIONSORDNUNG

§8 Abs. 1 lit. c PromO

Ich versichere hiermit, dass die elektronische Version meiner Dissertation mit der schriftlichen Version übereinstimmt.

§8 Abs. 1 lit. d PromO

Ich versichere hiermit, dass zu einem vorherigen Zeitpunkt noch keine Promotion versucht wurde. In diesem Fall sind nähere Angaben über Zeitpunkt, Hochschule, Dissertationsthema und Ergebnis dieses Versuchs mitzuteilen.

§9 Abs. 1 PromO

Ich versichere hiermit, dass die vorliegende Dissertation selbstständig und nur unter Verwendung der angegebenen Quellen verfasst wurde.

§9 Abs. 2 c PromO

Die Arbeit hat bisher noch nicht zu Prüfungszwecken gedient.
Darmstadt, 23. September 2024

Till Lukas Böhmer